

THE DESIGN OF PION AND MUON CHANNELS

by

Nadhim Mohamed Mustafa AL-QAZZAZ

M.Sc., University of Victoria, 1969

A DISSERTATION SUBMITTED IN PARTIAL FULFILLMENT

OF THE REQUIREMENTS FOR THE DEGREE OF

DOCTOR OF PHILOSOPHY

in the Department of

Physics

ACCEPTED
FACULTY OF GRADUATE STUDIES

[Redacted Signature]

DEAN

DATE

15 Sep/72

We accept this thesis as conforming

to the required standard

[Redacted Signature]

© Nadhim Mohamed Mustafa AL-QAZZAZ, 1972

UNIVERSITY OF VICTORIA

August 1972

ABSTRACT

Supervisor: Professor R.M. Pearce

Various concepts for the transportation of pions and muons from production targets external to the TRIUMF accelerator have been studied. A dual purpose magnetic channel capable of providing a pion beam and a muon beam has been designed.

Phase One of the system consists of five quadrupoles and two bending magnets, and forms the pion collection section of the muon channel. It also serves as a stopped pion channel. The maximum solid angle of acceptance of this channel is 26 msr and the range of accepted momenta extends 17.5% on each side of the central momentum. For a 100 μA proton beam incident on a 10 cm long beryllium target, the calculated maximum stopping density of pions in an area of 25 cm x 25 cm is $1 \times 10^8 \pi^- (\text{sec} \cdot \text{g}/\text{cm}^2)^{-1}$ when the channel is operated at a central momentum of 100 MeV/c. A maximum muon stopping density of $7 \times 10^6 \mu^- (\text{sec} \cdot \text{g}/\text{cm}^2)^{-1}$ can be obtained if the pions are separated by range absorption. Better muon beam purity is obtained by tuning the second half of the channel to 90 MeV/c to collect muons from the decay of pions in the backward direction when the first half is set at 160 MeV/c. In this case, a maximum muon stopping density of $1 \times 10^6 \mu^- (\text{sec} \cdot \text{g}/\text{cm}^2)^{-1}$ can be obtained. If a bending magnet is placed after the Phase One system to separate the muons and the pions by momentum analysis, a calculated maximum muon stopping density of $2 \times 10^6 \mu^- (\text{sec} \cdot \text{g}/\text{cm}^2)^{-1}$ can be obtained when the magnet is tuned to 85 MeV/c and the channel is set at 160 MeV/c.

Phase Two of the design consists of a long straight alternating gradient section and an analyzing section. The straight section provides an extra 5.5 meter length for pion decay. When the central momentum of the pion collection system is 160 MeV/c and the straight section is tuned to optimize the number of muons from the backward decay of pions, the calculated maximum muon stopping density in a 25 cm x 25 cm area is $1 \times 10^7 \mu^-(\text{sec} \cdot \text{g}/\text{cm}^2)^{-1}$. The analyzing section consists of a 90° bending magnet and a quadrupole triplet. With the pion collection system and the straight section set as described above and the analyzing section tuned to 82 MeV/c, a calculated maximum stopping density is $3.2 \times 10^6 \mu^-(\text{sec} \cdot \text{g}/\text{cm}^2)^{-1}$ in a 25 cm x 25 cm area and $1.1 \times 10^6 \mu^-(\text{sec} \cdot \text{g}/\text{cm}^2)^{-1}$ in a 10 cm x 10 cm area. An average muon polarization of between 70% and 90 % may be obtained. The yields of π^+ and μ^+ are about three times larger than the π^- and μ^- yields.

The accuracy of the calculation procedures was checked by comparing calculated and measured values for a pion channel, designed and set up at the Lawrence Laboratory at Berkeley. The two sets of values were found in agreement to within experimental error.

[REDACTED]

[REDACTED]

ACKNOWLEDGEMENTS

The author wishes to thank Dr. R.M. Pearce for his guidance during the progress of this work, and Dr. G.R. Mason for his supervision while Dr. Pearce was away on sabbatical leave. Thanks are also due to Dr. L.P. Robertson, Mr. P.A. Reeve and Dr. Q. Ingram for their help concerning the experimental part of the work at Berkeley.

For reading the draft and offering valuable comments, the author wishes to thank Dr. J.B. Warren, Dr. H.W. Dosso, Dr. T.W. Dingle, Dr. D.E. Lobb and Dr. L.P. Robertson. The author also wishes to thank Mrs. J.R. Hunt and Miss E. Tanner for the careful typing of the final manuscript, and the staff of the Computing Centre for their patience and smooth running of the computer programs used in this work.

Financial support from the University of Victoria, in the form of Graduate Fellowships and Scholarships, and from TRIUMF is gratefully acknowledged.

TABLE OF CONTENTS

Page

ABSTRACT

ACKNOWLEDGEMENTS

LIST OF TABLES

LIST OF FIGURES

CHAPTER 1	INTRODUCTION	1
	1.1 Mesons, Meson Factories and TRIUMF	1
	1.2 Beam Transport Systems and Meson Channels	6
	1.3 The Use of Stopped Pions and Muons in Scientific Research	8
	1.4 General Criteria	10
CHAPTER 2	PION AND MUON PRODUCTION AND DECAY	12
	2.1 Pion Production	12
	2.2 Pion Decay	22
	2.3 Decay Kinematics and Muon Production	24
	2.4 Muon Polarization	31
	2.5 Mesic Atoms	33
CHAPTER 3	A REVIEW OF STOPPED MESON CHANNELS	35
	3.1 Alternating Gradient (A.G.) Channels	35
	3.2 Solenoid Channels	36
	3.3 Coaxial Channels (Beam Guides)	38
	3.4 Helical Quadrupole Channels	40
	3.5 Channels Collecting the Muon Clouds Near the Pion Production Target	41

3.6	Channels in Which Pions Decay at Rest	42
3.6.1	Muons from Pion Decay at Rest in an Absorber (Jakobson Type)	43
3.6.2	Muons from Pion Decay at Rest in the Production Target	43
3.7	Channels Using Time of Flight	44
CHAPTER 4	PROPOSED TRIUMF STOPPED PION/MUON CHANNEL, PHASE ONE . .	46
4.1	Introduction	46
4.2	Channel Design	47
4.2.1	Design Aims	47
4.2.2	Design Methods	49
4.2.3	Parameter Optimization	50
4.2.4	Cost Optimization	60
4.2.5	Description of the Optimized Channel	63
4.3	Expected Performance	67
4.3.1	Channel Characteristics	67
4.3.2	Optics	74
4.3.3	Tolerances	79
4.3.4	Calculated Yields and Variation with Energy . . .	81
4.3.5	Beam Spill	87
4.3.6	Contamination	89
4.3.7	Muon Polarization	93
4.4	Modes of Operation	94
4.4.1	Operation as a Stopped Pion Channel	94
4.4.2	Operation as a Stopped Muon Channel	98
4.4.3	Operation of the Channel with the Analyzing Magnet	120

CHAPTER 5	PROPOSED TRIUMF STOPPED PION/MUON CHANNEL, PHASE TWO. . .	130	0
	5.1 Choice of Straight Section	130	2
	5.2 Design of the Straight Section	132	7
	5.2.1 Design Aims and Procedure	132	0
	5.2.2 Parameter Optimization	133	1
	5.3 Design of the Momentum Analyzing Section	139	3
	5.4 Calculated Performance	142	16
	5.4.1 Output Beam at the End of the Straight Section .	142	17
	5.4.2 Output Beam After the Analyzing Magnet	153	19
	5.4.3 Output Beam at the Stopping Target	160	19
CHAPTER 6	COMPARISON OF PREDICTION WITH EXPERIENCE ON A CHANNEL		11
	AT BERKELEY	168	12
	6.1 Introduction	168	14
	6.2 Channel Design	169	
	6.2.1 Design Criteria	169	15
	6.2.2 Parameter Optimization	170	15
	6.3 Calculated Performance	174	16
	6.3.1 Channel Characteristics	174	17
	6.3.2 Expected Flux	179	18
	6.4 Procedure and Data Analysis for Setting Up and		
	Testing the Channel	182	
	6.4.1 Counter Arrangement	182	
	6.4.2 Multiple Scattering at 50 MeV	184	
	6.4.3 Setting up Region I	186	
	6.4.4 Setting up Region II	189	

6.4.5	Achromaticity	190
6.4.6	Dispersion in Region II	192
6.4.7	D/M Ratio	197
6.4.8	Magnification of Region II	200
6.4.9	Resolution	201
6.4.10	Other Effects	203
6.4.11	Second Order Effects	206
6.4.12	Comparison of Calculated and Measured Pion Flux	207
CHAPTER 7	MISCELLANEOUS TOPICS	209
7.1	Comparison With Other Channels	209
7.2	Possible Use of the Pion Collection System for Scattering Experiments	211
7.3	Beam Switching	212
7.4	Vacuum, He, or Air	214
7.5	Some Comments on the Engineering Aspects of the Channel	215
7.5.1	Magnet Spacing	215
7.5.2	Magnet Length	216
7.5.3	Special Arrangement for Pion Experiments . . .	217
CHAPTER 8	CONCLUSIONS	218

Appendix A	SOME BASIC PROPERTIES OF PIONS AND MUONS	222
Appendix B	BASIC CONCEPTS OF BEAM TRANSPORT SYSTEMS	223
Appendix C	π - μ KINEMATICS	239
Appendix D	STOPPED PION CHANNELS	250
Appendix E	STOPPED PION/MUON CHANNELS	257
Appendix F	ALTERNATING GRADIENT PERIODIC SYSTEM, MATRIX TREATMENT	264
Appendix G	SOME EXAMPLES OF ALTERNATING GRADIENT CHANNELS	267
Appendix H	SOME EXAMPLES OF SOLENOID CHANNELS	280
Appendix I	AN EXAMPLE OF A COAXIAL BEAM GUIDE	288
Appendix J	AN EXAMPLE OF A MUON CLOUD CHANNEL	289
Appendix K	COMPUTER PROGRAMS	294
Appendix L	THE PROGRAM 'MBEND'	301

REFERENCES

LIST OF TABLES

<u>Table</u>		<u>Page</u>
4.1	Magnets and Power Supply Costs in \$1000	62
4.2	Optimized Channel Parameters	65
4.3	Summary of Beam Characteristics	77
4.4	Variation of Pion and Muon Yields with Energy	82
4.5	Beam Spill	88
4.6	Negative pion Flux, Momentum Acceptance, and Beam Spot Size for Various Settings of the Slits	97
5.1	Muon Beam Characteristics at the End of the Straight Section	152
5.2	Muon Beam Characteristics at the Stopping Target	167
6.1	Optimized Berkeley Channel Parameters	173
7.1	Comparison of the TRIUMF, LAMPF, and SIN Channels	210
8.1	Some Examples of Calculated Number of Stops in Carbon Targets for Various Modes of Operation	220
C.1	π - μ Decay Kinematics	243
C.2	Pion Kinematics	246
C.3	Muon Kinematics	247
C.4	Range and dp/dR for Pions in Carbon	248
C.5	Range and dp/dR for Muons in Carbon	249
G.1	Muon Beam Characteristics from the Pion Decay Portion of the LAMPF Channel	274
G.2	Calculated Fluxes for the Nevis Muon Channel	279
H.1	Expected Performance of the SIN Channel	282

LIST OF FIGURES

	<u>Page</u>
1.1 Layouts of beams and experimental areas at TRIUMF	4
2.1 Negative pion production cross section as a function of energy plotted from the Los Alamos data	13
2.2 Positive pion production cross section as a function of energy plotted from the Los Alamos data	15
2.3 Electron contamination versus pion production angle	16
2.4 Negative pion production cross section as a function of energy at 2.15° , CERN data	17
2.5 Positive pion production cross section as a function of energy at 0.8° , CERN data	18
2.6 Positive pion production cross section as a function of energy at 21.5° , CERN data	19
2.7 Pion production cross section as a function of energy for 660 MeV protons on carbon	20
2.8 Pion production cross section as a function of energy for 450 MeV protons on carbon	21
2.9 Pion decay length as a function of pion momentum	25
2.10 Percentage fraction of pions surviving decay as a function of distance for several pion momenta	26
2.11 Upper and lower limits on the range of decay muon momenta versus pion momentum	28
2.12 Decay angle versus muon momentum for several pion momenta	29
2.13 Fraction of muons decaying into a laboratory angle $\theta < \theta_0$ for various pion momenta	30
3.1 The experimental beam intensity of the Arizona channel for muons generated in the pion production target	45

4.1	Angular distribution of cascade neutrons for 100 MeV pions on 4.5 g/cm ² C target	53
4.2	Total pion flux versus quadrupole aperture for three values of the magnet gaps	58
4.3	Total muon flux versus quadrupole aperture for three values of the magnet gaps	59
4.4	Increase in total flux versus increase in cost for three magnet-quadrupole combinations	61
4.5	Schematic layout of the Phase One channel (Pion Collection System)	64
4.6	Solid angle of acceptance as a function of $\Delta p/p$ for the Phase One channel	68
4.7	Pion and muon momentum spectra for the Phase One channel	70
4.8	Pion and muon range spectra for the Phase One channel	71
4.9	Pion distribution in the transverse plane for $\Delta p/p = 0$	72
4.10	Pion distribution in the transverse plane for $\Delta p/p \pm 10\%$	73
4.11	Horizontal and vertical envelopes and the dispersion trajectory for the Phase One channel	75
4.12	Maximum percentage increase of beam spot size due to second order chromatic aberrations	78
4.13	Total flux as a function of channel central momentum for the Phase One channel	83
4.14	Maximum differential flux as a function of channel central momentum for the Phase One channel	85
4.15	Maximum stopping density as a function of channel central momentum for the Phase One channel	86
4.16	Muon polarization as a function of momentum for the Phase One channel	95
4.17	Muon flux of a given polarization versus polarization for the Phase One channel	96
4.18	Pion and muon momentum spectra for the Phase One channel in the pion mode when the slits are set to ± 1.0 cm.	99

4.19	Pion and muon range spectra for the Phase One channel in the pion mode when the slits are set to ± 1.0 cm.	100
4.20	Pion distribution in the transverse plane for the Phase One channel in the pion mode when $\Delta p/p$ is	101
4.21	Pion and muon momentum spectra at the entrance to the second bending magnet M2 for $p_0 = 100$ MeV/c	102
4.22	Muon momentum spectrum obtained with the second half of the Phase One channel tuned to 40 MeV/c and the first half unchanged at 100 MeV/c	104
4.23	Muon range spectrum obtained with the second half of the Phase One channel tuned to 40 MeV/c and the first half unchanged at 100 MeV/c	105
4.24	Muon polarization as a function of momentum for the Phase One channel with the second half tuned to 40 MeV/c and the first half unchanged at 100 MeV/c	106
4.25	Pion and muon momentum spectra at the entrance to the second bending magnet M2 for $p_0 = 160$ MeV/c	107
4.26	Muon momentum spectrum obtained with the second half of the Phase One channel tuned to 90 MeV/c and the first half unchanged at 160 MeV/c	108
4.27	Muon range spectrum obtained with the second half of the Phase One channel tuned to 90 MeV/c and the first half unchanged at 160 MeV/c	109
4.28	Muon polarization as a function of momentum for the Phase One channel with the second half tuned to 90 MeV/c and the first half unchanged at 160 MeV/c	111
4.29	Momentum spectrum of the muon halo when a 6 cm high plug is used to stop the pions	113
4.30	Range spectrum of the muon halo when a 6 cm high plug is used to stop the pions	114
4.31	Muon momentum spectrum transmitted through an absorber that stops all the pions at the end of the Phase One channel	116
4.32	Muon range spectrum after an absorber to stop all the pions at the end of the Phase One channel	117

4.33	Total muon flux as a function of channel central momentum when the Phase One channel is operated in the Arizona mode to collect 4 MeV muons generated in the pion production target	119
4.34	Muon momentum spectrum at the end of a 90° bending magnet placed after the Phase One channel to collect 85 MeV/c backward muons	121
4.35	Muon range spectrum at the end of a 90° bending magnet placed after the Phase One channel to collect 85 MeV/c backward muons	122
4.36	Muon polarization as a function of momentum at the end of a 90° bending magnet placed after the Phase One channel and tuned for the 85 MeV/c backward muons	123
4.37	Muon momentum spectrum at the end of a 90° bending magnet placed after the Phase One channel to collect 45 MeV/c backward muons	124
4.38	Muon range spectrum at the end of a 90° bending magnet placed after the Phase One channel to collect 45 MeV/c backward muons	125
4.39	Muon polarization as a function of momentum at the end of a 90° bending magnet placed after the Phase One channel and tuned for the 45 MeV/c backward muons	126
4.40	Muon momentum spectrum at the end of a 90° bending magnet placed after the Phase One channel to collect 132.5 MeV/c forward muons	128
4.41	Muon range spectrum at the end of a 90° bending magnet placed after the Phase One channel to collect 132.5 MeV/c forward muons	129
5.1	Variation of the backward muon flux with the A.G. field gradient of the straight section	134
5.2	Variation of the backward muon flux with the quadrupole aperture of the straight section	136
5.3	Variation of the backward muon flux with the length of the straight section	137
5.4	Dispersion as a function of angle of bend for three values of the effective length ℓ	140

5.5	Schematic layout of the complete muon channel (Phase One and Phase Two)	143
5.6	Pion and muon momentum spectra at the end of the straight section for $p_0 = 160$ MeV/c	144
5.7	Pion and muon range spectra at the end of the straight section for $p_0 = 160$ MeV/c	145
5.8	Muon polarization at the end of the straight section for $p_0 = 160$ MeV/c	146
5.9	Muon flux of a given polarization versus polarization at the end of the straight section for $p_0 = 160$ MeV/c	147
5.10	Pion and muon momentum spectra at the end of the straight section for $p_0 = 100$ MeV/c	148
5.11	Pion and muon range spectra at the end of the straight section for $p_0 = 100$ MeV/c	149
5.12	Muon polarization at the end of the straight section for $p_0 = 100$ MeV/c	151
5.13	Muon momentum spectrum after the straight section and the 90° analyzing magnet tuned for 82 MeV/c backward muons . . .	154
5.14	Muon range spectrum after the straight section and the 90° analyzing magnet tuned for 82 MeV/c backward muons . . .	155
5.15	Muon polarization as a function of momentum after the straight section and the 90° analyzing magnet tuned for 82 MeV/c backward muons	156
5.16	Muon momentum spectrum after the straight section and the 90° analyzing magnet tuned for 132 MeV/c forward muons .	157
5.17	Muon range spectrum after the straight section and the 90° analyzing magnet tuned for 132 MeV/c forward muons . . .	158
5.18	Muon polarization as a function of momentum after the straight section and the 90° analyzing magnet tuned for 132 MeV/c forward muons	159
5.19	Muon momentum spectrum at the stopping target with the analyzing section tuned for 82 MeV/c backward muons	161
5.20	Muon range spectrum at the stopping target with the analyzing section tuned for 82 MeV/c backward muons	162

5.21	Muon polarization as a function of momentum at the stopping target with the analyzing section tuned for 82 MeV/c backward muons	163
5.22	Muon momentum spectrum at the stopping target with the analyzing section tuned for 132 MeV/c forward muons	164
5.23	Muon range spectrum at the stopping target with the analyzing section tuned for 132 MeV/c forward muons	165
5.24	Muon polarization as a function of momentum at the stopping target with the analyzing section tuned for 132 MeV/c forward muons	166
6.1	A layout diagram of the pion channel for the π, d experiment at Berkeley	171
6.2	Solid angle of acceptance as a function of $\Delta p/p$ for the pion channel at Berkeley	175
6.3	Horizontal and vertical envelopes and the dispersion trajectory for the pion channel at Berkeley	178
6.4	Pion distribution in the transverse plane at the end of the Berkeley channel	180
6.5	Pion energy spectrum for the Berkeley channel	181
6.6	Counter arrangement used in setting up and testing the Berkeley channel	183
6.7	Effects of detuning Q5 from the calculated value on the focus at the end of the Berkeley channel	191
6.8	Centroid position of the pion distribution versus the % change in the field of the second bending magnet	193
6.9	Centroid position of the pion distribution versus the position of the cross counters and the TEC	196
6.10	Centroid position of the pion distribution versus the position of the hodoscope counters for a fixed position of the TEC	198
6.11	Centroid position of the pion distribution versus hodoscope elements position for five values of $\Delta B/B$	199
6.12	Resolution for individual hodoscope counters for three values of Q5	204

6.13	Dependence of resolution on $\Delta p/p$ for several hodoscope elements	205
6.14	Experimental pion energy spectrum	208
7.1	A schematic diagram showing the arrangement for beam switching between two users	213
B.1	The ideal quadrupole field	225
B.2	The hard-edge model	225
B.3	Bending magnet, a plan view showing magnet parameters	229
B.4	Phase space ellipse, relation to ellipse parameters	236
D.1	LAMPF low energy, general purpose pion channel	251
D.2	Nevis low energy pion-muon channel, two configurations	255
E.1	SREL pion/muon channel	258
E.2	Range curves obtained with the SREL channel	260
E.3	Saclay pion/muon channel	261
E.4	π^+ yields from the Saclay channel	263
G.1	The CERN channel	268
G.2	The Chicago channel	270
G.3	The proposed LAMPF channel	272
G.4	Calculated muon and pion momentum spectra from the LAMPF channel, operation at 180 MeV/c	275
G.5	Calculated muon and pion momentum spectra from the LAMPF channel, operation at 90 MeV/c	275
G.6	Proposed Nevis muon-pion channel	278
H.1	The proposed SIN channel	281
H.2	Calculated pion and muon momentum spectra for the solenoid and a quadrupole channel at the entrance to the analyzing section	284
H.3	Calculated momentum spectra at the stopping target for the SIN solenoid	285

H.4	Calculated momentum spectra at the stopping target for an equivalent quadrupole channel to the SIN solenoid	286
J.1	A proposed muon cloud channel, LAMPF design	290
J.2	Calculated pion-to-muon ratios at the entrance to the muon cloud channel	291
J.3	Calculated muon momentum spectrum for the muon cloud channel	293

CHAPTER 1

INTRODUCTION

1.1 Mesons, Meson Factories and TRIUMF

The understanding of the nature and origin of the forces that bind the protons and neutrons together to form a nucleus has been the ultimate aim of nuclear physics. In an attempt to explain these forces Yukawa (Yukawa, 1935) advanced a theory in which he postulated the existence of short-range nuclear forces that act between nucleons (protons and neutrons). The nucleons are thought to be held together by a field of force, known as the meson field, which has associated with it particles, the mesons, acting as the field quanta in a manner analogous to the way photons are the quanta of the electromagnetic field. According to the Yukawa theory, the meson should have a mass intermediate between the electron and the nucleon, approximately 200 MeV.

In cloud chamber studies of cosmic rays (Anderson and Neddermeyer, 1937; Street and Stevenson, 1937) a particle which had a mass of ~ 100 MeV and a lifetime of $\sim 2 \times 10^{-6}$ sec was discovered. Although it had a smaller mass and a longer lifetime than predicted, this particle was assumed to be the Yukawa meson. However, considerable doubt was thrown on this assumption by an experiment (Conversi *et al.*, 1947) which showed that the particle had a very weak nuclear interaction with matter. Some of the particles decayed when brought to rest instead of interacting. This was contrary to the predicted properties of the Yukawa mesons which would have interacted readily and been absorbed in a nucleus of the material.

These contradictions led to the suggestion (Sakata and Inoue, 1947; Bethe and Marshak, 1947) that there were two types of mesons. The Yukawa meson was postulated to be a parent meson decaying into the long lived meson observed in cosmic rays. Cosmic ray events observed in nuclear photographic emulsions exposed at high altitudes (Lattes *et al.*, 1947) confirmed this very postulate. These events were interpreted as the decay at rest of a positive heavy meson (mass ≈ 150 MeV) into a light meson (mass ≈ 100 MeV). The energy of the latter meson was found to be a constant, implying a two body decay. The heavier meson was designated as the pi-meson or pion and the lighter one as the mu-meson. of muon. Basic properties of pions and muons are summarized in Appendix A.

Although both the pions and the muons were discovered in experiments on cosmic rays, the intensity (about one particle per minute per square centimeter at sea level) is too small for carrying out most experiments. Thus, alternative sources of pions and muons are required.

Pions were first created in the laboratory at Berkeley (Gardner and Lattes, 1948). When two nucleons collide, the momentum that is transferred from one to the other may be visualized as being carried by the exchange of a virtual meson. If the available energy in the centre of mass system is greater than the meson rest mass, then a free meson may be created. Nuclear reactors and Van de Graff type accelerators do not provide neutrons and protons of sufficient energy for pion production. The intermediate energy accelerators built in the early fifties and the

modern medium energy accelerators provide protons of sufficiently high energy but not high enough current to produce reasonably intense beams of mesons. The latter are required to carry out experiments more accurately and to study interactions which have low probability of occurrence; therefore, there is a need for meson factories. The ones currently planned are designed to provide particle beams two to four orders of magnitude more intense than existing ones, and ranging in energy between 200 and 800 MeV. Particles with this range of energy have the correct de Broglie wave length for studying the interesting details of nucleon-nucleon interaction inside the nucleus. For the reasons discussed above and because little research has been carried out in intermediate energy physics, all the meson factories being built to date plan to operate within this energy range.

The meson facility TRIUMF of the universities of Alberta, British Columbia, Simon Fraser and Victoria (Vogt and Burgerjon, 1966) is now under construction. Variable energy, good energy resolution, multiple proton beams, and the acceleration of negative hydrogen ions are unique features of the TRIUMF project.

A schematic diagram of the facility is shown in Fig. 1.1. H^- ions from a 300 keV ion source are injected at the centre of the sector-focussed isochronous cyclotron. The ions go into nearly circular orbits and are accelerated each time they pass a gap between two sets of RF resonators which develop 200 keV across the gap. They are confined to follow these orbits by the magnetic field developed by the six sectors

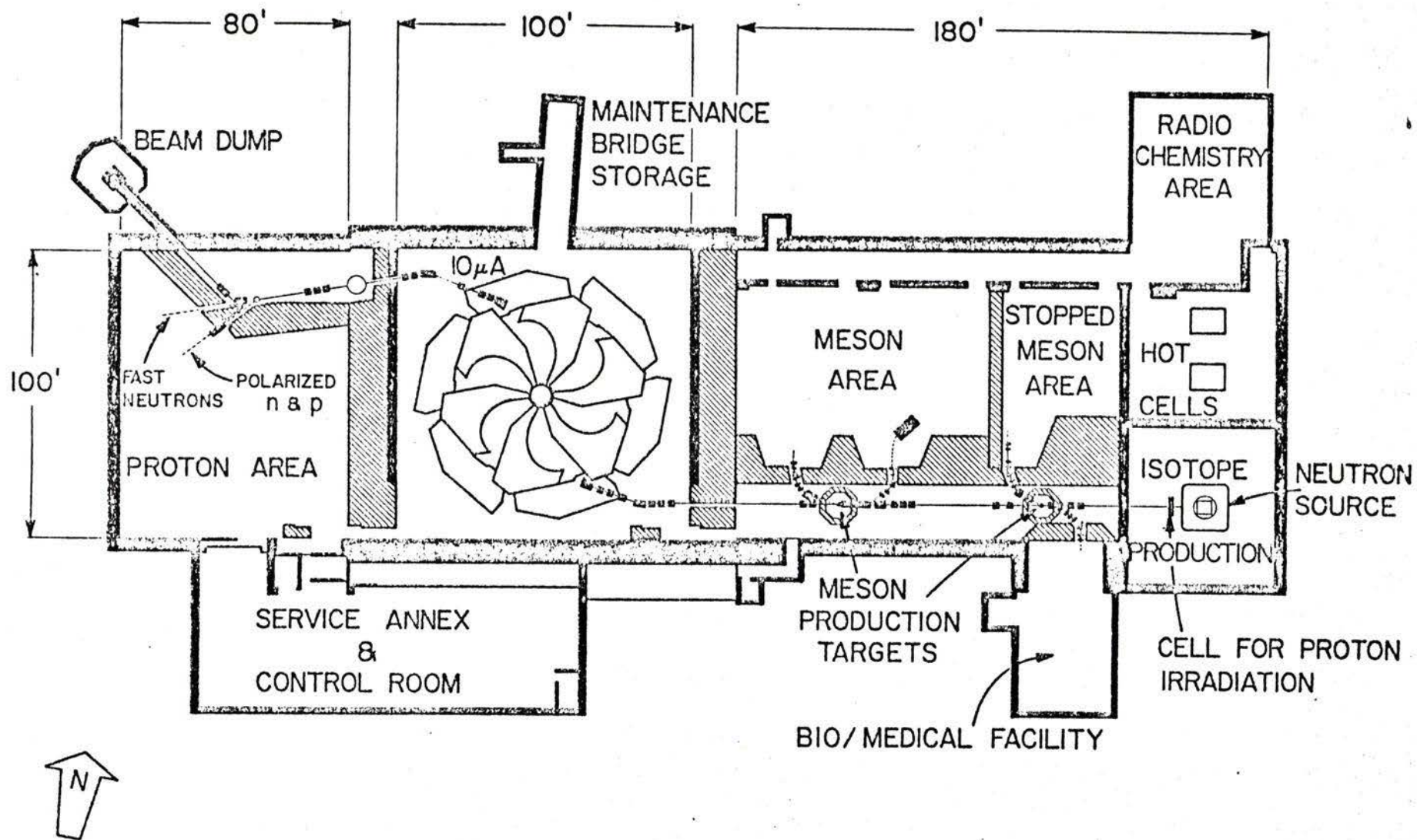


Fig. 1.1 Layout of beams and experimental areas at TRIUMF.

of the cyclotron magnet. The sectors are shaped so as to achieve radial and vertical focussing of the ion beam and to take account of the relativistic increase in mass. Protons are then extracted very efficiently by passing the ion beam through a thin foil which strips the two electrons from the H^- ion. The energy of the protons can be varied by changing the radial position of the stripping foil inside the cyclotron. In principle, six proton beams may be extracted simultaneously by placing stripping foils which partially intercept the H^- beam at six locations around the perimeter of the gaps between the six sectors of the cyclotron. In practice, the location of the resonators may limit the number of extracted beams to four.

Initially, only two proton beams are to be extracted, as indicated by the two beam lines in Fig. 1.1. The beam extracted at the southwest corner is to be used for meson production at two targets and will terminate at the neutron facility. The total proton current available ranges from $70 \mu A$ at the maximum energy of 525 MeV to about $320 \mu A$ at an energy of 450 MeV. The protons are transported to the second pion production target where the stopped meson channel is located. The fact that the production target is external to the cyclotron and not internal provides greater freedom in choosing the type of channel compared to proton accelerators which have internal targets.

1.2 Beam Transport Systems and Meson Channels*

The extracted beams of particles from an accelerator have to be transported away from the background radiation near the accelerator to the locations where experiments are to be carried out. The development of efficient systems for the transport of particle beams became possible when the principle of "strong focussing" or the "alternating gradient theory" was developed (Courant *et al.*, 1952) in connection with an investigation of the feasibility of alternating gradient synchrotrons. Strong focussing lenses, or quadrupoles, were developed in which the magnetic field is perpendicular to the direction of motion and proportional to the distance from the axis passing through the centre of the lens. The resulting force acts directly to focus a particle towards the axis of the quadrupole in one transverse plane and to defocus it in the other.

Several such quadrupoles can be combined to contain a beam of particles which, together with bending magnets, form a beam transport system. These magnets and lenses, together with the free spaces separating them, are called beam transport elements. The motion of charged particles through the elements of a beam transport system is described by second order differential equations (Steffen, 1964; Banford, 1966; Brown, 1967). These equations can be integrated to find the trajectory of the particles. The solutions may be expressed as Taylor series

* In this section and in the remaining Chapters of this work, it is convenient to use the word "meson" for both the pion and the muon.

expansions in the initial coordinates and are conveniently represented by matrices. The matrices of the individual elements can be multiplied together to give the transfer matrix for the system. Basic concepts of beam transport systems and the techniques of matrix representation which are used in this thesis are discussed more fully in Appendix B.

Meson channels are specialized types of beam transport systems; they are reviewed in Chapter 3. After this review and considering the availability of funds, it was decided at TRIUMF to design a dual purpose channel, serving both as a pion and as a muon channel. The design work was divided into two phases. In Phase One, discussed in Chapter 4, a short channel is designed to provide a pion and a muon beam. In Phase Two, discussed in Chapter 5, a long straight pion-decay section is added; Phase One would now be used as a pion channel and also serve as the injection section for the more elaborate muon channel. The design procedures used above were tested by designing a pion channel for the Berkeley pion-deuteron scattering experiment (Auld *et al.*, 1971). This is discussed in Chapter 6.

1.3 The Use of Stopped Pions and Muons in Scientific Research

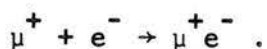
Space permits only a brief indication of the types of experiments that may be carried out with stopped pions and muons and the information obtainable from them in several fields of science in which these particles may find use. More detailed discussions of such experiments are to be found in proposals for the various meson factories (Vogt and Burgerjon, 1966; LASL Staff, 1964; Yale Staff, 1964).

For nuclear structure studies, negative pions and muons make excellent probes. They have masses over 200 times the mass of an electron and therefore, when they are captured by nuclei to form mesic atoms, their Bohr orbit is smaller by this same factor. Consequently, their wave function appreciably overlaps that of the nucleus; in other words, they spend a significant part of their time inside the nucleus. The energy of the mesic x-rays produced as the meson cascades down to lower orbits is affected by the overlap referred to above. Pi-mesic x-rays yield basic information on the distribution of nuclear charge and the magnetic moment distribution, nuclear polarization, and the nuclear quadrupole moments of the ground state. Mesic x-ray experiments may also be used to verify the quantum electro-dynamic effect called vacuum polarization, since the muon mass can be independently determined.

In the field of fundamental particle physics, the properties of the pions and muons and their basic interactions (strong, electromagnetic and weak) are of great interest. For example, more precise knowledge of rare decay modes, facilitated by the availability of intense

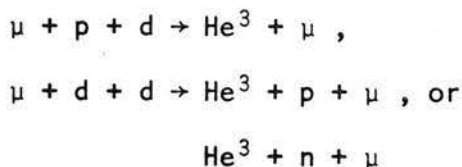
meson beams, will contribute to the understanding of the weak interaction. Also, observation of muonium-antimuonium coupling may help to determine whether the muonic lepton number is additive or multiplicative.

Atomic and molecular systems formed by the muon with other particles, atoms or molecules are still an open field of research where further experimentation is required. Muonium is formed by the positive muon with an electron



Information is needed on depolarization mechanisms of polarized muons stopped in gases, liquids or solids, as well as study of muonium properties and its hyperfine structure.

Muon induced nuclear fusion such as



can be investigated by stopping muons in liquid hydrogen and deuterium.

Stopped pions and muons find applications in other fields of science. The muon may be used as a probe for solid state studies such as radiation damage and activation in solids. Radiation therapy and medical applications of pions are other fields where a great deal of experimentation will be valuable. Chemical experiments using pions or muons will become numerous. For example, pion-induced reactions and their rates could be investigated.

1.4 General Criteria

It is not possible to set exact design criteria because of the different beam requirements for the great variety of experiments using stopped mesons, as seen in the previous section. However, some general criteria that apply to all types of experiments and for both pion and muon channels may be formulated.

Firstly, the stopped meson density is to be maximized. The figure of merit employed here is the meson stopping rate per unit range (in g/cm^2). Optimizing for total stopping rate is not suitable since only very thick targets are capable of stopping all the mesons in the wide momentum range accepted by the channel. On the other hand, choosing the stopping rate per gram of target material as a figure of merit would be suitable only in a case where a small mass of target is available and if the meson beam could be focussed to a small spot. This may be possible with the pion beam which has reasonably good optics, but not with the muon beam which comes from an extended source and in principle cannot be focussed to a small spot. This figure of merit leads to a very low pion energy since the stopping volume is in the denominator.

Secondly, contamination of the meson beams with other particles is to be minimized. Upper limits on these contaminants were set as a result of a questionnaire answered by prospective users (Sperry, 1970).

These are:	Gamma Rays	1%
	Electrons	10%
	Protons	1%
	Neutrons	1%
	Muons	1% for the pion beam
	Pions	1% for the muon beam

The inclusion of bends in the channel will almost eliminate neutral particles generated near the production target. This subject of beam purity will be considered in Chapter 4 where channel design is discussed.

Thirdly, the beam spot size at the experimental target should be reasonably small since detectors are normally small and some target materials cannot be obtained in large quantities at reasonable cost. A cross section area of about 100 cm^2 was used as a reasonable beam size for the muon beam.

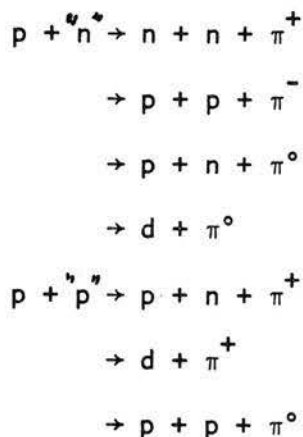
Finally, the design has to be flexible in order to operate the channel in several different modes, depending on experimental requirements and to facilitate possible future modifications.

CHAPTER 2

PION AND MUON PRODUCTION AND DECAY

2.1 Pion Production

At the energies available in TRIUMF, single production in proton-nuclear interactions is the dominant process for pion production. When a proton beam hits target nuclei, the following interactions, among others, may take place:



The threshold energy is slightly different for each of these reactions but has an average value in the neighbourhood of 285 MeV. The threshold energy in the laboratory system depends on the target nuclei because of the Fermi motion of the nucleons inside the nucleus and is lower for large nuclei than for light nuclei.

Pion production cross section data are not plentiful. The most comprehensive set of measurements are those carried out by a Los Alamos group at Berkeley (Nagle *et al.*, 1969). Fig. 2.1 shows some of

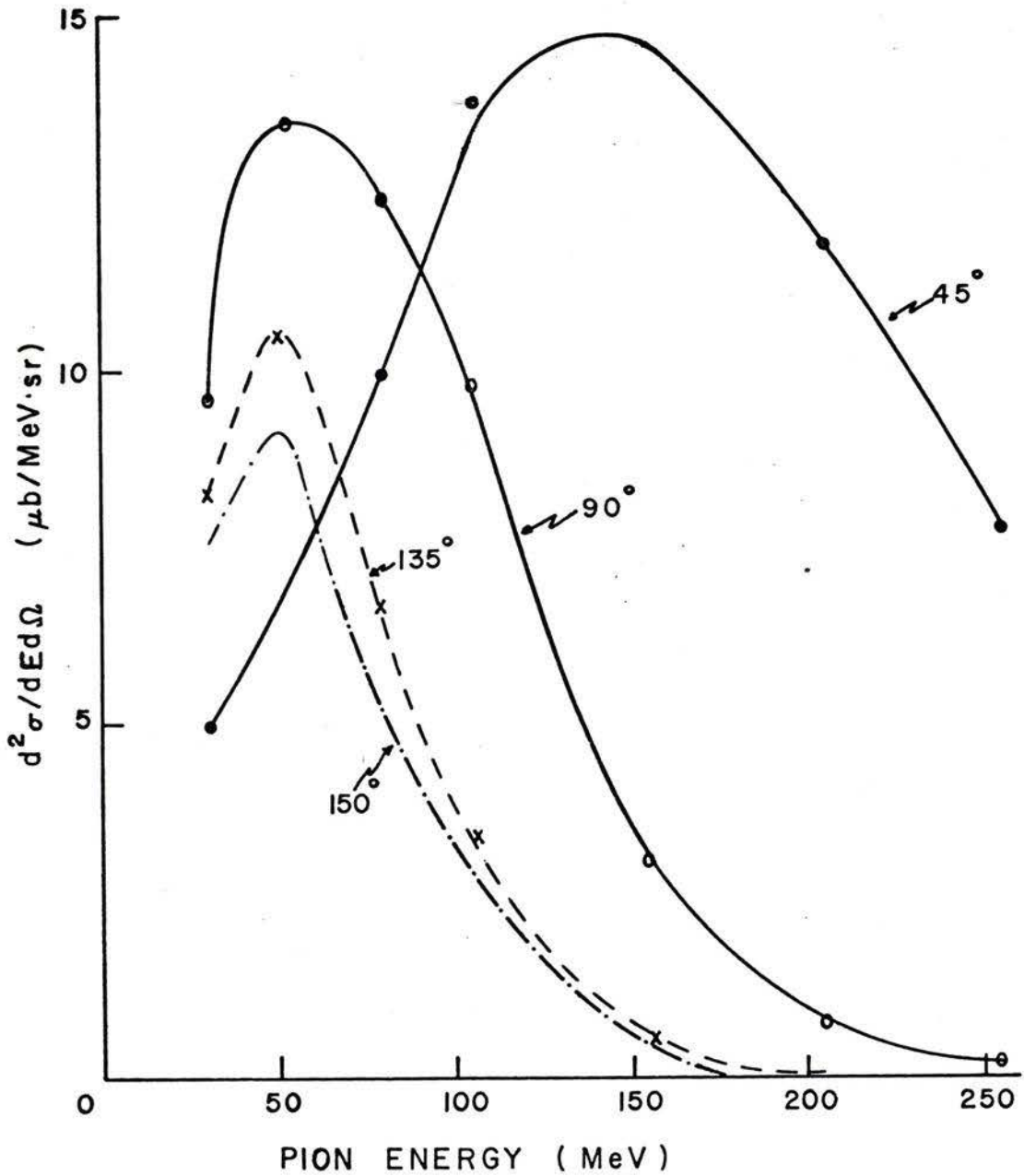


Fig. 2.1 Negative pion production cross section as a function of pion energy for the angles indicated plotted from the Los Alamos data (Nagle *et al.*, 1969). Data are for 747 MeV protons on Be.

these results for 747 MeV protons on a Be target for the laboratory angles 45° , 90° , 135° and 150° . It is seen that, for large angles, the negative pion production cross section increases to a peak as the pion energy decreases down to ~ 50 MeV and, at this energy, does not vary significantly as a function of angle. Fig. 2.2 shows similar data for the positive pion cross section. The Los Alamos data also indicate a reduction in electron contamination at large angles as shown in Fig. 2.3.

The increase in the π^- cross section with decreasing pion energy is also indicated by the CERN measurements at 600 MeV (Hirt *et al.*, 1969) as seen in Fig. 2.4 for several target materials at 21.5° . The π^- results, however, indicate a peak around 200 MeV; but if one compares the results for 0.8° shown in Fig. 2.5, and for 21.5° shown in Fig. 2.6, a shift in the peak towards the lower energy side is noticed for the larger angle. Also for the heavier elements the curves start to peak up again below 100 MeV, which suggests that for even larger angles one would expect the cross sections behaviour to be similar to that of the Los Alamos results. This is supported by some older measurements made by various workers. The 660 MeV protons on carbon data (Meshkovskii *et al.*, 1958) are shown in Fig. 2.7 for the angles 19.5° , 38° and 65° ; it indicates a rise in π^+ cross sections, with decreasing energy, to a peak around 100 - 200 MeV. It is seen here again that the peak moves towards the lower energy end as the angle of production increases. The 450 MeV data (Lillethum, 1962) shown in Fig. 2.8 indicate similar behaviour.

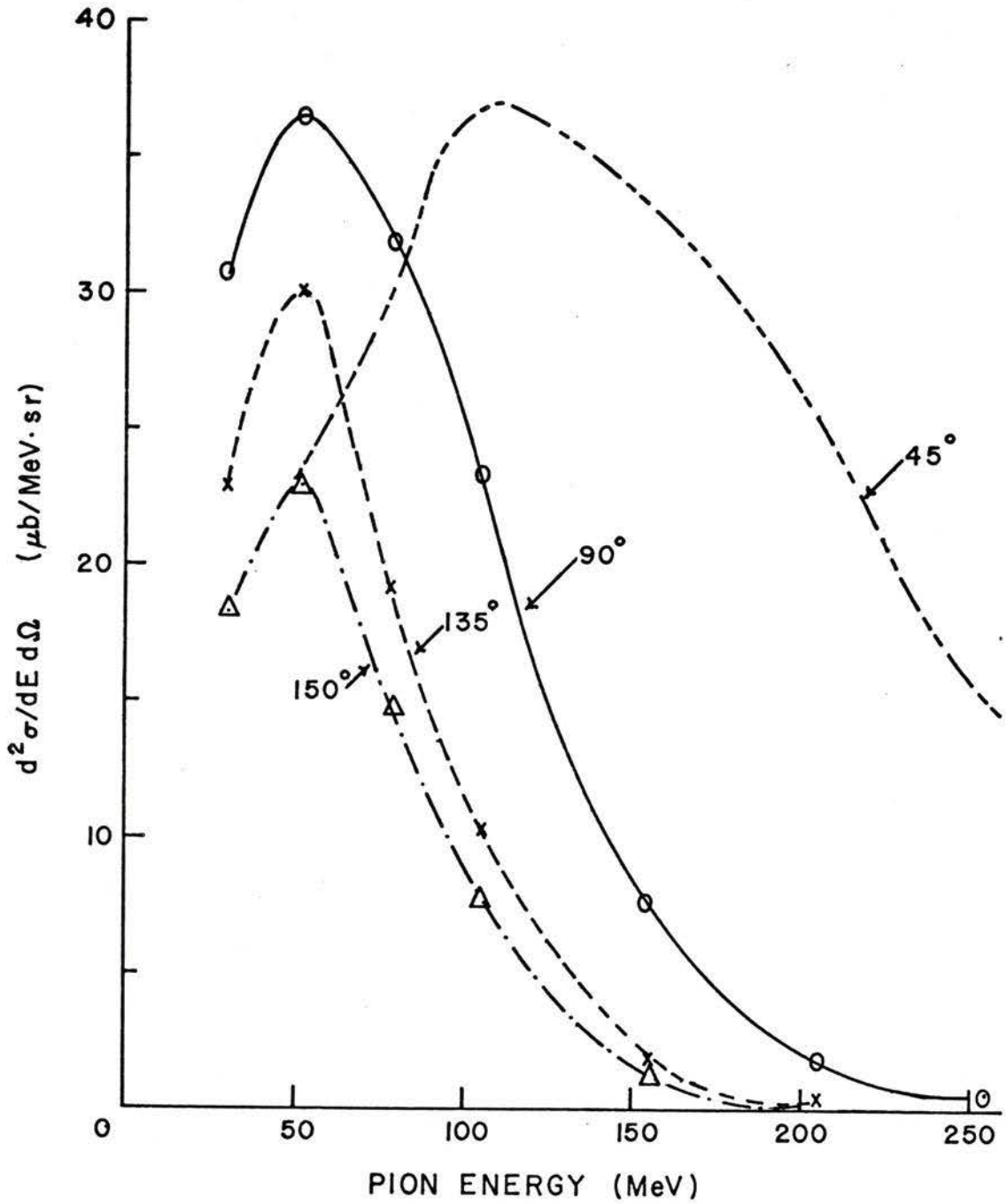


Fig. 2.2 Positive pion production cross section as a function of pion energy for the angles indicated plotted from the Los Alamos data (Nagle *et al.*, 1969). Data are for 747 MeV protons on Be.

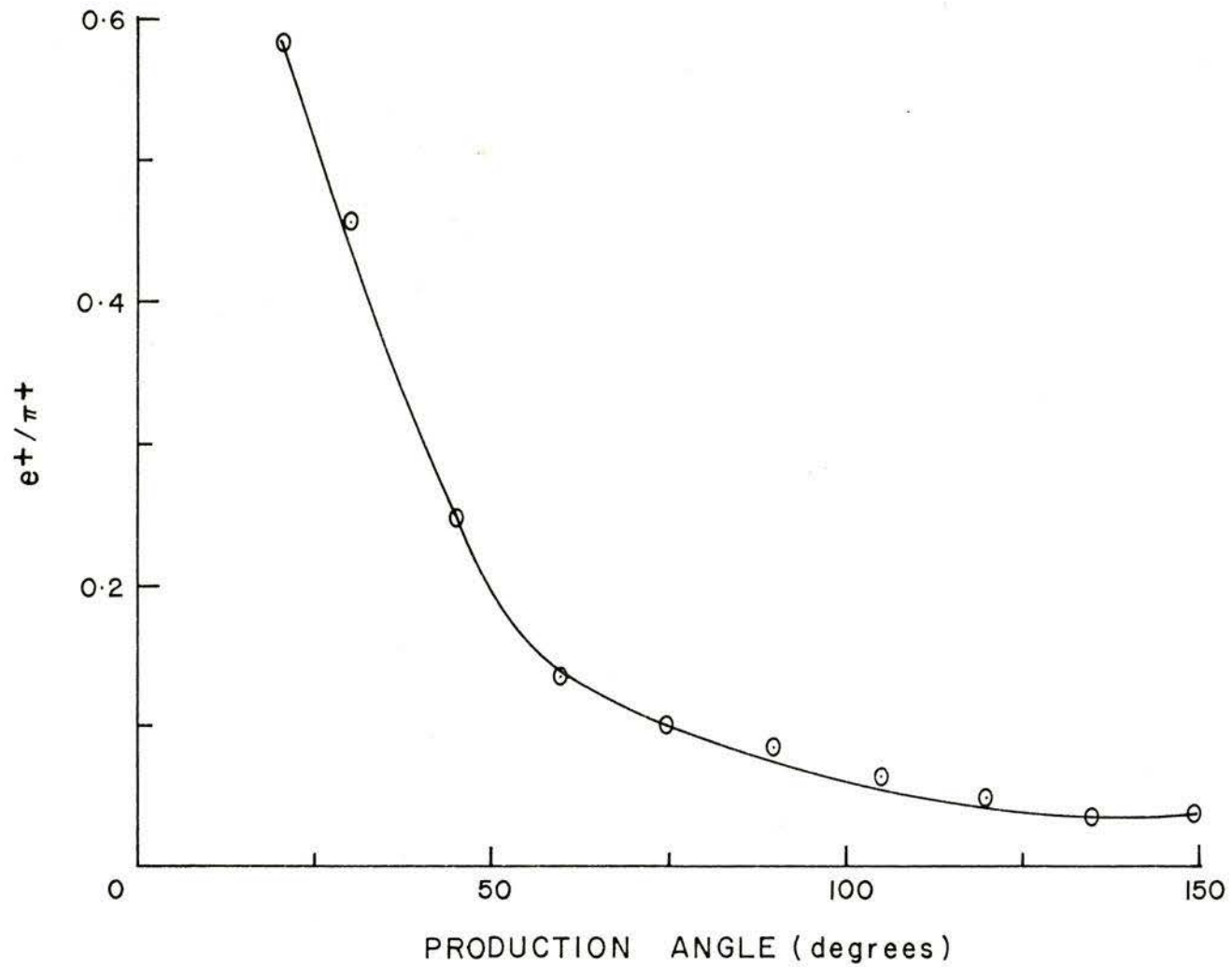


Fig. 2.3 Electron contamination versus pion production angle for the data of Fig. 2.2 .

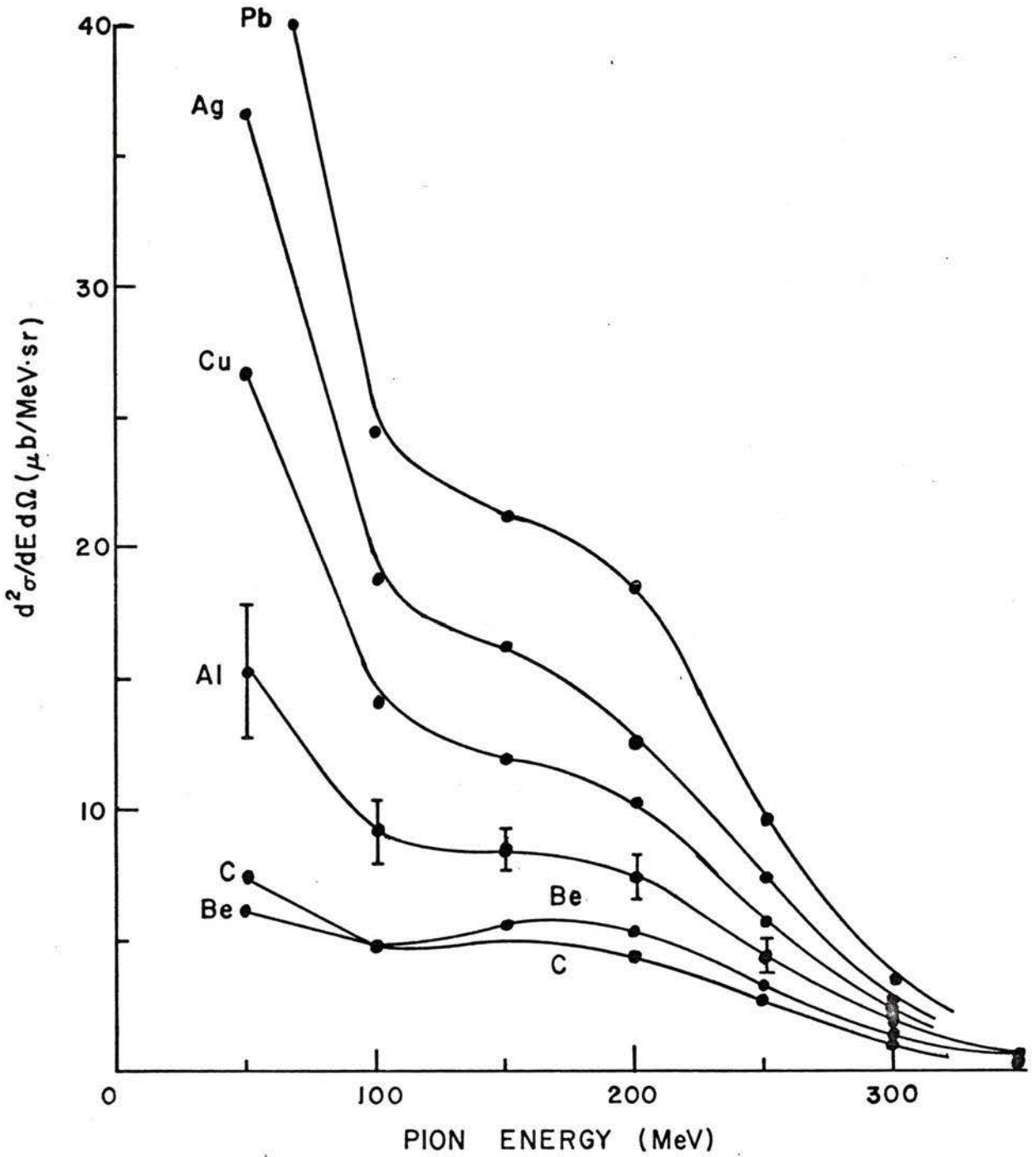


Fig. 2.4 Negative pion production cross section as a function of pion energy at 21.5° for 600 MeV protons on the materials indicated. Reproduced from the CERN report (Hirt *et al.*, 1969).

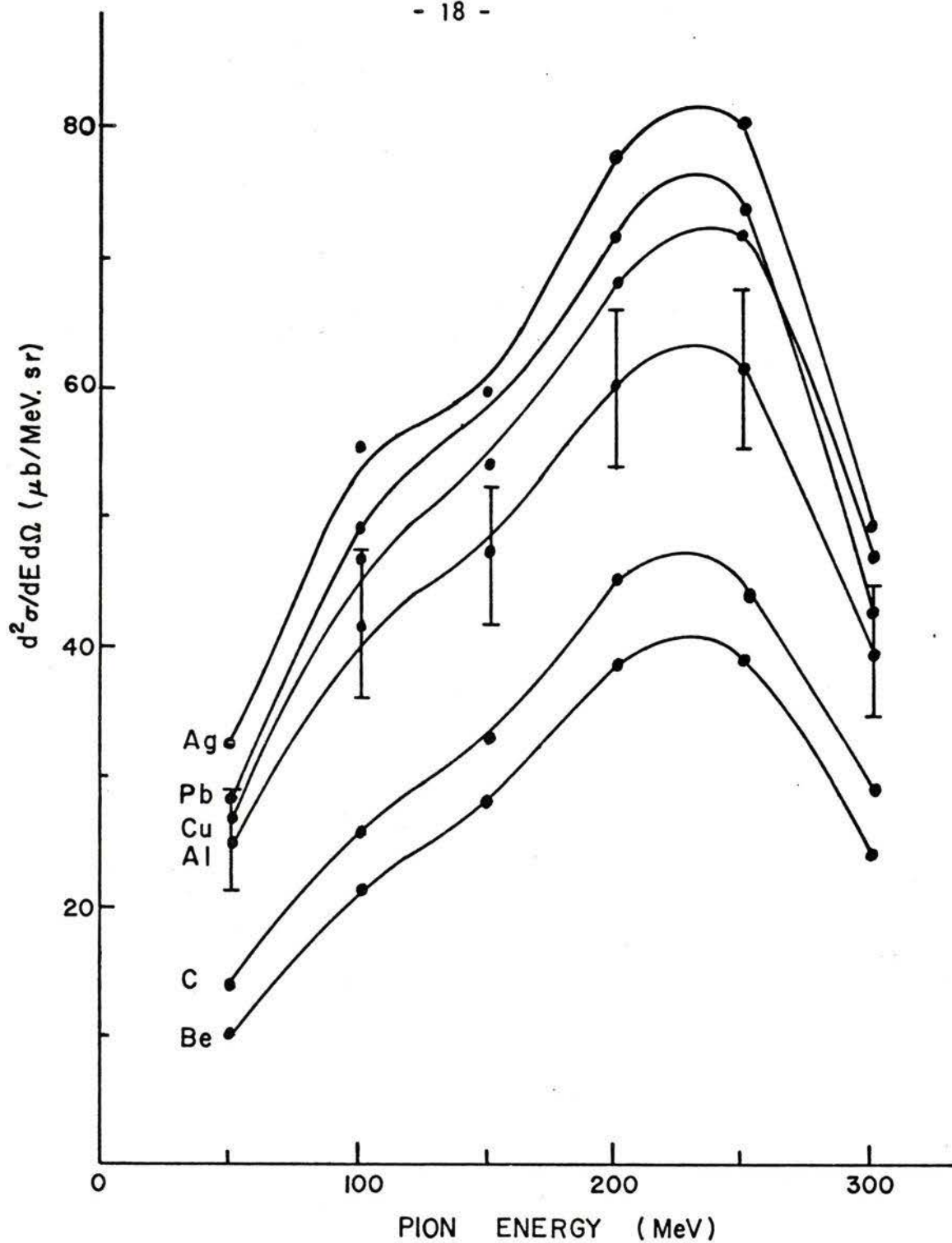


Fig. 2.5 Positive pion production cross section as a function of pion energy at 0.8° for 600 MeV protons on the materials indicated. Reproduced from the CERN report (Hirt *et al.*, 1969).

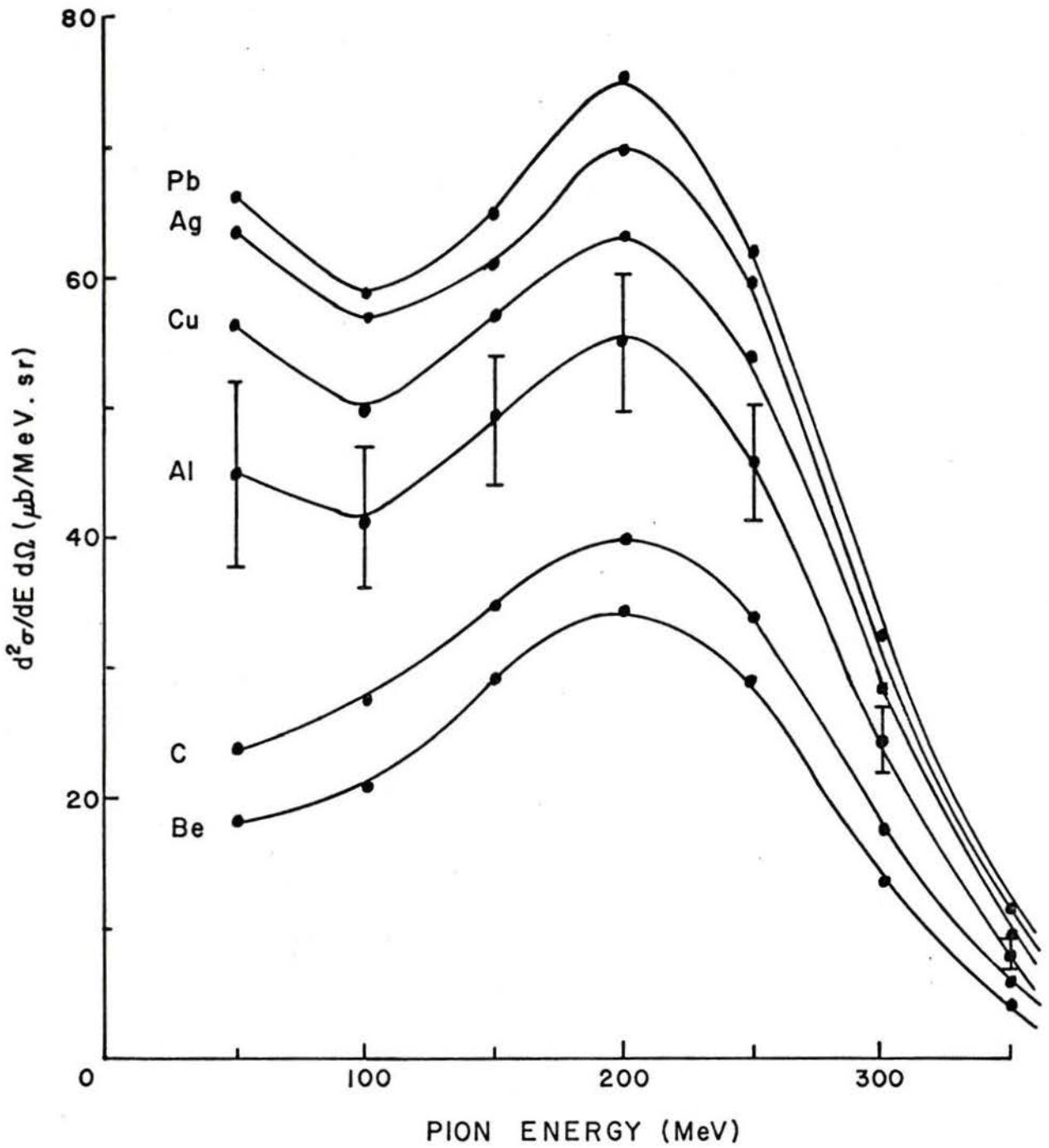


Fig. 2.6 Positive pion production cross section as a function of pion energy at 21.5° for 600 MeV protons on the materials indicated. Reproduced from the CERN report (Hirt *et al.*, 1969).

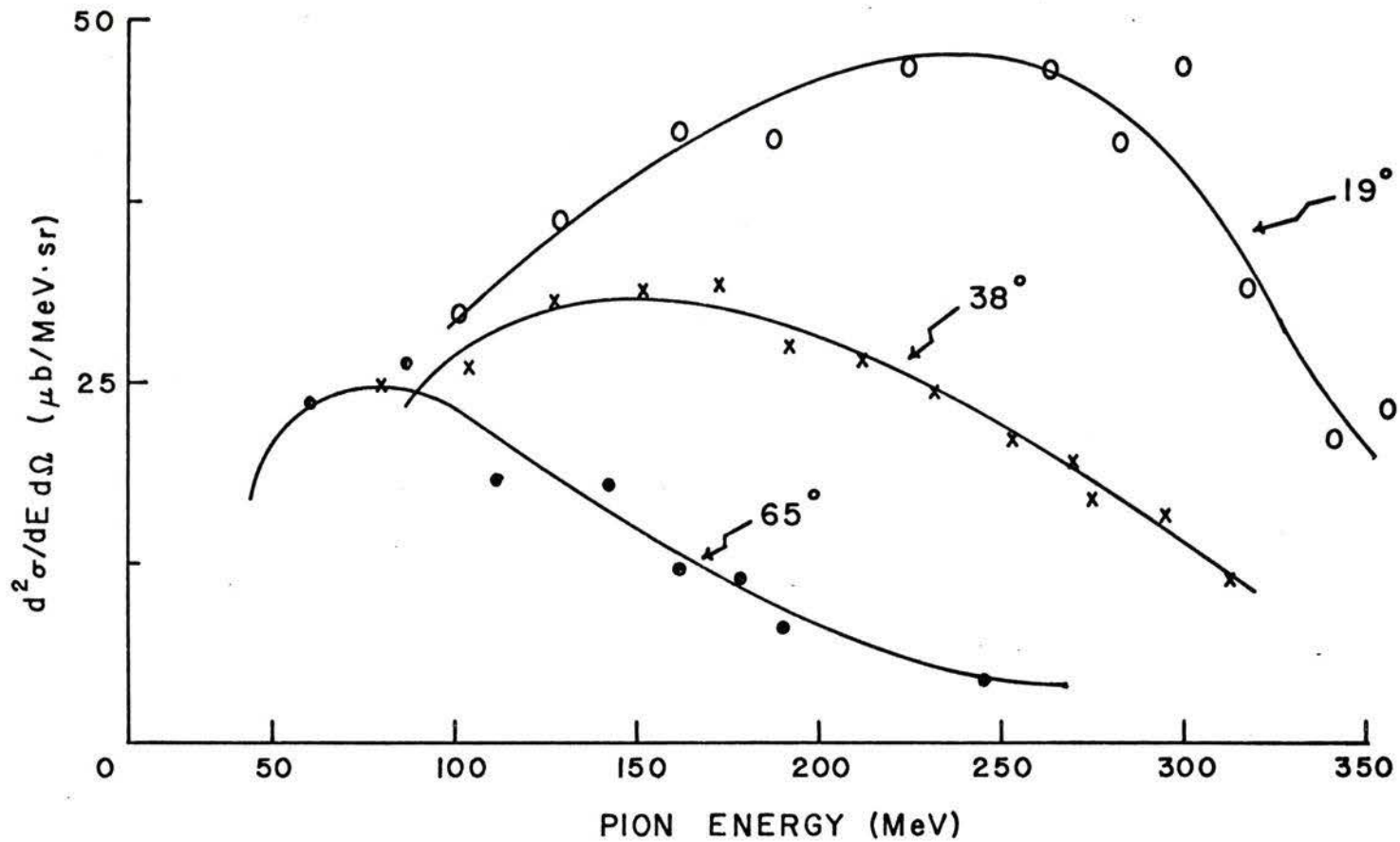


Fig. 2.7 Pion production cross section as a function of pion energy for 660 MeV protons on carbon and the angles indicated. Plotted from original data (Meshkovskii *et al.*, 1958).

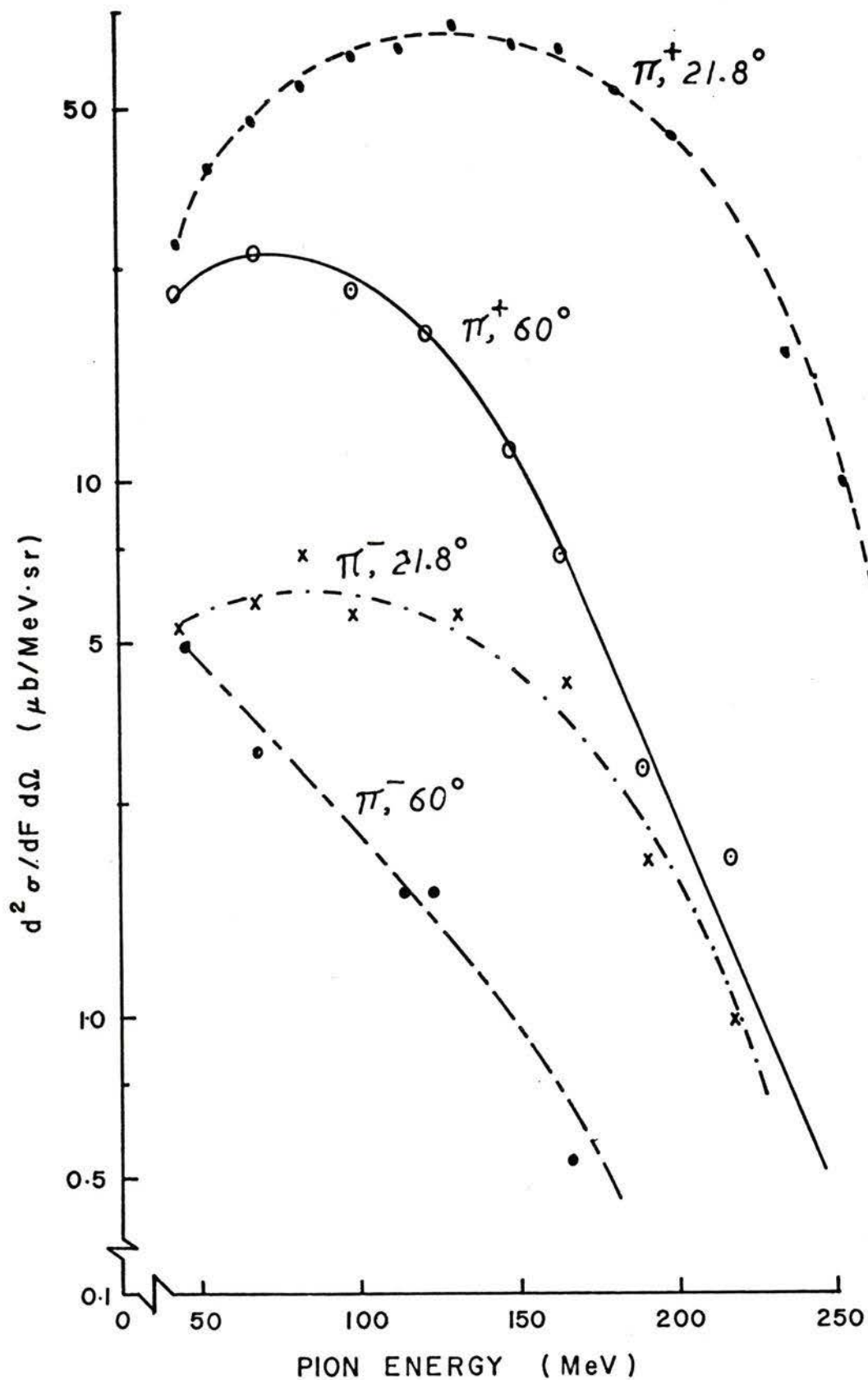


Fig. 2.8 Pion production cross section as a function of pion energy for 450 MeV protons on carbon and the angles indicated. Plotted from original data (Lillethum, 1962).

Preliminary results of a pion production cross section experiment being carried out at SREL* (Robertson *et al.*, 1972) at 580 MeV, suggest similar tendencies to those indicated by the Los Alamos data.

2.2 Pion Decay

Pion decay is a weak interaction process which is assumed to be described by the universal Fermi interaction theory. Weak interactions violate spatial parity, and this was postulated (Lee and Yang, 1956) to explain the two modes of decay of the K-meson. The violation of parity in $\pi \rightarrow \mu$ decay was confirmed experimentally (Garwin *et al.*, 1956) by searching for asymmetry in the angular distribution of positrons from $\mu^+ \rightarrow e^+$ decay. The violation of parity led to the revival of the two-component theory of the neutrino which had been rejected earlier (Pauli, 1933) on the ground that it led to parity violation. In this theory, the neutrino is described by two-component wave functions forming the solution to the Dirac equation for particles of zero rest mass which has the form:

$$(\vec{\sigma} \cdot \vec{p})\psi^2 = |p|\psi^2 \quad (2.2.1)$$

where \vec{p} is the momentum, $\vec{\sigma}$ the Pauli spin matrix, and $|p|$ is the eigenvalue corresponding to the eigenvector ψ^2 (since $E = |p|$ for massless particles). This equation has the eigenvalues $(\vec{\sigma} \cdot \vec{p}) = \pm p$ corresponding to wave functions for spins which are parallel or anti-parallel to the momentum.

* Space Radiation Effects Laboratory, Newport News, Virginia, U.S.A.

The neutrino helicity is defined as

$$H = \frac{\vec{\sigma} \cdot \vec{p}}{|\vec{p}|} = +1 \text{ for spin parallel to momentum,}$$

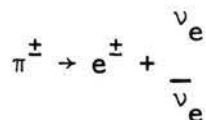
-1 for spin anti-parallel to momentum.

This means that the neutrino can be found in one of two possible states with equal and opposite energies. The particle which has negative helicity (left-handed) is called the neutrino, and the one with positive helicity (right-handed) is called the anti-neutrino.

The dominant decay mode of the pion into a muon and a neutrino may be represented schematically as:

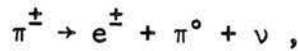
It is seen that parity is violated since the mirror image of, say, the π^+ decay implies a right-handed neutrino which does not exist. A charge conjugation operation in addition to the parity operation will result in the situation on the right which is allowed since the anti-particles have the opposite helicity.

The charged pions (mean life 26.04 nsec) undergo other decay modes. The decay scheme



has a branching ratio of about 10^{-4} , as predicted by the universal Fermi interaction theory.

The β -type decay mode,



was estimated to have a branching ratio of about 10^{-8} (Zel'dovich, 1954). The experimental value (Dunaitsev, 1962 and 1974) is in good agreement with theoretical estimates.

The neutral pion (with a mean life of about 2×10^{-16} sec) decays into two γ -rays in an electromagnetic type interaction



This explains the difference of its mean life in comparison to the charged pions which decay through the weak interaction as indicated above.

2.3 Decay Kinematics and Muon Production

The mean lifetime of the pion is 26.04 nsec and the decay length, calculated from the relation

$$\lambda = \lambda_0 p_{\pi} \quad (\lambda_0 = c\tau/m_{\pi} = 5.593 \text{ cm/MeV/c}) \quad (2.3.1)$$

as a function of momentum, is shown in Fig. 2.9 which indicates that for the range of energies being considered (see Chapter 4) the decay length is between 3 and 7 meters. Fig. 2.10 shows the percentage of pions surviving decay as a function of distance for various pion momenta. It is seen that at a distance of 8 meters, at least 80% of all pions with momenta less than 100 MeV/c would have already decayed.

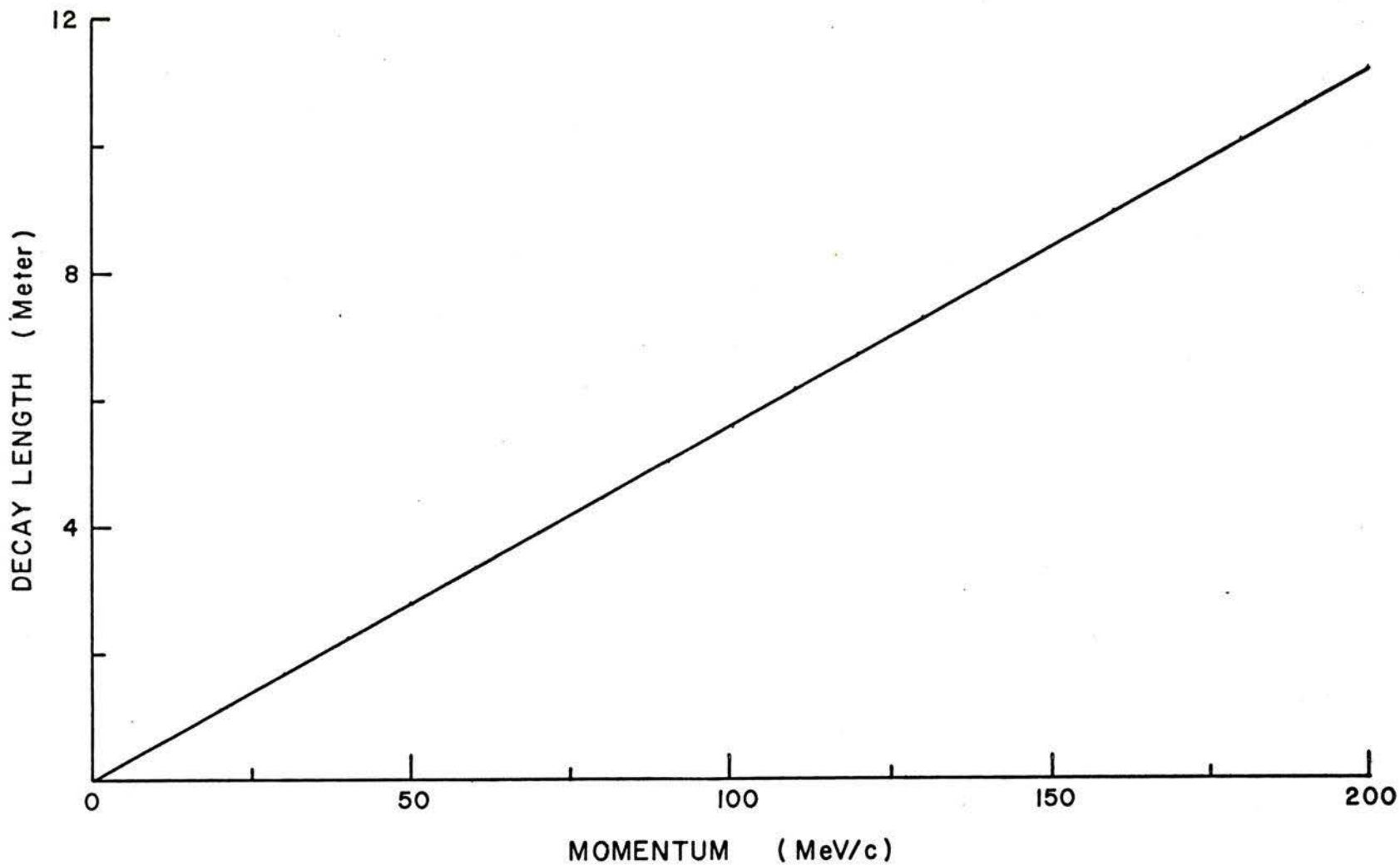


Fig. 2.9 Pion decay length as a function of pion momentum.

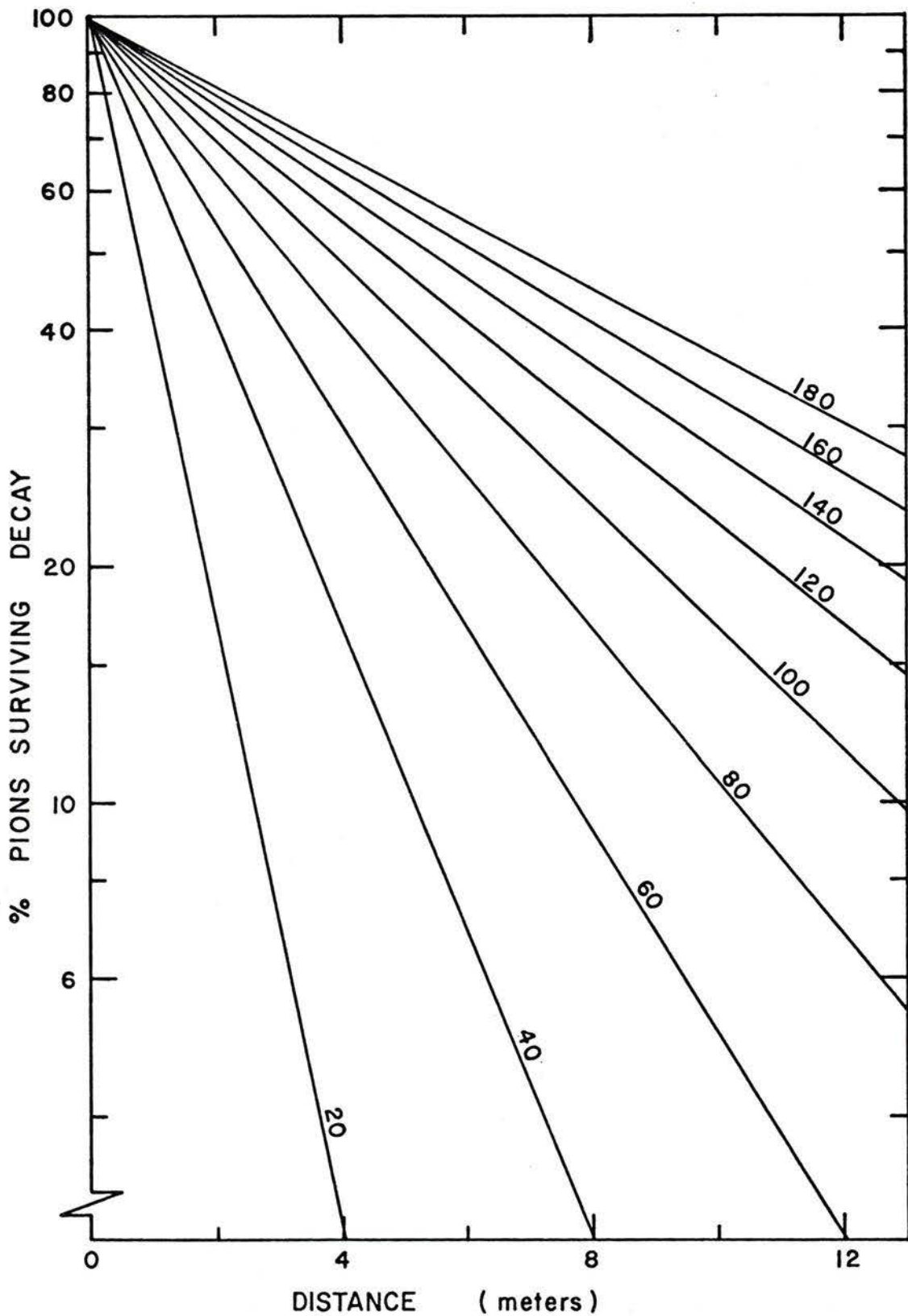


Fig. 2.10 Percentage fraction of pions surviving decay as a function of distance for the pion momenta indicated.

In the frame of the pion at rest (the variables in this frame will be starred), the decay is isotropic and the muon momentum vector has a constant magnitude of 29.8 MeV/c (4.12 MeV) which corresponds to a velocity of $\beta_{\mu}^* = 0.2714$ relative to the speed of light. If in the laboratory frame the pion is moving with velocity β_{π} , the decay muon will have a range of momenta with limits

$$p_{\mu} = \frac{\beta_{\mu} \pm \beta_{\mu}^*}{\beta_{\pi} (1 + \beta_{\mu}^*)} p_{\pi}, \quad (2.3.2)$$

which are indicated graphically in Fig. 2.11. Since generally no particle goes backward in the laboratory frame for decay in flight, except for extremely low energy pions, there will be a maximum decay angle θ_{\max} which is given by (see Appendix C)

$$\theta_{\max} = \arctan[(1 - \beta^2)/(g^2 - 1)]^{1/2} \quad (2.3.3)$$

The decay angle dependence on p_{μ} is shown in Fig. 2.12 for several values of p_{π} . The angular distribution of the decay muons is given by (see Appendix C)

$$\frac{dN}{d\theta} = \frac{\sin\theta^*}{2\gamma} \frac{\gamma^2(g + \cos\theta^*) + \sin^2\theta^*}{(g + \cos\theta^*)} \quad (2.3.4)$$

This function and its integral have been computed and represented graphically (Vogel, 1967) as a function of the decay angle and the momentum. Fig. 2.13, reproduced from Vogel, shows a plot of $dN/d\theta$ as a function of θ for various pion momenta. Derivation of the above relations and some useful kinematic tables are given in Appendix C.

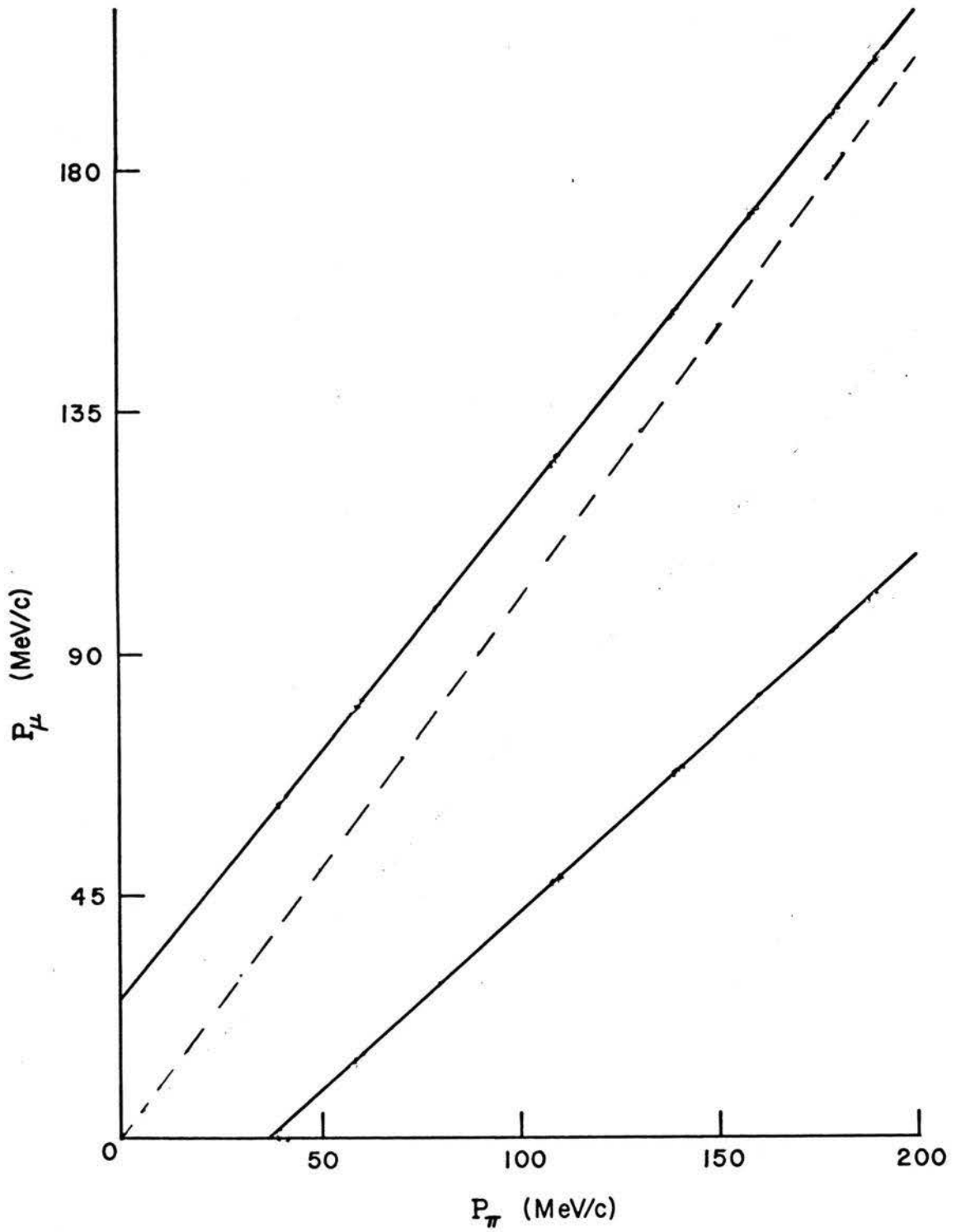


Fig. 2.11 Upper and lower limits on the range of decay muon momenta versus pion momentum.

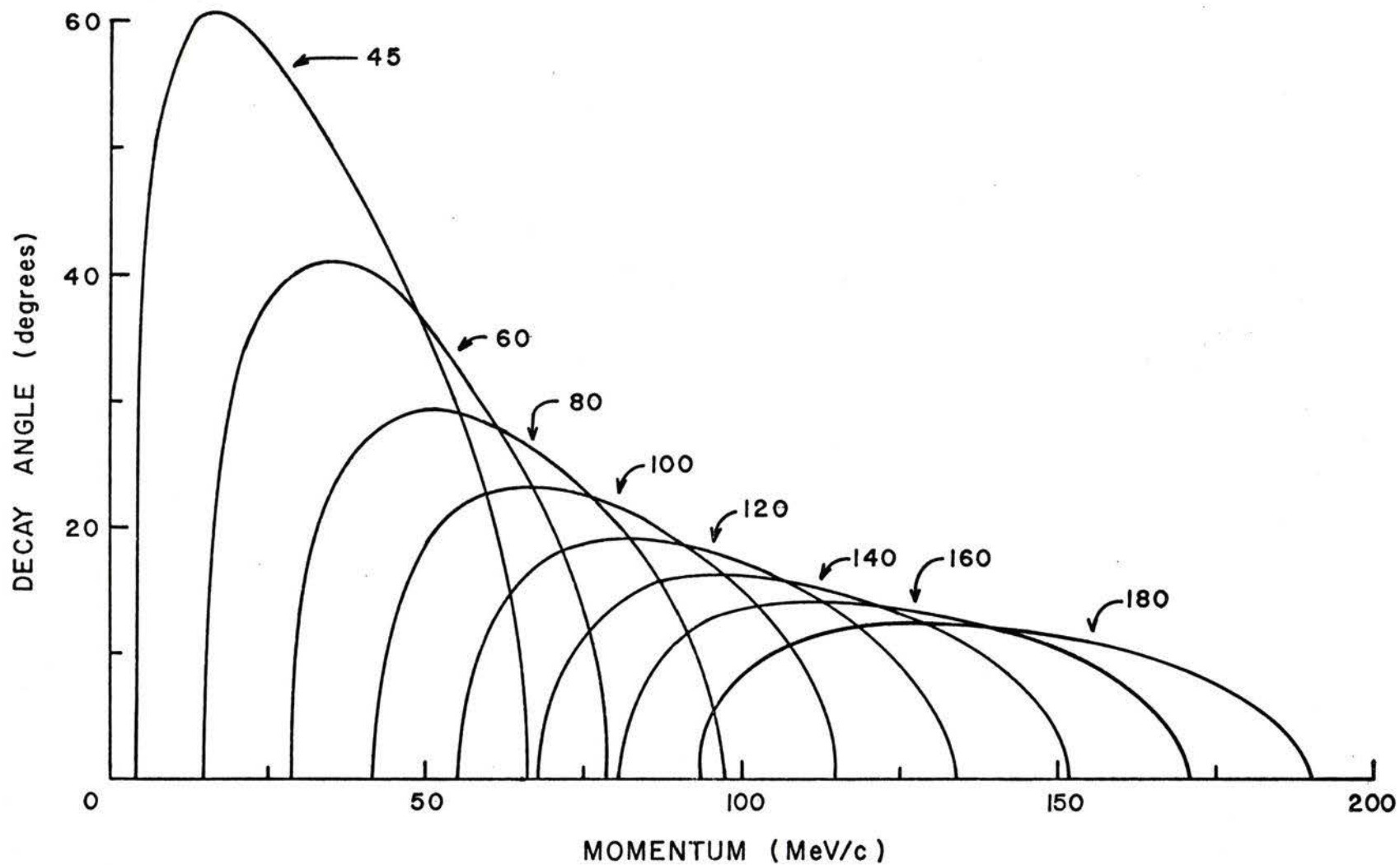


Fig. 2.12 Decay angle versus muon momentum for the pion momenta indicated on each curve.

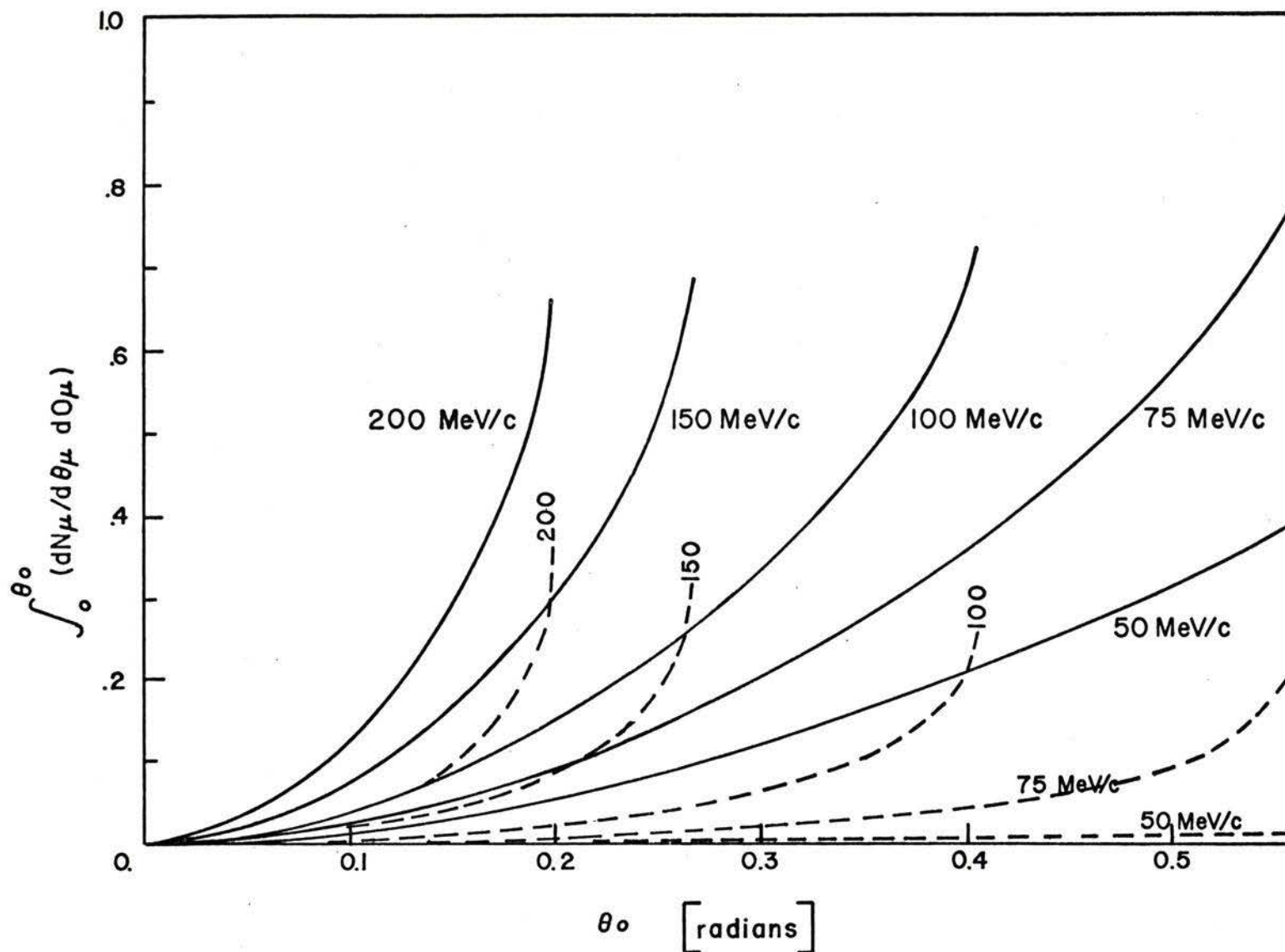


Fig. 2.13 Fraction of muons decaying into a laboratory angle $\sigma < \sigma_0$ for the various pion momenta indicated on each curve. Solid curves represent the forward decay muons and dashed curves the backward muons. Reproduced from the LAMPF report (Hughes *et al.*, 1971).

2.4 Muon Polarization

The concept of polarization may be explained if one considers a particle with spin S having $2S+1$ possible orientations with respect to a given direction along the unit vector \hat{n} . For a beam of such particles, the spin component in the direction \hat{n} will have a certain expectation value $\langle \bar{s} \cdot \hat{n} \rangle$. This value will be zero for an unpolarized beam; otherwise, a certain direction \hat{n}_0 exists such that the expectation value is a maximum; i.e.,

$$\max \langle \bar{s} \cdot \hat{n} \rangle = \langle \bar{s} \cdot \hat{n}_0 \rangle = \zeta ; \quad (2.4.1)$$

ζ is called the degree of polarization of the beam. The polarization three-vector is defined by

$$\bar{\zeta} = \hat{n}_0 \cdot \zeta . \quad (2.4.2)$$

The direction in which ζ is maximum is the direction of the polarization vector $\bar{\zeta}$. The magnitude of the vector $|\bar{\zeta}|$ varies between zero for unpolarized beams and 1 for completely polarized beams.

If the momentum vector \bar{p} of the beam is parallel or anti-parallel to the polarization vector $\bar{\zeta}$, the beam is said to be longitudinally polarized. In this case, a muon helicity h is defined by

$$h = \frac{\bar{p} \cdot \bar{\zeta}}{|\bar{p}| |\bar{\zeta}|} \quad (2.4.3)$$

If \bar{p} and $\bar{\zeta}$ are in the same direction, $h = \pm 1$; if they are in the opposite direction (anti-parallel) then $h = -1$.

The muons from pion decay in flight are not 100% polarized since muons emitted forwards and backwards in the pion rest system have opposite polarization. Also there is an appreciable kinematic depolarization caused by the relatively large accepted angular range in the pion rest system. Both positive and negative muons suffer equally from kinematic depolarization.

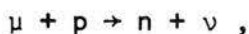
Depolarization during the slowing down of the muons is due mainly to Coulomb scattering and is very small. A larger depolarization takes place after the stopping of the muons. The amount of depolarization in this case depends on the material in which the muons are slowed down or stopped and is different for the positive and negative muons. For positive muons, the mechanisms responsible for depolarization after stopping in a material medium are mainly the formation of muonium and the interaction between the magnetic moment of the positive muon and the magnetic fields in the medium, with the former mechanism being more important. For negative muons, the spin-orbit interaction is the main mechanism of depolarization. Extensive literature on muon depolarization is available (Garwin *et al.*, 1956; Ignatenko *et al.*, 1958; Mann and Rose, 1961; Weissenburg, 1967).

2.5 Mesic Atoms

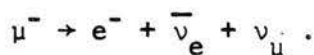
When pions and muons are incident on material targets, their history is carried out in several stages. In the first stage, mesons lose energy by collision with atomic electrons until their energy is of the order of a few keV when this loss mechanism ceases to operate. In the second stage, the meson is considered as moving inside a degenerate electron gas, their velocity being smaller than the maximum velocity of the atomic electrons. After the mesons are thermalized, the third stage depends on the charge of the meson.

The negative mesons are captured into high molecular or atomic orbitals. The energy loss mechanism and the capture process is not understood. The Bohr orbit of the meson is smaller than that of the electron by the ratio of their masses. The meson then cascades down to an orbit in the neighbourhood of the electronic K-shell where the nuclear field is virtually unscreened by atomic electrons. The radius of the electronic K-shell corresponds approximately to the $n = 14$ orbit for the negative muon and the $n = 16$ for the negative pion. The next stage involves the cascade of the meson from this outer orbit down to the ground state in a hydrogen-like potential. This part of the cascade is well understood. The process takes of the order of 10^{-12} seconds. At the higher orbits, Auger transitions predominate. As the meson reaches lower levels, radiative transitions (involving x-ray emissions) become more important until finally, at some lower value of n depending on the atomic number of the material, the radiative transitions become dominant.

In the case of the negative pion, towards the end of the cascade, the pion is readily absorbed by the nucleus often before reaching the 1S level because of its strong interaction. The probability of decay of the pion is very small. On the other hand, in the case of the negative muon, the 1S level is almost always reached. Two processes then compete; namely, nuclear capture,



and muon decay (mean life 2.2 microseconds)



As in the case of the pion, this decay is a weak interaction process violating parity.

For the positive mesons, the final stage involves the formation of atomic systems or decay. The positive muons form muonium ($\mu^+ e^-$) and, in theory, the positive pions can form pionium. The latter, however, has not been observed, since the pion decays readily.

CHAPTER 3

A REVIEW OF STOPPED MUON CHANNELS

Stopped meson channels may be classified into three main categories: stopped pion channels, dual purpose stopped pion/muon channels, and stopped muon channels. The first category includes channels which are specifically designed to provide stopped pions and low energy pion channels that can be used for stopped pion experiments. These channels are all basically similar beam transport systems consisting of several quadrupoles and bending magnets. Examples of stopped pion channels are given in Appendix D. The second category includes channels which are designed specifically to provide both stopped pions and stopped muons. Examples of these channels are given in Appendix E. The stopped muon channels are normally designed specifically to provide muons and are classified below according to their design philosophy.

3.1 Alternating Gradient (A.G.) Channels

This type of channel has been studied extensively (Citrön *et al.*, 1963; Yale Staff, 1964; Telegdi *et al.*, 1964). The basic concept is to collect as many pions as possible from a production target, pass it through a bending system for initial momentum selection, then through a straight long section of alternating gradient quadrupoles allowing as many of the pions as possible to decay, and finally through a second bending system to separate off the pions. Matrix treatment of periodic systems is well covered in the literature (Steffen, 1964; Banford, 1966) and a simple treatment is given in Appendix F.

The principle merits of the A.G. channel are flexibility, good optics due to the decoupling of the x-plane and y-plane motions, and proven performance in existing channels. The muon capture efficiency of this type of channel is typically 10-12%. The classical examples are the CERN^{*} and Chicago Channels. The basic characteristics of these two channels, together with those of the proposed LAMPF[†] and Nevis channels, are reviewed in Appendix G.

3.2 Solenoid Channels

In a solenoid, the pions describe helical trajectories around the magnetic field lines along the axis of the solenoid. The decay muons follow similar orbits once they are generated. Two solenoid channels have been proposed, the SIN[‡] and the Saclay channels. Test sections of the SIN channel are under construction. These two channels are reviewed in Appendix H.

The most important characteristic of solenoids is their high capture efficiency for decay muons which approaches 90%, or even 100% for low momentum muons. But they have several disadvantages. The coupling between the x-plane and y-plane motions makes it difficult to efficiently match to magnets and quadrupoles in the system. Then there is the fact that the large acceptance of the solenoid cannot be usefully

* European Organization for Nuclear Research, Geneva, Switzerland

† Los Alamos Meson Physics Facility, Los Alamos, New Mexico 87544

‡ Swiss Institute for Nuclear Research, Zurich, Switzerland

utilized since the acceptance of the injection system, consisting of quadrupoles and bending magnets, is not so large. Also the solenoid is a special purpose device and, therefore, lacks the flexibility of the alternating gradient channels.

The solenoid has been studied extensively (Petitjean, 1969(a), (b) and (c); 1970(a), (b) and (c); 1971; Petitjean and Vécsey, 1971) by the SIN group, and the coils are now in the construction phase. It was considered perhaps less extensively (Hughes *et al.*, 1971) by the LAMPF group and rejected in favour of an A.G. type channel. Here, it is sufficient to summarize their findings. The figures below (Petitjean and Vécsey, 1971) compare the calculated performance of the SIN solenoid (described in Appendix H) and an equivalent quadrupole channel:

	<u>Solenoid</u>	<u>Quadrupole</u>
Aperture (cm)	14	25
$\Delta\Omega$ (mstr)	75	75
Δp (MeV/c)	27	25
Pions accepted 10^9 x	4.6	4.6
Muons at 70 cm ² target $10^6 \mu^- (\text{sec}\cdot\text{MeV}/c)^{-1}$	3.9	1.6
Max. stopping rate (1 cm ²) $10^6 \mu^- (\text{g}\cdot\text{sec})^{-1}$	1.0	0.3

which indicates that the solenoid provides twice or three times as many muons as the quadrupole. A gain factor of 2 is also indicated by the LAMPF calculation (Hughes *et al.*, 1971). On the other hand, the latter calculation shows that at most 10% of the muons available at the end of

the solenoid can be transported through the analyzing section. The SIN group assumes this efficiency to be 25%. This is because an alternating gradient analyzing magnet is used. This type of magnet, however, has a wide momentum acceptance and, consequently, the π - μ separation may not be complete.

3.3 Coaxial Channels (Beam Guides)

This type of channel was originally proposed (Van der Meer, 1962) at CERN. Further contribution to its theory was also made at CERN (Regenstreif, 1964). As in a coaxial transmission line, the field in the beam guide between the inner and outer conductor is rotationally symmetric. Charged particles, introduced into this field and not coplanar with the axis, will follow a screw-type trajectory around and along the inner conductor. The trajectory is a rather complicated periodic function of the axial coordinate along the beam direction. For some range of initial conditions, the particles do not touch the conductors. The focussing action may be considered as arising from the attraction between the current flowing through the inner conductor and the current formed by the moving charged particles.

The obvious advantage of this type of channel is the considerably lower cost compared to other systems, but there are several disadvantages. As in the case of the solenoid, there is strong coupling between the two transverse planes which results in poor matching to other elements of the system. This is particularly the case for matching to the bending magnet

in the momentum analyzing section. For a straight beam guide, the solid angle of acceptance is rather small. For the guide described in the CERN report (Van der Meer, 1962) the maximum solid angle of acceptance is less than 8 msr for a guide 7 cm in diameter placed 0.8 m from the target and for a current-to-momentum ratio less than $1 \times 10^{-4} \text{ Amp (eV/c)}^{-1}$. Another disadvantage is the bad optics of such devices arising from their non-linear properties which distribute the beam over the whole cross section of the tube. Thus, the beam cannot be focussed into a reasonably small spot. Finally, as in the case of the solenoid, the beam guide lacks the flexibility of conventional quadrupole channels; it is also a single purpose device.

If the maximum solid angle, 8 msr, accepted by a straight guide is used, then using the TRIUMF pion flux available at the 10 cm Be target, about 2.4×10^7 pions are transmitted by the guide. Assuming 80% of the pions decay (100 MeV/c pions at 10 m) and taking the capture efficiency of the Carnegie-Mellon beam guide of 11% (Foss, 1968), the maximum muon flux possible is $2 \times 10^6 \text{ muons (sec} \cdot \frac{\text{MeV}}{\text{c}})$. If a bending magnet is added for momentum analysis, this flux will be reduced. The solid angle of acceptance is reduced by a factor of 6 (Van der Meer, 1962) when the guide is bent through a few degrees. However, at Carnegie-Mellon (Foss, 1968) a design in which a bent beam guide passes through a bending magnet whose field is superimposed on the field of the guide is claimed to have an observed transmission of 70%. This means a maximum muon flux of $1.5 \times 10^6 \text{ (sec} \cdot \frac{\text{MeV}}{\text{c}})^{-1}$ but the channel is more sophisticated now and the

advantage of low cost has largely disappeared because of the special design for the magnet and the curved beam guide. No published performance data are available for the Carnegie-Mellon guide. It is described briefly in Appendix I.

3.4 Helical Quadrupole Channels

In a helical quadrupole channel, the quadrupole field rotates about the longitudinal axis with distance down the channel. An approximation to this is obtained if a series of thin quadrupoles are placed next to each other such that each quadrupole is rotated through a small angle about the optic axis with respect to the one preceding it. The motion of charged particles through such systems and their focussing properties have been studied extensively (for example, Krienen, 1957; Couteur, 1967; Salardi *et al.*, 1968; Pearce, 1970). This type of channel is stronger focussing than an equivalent conventional alternating gradient channel (Pearce, 1970). It also has about 20% larger phase space acceptance. An important advantage is that the cost could be considerably less than that of an A.G. channel.

There are several disadvantages to this type of channel. In the first place, there is strong coupling between the motions in the two transverse planes which makes perfect matching to ordinary quadrupoles and bending magnets in the system impossible. Secondly, as indicated by Ohnuma, it has low acceptance for momenta which deviate by more than about 20% from the central momentum p_0 . In particular, lower momenta

which are less than $0.8 p_0$ are strongly attenuated compared to a conventional channel, which accepts particles with momenta as low as $0.6 p_0$. This is an important disadvantage since decay muons may have momenta which differ from the reference momentum by more than 40 or 50%. Ohnuma showed that the momentum acceptance of the helical channel is 60% less than an equivalent A.G. channel and that the low momentum cut-off is $0.75 p_0$ for the former but $0.64 p_0$ for the latter. Thirdly, although it has 20% larger acceptance than a conventional quadrupole channel, the distribution of this acceptance in phase space is such that the pion beam cannot be efficiently injected (Ohnuma, 1969). Finally, a helical channel is less flexible than an A.G. one; it is a single purpose device.

No proposal for a muon channel using the helical quadrupole has been made except for an old suggestion at CERN (Morpurgo, 1957) for a 10 cm radius helical quadrupole with a field gradient of 11 Web/m³ having a winding pitch of 1.43. For a pion momentum of 285 MeV/c the channel capture efficiency for equimomentum muons was estimated at about 28%.

3.5 Channels Collecting the Muon Cloud Near the Pion Production Target

The recent data (Nagle *et al.*, 1969) indicates that the pion production cross section at low pion energy is not insignificant. Consequently, in the neighbourhood of the pion production target, a significant flux of muons resulting from the decay of low energy pions is to be expected. Thus, a muon source extended in all directions away from the pion source is available. If the channel is placed such that it is not looking directly at the pion target, i.e. its axis is misaligned

with respect to the pion target, the muon flux transmitted by the channel is not much reduced because of the extended muon source. The pion flux, on the other hand, is drastically reduced because the origin of all pions is the pion production target.

A channel utilizing this principle was considered by the LAMPF design group (Tanabe, 1970) and is described in Appendix J. Tanabe's work indicates that complete separation of the pions from the muons is not possible by simply misaligning the channel with respect to the pion production target. In addition to misalignment, it is necessary to use slits and detune the second half of the channel to a different momentum from that of the first half in order to obtain a pion-free muon beam. But this procedure results in reduction of the muon flux at the channel exit. If the yields obtained by Tanabe are normalized to the TRIUMF production target and proton current and energy, the total flux obtained is $1.5 \times 10^7 \mu^-/\text{sec}$ integrated over an area of 27.5 cm x 27.5 cm at the exit. Thus, this type of channel does not seem to have any advantages compared to a conventional channel where detuning is employed (see Section 4.4.2).

3.6 Channels in Which Pions Decay at Rest

The pions are stopped and the 4.12 MeV muons from the decay of pions at rest are collected. This method is possible only for positive pions since negative pions interact readily with the stopping material before decaying. Two types of channels, based on this principle, are possible.

3.6.1 Muons from Pion Decay at Rest in an Absorber (Jakobson Type)

If positive pions are brought to rest in an absorber, the decay muons will have a maximum energy of 4.12 MeV and can be collected and focussed onto a stopping target. A channel utilizing this concept was suggested (Jakobson, 1968). A superconducting magnet would be employed to trap the pions, after a suitable degrader reduced their energy to a few MeV. Inside the magnet, a low density absorber such as styrofoam slows down the pions to rest after a few orbits. The decay muons would be collected into a transport system at right angles to the plane containing the orbits of the pions. To increase the pion flux, a wedge absorber may be placed at the dispersed focus of a bending magnet forming part of the pion beam transport system.

With the above arrangement, it should be possible to obtain an almost contamination-free muon flux of about $4 \times 10^7 \mu^+$ /sec, assuming a 1 mA beam of 800 MeV protons on a 3.4 cm Cu target. The channel is of limited use because only positive muons can be obtained.

3.6.2 Muons from Pion Decay at Rest in the Production Target

The concept of collecting low energy muons generated from the decay of low energy pions stopped in the production target (using any type of channel) is different from concepts considered earlier. Although the pion production cross section is relatively low for pions of a few MeV energy, the capture of the muon in the channel is a one-step process in contrast to the usual two steps - capturing first a pion, then the decay muon. This concept was tested experimentally by the Arizona group

(Pifer *et al.*, 1971) using the 184" cyclotron at the Radiation Laboratory of the University of California, Berkeley. The muons emerging from the production target have a maximum energy of 4.12 MeV. The muon flux as a function of momentum obtained by the Arizona group is shown in Fig. 3.1, which indicates a peak at 28 MeV/c. This is for a 30 nA, 750 MeV protons on a 5" long tungsten target. The channel used, a conventional quadrupole and bending magnet channel, had a solid angle of acceptance of 40 msr. In Section 4.4.2, the corresponding flux for the TRIUMF case is discussed.

3.7 Channels Using Time-of-Flight

Because of the mass difference between the pions and the muons, the velocity of a muon is slightly greater than that of a equimomentum pion. These pions and muons can be separated by time-of-flight, which is much cheaper than magnetic analysis. In any such separation scheme, it is not possible to separate muons which are born between the two spatial points where the timing is performed.

The possibility of using the proton pulse as a starting pulse has been investigated (Pearce, 1969). Even with a channel which is designed to be isochronous for pions, there are difficulties from the time length of the proton pulse and from the finite momentum acceptance of the channel. It should be possible to obtain the starting pulse from counters located at the midpoint. Using several counters dispersed in the transverse direction to use the spatial dispersion of the pion beam, the effect of the finite momentum range could be nullified.

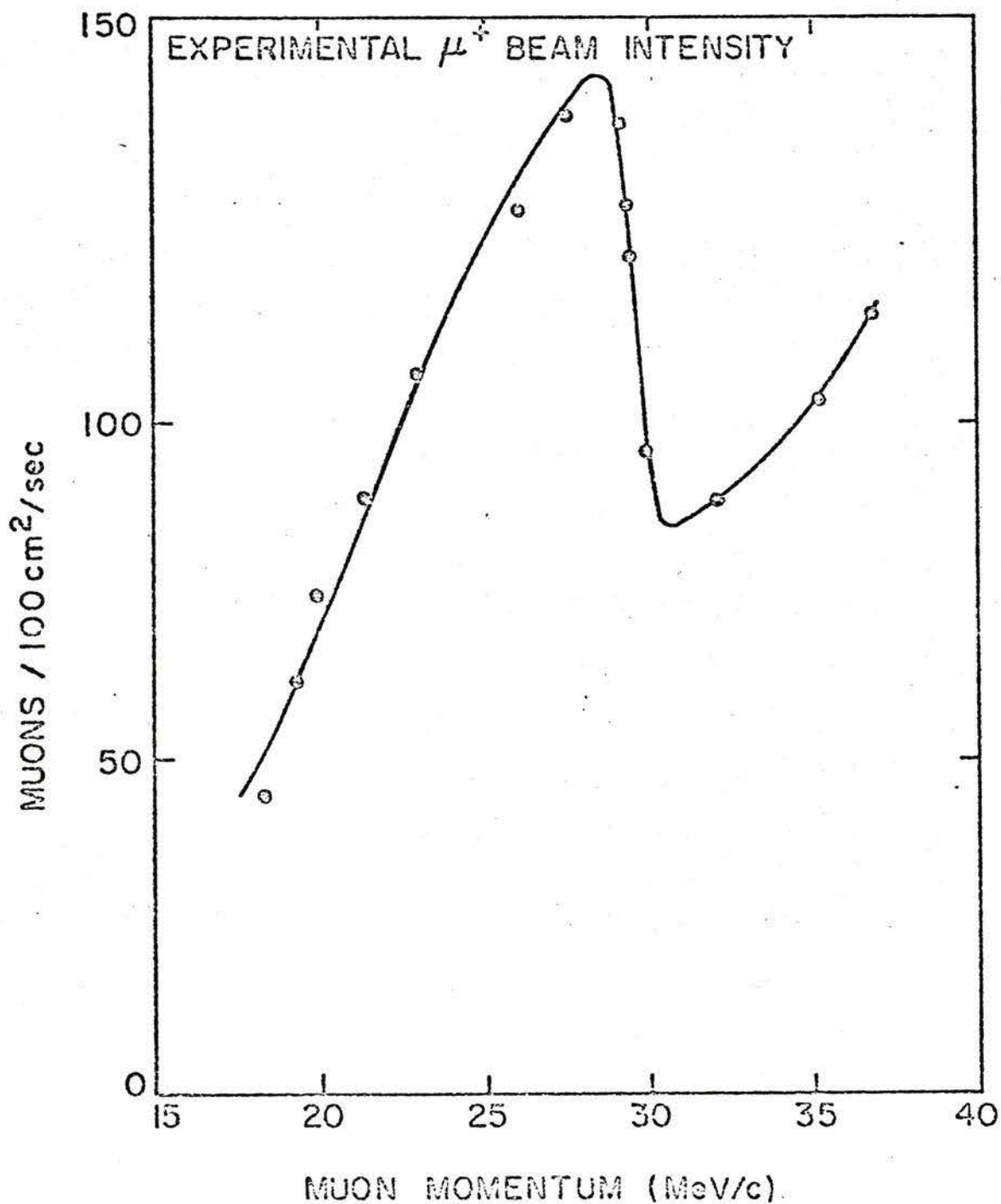


Fig. 3.1 The experimental beam intensity of the Arizona channel for muons generated in the pion production target for a 30 nA beam of 750 MeV protons on 5" tungsten target. Reproduced (Pifer *et al*, 1971).

CHAPTER 4

PROPOSED TRIUMF STOPPED PION/MUON CHANNEL

PHASE ONE

4.1 Introduction

The requirement, as indicated by the users, is for a dual purpose channel to provide both pions and muons. This, together with the general criteria discussed in Section 1.4, eliminated some of the channels discussed in Chapter 3, such as the muon cloud type and the Jakobson type. Also, as shown in Section 4.2.3, a bend is essential for any channel and, in order to obtain reasonably good pion optics and an achromatic beam, at least two bends are required. The proposed channel consists of three main sections:

- 1) an achromatic pion collection section which will also form the stopped pion channel by itself,
- 2) a straight pion decay section to collect decay muons, and
- 3) a momentum analyzing section to separate the pions from the decay muons.

The rest of this chapter will be restricted to the discussion of the first section, its use as a stopped pion channel, and its possible use as a stopped muon channel. Separation of pions from muons by an analyzing magnet placed immediately after the collection system is also discussed in this chapter. The performance of the muon channel with straight section and analyzer will be discussed in Chapter 5. This division coincides with the two phases of the construction program.

4.2 Channel Design

4.2.1 Design Aims

The following design aims are used in optimizing the system.

- 1) The channel is to be capable of providing both positive and negative pions and muons, although it should be optimized for negative mesons.
- 2) The stopping rate of pions (pions per gram/cm² per sec) is to be maximized with due consideration of the funds available. This implies, among other things which are not variable design parameters, that one should aim at:
 - (a) as short a channel as practicable,
 - (b) an achromatic channel,
 - (c) a large solid angle of acceptance,
 - (d) a large accepted momentum bite, and
 - (e) a thick pion production target of high luminosity.Except for item (a), the above criteria also lead to increasing the muon flux.
- 3) Contamination with neutral particles, electrons and protons is to be minimized. This implies that one should aim at:
 - (a) using bends which attenuate neutrons,
 - (b) a large angle of pion extraction which minimizes the number of electrons (see Fig. 2.3) and high energy neutrons (cochrane and Jakobson, 1967),
 - (c) low energy operation which reduces protons because low energy protons having the same momentum as the pions are easily absorbed in thin absorbers.

- 4) The pion beam spot size at the stopping target is to be minimized, which implies that one should aim at:
- (a) a small production target,
 - (b) a large backward angle (or a small forward angle) to reduce the projected length of the target, and
 - (c) good beam optics.

One cannot do very much to minimize the muon beam size because of its large emittance due to the extended source of muons. However, 100 cm² is used as a reasonable size to aim at.

- 5) The pion beam should be brought to a focus near the midplane so that a momentum-defining slit may be placed there to limit the accepted momentum band.
- 6) The channel should be capable of providing polarized muons. Although polarization is not required for mesic x-ray studies, it is required for muonium studies.
- 7) The channel should be flexible in order to accommodate the varying requirements of the various users and to make future modifications or additions possible without radical changes.
- 8) Cost should be kept as low as possible which implies that one should not aim at more sophistication when the improvement in performance is only marginal.

4.2.2 Design Methods

The general configuration and initial parameters for the beam transport system were obtained using a hybrid analog computer (Al-Qazzaz, 1969). This was followed by an optimization using the program TRANSPORT (Brown and Howry, 1970) with its first order optimization routine. This program is described in more detail in Appendix K. The program TRANS (Chan, Hunt and Lobb, 1972) was also used occasionally for this purpose and for calculating the various tolerances of the systems elements. This program is also described in Appendix K. For second order optics, TRANSPORT was used to calculate the second order transfer matrices. The system acceptance and beam emittance were calculated using the program ACCEPTANCE (Harrison and Lobb, 1968) which also calculates the acceptance solid angle (see Appendix K). The beam was then simulated using the Monte Carlo program NPFLUX (Hutson, 1970) and a slightly modified version of it. This program uses the first and second order matrices from TRANSPORT to calculate the solid angle of acceptance, particle density distribution in the beam, and the horizontal and vertical histograms of this distribution at any given point in the beam line (see Appendix K). However, NPFLUX does not calculate pion decay.

Momentum spectrum for the pions and the decay muons are calculated using the program MBEND which is a modified version of the program BEND (Ohnuma, 1969). This program is also used for the final optimization of the channel. The modified version MBEND has facilities for tracing the pions and the muons through the different sections of the channel which

are tuned to different central momenta. It also calculates the stopping density of the pions and muons as functions of range in g/cm^2 of carbon. More detailed description is given in Appendix L. A plotting program, PLOTS, to plot the quantities calculated by MBEND, is also described in Appendix L.

4.2.3 Parameter Optimization

The design parameters for the system are:

- (a) primary proton current,
- (b) pion production target material and size,
- (c) pion energy,
- (d) angle of extraction (production angle),
- (e) distance of the first magnet from the production target,
- (f) total system length,
- (g) accepted momentum band,
- (h) the number and angle of bends,
- (i) strengths and spacings of the quadrupoles, and
- (j) apertures of the dipoles and quadrupoles.

These parameters are to be chosen to satisfy, as far as possible, the aims discussed in Section 4.2.1.

- (a) The maximum primary proton current available depends on the choice of energies and currents made at that time by other users on both beam lines of TRIUMF. For the purpose of this study, yields will be quoted assuming a design current of $100 \mu\text{A}$.

(b) Various materials have been considered for the pion production targets (Hodges, 1970). Of the several target materials studied, Cu, C and Be seem to be acceptable. Be is preferred unless short targets (less than 4 cm) are required, as is the case in some pion experiments when the image size has to be small. Again, because the target is shared by another user (the medical pion channel), one is not completely free in choosing the type of target material. The choice of the target thickness is limited by the degradation and energy loss of the proton beam which is to be used by the neutron facility further downstream. For the purpose of this design, a 10 cm long Be target is chosen. The target size as seen by the channel will depend on the angle of productions.

(c) The choice of pion momentum is based on three main considerations. First, the Los Alamos pion production cross section measurements discussed in Section 2.1 indicate a rise in cross section to a peak as the pion momentum decreases to ~ 50 MeV for large angles. This is supported by the CERN and other data discussed in Section 2.1. Secondly, the muon decay cone angle decreases with increasing pion momentum which improves the efficiency of the channel for trapping muons. However, this has to be balanced against the increase in the pion decay length at higher momentum which reduces the decay fraction in a given length of channel. The final consideration is the fact that choice of high energy pions leads eventually to the use of thick degraders to slow down the meson before stopping in the target. Thick degraders cause losses due to multiple scattering and although this

may be minimized by placing the degrader as close as possible to the target, the neutrons and other particles produced in the degrader result in a low signal-to-noise ratio in the detector system. Thus for the pion beam, an energy of less than 50 MeV (130 MeV/c) would be chosen. However, for the muon beam, using higher energy and collecting backward decaying muons leads to a choice of high pion energy. But, as will become clear in the forthcoming discussion, this pion energy is only slightly higher. It was, therefore, decided to optimize the channel for a pion momentum of 100 MeV/c (32 MeV) and design it to be tunable between 0 - 160 MeV/c (0 - 70 MeV).

- (d) The choice of production angle does not appear to be critical at the low energy range chosen above as far as the production cross section is concerned, as indicated in Section 2.1. However, there are good reasons for choosing a large angle. First, as shown in Fig 2.3, electron contamination decreases at large angles. Secondly, a Monte Carlo calculation for 800 MeV protons on 4.5 g/cm² C target (Cochran and Jakobson, 1967) indicates that at angles larger than 90° high energy cascade neutrons are reduced by a factor $\sim 10^4$ and neutrons of all energies are reduced by a factor $\sim 10^2$. This is shown in Fig. 4.1, reproduced from the report quoted above. Thus, both on account of reduced contamination and the decision to choose low energy pions, a large (backward) angle seems preferable. On the other hand, to increase the solid angle of acceptance, the first magnet element has to be as close to the target as possible. On this account an angle of 90° will be preferable. However, this will make the projected size of the target large and, therefore, the beam spot size will be large.

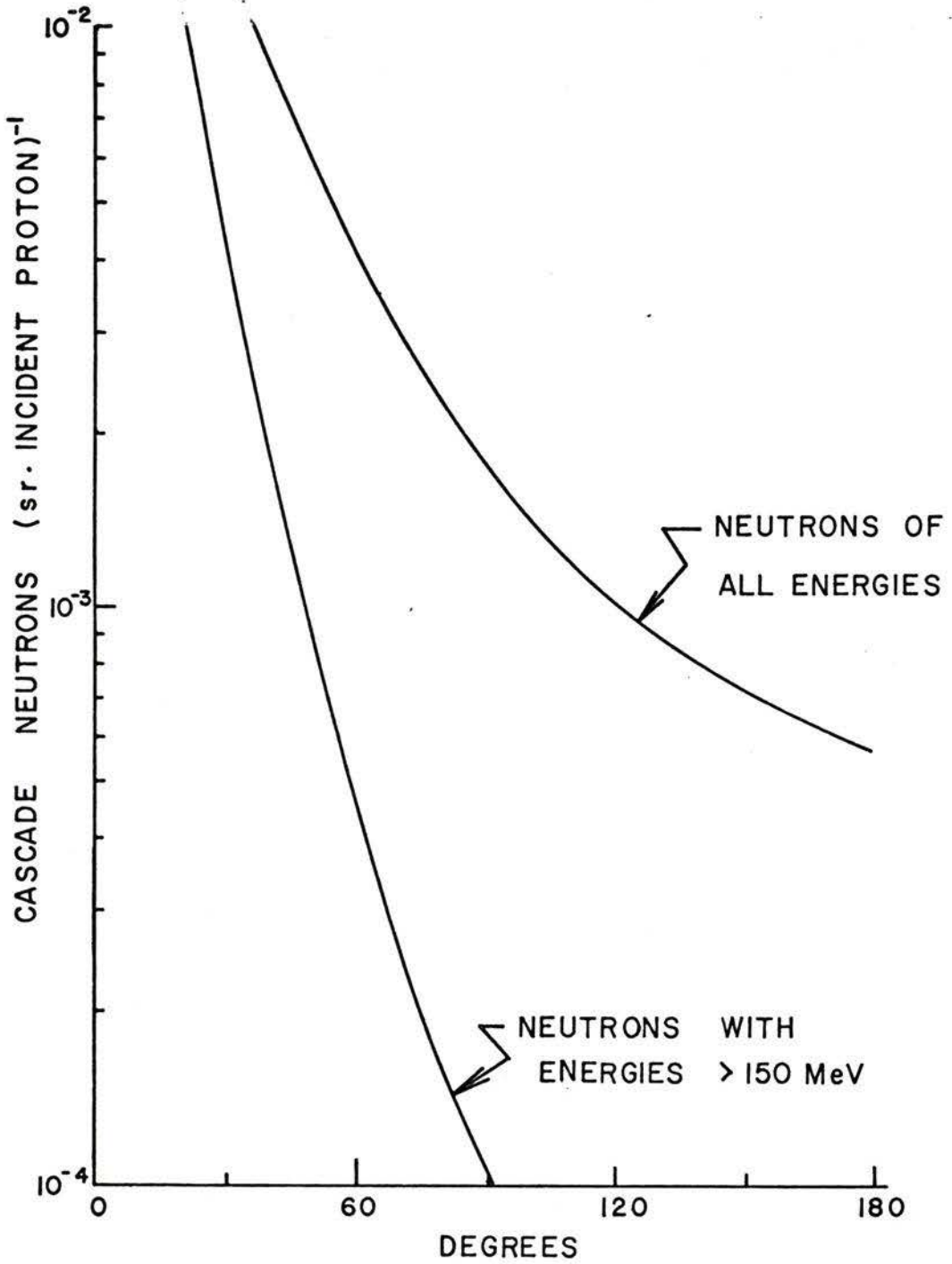


Fig. 4.1 Angular distribution of cascade neutrons, a Monte Carlo calculation for 800 MeV protons on 4.5 g/cm² C target (Cochran and Jakobson, 1967).

A production angle of 135° was chosen as the optimum for the case where the first quadrupole element is 8" in aperture. This will be discussed further below.

- (e) This distance of the first quadrupole from the production target should be as small as possible in order to maximize the solid angle of acceptance. This may be achieved by choosing a production angle of 90° as mentioned above but, for the reasons given there, 135° was chosen. At this angle, the distance is determined by the size of the quadrupole element. The minimum distance for an 8" aperture quadrupole is 0.5 m and for a 12" quadrupole is 0.7 m if the quadrupoles are not to interfere with the proton beam.
- (f) The total length of the system was minimized to reduce the pion decay. Although this is not optimum for muons, it is felt that more elements could be added to increase the muon beam. This is particularly so if one wants to collect muons from backward-decaying pions. In any case, in the energy range likely to be used, the pion decay length is about 4 to 7 meters (see Fig. 2.9) and the channel cannot be made as short as one decay length for reasons to do with the physical dimensions of the magnets and the necessity to penetrate the shielding wall. Even with this minimum length, a considerable fraction of the pions would have decayed at the pion energy likely to be used.
- (g) The momentum pass band chosen will depend on other system parameters, particularly the number of bending magnets and the angle of bend. A band of not less than $\pm 10\% p_0$ is aimed at in order to increase the accepted pion flux. If, for some experiment, a narrower band is required, provision is made for a momentum-defining slit to be placed at a dispersed focus near the midplane of the channel.

(h) The argument for the inclusion of bends (Pearce, 1970) centres around, principally, the problem of the attenuation of low energy evaporation neutrons. High energy neutrons are eliminated by the choice of an angle of pion extraction greater than 90° , as mentioned earlier in this section. Low energy neutrons are produced isotropically from the target and their rate of production depends on the energy of the proton beam and the target material. The necessity for bends can be demonstrated with the following order-of-magnitude calculations. If it is assumed that one neutron is produced for each proton making an inelastic collision, which is a reasonable assumption when compared with experimental measurements (Gross, 1957) for 190 MeV protons on carbon, the neutron intensity would be about 10^{14} per sec. Assuming a 10 meter long channel with 10^{11} aperture and a pion flux at the channel exit of 10^8 per sec, the table below summarizes the calculation results obtained using the methods discussed in Section 4.3.6.

Number of bends	Channel attenuation factor	<u>At Channel Exit</u>	
		neutron flux/sec	neutron/pion
No bend	10^{-4}	10^0	10^2
One bend	10^{-8}	10^6	10^{-2}
Two bends	10^{-11}	10^3	10^{-5}

Obviously, at least one bend is essential. However, only neutrons produced in the target were considered in the above calculation.

The intensity of secondary neutrons produced in the channel walls as the result of stopping pions and protons is difficult to estimate. For the purpose of this argument, though, it is assumed that they have a minimum flux equal to the pion flux; that is, $\sim 10^8$ neutrons per sec, which will mostly be generated in the first half of the channel where the beam spill is high. To attenuate these neutrons, a second bend is desirable. This second bend will also make it possible to design an achromatic system that will contribute to increasing intensity.

Once the necessity of bends is established, the question of the angle of bend can be studied. To increase the momentum pass band of the channel, a small angle should be chosen since the momentum acceptance of the system decreases as the bending angle increases. On the other hand, a small angle leads to greater separation between the bending magnet and the quadrupole that follows it in order to allow for neutron traps, which leads to a longer channel and to a decrease in the solid angle of acceptance. A bending angle of 45° was chosen, which maintained a momentum band not less than $\pm 10\% p_0$. Two rectangular 45° bending magnets were chosen; the rectangular magnets have pole-face rotations providing vertical focussing which is sufficient to make it possible to eliminate a second quadrupole between the two dipoles.

- (i) Two quadrupoles were found to be the minimum number needed to form a nearly parallel beam in the horizontal plane with a waist in the vertical plane at the first bending magnet, then to form a horizontal focus at the midplane.

Two other quadrupoles were necessary to form a double focus or a double waist at the pion stopping target. The centre quadrupole was adjusted to get an achromatic beam. The strengths and spacings of these quadrupoles were varied, subject to those constraints which ensure that the channel remains achromatic with a horizontal focus at midplane. The criteria were maximum acceptance, and consequently pion and muon fluxes, subject to the above constraints. The procedure was to choose a value for the field of the first quadrupole Q1, then compute the acceptance using TRANSPORT for several values of the drift lengths between the two bending magnets, always maintaining the criteria mentioned above. The fluxes of pions and muons were computed using the program MBEND and an optimum system which maximized these fluxes was chosen.

- (j) The quadrupole apertures and magnet gaps were optimized by calculating pion and muon fluxes for each of three aperture sizes, 8", 10" and 12" and magnet gaps 6.5", 8" and 10". The results are shown in Fig. 4.2 for pions and Fig. 4.3 for muons. This indicates a steep rise in flux for both pions and muons as the apertures and gaps increase in size. However, bearing cost in mind, it was decided to choose 12" quadrupoles and 10" gaps.

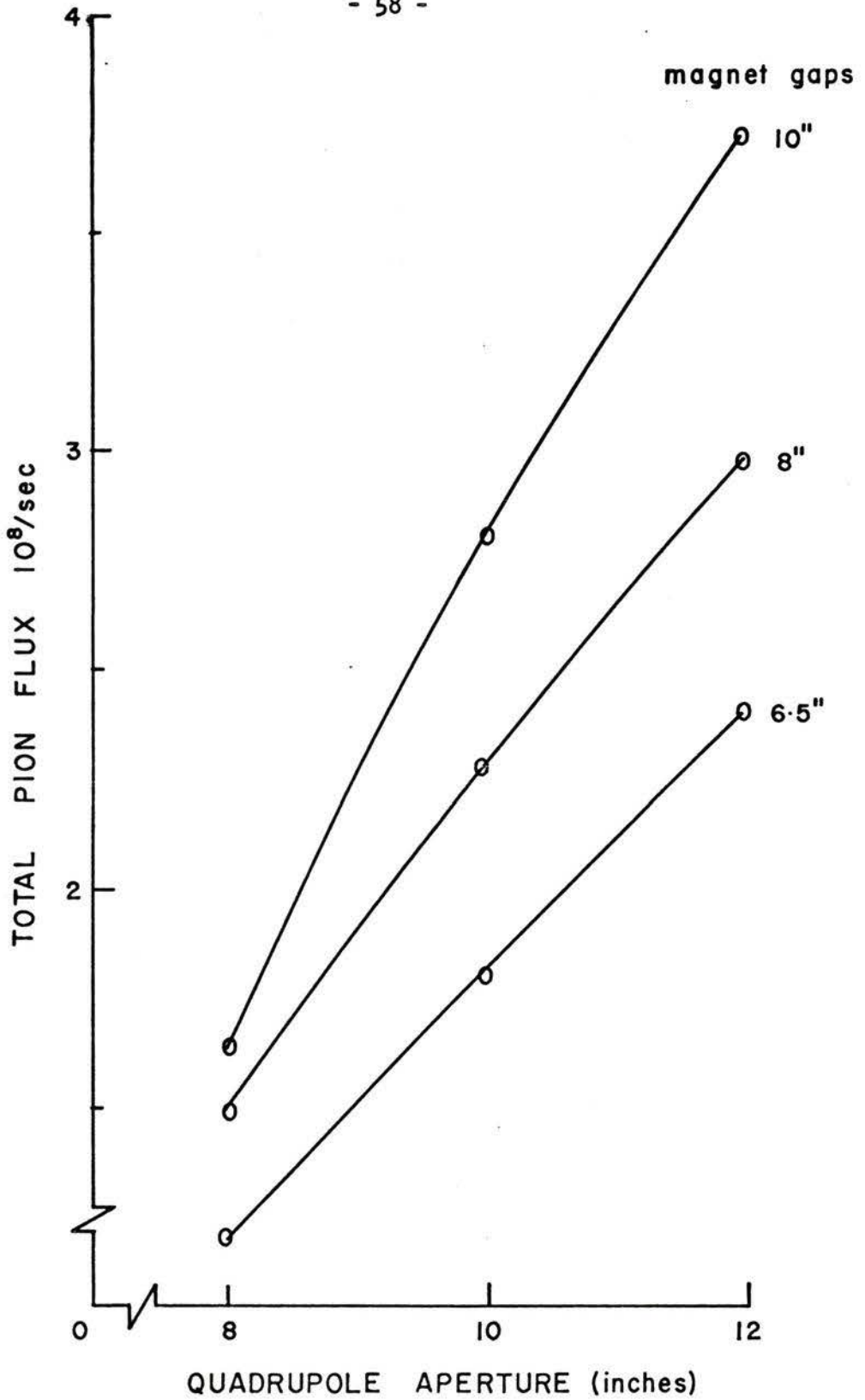


Fig. 4.2 Total pion flux versus quadrupole aperture for three values of the magnet gaps. Fluxes are for $p_0 = 100 \text{ MeV}/c$ integrated over an area of $25 \text{ cm} \times 25 \text{ cm}$.

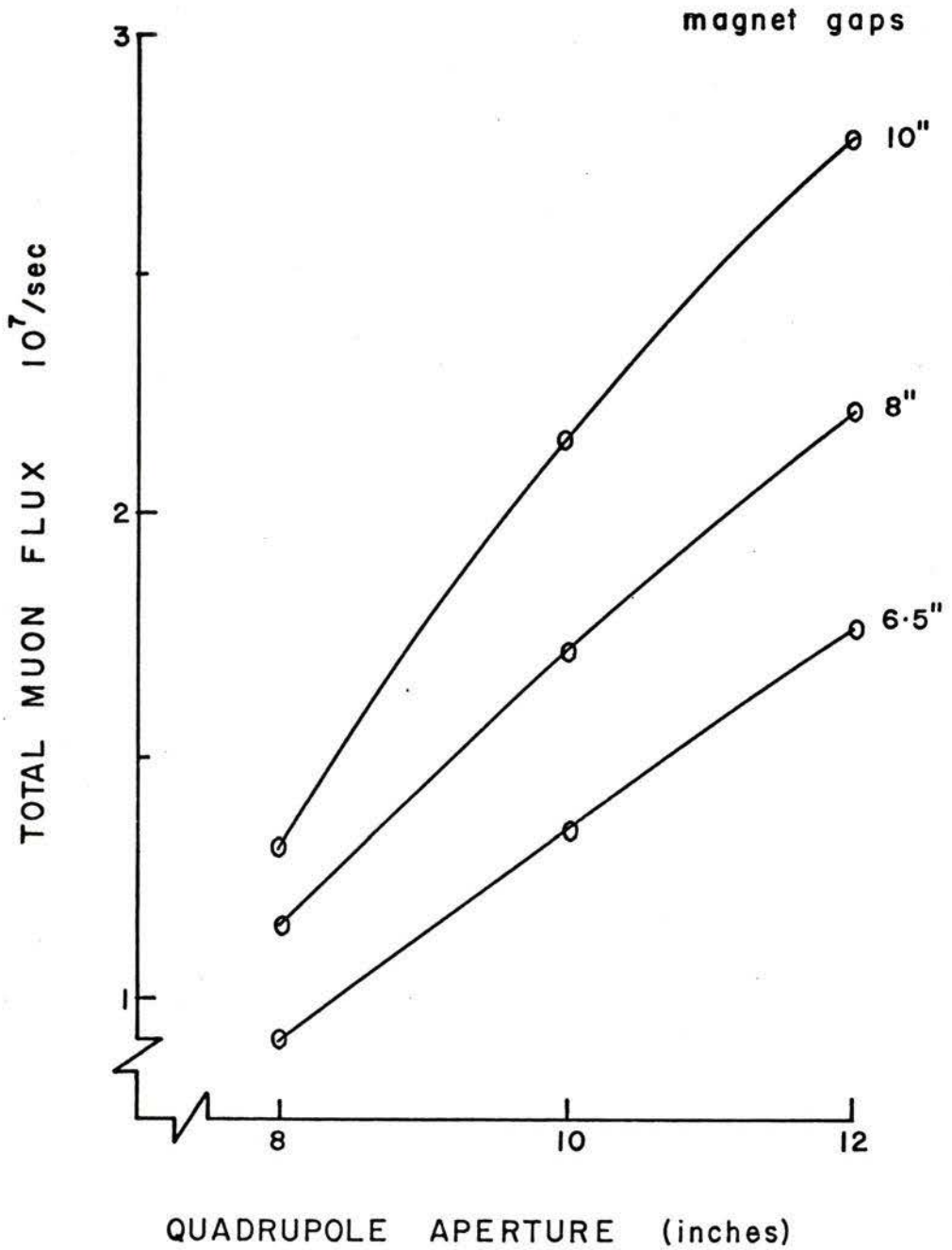


Fig. 4.3 Total muon flux versus quadrupole aperture for three values of the magnet gaps.
Fluxes are for $p_0 = 100 \text{ MeV}/c$ integrated over an area of $25 \text{ cm} \times 25 \text{ cm}$.

4.2.4 Cost

The cost was minimized by using the minimum number of magnets that would perform the job, subject to the specifications set in Section 4.2.1, and by choosing magnets which are reasonably inexpensive. The costs of magnets and power supplies were estimated using two programs (Otter, 1970(a) and (b)) for the dipole and quadrupole magnets respectively, employing up-to-date material and fabrication costs. Costs of supports, monitors, vacuum, alignment, engineering and installation are not included. It is assumed that these costs are not affected significantly by the size of magnets used. The percentage increase in the pion and muon fluxes as a function of the percentage increase in the cost of magnet and power supplies was calculated and plotted in Fig. 4.4. It is seen that the integrated pion and muon fluxes are doubled by using 10" gaps and 12" quadrupoles, while the cost increases by about 35% only. The total estimated cost of magnets and power supplies for the optimized channel is given in Table 4.1 for the two cases when the maximum operating momentum is 140 MeV/c (60 MeV) and 160 MeV/c (72 MeV).

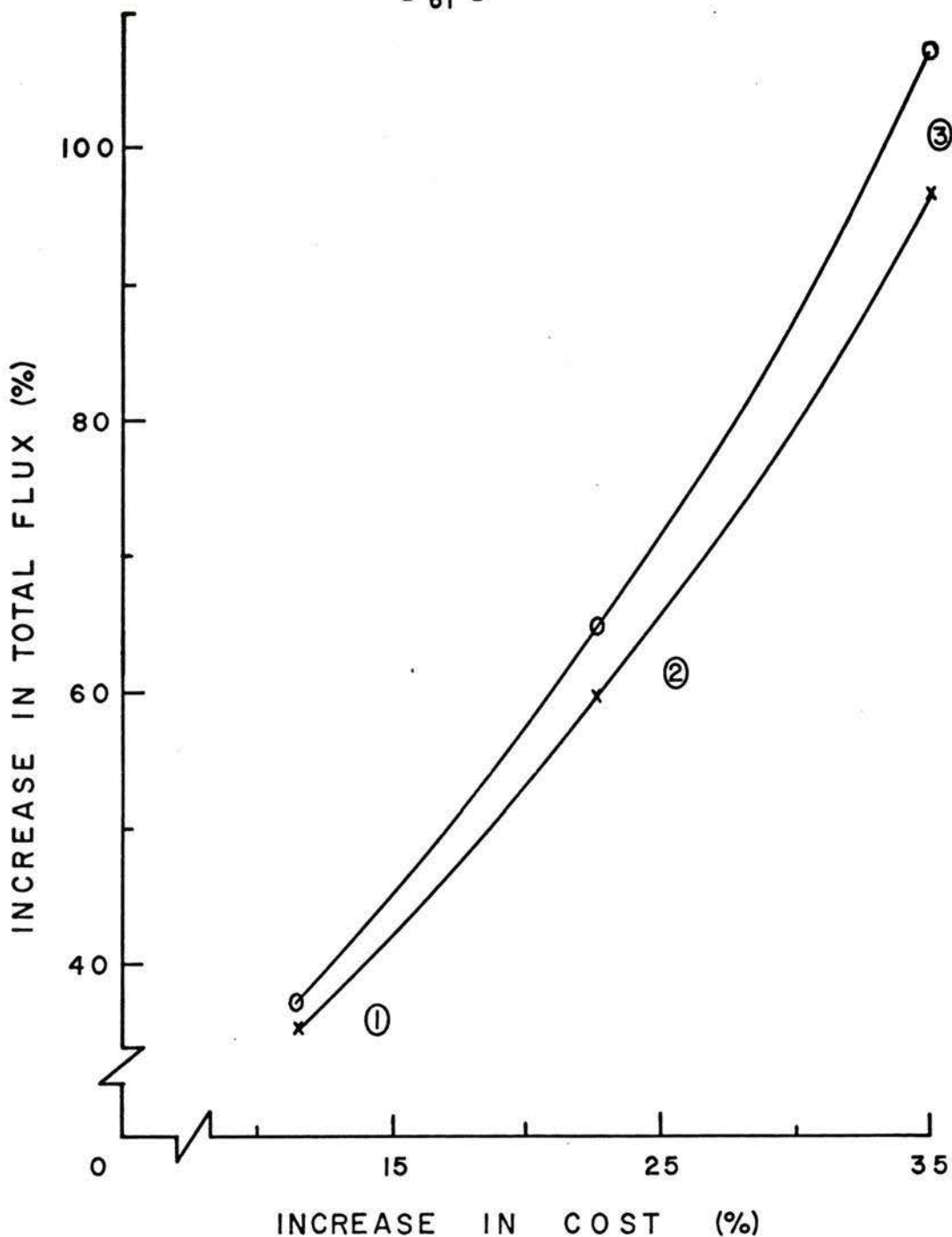


Fig. 4.4 Increase in total flux versus increase in cost for three magnet-quadrupole combinations, relative to a reference system with 6.5" magnet gaps and 10" quadrupole apertures.

- ① 8" gaps and 10" apertures (except Q3 with 12" aperture)
- ② 8" gaps and 12" apertures
- ③ 10" " " " "

Fluxes are for $p_0 = 100$ integrated over an area of 25 cm x 25 cm.

Table 4.1

Magnets and Power Supply Costs in \$1000

	number <u>required</u>	Maximum Momentum <u>140 MeV/c</u>			Maximum Momentum <u>160 MeV/c</u>		
		magnet	power	total	magnet	power	total
			<u>supply</u>	<u>cost</u>		<u>supply</u>	<u>cost</u>
<u>Quadrupoles</u> [*]							
8QN16M/2.2(2.6)	1	5.4	4.0	9.4	5.7	4.2	9.9
12Q12/4.1(4.7)	4	8.8	5.6	58.0	9.5	6.0	62.0
<u>Bending Magnets</u> [†]							
C20 x 20/4.9(5.6)	2	17.7	9.8	<u>55.0</u>	19.9	11.0	<u>61.8</u>
				122.4			133.7

* The LAMPF code is used.

The first figure is the quadrupole aperture; the second is the pole length; N stands for narrow and M for mineral insulation. The figures after the slash are the pole-tip fields for maximum operating momentum at 140 and (in brackets) 160 MeV/c.

† C designates a C-type magnet. The dimensions follow the C in this order: pole width, gap (in Roman numerals) and pole length. Pole-tip fields are as for quadrupoles.

4.2.5 Description of the Optimized Channel

A schematic layout diagram is shown in Fig. 4.5 and values of the various parameters are given in Table 4.2 in the case where pole tip fields are set to produce a focus at the midplane and a small first order spot at the channel end.

The pions are extracted at 135° . Quadrupoles Q1 and Q2 bring the beam, after bending through 45° , to a focus either at the centre of Q3 (if the channel is used for muons) or 10 cm upstream from Q3 at the location of the momentum defining slit when the channel is used for pions. The beam is then bent through another 45° and brought to a double focus, a double waist or a minimum size spot according to the field settings of the quadrupoles Q4 and Q5. The total length of the channel is 7.9 m.

The two 45° bending magnets have 20" x 20" rectangular pole pieces and 10" gaps. A C-type magnet may be preferred for M1 in order that charged particles of the sign opposite to those accepted may be deflected out into a trap. With a window frame type magnet, and to a lesser extent an H-frame, these particles hit the walls of the magnet and become a source of neutrons and other secondary particles. The second magnet M2 does not have to be a C-type.

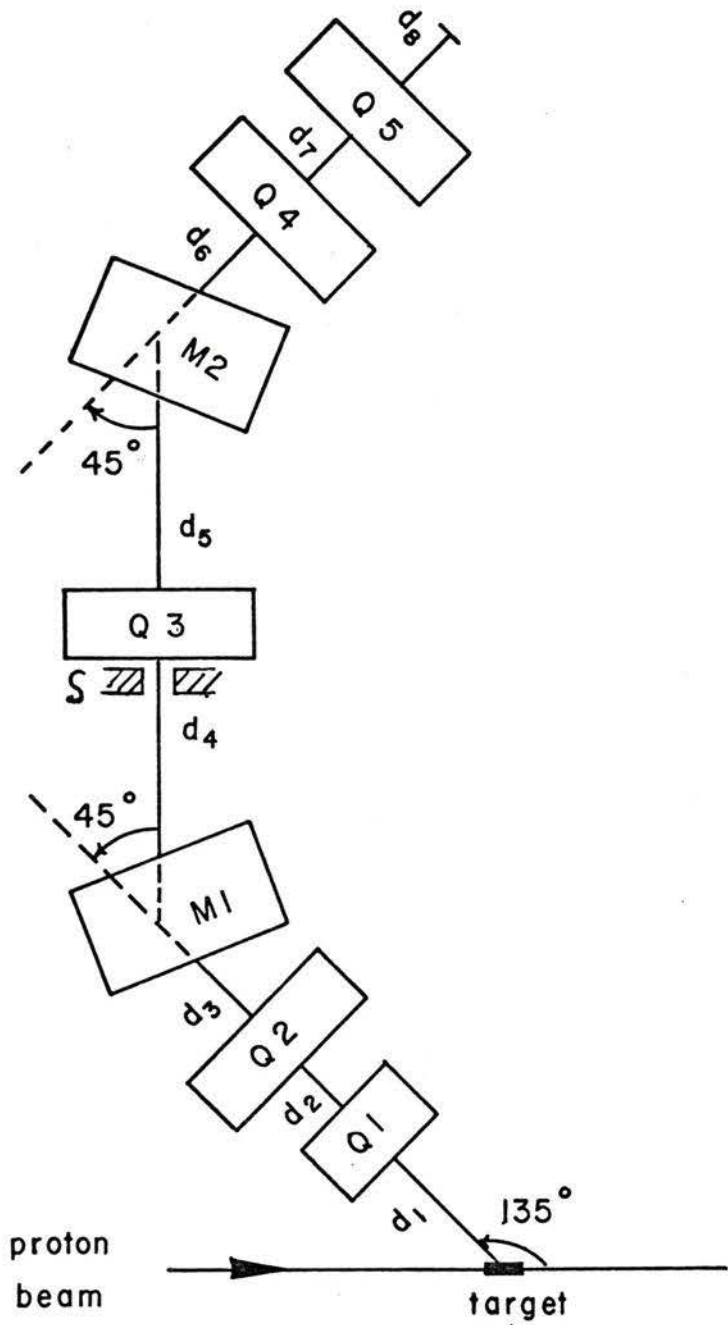


Fig. 4.5 Schematic layout of the Phase One channel (Pion Collection System).

Table 4.2
Optimized Channel Parameters

Element	Effective Length (inches)	Pole-tip Field* (kG)	Quadrupole Aperture (inches)	Magnet Gap (inches)	Magnet Width (inches)
d ₁	22.4	—	—	—	—
Q1	20.0	-1.6	12	—	—
d ₂	8.0	—	—	—	—
Q2	18.0	1.898	—	—	—
d ₃	20.9	—	—	—	—
B1	30.0	3.493	—	10	20
d ₄	27.5	—	—	—	—
Q3	18.0	1.964	12	—	—
d ₅	27.5	—	—	—	—
B2	30.0	3.493	—	10	20
d ₆	26.0	—	—	—	—
Q4	18.0	1.946	12	—	—
d ₇	8.0	—	—	—	—
Q5	18.0	-2.898	—	—	—
d ₈	20.0	—	—	—	—

* Negative fields imply vertical focusing quadrupoles.

Fields are quoted for operation at $p_0 = 100$ MeV/c.

The quadrupoles, except for Q1, have 12" long pole pieces and 12" apertures. Q1 has a 16" long pole piece, 8" aperture, and is radiation hardened. The 8" aperture instead of 12" reduces the solid angle of acceptance of the channel by almost 30%. However, design and drawings for the 8" lens are available readily, and because of limitations of time and effort, the 8" aperture has been chosen for Q1.

The slit in front of Q3 is to be remotely controlled and will be used to adjust the momentum bite accepted for some pion experiments; otherwise it will remain fully open. Two neutron traps are to be provided after M1 and M2. The distances d_4 and d_6 were determined so that a beam of neutral particles will not touch Q3 and Q4 respectively. Some provision is to be made for absorbing the charged particles deflected to the left (looking along the beam direction) after the first magnet, M1, in order to minimize scattering back into the channel and secondary emission.

4.3 Expected Performance

In this section, the calculated performance for π^- and μ^- of the channel shown in Fig. 4.5 is discussed, with the elements positioned as indicated in Table 4.2. The central momentum p_0 is 100 MeV/c, except in Section 4.3.4, where the yield as a function of momentum is investigated and the fields indicated in Table 4.2 are scaled accordingly.

4.3.1 Channel Characteristics

(a) Pion Energy

The energy is variable but the calculations were carried out for several energies between 12 MeV (60 MeV/c) and 73 MeV (160 MeV/c). Optimization was carried out at a central momentum of 100 MeV/c and parameters were scaled up or down when calculating performance at other momenta. Calculated yields for various energy settings will be discussed in Section 4.3.4.

(b) Channel Acceptance for Pions

The acceptance of the channel was calculated using several methods. First, using the program NPFLUX, the solid angle was calculated as a function of $\Delta p/p_0$ and the results are plotted in Fig. 4.6. The maximum solid angle at $\Delta p/p_0 = 0$ is seen to be 25.9 msr. These calculations also indicated that the momentum bite accepted is $\pm 17.5\% p_0$. The FWHM (Full Width at Half Maximum) of the curve is $\pm 9\%$, which may be used in conjunction with the maximum solid angle for estimating pion yields. The above results include second order

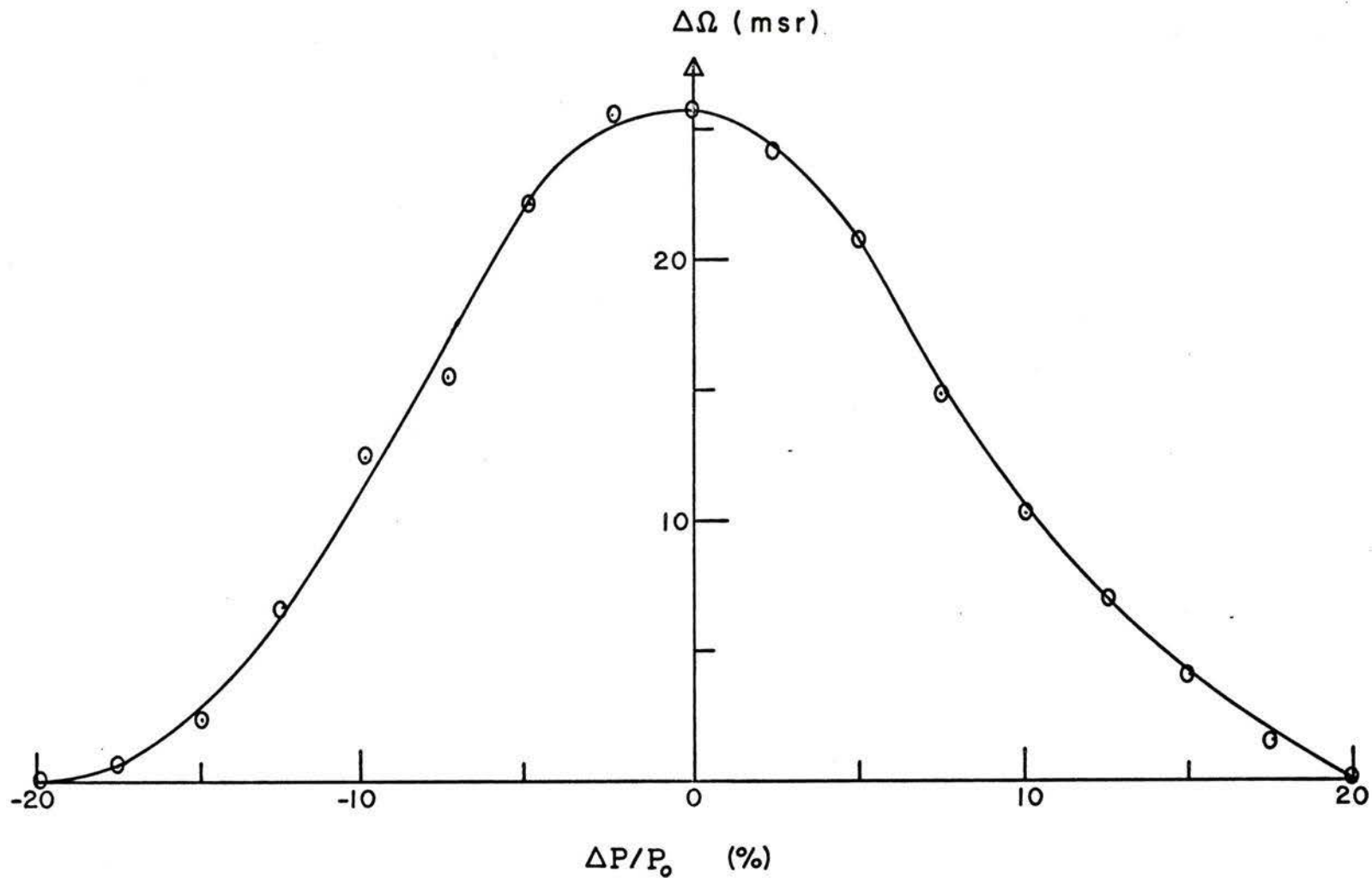


Fig. 4.6 Solid angle of acceptance as a function of $\Delta p/p$ for the reference system described by Fig. 4.5 and Table 4.2.

effects. The pion momentum bite transmitted to the end of the channel is obtained from the flux calculations with MBEND and is between 85 MeV/c and 120 MeV/c; i.e., a momentum acceptance of $\pm 17.5\%$ in agreement with the NPFLUX results. The phase space areas, calculated by the program ACCEPTANCE, are:

2.00 cm-rad for the horizontal plane, and
0.32 cm-rad for the vertical plane.

(c) Flux

For the reference settings indicated in Table 4.2, the calculated momentum spectra of pions and muons are shown in Fig. 4.7 and the corresponding range curves in Fig. 4.8. These are calculated from the relations discussed in Section 4.3.4 for the condition stated there. The total π^- flux is $2.9 \times 10^8/\text{sec}$, and μ^- flux is $4.8 \times 10^7/\text{sec}$, and the pion-to-muon ratio is 5.9. Maximum differential flux and stopping rate for pions are $1.54 \times 10^7 \pi^- (\text{sec} \cdot \text{MeV}/c)^{-1}$ and $1.04 \times 10^8 (\text{sec} \cdot \text{g}/\text{cm}^2)^{-1}$ respectively. The corresponding figures for muons are $1.35 \times 10^5 \mu^- (\text{sec} \cdot \text{MeV}/c)^{-1}$ and $2.67 \times 10^6 \mu^- (\text{sec} \cdot \text{g}/\text{cm}^2)^{-1}$ respectively. These fluxes are all quoted for $p_0 = 100 \text{ MeV}/c$ and an area of 25 cm x 25 cm. The distribution of the pion beam in the transverse planes for $\Delta p/p = 0\%$ and $\Delta p/p = 20\%$ are shown in Fig. 4.9 and Fig. 4.10 respectively.

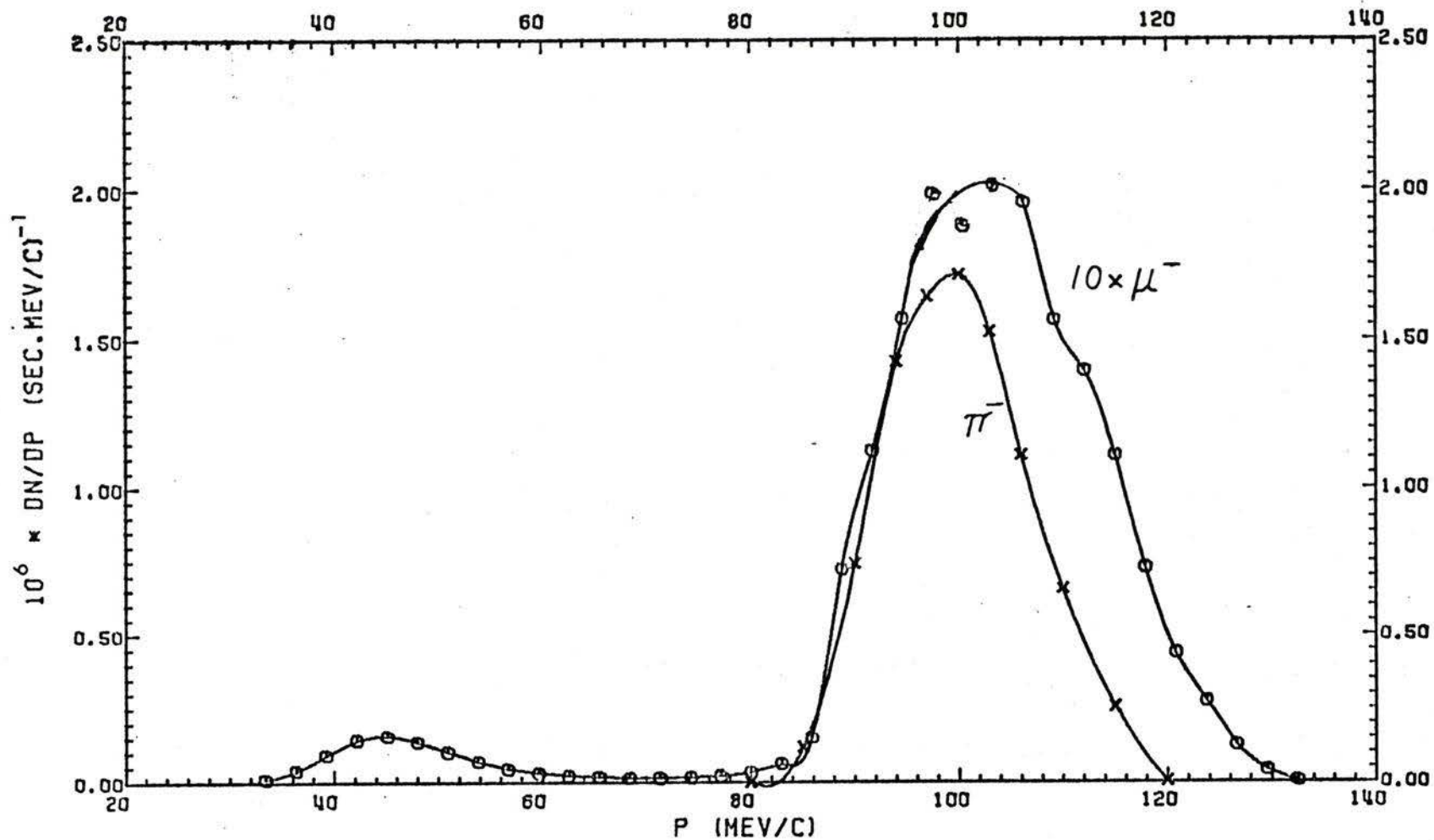


Fig. 4.7 Pion and muon momentum spectra for the reference system described by Fig. 4.5 and Table 4.2 at $p_0 = 100 \text{ MeV}/c$.

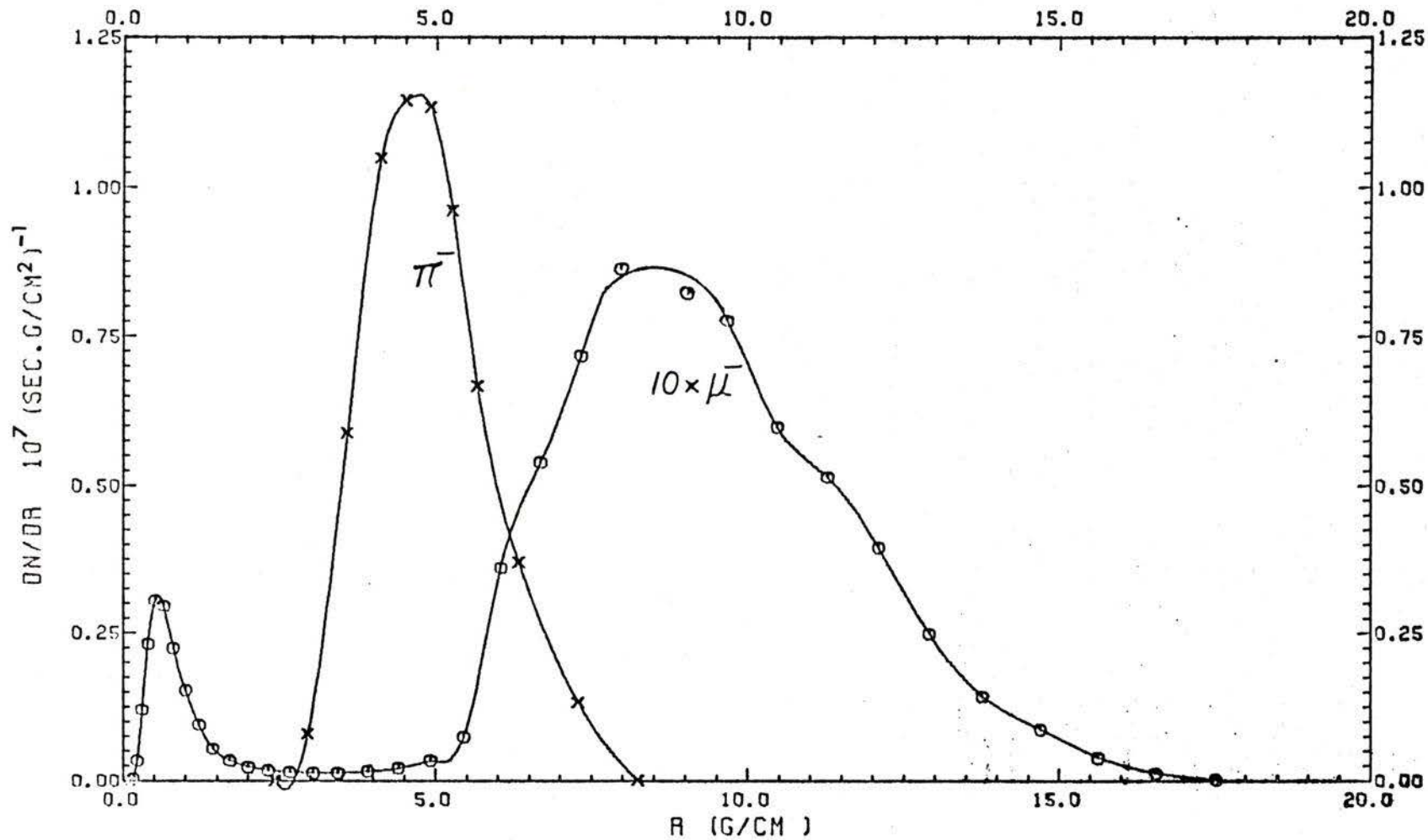


Fig. 4.8 Pion and muon range spectra for the reference system described by Fig. 4.5 and Table 4.2 at $p_0 = 100 \text{ MeV/c}$.

0	0	0	0	0	0	1	0	1	0	0	0	0	0	1	1	0	0	0	0
0	0	1	1	0	0	0	0	0	1	0	1	1	0	0	0	1	2	0	1
0	0	0	0	3	2	2	4	7	4	8	7	6	1	1	0	5	2	0	
1	0	1	0	2	3	2	9	5	8	4	7	8	4	4	4	0	0	3	
0	1	2	1	3	5	8	21	17	16	13	15	15	8	7	2	4	0	3	
1	0	1	1	1	5	13	40	24	25	33	39	30	18	10	10	1	4	0	
2	0	0	3	5	7	19	35	46	42	41	44	44	8	8	5	4	1	0	
0	0	3	3	5	10	19	44	50	53	50	53	53	7	7	6	0	5	2	
0	2	1	3	8	11	19	28	37	24	34	41	23	18	10	9	4	2	6	
0	0	2	1	4	11	10	13	10	17	10	18	17	15	9	7	6	1	0	
0	1	1	1	5	8	7	4	5	3	8	4	3	5	6	7	2	0	0	
1	0	2	1	3	0	2	3	6	2	2	4	2	3	2	3	1	1	0	
0	0	0	0	1	1	1	0	2	2	1	1	1	1	0	0	0	0	1	

Fig. 4.10 Calculated pion distribution in the transverse plane for $\Delta p/p = \pm 10\%$ generated randomly in the range $\pm 10\%$ and for the reference system described by Fig. 4.5 and Table 4.2 at $p_0 = 100$ MeV/c. The grid mesh is 1 cm in the horizontal and 0.25 in the vertical plane.

4.3.2 Optics

First order optics were calculated using the programs TRANSPORT and TRANS. Fig. 4 shows first order horizontal and vertical envelopes and the dispersion trajectory (see Appendix B) obtained from TRANS which has a plotting routine. It is seen that the system is dispersionless. The transverse midplane passes through the centre of Q3.

The first order matrix at the midplane, obtained from TRANSPORT (see Appendix K for the meaning of the elements and their units) is:

$$\begin{pmatrix} -0.699 & 0. & 0. & 0. & 0. & 0.956 \\ -10.833 & -1.431 & 0. & 0. & 0. & 0. \\ 0. & 0. & -4.099 & 0.012 & 0. & 0. \\ 0. & 0. & -35.265 & -0.144 & 0. & 0. \\ -1. & -0.137 & 0. & 0. & 1.0 & -0.075 \\ 0. & 0. & 0. & 0. & 0. & 1.0 \end{pmatrix}$$

which indicates a horizontal focus ($R_{12} = 0$), an approximate vertical focus ($R_{34} = 0.012$) and a dispersion of 0.956 cm per % in x and 0 in x' . The image is inverted with an x -magnification of 0.7. At the channel end, the matrix is:

$$\begin{pmatrix} 0.661 & -0.055 & 0. & 0. & 0. & 0. \\ 11.248 & 0.580 & 0. & 0. & 0. & 0. \\ 0. & 0. & 0.103 & -0.004 & 0. & 0. \\ 0. & 0. & 231.943 & 0.164 & 0. & 0. \\ 0. & 0. & 0. & 0. & 1. & -0.150 \\ 0. & 0. & 0. & 0. & 0. & 1. \end{pmatrix}$$

STOPPED PION/MUON CHANNEL

MOMENTUM = 0.100 (GEV/C)

▲ HORIZONTAL PLANE ENVELOPE (CM)

● VERTICAL PLANE ENVELOPE (CM)

■ DISPERSION TRAJECTORY (CM/X)

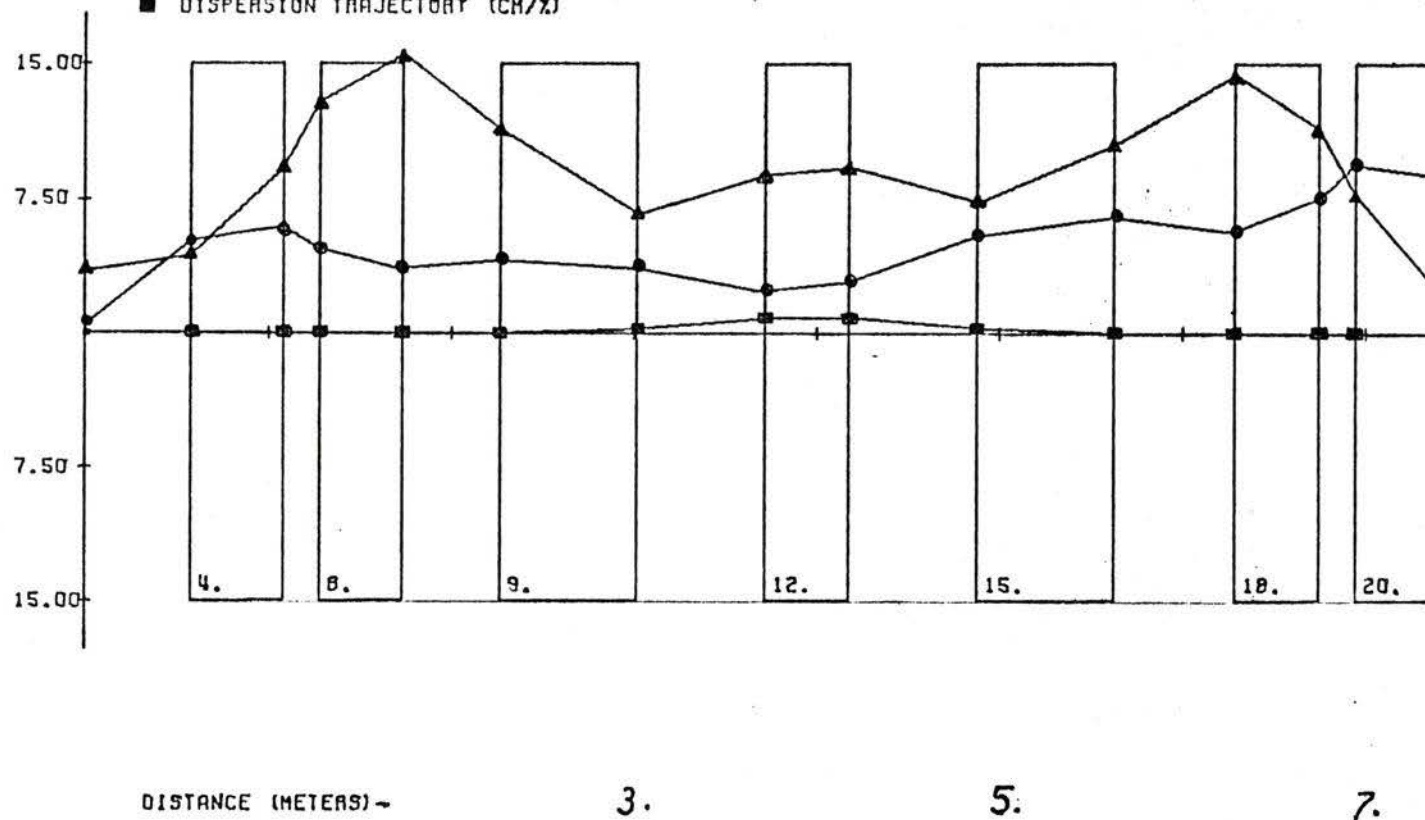


Fig. 4.11 Horizontal and vertical envelopes and the dispersion trajectory for the reference system described by Fig. 4.5 and Table 4.2. at $p_0 = 100$ MeV/c.

This indicates a doubly achromatic beam ($R_{16} = R_{26} = 0$). A focus in both planes at the channel end may be obtained by adjusting Q4 and Q5. The spot size at the focus depends on the distance from Q5 and the beam divergence that can be tolerated. One may trade spot size for lower divergence. A double waist (in both horizontal and vertical planes) or a beam of very small divergence may be obtained. In Table 4.3, a summary of the various conditions and spot sizes is given with corresponding settings for quadrupoles Q4 and Q5 and the drift space d_8 . The spot sizes were calculated using the program NPFLUX, which employs the first and second order transfer matrices provided by TRANSPORT (see Appendix K). The first order spot sizes were obtained by replacing the elements of the second order matrices with zeros.

Second and higher order effects make the pion beam spot size about twice as large as its first order size in both the horizontal and the vertical planes. This is due almost completely to the second order chromatic aberrations* caused by the large accepted momentum bite of $\pm 17.5\% p_0$. This may be seen in Fig. 4.12, which displays the percentage increase in the horizontal spot size of the beam as it travels along the channel. This increase was calculated using a method (Lobb, 1972a) which determines the maximum value of the position coordinate when second order chromatic effects are present in a first order achromatic system. The horizontal spot size of beam at the end of the system is about 65% larger than the first order size. The difference between this result and those of Table 4.3 is partly due to different input assumption. In the method

* Chromatic aberration is a term used to describe the change in trajectories due to the momentum deviation Δp .

Table 4.3

Summary of Beam Characteristics

Pion beam requirement	distance d_8 (m)	Fields (kG)		beam size x(cm) · y(cm)	
		Q4	Q5	1st order	2nd order
Double focus ($R_{12}=R_{34}=0$)	0.5	1.989	-3.244	7 x 3.5	16 x 8
" "	0.75	1.876	-2.667	8 x 5	17 x 10
" "	1.0	1.794	-2.337	9 x 6	18 x 12
Double waist ($\sigma_{21}=\sigma_{43}=0$)	0.5	1.527	-0.828	6 x 20	12 x 26
" "	0.75	1.424	-0.787	8 x 20	14 x 26
x-focus, min y ($R_{12}=0, \sigma_{33}=\text{small}$)	0.5	1.942	-2.873	6 x 1	15 x 4
Parallel beam ($R_{22}=R_{44}=0$)	1.0	1.228	-1.097	16 x 10	24 x 18

1. σ_{ij} are beam matrix elements in the TRANSPORT notation (see Appendix K)
2. See Fig. 4.5 for location of d_8 , Q4 and Q5.
3. 1st and 2nd order sizes are obtained using NPFLUX, based on a 10 cm long and 1 cm high production target. The sizes quoted contain at least 95% of the beam.

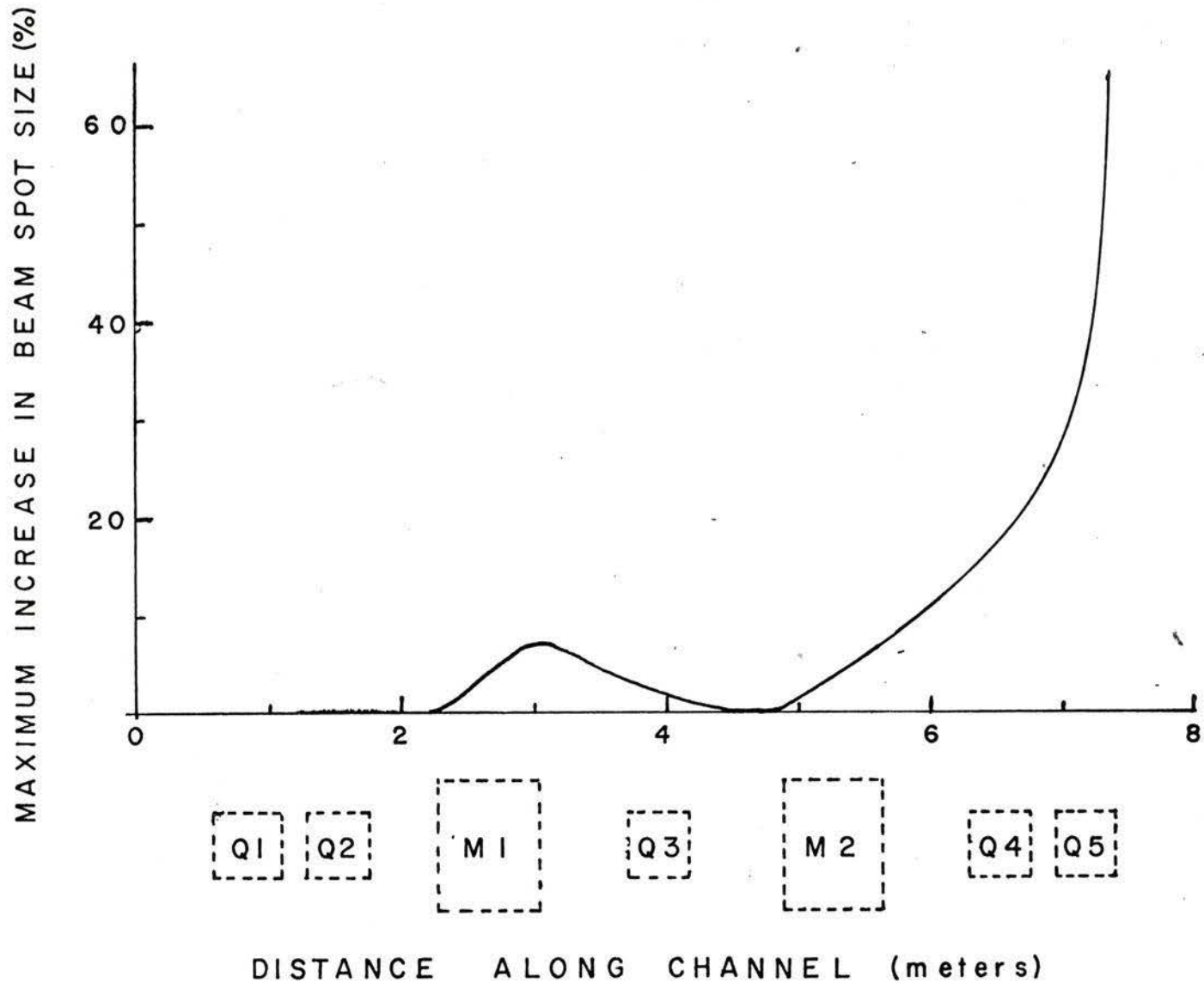


Fig. 4.12 Maximum percentage increase in beam spot size as the beam travels along the channel due to second order chromatic aberrations.

used to calculate the data of Fig. 4.12, an ellipsoidal beam was assumed which may or may not be representative.

Correction for second order effects was attempted using curvature of the edges of the two bending magnets but no significant improvement was found. Slight improvement was obtained using sextupole magnets but it was considered insufficient to warrant inclusion of such magnets.

4.3.3 Tolerances

The tolerances for the various system parameters (Lobb, 1972b) were calculated using the program TRANS (Chan, Hunt and Lobb, 1972). For magnet current tolerances and for tolerances on quadrupole rotation a required tolerance on the beam spot of $\pm 10\%$ is assumed. For the tolerance on the bending magnet rotation (twist) the fractional change of the beam spot size caused by a 10 mrad input twist is calculated. The effects of a harmonic content of 1% and 2% of the basic quadrupole field at 80% of aperture on the beam size is calculated by this program. These tolerances are rather small for the requirements of a stopped meson channel.

For the bending magnets, the calculated current tolerance is 0.46% for a 10% increase in spot size which, in practice, is easily obtainable with commercially available power supplies. The current tolerance is the same for both bending magnets. Results of a 10 mrad twist of each of the two bending magnets indicates a maximum increase of 0.6% in the spot size for the second magnet in the y-plane. It is

half of this value for the first magnet. In the x-plane, it is about 0.02% for both magnets. Thus, if alignment to within 20 to 30 mrad (1° to 1.5°) is achieved, the beam spot size increases by only 1 or 2%.

For the quadrupoles, the current tolerance is 0.7% for a 10% increase in beam spot size. This is readily obtainable with commercial power supplies. The same increase in the beam spot size is produced by a rotation of 40 mrad in the x-plane or 9 mrad in the y-plane. This y-plane tolerance is small. Although in practice the quads can be aligned to within about 10 mrad, very careful alignment is not necessary because, as mentioned earlier in this section, an increase in beam spot size of more than 10% can be tolerated and also because it is possible to correct for the effects of these rotations by empirical adjustments of the system settings.

A 1% higher harmonic error field produces a maximum possible increase in the beam spot size of 1.5 cm in the x-plane for quadrupole Q2. However, in most other cases, the increase is less than 1 cm. The quadrupoles which are most critical are Q2, Q4 and Q5, in that order. The effects are negligible in the y-plane. A harmonic content of 2% produces a maximum increase of 3 cm in the beam size for the x-plane and negligibly small increase for the y-plane. Thus, although 2% harmonic content is tolerable, 1% is preferable.

The errors introduced by displacing a quadrupole 0.5 cm along the beam axis leads to an increase of 2 cm in beam size for the x-plane and 0.3 cm for the y-plane when the errors for all the quadrupoles are combined together. Therefore, the quadrupoles should be positioned to

within 0.5 cm or less. Bending magnets should be positioned much more precisely along the beam axis — to within 1 or 2 mm.

4.3.4 Calculated Yields and Variation with Energy

Pion and muon yields were calculated using the program MBEND. The initial differential pion flux $\frac{dn}{dp}$ entering the channel was calculated from the relation:

$$\frac{dn}{dp} = I_p \cdot N_t \cdot \frac{d^2 \sigma}{d\Omega dE} \cdot \frac{dE}{dp} \cdot \Delta\Omega \quad (4.3.1)$$

where I_p = primary proton current — protons per second,

N_t = number of target nuclei per cm^2 ,

$\Delta\Omega$ = solid angle subtended at the source by the first quadrupole in steradians, and

$\frac{d^2 \sigma}{d\Omega dE}$ = pion production cross section in $\text{cm}^2 (\text{MeV} \cdot \text{sr})^{-1}$.

The cross section was assumed constant over the range of energy considered. The yields are quoted for a 100 μA beam of 500 MeV protons, a 10 cm long Be production target, and the geometry of Fig. 4.5, assuming a pion production cross section of 5.5 $\mu\text{b} (\text{MeV} \cdot \text{sr})^{-1}$.

The calculated yields as a function of energy are summarized in Table 4.4. Fig. 4.13 shows the yields as a function of central momentum. It is to be noted that both pion and muon fluxes increase with momentum, particularly the backward decay muons. The increase of muons with energy, although the fraction of pions decaying in the channel decreases with increasing energy, is due to the increase in muon capture efficiency because of the smaller decay angles at higher energy.

Table 4.4

Variation of Pion and Muon Yields with Energy

p_0 (MeV/c)	60	80	100	120	140	160	180
K.E. (MeV)	12.4	21.3	32.1	44.1	58.6	72.8	88
Total flux (sec) ⁻¹							
$10^8 \times \pi^-$	0.42	1.35	2.81	4.87	7.38	10.1	13.3
$10^7 \times$ total μ^-	0.60	2.50	4.42	7.28	11.6	16.5	21.8
$10^6 \times$ backward μ^-	0.07	0.40	1.46	3.66	7.38	15.6	23.7
π/μ ratio	7.0	5.4	6.4	6.7	5.7	6.1	6.1
Max. diff. flux (sec . MeV/c) ⁻¹							
$10^7 \times \pi^-$	0.38	0.93	1.48	2.13	2.80	3.54	3.93
$10^6 \times$ forward μ^-	0.68	1.28	1.74	2.52	3.54	4.45	4.78
$10^5 \times$ backward μ^-	0.08	0.35	0.94	1.92	3.57	5.52	7.49
π/μ (forward)	5.5	7.3	8.5	8.4	7.9	8.0	8.2
Max. stopping rate (sec . g/cm) ⁻¹							
$10^7 \times \pi^-$	7.16	10.2	9.77	10.8	11.2	12.2	11.6
$10^6 \times$ forward μ^-	6.63	6.46	6.88	8.62	10.3	11.5	11.5
$10^6 \times$ backward μ^-	2.42	2.36	1.85	2.16	2.71	3.12	3.19

Fluxes calculated for 100 μ A protons on a 10 cm Be target and on an area of 25 cm x 25 cm. "Backward μ^- " integrated over the backward muons peak.

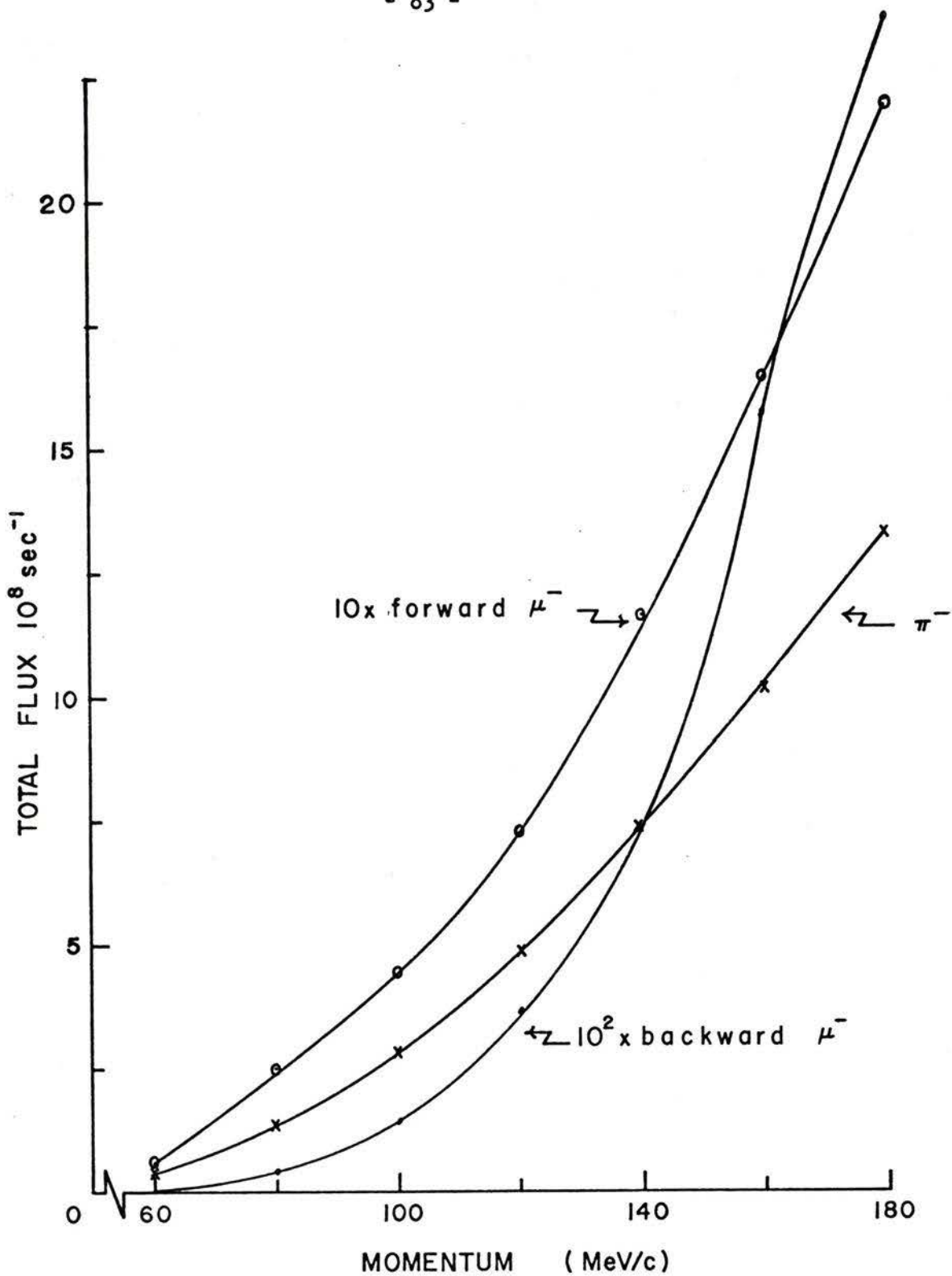


Fig. 4.13 Total flux as a function of channel central momentum for pions, forward muons, and backward muons and for the reference system described by Fig. 4.5 and Table 4.2. Fluxes calculated for 100 μA protons on a 10 cm Be target and an area of 25 cm x 25 cm with the channel set to 100 MeV/c .

However, the rate of increase starts to diminish after 160 MeV/c, as seen by the change in direction of the curve for the backward decay muons. Fig. 4.14 indicates similar tendencies for the variation of the maximum differential flux with momentum. The curves tend to flatten out after 160 MeV/c.

The change in the maximum stopping rate with momentum in Fig. 4.15 is seen to have less momentum dependence. This is because another factor is involved; namely, the dp/dR values used to calculate the stopping density from the relation:

$$\frac{dn}{dR} = \frac{dn}{dp} \cdot \frac{dp}{dR} \quad (4.3.2)$$

where R is the range. dp/dR is a non-linear function of momentum and has large values at low momenta decreasing as the momentum increases. A table of R and dp/dR (in MeV/(g/cm²)) is given in Appendix C. The stopping rates for pions shows two maxima, a low energy one at 80 MeV/c and a high energy one at 160 MeV/c. However, for pions, operation at low energy is preferred in order to avoid the need for thick degraders. The stopping rates for forward muons reach a maximum at about 160 MeV/c, then flatten out. The maximum for backward muons is at 180 MeV/c. However, it is almost flat between 160 and 180 MeV/c.

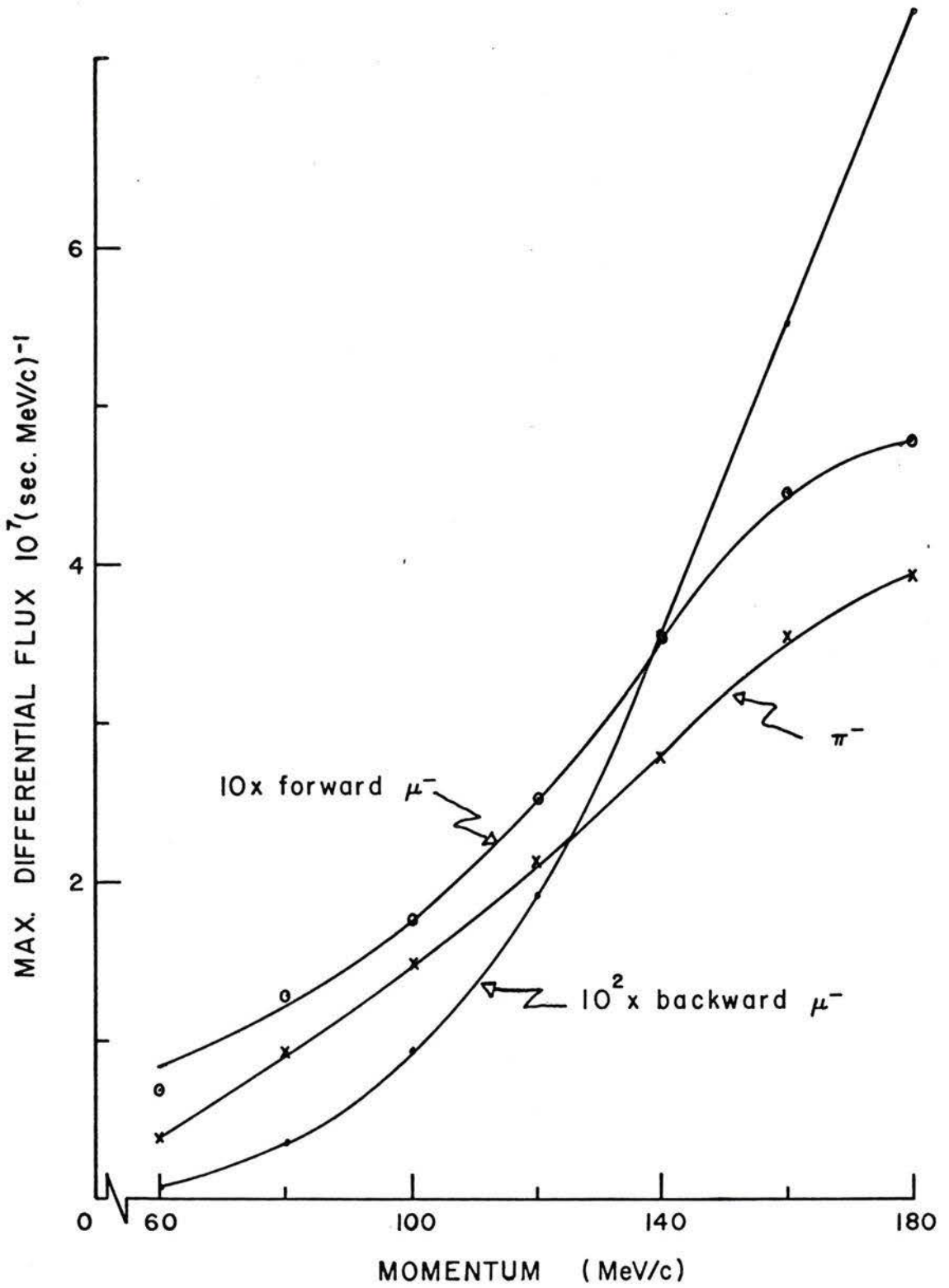


Fig. 4.14 Maximum differential flux as a function of channel central momentum for the same setup as Fig. 4.13.

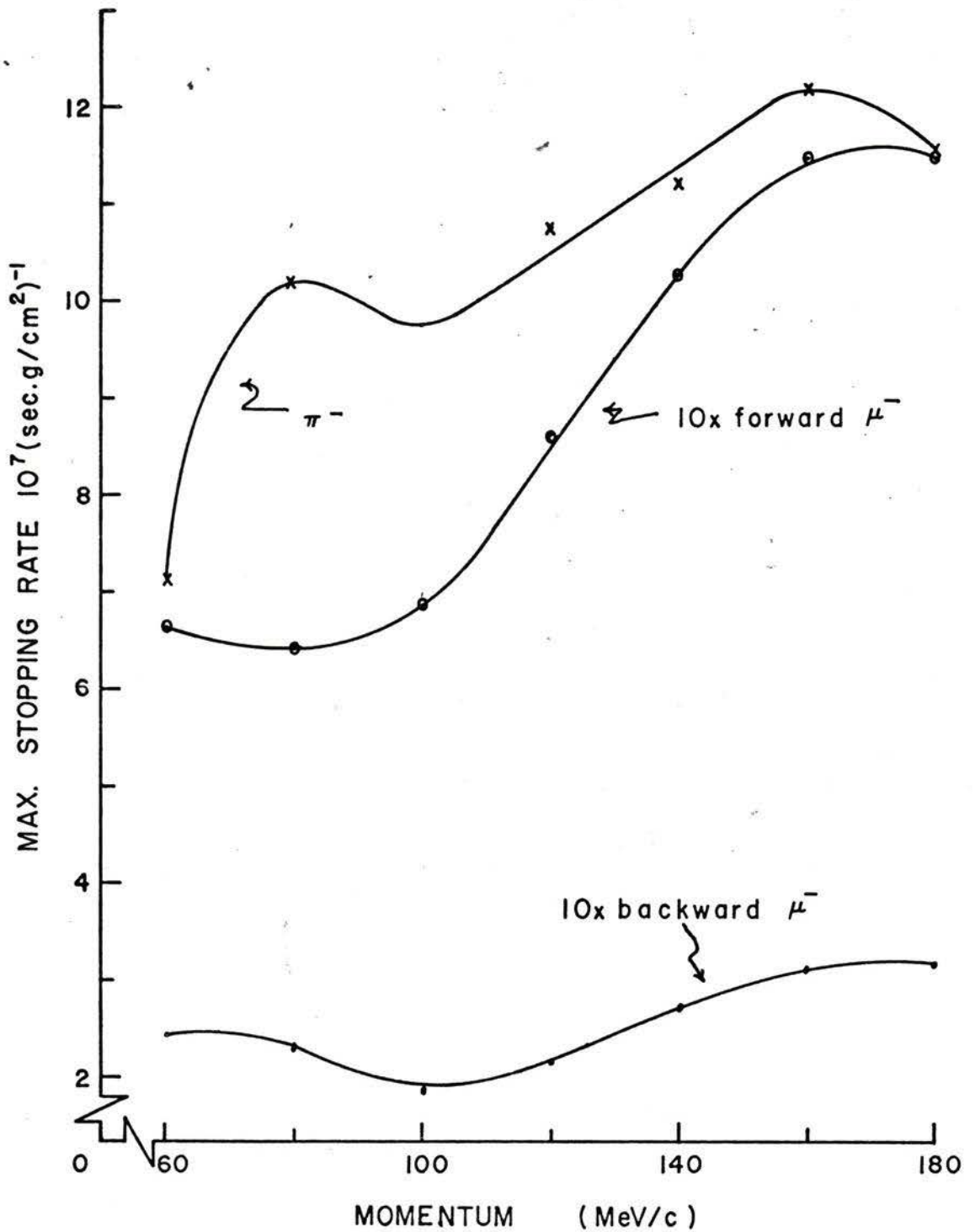


Fig. 4.15 Maximum stopping density as a function of channel central momentum for the same setup as Fig. 4.13.

It should be noted that, although the stopping rates for forward muons, as indicated in Fig. 4.15 or Table 4.4, is between 3 and 4 times the rates for backward muons; only a fraction of these can be extracted since the pion and forward muon peaks coincide. This point will be discussed further in Section 4.4.

4.3.5 Beam Spill

To calculate the beam spill at various locations, a beam containing particles originating at the pion production target is defined by a cone formed by the target and the first aperture of the channel. Each particle is generated at the target with random position, slope, and momentum deviation (within ± 10 MeV/c). Its displacement from the axis is then calculated at the end of each element of the system and compared with the specified aperture radius of the element. If it is smaller than the aperture, the particle is passed to the next element, otherwise it is considered lost and is added to the spill at the location of that element. The apertures are assumed circular except for the bending magnets where rectangular apertures are assumed.

The calculations were carried out using the program NPFLUX. The results for a sample of 2×10^4 particles are summarized in Table 4.5, which indicates that most of the spill occurs within the first section before the first bending magnet. To obtain actual fluxes of spilled particles at the various locations, the initial total pion flux generated at the target is multiplied by a maximum solid angle

Table 4.5

Beam Spill

<u>Spill location</u> *	<u>Apertures (cm)</u>		<u>Spill (%)</u>
	<u>Quad or drift</u> <u>radius</u>	<u>Magnet</u> <u>x</u> <u>y</u>	
end of d ₁	15		58.6
" " Q1	10		28.5
" " Q2	15		0.9
" " d ₃	15		0
" " M1	—	20 12.5	0
centre of Q3	15		0
end of d ₅	15		0.2
" " M2	—	20 12.5	0.8
" " d ₆	15		1.4
" " d ₇	15		0.7
" " Q5	15		0
" " d ₈	15		0

* See Fig. 4.5 for element designation.

calculated by NPFLUX. This angle is 0.386 sr for the system described by Fig. 4.5 and Table 4.2. The product is used in conjunction with the percentages listed in Table 4.5.

4.3.6 Contamination

In this section, contamination of the meson beams by protons, electrons and neutral particles is discussed. The pion content of the muon beam and muon content of the pion beam is discussed in Section 4.4 for the various modes of operation. The neutral particles flux for a channel with bends is low because they are not affected by electromagnetic bending devices. In the following paragraphs, an estimate of the flux of some of these contaminants is made.

(a) Neutrons

Neutrons originate from the primary production target and from protons and pions stopped along the channel, in the degraders, and in the secondary experimental targets. Data on neutrons generated in a Be target by a 500 MeV proton beam are not available. However, available experimental and calculated data are summarized in the Yale report Y12 (Yale Staff, 1964). Using these data, an estimate of the low energy neutron flux generated at the target indicates 5×10^{13} neutrons per second. Higher energy cascade neutrons are greatly reduced by the choice of a backward production angle. The attenuation coefficient for the channel is calculated from the following relations (Yale Staff, 1964):

$$g(x) = \frac{1}{4} \left(\frac{a}{x}\right)^2 (1 + k \cdot \frac{a}{x}) \quad \text{for a straight section,} \quad (4.3.3)$$

and $\quad = c/\sin \theta$ for a bend

where a is a semi-aperture

x is the distance along the channel,

$C = 0.1$, assuming a void facing the bend,

and k is a number depending on the albedo of the shielding for neutrons. If $k = 0$, then one has the straight geometry term $\frac{1}{4} \left(\frac{a}{x}\right)^2$. Using the above relations, the calculated attenuation factor of the channel is $\sim 1 \times 10^{-10}$. Thus, the neutron flux at the channel exit is $\sim 5 \times 10^4$. With a pion flux of 3×10^8 /sec available at the channel exit, the neutron-to-pion ratio is 1.4×10^{-4} . Since the muons are roughly one tenth the intensity of the pions, the neutron-to-muon ratio is ten times that for pions.

It is difficult to estimate the neutron flux generated by pions and protons stopping along the channel. However, some order of magnitude estimates are possible. As shown in Table 4.5, about 93% of the pions admitted into the channel are lost within the first section before the magnet M1. The contribution of these pions to the neutron flux is negligible, as they are close to the target and are attenuated by the same factor as those generated in the target. The remaining 7% include pions within the momentum range accepted by the channel, which amounts to 5%, and those outside this momentum range, which make the remaining 2% lost in the rest of the channel, mostly at the second bend and the drift following it. These 2% amount to

1×10^8 pions/sec for $p_0 = 100$ MeV/c. It is assumed that each positive (negative) pion stopping in the walls produces 0.2 (2) neutrons (Hughes *et al.*, 1971). Thus 2×10^7 (1×10^8) secondary neutrons are generated. The combined attenuation factor for the second bending magnet and the section following it is 2×10^{-4} . The secondary neutron flux due to pions lost in the channel is, therefore, 4×10^3 (2×10^4) neutrons/sec, which shows that this is a more important source of neutrons than the production target.

For negative meson beams, the secondary protons generated in the target are eliminated by the first bend and their contribution to neutron production is negligible. Therefore, the total neutron flux from the target and the channel walls would be $\sim 7 \times 10^4$ giving a neutron-to-pion ratio of 2×10^{-4} .

For positive meson beams, the secondary protons which pass the first bend and are lost near the second bend would be an important source of neutrons. However, these protons are peaked in the forward direction and, at the production angle of 135° chosen for this design, the protons production cross section for Be is a little less than half that of pions (Nagle *et al.*, 1969). Thus, the proton flux accepted into the channel may be assumed to be half the pion flux, or $\sim 5 \times 10^8$ protons/sec. Only about 2% of this flux is lost in the second half of the channel. Assuming each proton produces two neutrons, the neutron flux is $\sim 2 \times 10^7$ /sec. With an attenuation factor of 2×10^{-4} for the second bend and the last two quadrupoles, the neutron flux reaching the channel exit is 4×10^3 /sec. Therefore, the combined

flux from all sources is about 8.5×10^3 , giving a neutron-to-pion ratio $\sim 3 \times 10^{-5}$. When the channel is tuned for backward muons, however, the neutron-to-muon ratio is $\sim 6 \times 10^{-3}$ or 0.6%.

(b) Gamma Rays

Gamma rays, other than those produced in the experimental target, decay in or close to the production target. Neutron capture by nuclei of material in the beam line also produces gamma rays. Because the π^0 flux is much less than the neutron flux produced at the target, the number of gamma rays is about 10% of that of the neutrons (Hughes *et al.*, 1971). Since they are attenuated approximately by the same factor in the channel, their output flux is about 10% that of the neutrons. At the experimental target, however, gamma rays are produced from pions or protons stopping in the degrader.

(c) Protons

About 2×10^7 protons/sec with the same momentum as the pions are accepted by the channel. These are low energy protons (less than 5 MeV for 100 MeV/c) having a range of $\sim 0.1 \text{ g/cm}^2 \text{ C}$. Thus, they can easily be absorbed in thin foils and vacuum windows. The proton-to-pion ratio is, therefore, zero but proton scattering into the channel from surrounding material may give rise to a negligibly small value.

(d) Electrons

The principal source of electrons, other than the degraders and experimental target, is usually attributed to pair production from the gamma rays produced from π^0 decay in the production target. The choice of 135° for the angle of pion extraction reduced the electron-to-pion ratio as indicated in Fig. 2.3 of Section 2.1. Data for the 500 MeV TRIUMF beam are not available. However, using the Los Alamos data for Be (Nagle *et al.*, 1969) the e^+/π^+ ratio is .037 for 90 MeV pions, which should be lower for a proton energy of 500 MeV and 40 or 50 MeV pions. Assuming a ratio of 0.03, the electron flux accepted by the channel is $\sim 4 \times 10^7$, which also assumes that the channel acceptance for pions and electrons is identical. This gives a positron-to-pion ratio of about 12%. The ratio for negative pions is about three times higher since the cross section for negative pions is about three times smaller than that for positive pions and the e^- and e^+ yields are approximately equal.

4.3.7 Muon Polarization

The polarization of the muons (see Section 2.4) as a function of momentum is (Jensen and Øverås, 1958)

$$\cos \phi = \frac{(1 - \beta_\mu^*) E_\pi - E_\mu}{\beta_\mu^* P_\mu}, \quad (4.3.4)$$

where E_{π} , E_{μ} and p_{μ} are the pion and muon energies and muon momentum in the laboratory system, and β_{μ}^* is the muon velocity, relative to the velocity of light, in the rest system of the pions. The polarization was calculated, using MBEND, for the spectrum shown in Fig. 4.7 and is displayed as a function of momentum in Fig. 4.16. It is seen that if 90% polarization or better is required, forward muons having higher momenta than 90 MeV/c or backward muons having lower momenta than 40 MeV/c should be collected for the case where the channel central momentum is 100 MeV/c. The muon flux of a given polarization is in Fig. 4.17 against polarization. It indicates that muons in the forward peak are 90% polarized and those in the backward peak are 85% polarized.

4.4 Modes of Operation

4.4.1 Operation as a Stopped Pion Channel

For this case, the setting of quadrupole Q2, indicated in Table 4.2, is changed to 2.0 kGauss in order to obtain a focus at the position of the slits 10 cm upstream of Q3, the centre quadrupole. If the momentum bite is to be limited, the vertical slits are closed to the required size. In Table 4.6 are summarized the various settings of the slits with the corresponding fluxes, beam sizes, momentum bites Δp and solid angles $\Delta\Omega$ transmitted by the slits. With the slits fully open, a pion beam with an x-focus and minimum y-size is formed 0.5 m downstream from Q5 by adjusting the latter and Q4. The pion flux, momentum spread Δp and pion-to-muon ratio were calculated with MBEND. The spot sizes

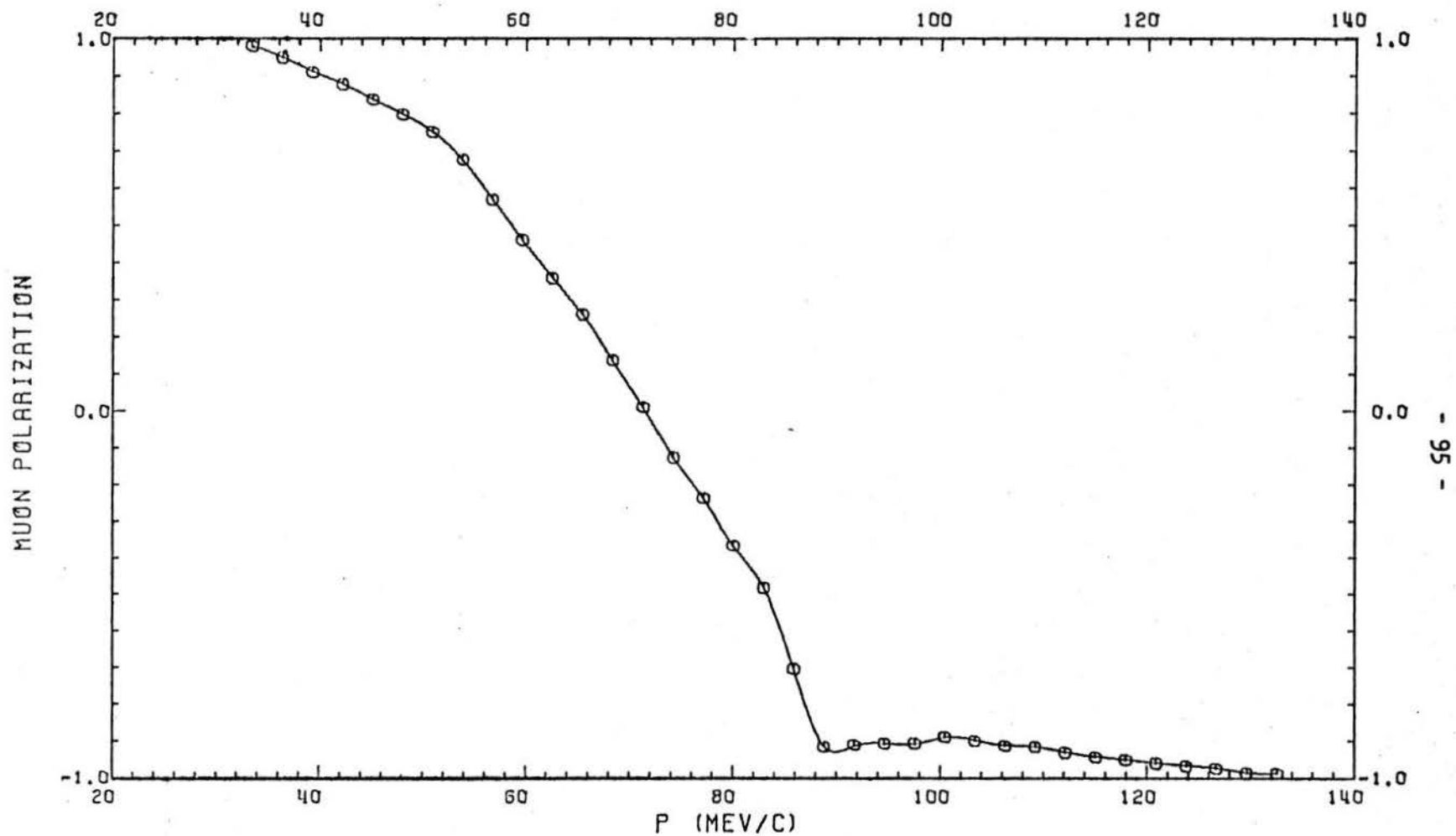


Fig. 4.16 Muon polarization as a function of momentum for the reference system described by Fig. 4.5 and Table 4.2 at $p_0 = 100$ MeV/c.

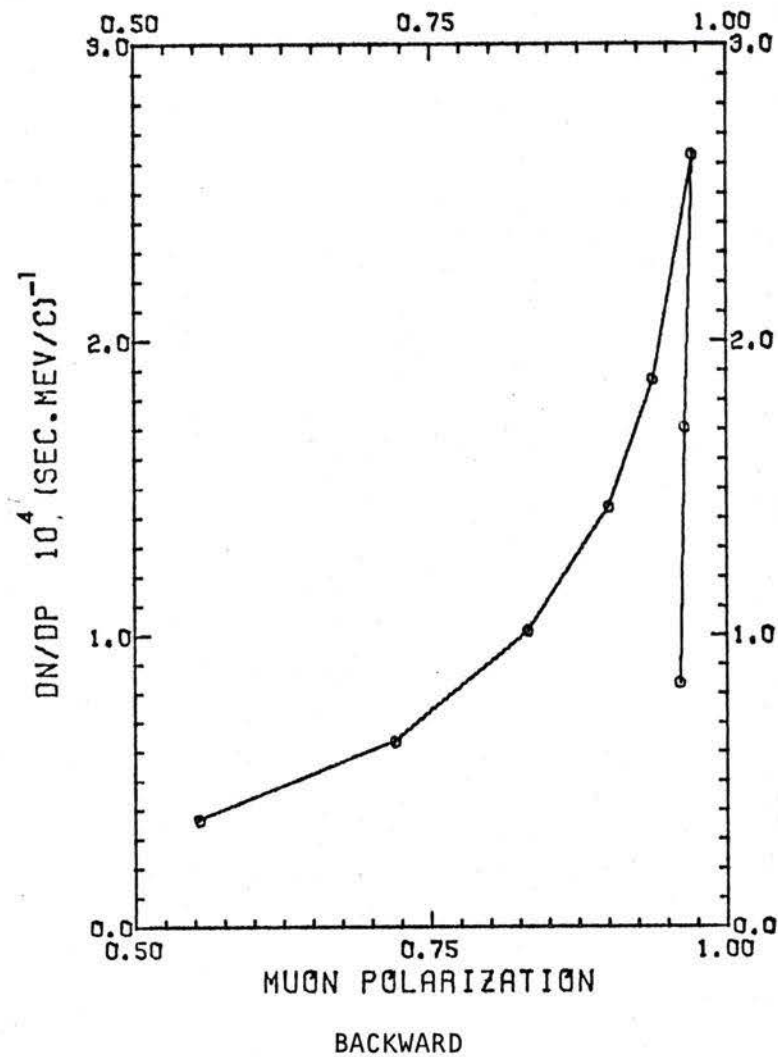
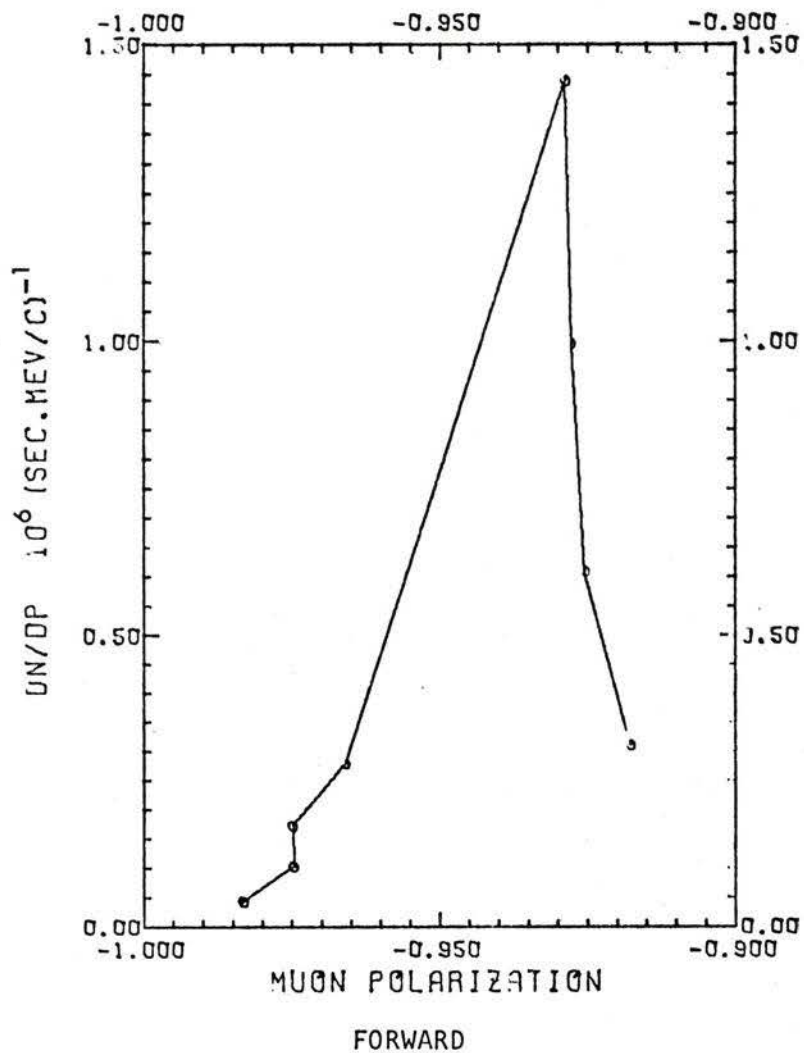


Fig. 4.17 Muon flux of a given polarization versus polarization for the reference system described by Fig. 4.5 and Table 4.2 at $p_0 = 100 \text{ MeV/c}$.

Table 4.6

Negative Pion Flux, Momentum Acceptance, and Beam Spot Size for Various Settings of the Slits

Slit Openings (cm)	Δp %	$\Delta\Omega$ msr	Spot Size x(cm) · y(cm)	Max Stopping Rates $10^8(\text{sec} \cdot \text{g}/\text{cm}^2)^{-1}$	Flux		Ratio π/μ
					Total $10^8/\text{sec}$	%	
Fully open	± 17.5	28.3	16 x 4.0	1.15	3.1	100	6.0
± 7.5	± 12.5	28.0	14 x 3.5	1.15	2.4	77.2	6.3
± 5.0	± 8.5	27.7	13 x 2.5	1.14	1.7	55.1	6.4
± 2.5	± 5.5	25.8	12 x 2.0	1.13	0.94	31.0	6.7
± 1.0	± 4.0	11.0	10 x 2.0	0.49	0.36	11.4	7.1
	\pm						

Channel central momentum p_0 is 100 MeV/c.

The spot sizes quoted contain at least 95% of the pion beam.

Yields are quoted for 100 μA , 500 MeV protons on a 10 cm Be target.

which contain 95% of the beam and the solid angles of acceptance were calculated to second order with NPFLUX. Table 4.6 indicates that, as expected, the pion flux decreases with narrower slit openings. But the pion-to-muon ratio increases and about 14% muon contamination is left when the slits are set to ± 1 cm. At this setting, the total pion flux is $3.6 \times 10^7/\text{sec}$, which is still more than adequate for a large number of experiments, and the momentum bite is ± 4 MeV/c.

The calculated momentum and range spectra are very similar to those shown in Fig. 4.7 and Fig. 4.8 when the slits are fully open. However, when the slits are set to ± 1.0 cm, corresponding to a $\Delta p/p$ of $\pm 4\%$, the calculated momentum spectrum is shown in Fig. 4.18 and the range spectrum in Fig. 4.19. The pion beam distribution in the transverse plane is shown in Fig. 4.20.

4.4.2 Operation as a Stopped Muon Channel

The use of the first part of the channel by itself, the pion collection system, as a muon channel is investigated. Several methods are studied.

(a) Collecting Backward Decay Muons by Detuning the Second Half of the Channel

In this method, the second bending magnet M2 and the quadrupoles Q4 and Q5 were tuned to collect low energy muons from backward decaying pions originating in the section between M1 and M2. The momentum spectrum at the entrance to M2, shown in Fig. 4.21, indicates that

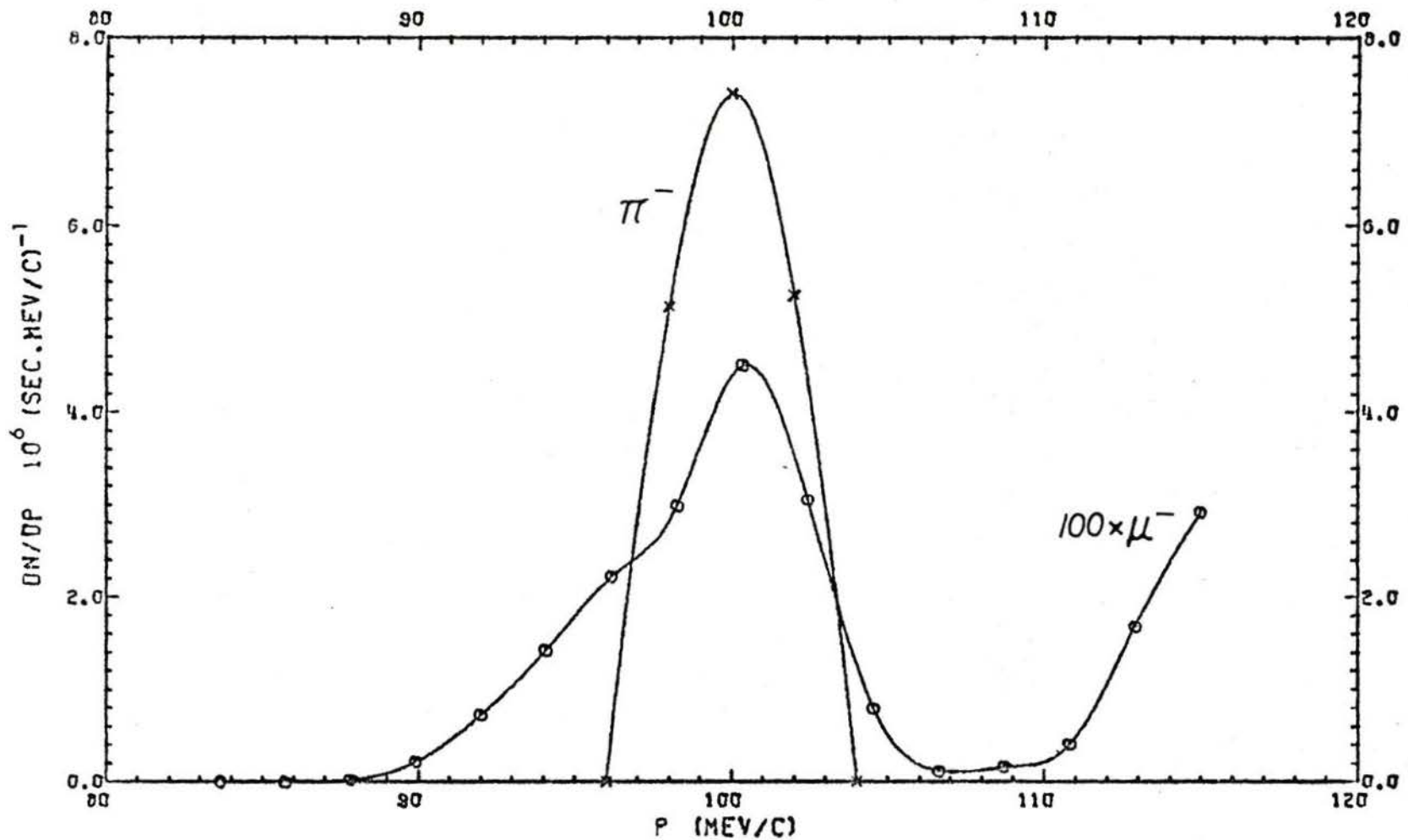


Fig. 4.18 Pion and muon momentum spectra for the channel in the pion mode when the slits are set to ± 1.0 cm and the channel operated at $p_0 = 100 \text{ MeV}/c$.

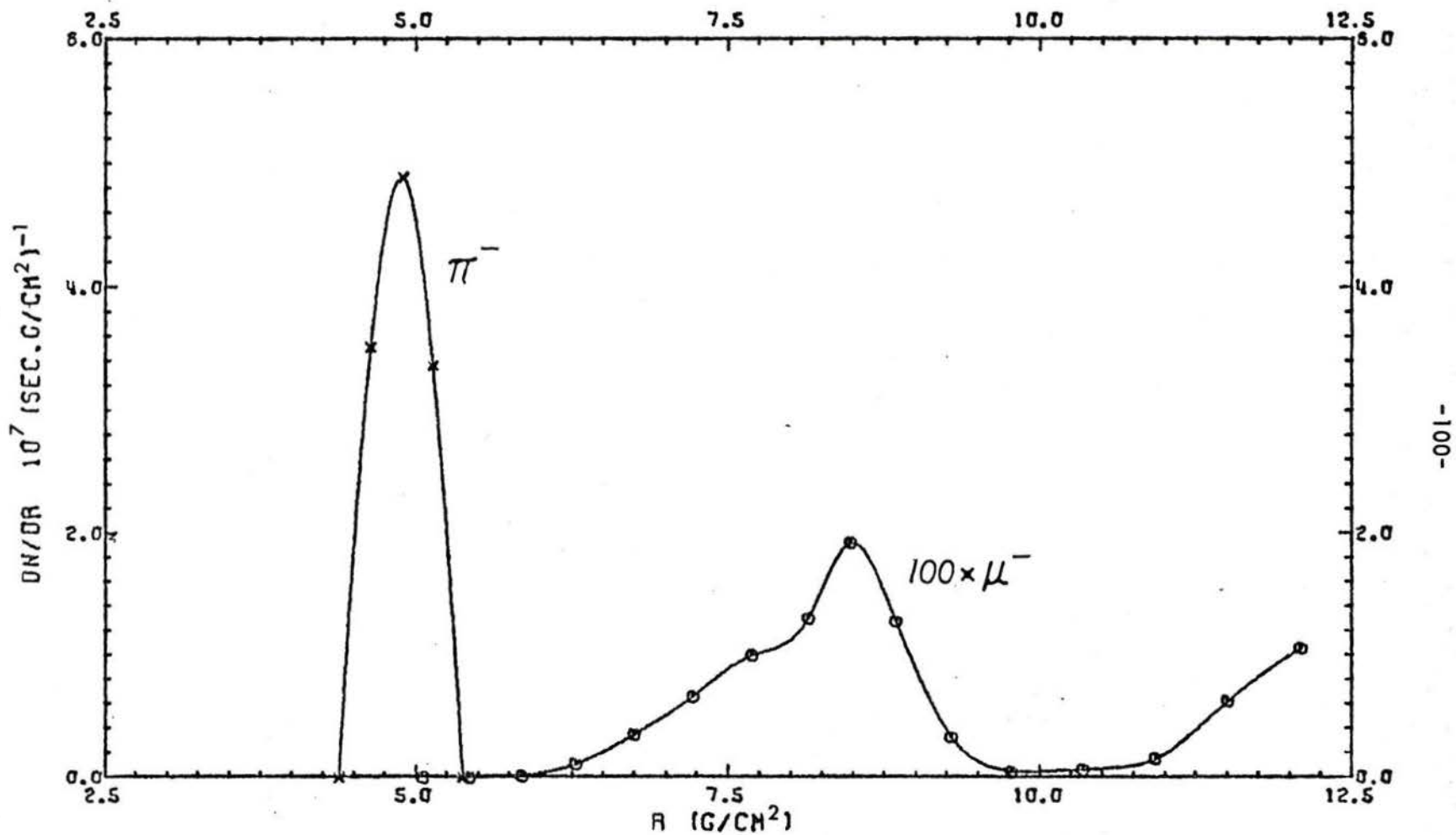


Fig. 4.19 Pion and muon range spectra for the channel in the pion mode when the slits are set to ± 1.0 cm and the channel operated at $p_0 = 100$ MeV/c.

0	0	0	0	0	0	0	0	0	1	1	0	0
1	1	1	0	0	1	0	0	0	0	2	0	0
3	1	3	3	7	10	4	9	7	13	6	2	0
0	4	7	10	18	21	17	21	20	10	10	2	2
1	9	3	13	21	18	17	19	20	14	9	4	1
2	3	3	12	12	18	23	17	21	15	11	4	3
0	6	4	9	13	10	5	9	19	17	9	4	1
2	3	3	2	4	1	0	9	9	8	7	2	2
0	0	0	0	0	0	0	0	2	4	1	0	1
0	0	0	0	0	0	0	0	0	2	1	2	0

Fig. 4.20 Calculated pion distribution in the transverse plane for $\Delta p/p = 0\%$. Channel operating in the pion mode with the slits set to ± 1 cm. The grid mesh is 1.0 cm in the horizontal and 0.2 cm in the vertical plane.

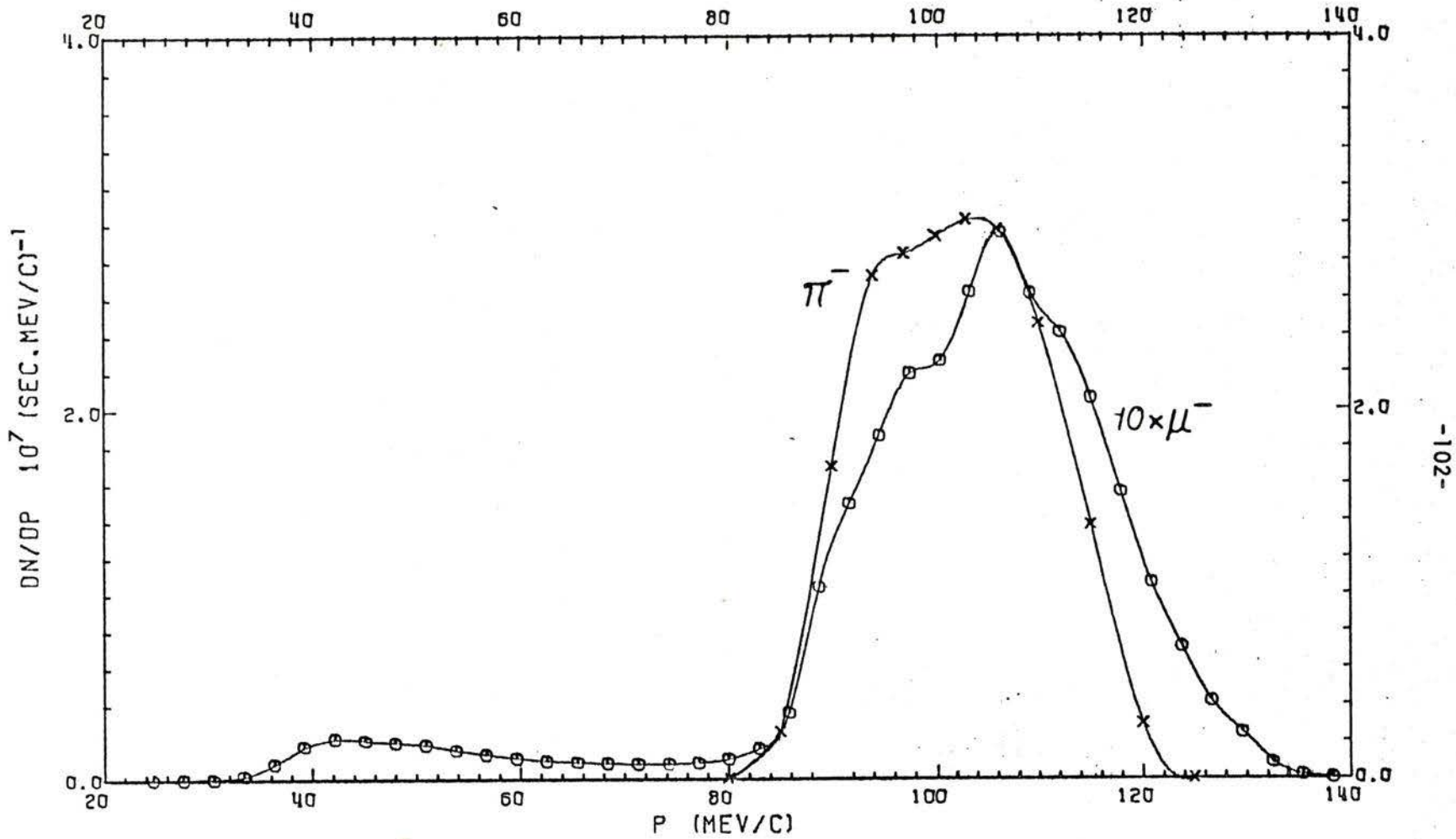


Fig. 4.21 Pion and muon spectra at the entrance to the second bending magnet M2 for $p_0 = 100$ MeV/c. Fluxes are integrated over an area of 25 cm x 25 cm.

the backward muon peak is centred at 42 MeV/c when the main channel is operated at a central momentum of 100 MeV/c. Maximum yield of low momentum muons was obtained when M2, Q4 and Q5 were set for a central momentum of 40 MeV/c while the first part of the channel was unchanged at 100 MeV/c. The muon output momentum and range spectra for this case are shown in Fig. 4.22 and Fig. 4.23 respectively. The maximum stopping density in a 10 cm x 10 cm target, as seen in Fig. 4.23, is $1 \times 10^6 \mu^- (\text{sec} \cdot \text{g/cm}^2)^{-1}$. However, the actual available yield is $4 \times 10^5 \mu^-/\text{sec}$; these may be stopped in a 0.6 g/cm² C target after a 0.2 g/cm² C degrader that does not stop any muons because of the low energy cutoff at 30 MeV/c. Muon polarization as a function of momentum is shown in Fig. 4.24, indicating that the maximum polarization is 90% for muons with momenta around 45 MeV/c which is the muon peak momentum. For a target 25 cm x 25 cm in area, the maximum stopping density is $2.7 \times 10^6 (\text{sec} \cdot \text{g/cm}^2)^{-1}$ and the total flux is 2.0×10^6 .

Higher yields may be obtained if the channel is operated at a higher momentum. This would be appropriate when thicker targets are used. A similar calculation to the above was carried out with the channel central momentum set at 160 MeV/c. The spectrum at the entrance to M2, shown in Fig. 4.25, indicates a backward muon peak at 90 MeV/c. M2, Q4 and Q5 were then tuned to this momentum and the output pion-free spectra are shown in Fig. 4.26 and Fig. 4.27 for the momentum and range spectrum respectively. For this case, the total negative muon flux in a 10 cm x 10 cm area is $2.5 \times 10^6/\text{sec}$. Thus, for a

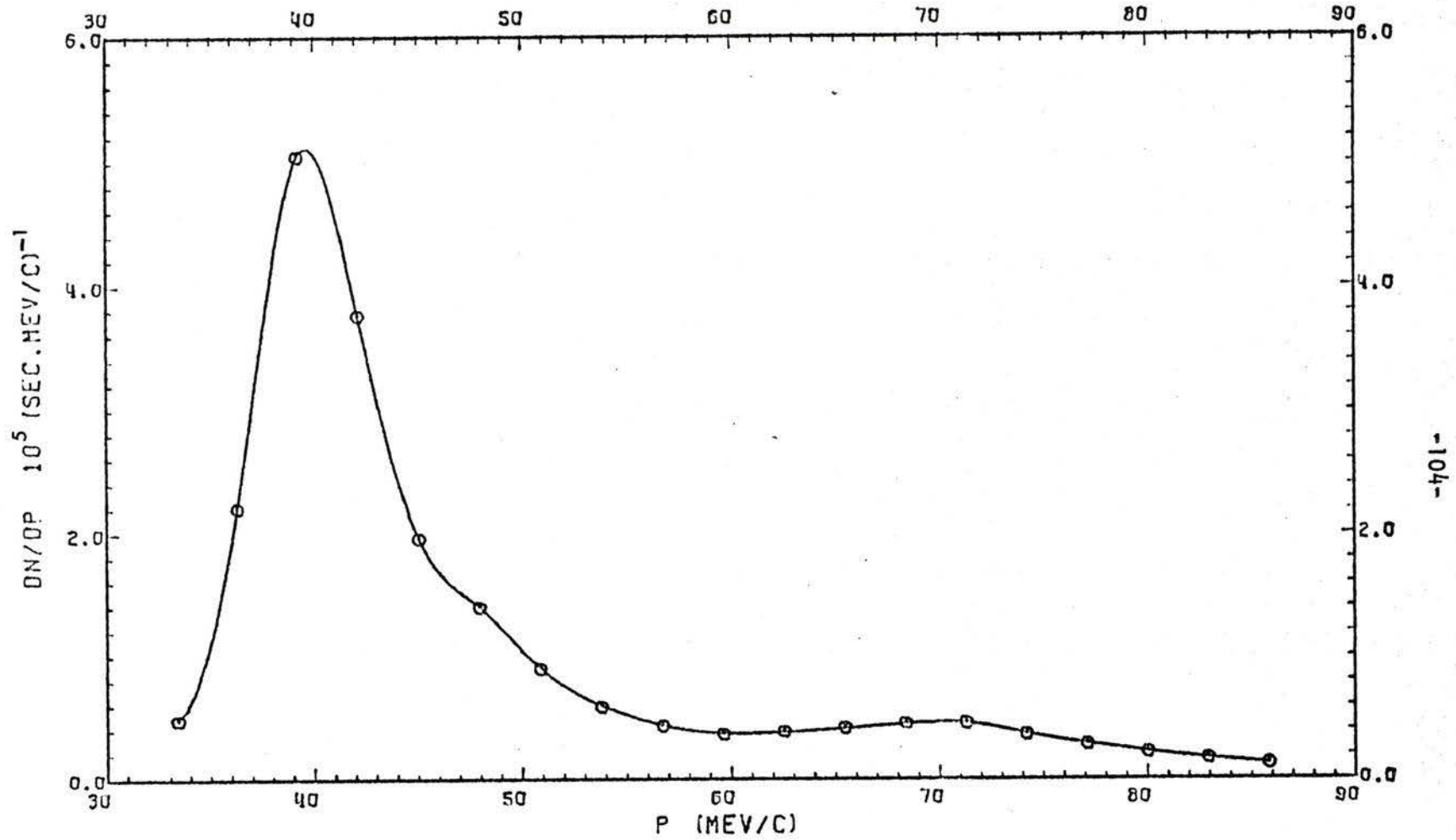


Fig. 4.22 Muon momentum spectrum obtained with the second half of the channel tuned to 40 MeV/c and the first half unchanged at $p_0 = 100$ MeV/c. Flux integrated over an area of 10 cm x 10 cm.

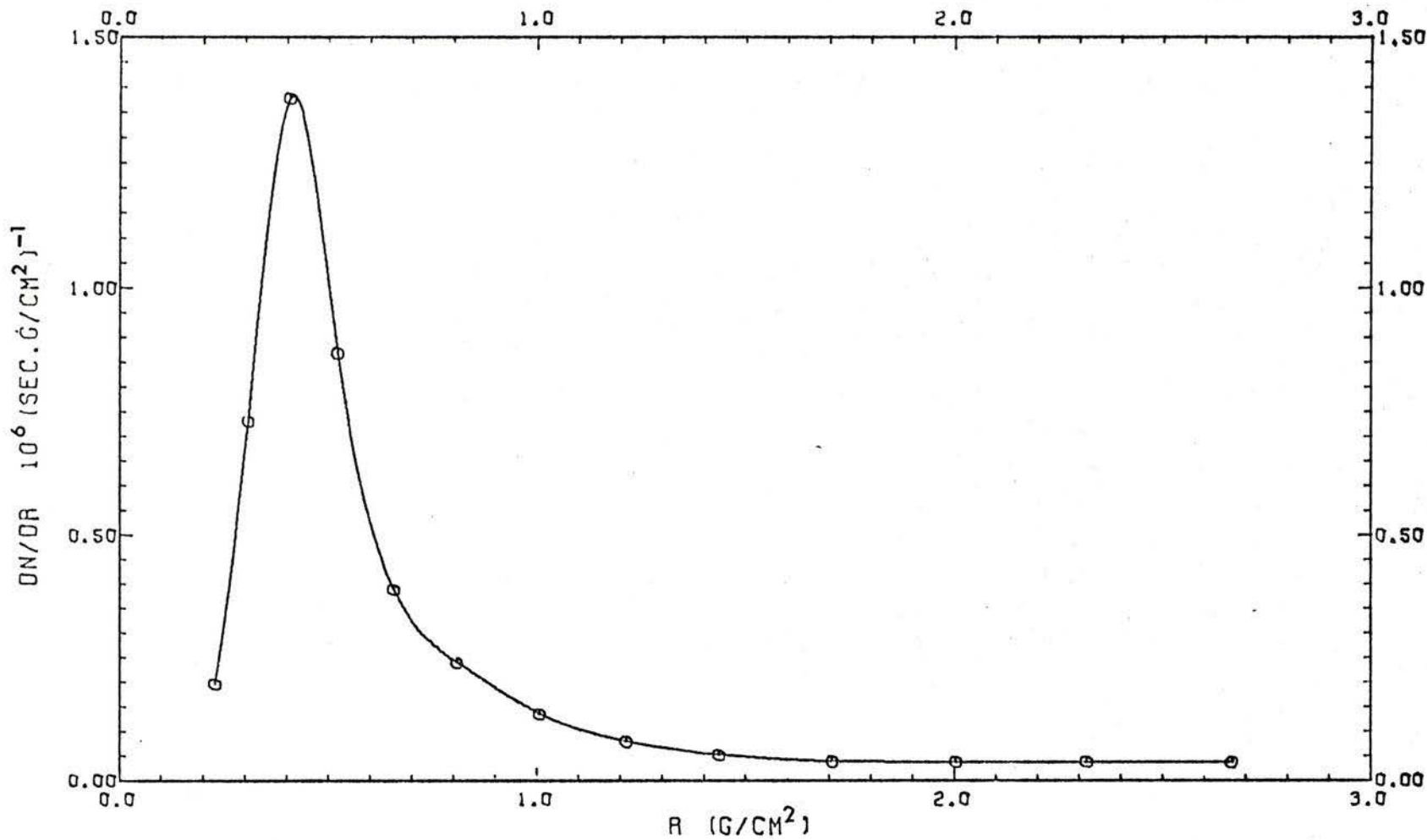


Fig. 4.23 Muon range spectrum obtained with the second half of the channel tuned to 40 MeV/c and the first half unchanged at $p_0 = 100$ MeV/c. Flux integrated over an area of 10 cm x 10 cm.

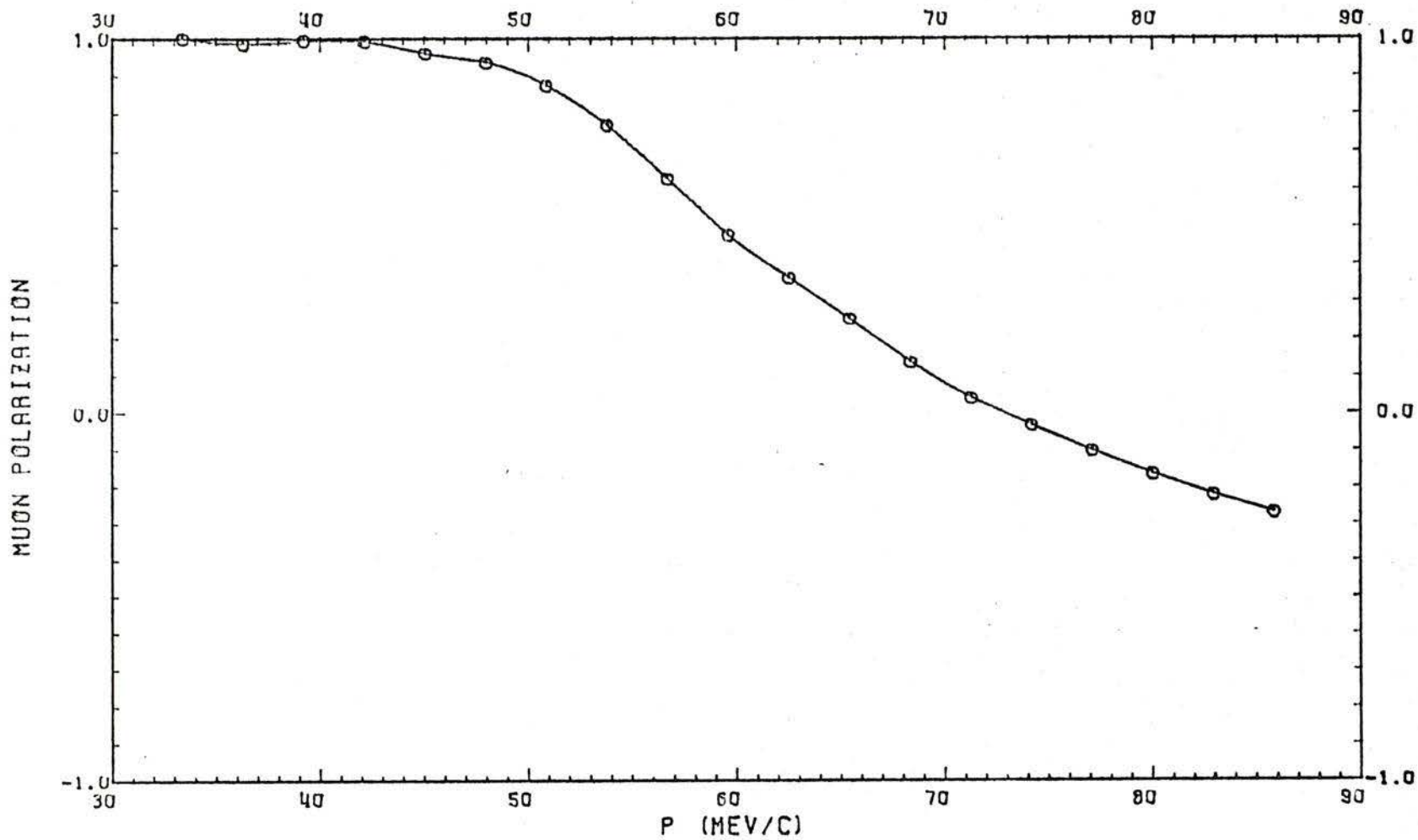


Fig. 4.24 Muon polarization as a function of momentum with the channel as set up for Fig. 4.22.

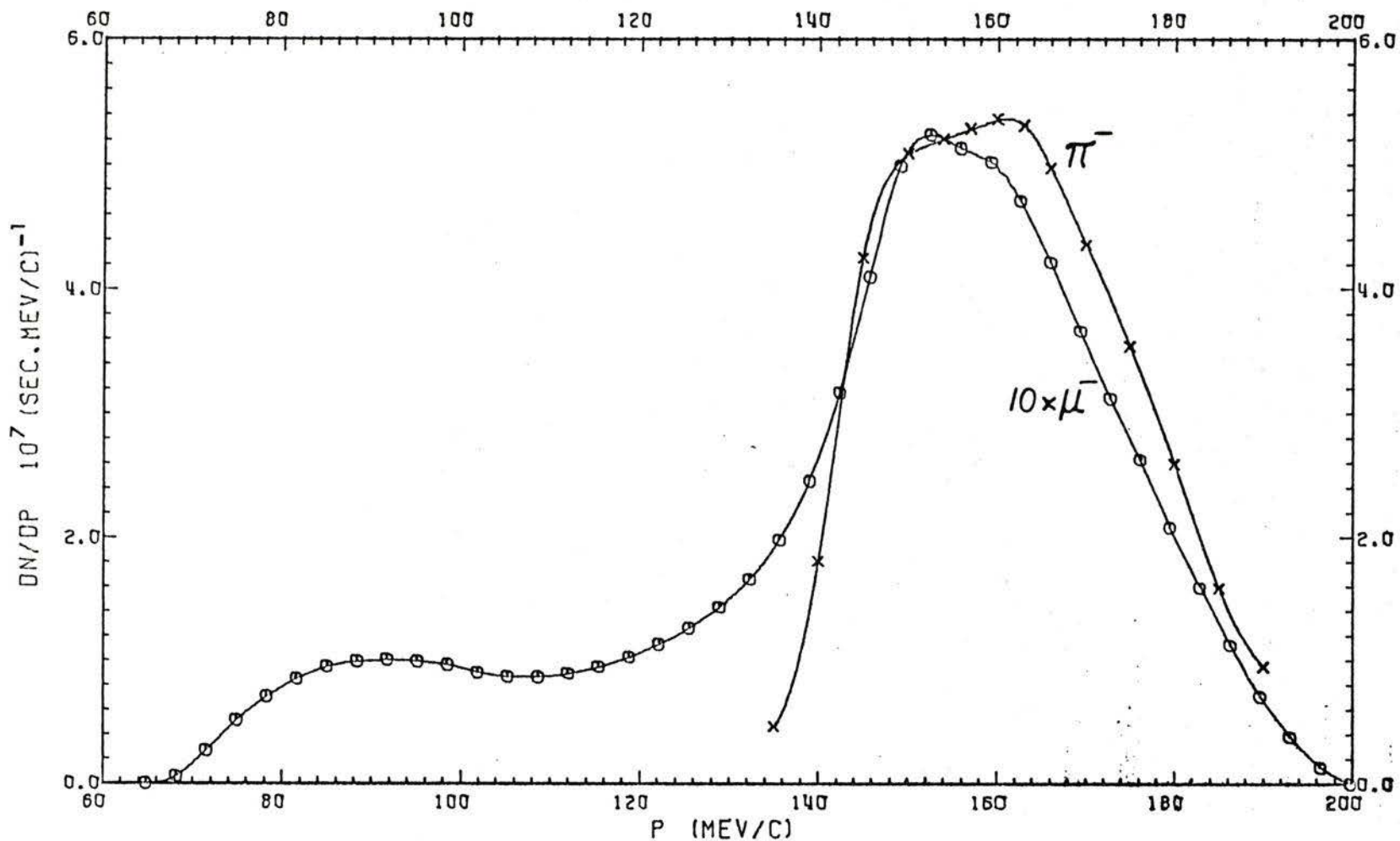


Fig. 4.25 Pion and muon spectra at the entrance to the second bending magnet M2 for $p_0 = 160$ MeV/c. Fluxes are integrated over an area of 25 cm x 25 cm.

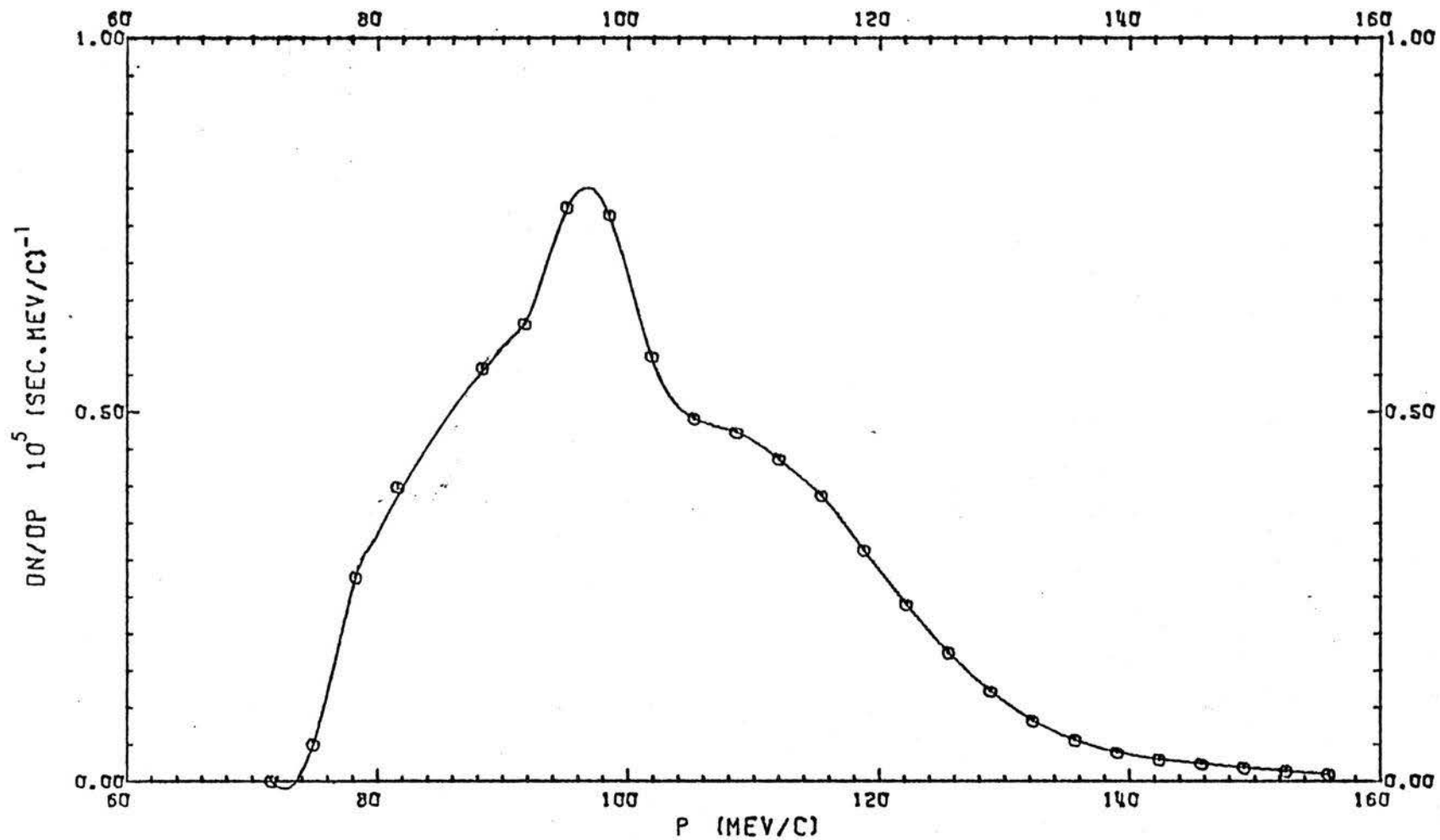


Fig. 4.26 Muon momentum spectrum obtained with the second half of the channel tuned to 90 MeV/c and the first half unchanged at 160 MeV/c. Flux integrated over an area of 10 cm x 10 cm.

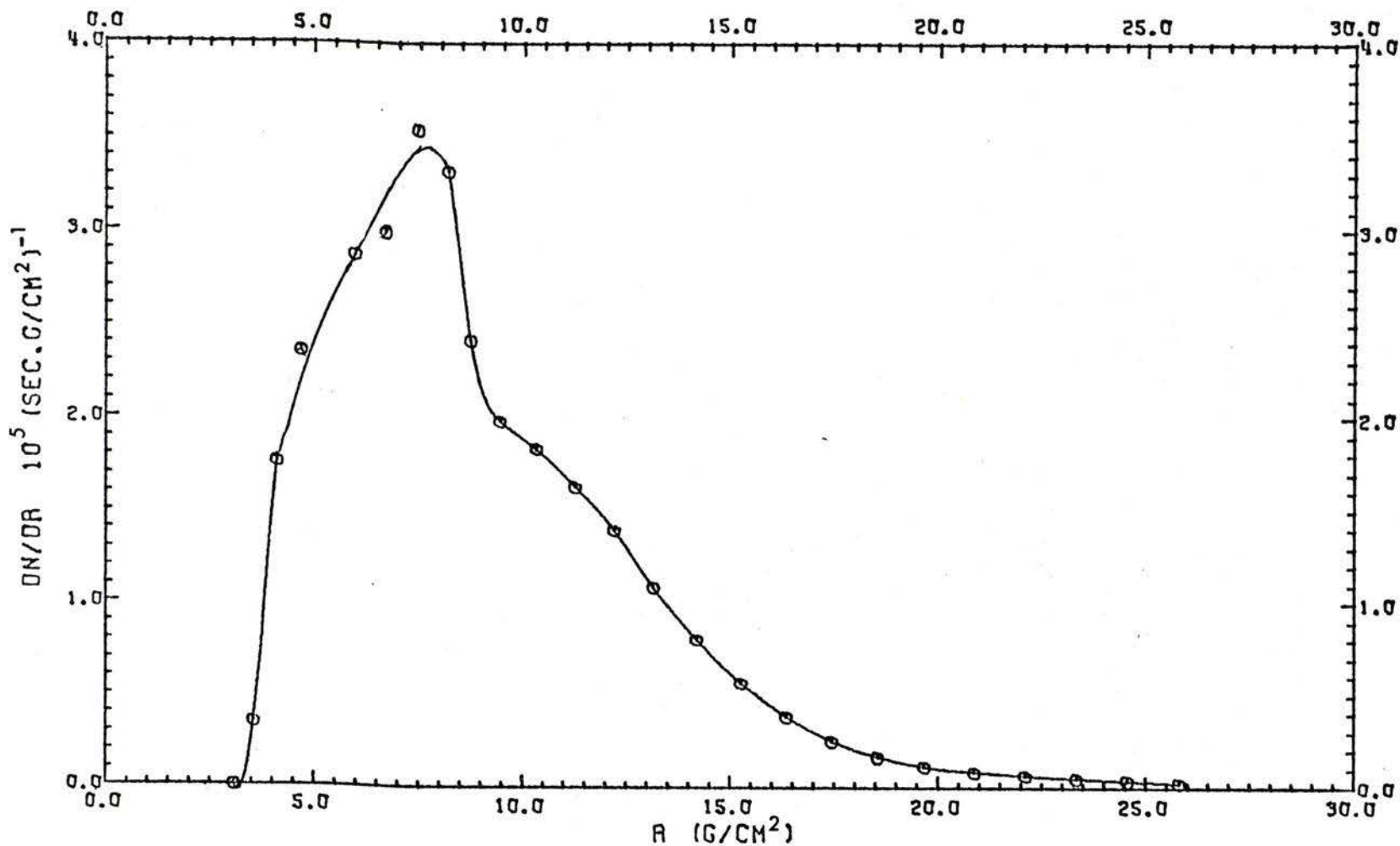


Fig. 4.27 Muon range spectrum obtained with the second half of the channel tuned to 90 MeV/c and the first half unchanged at 160 MeV/c. Flux integrated over an area of 10 cm x 10 cm.

2 g/cm² carbon target, for example, it is possible to stop 1.5×10^6 /sec using an approximately 6 g/cm² carbon degrader. The muon polarization as a function of momentum is shown in Fig. 4.28. For a target 25 cm x 25 cm in area, the maximum stopping density is 1.0×10^6 and the total flux is 7.1×10^7 .

(b) Using a Plug to Stop the Pions and Collecting the Muon Halo

In this mode, the pions are focussed into a narrow strip which covers a small part of the total area of the muon beam (it is not possible to focus the pions into a small spot because of the second order effects discussed in Section 4.3.2). An absorber, extending across the full width of the beam pipe in the horizontal plane and having the same height as the pion beam in the vertical plane, is placed at the pion focus. The thickness of this plug depends on the maximum momentum of the pions and is chosen so that all the pions are stopped.

For the case considered here, the channel central momentum is set at 100 MeV/c and the maximum momentum transmitted is 120 MeV/c. The range of 120 MeV/c pions is 8.25 g/cm² carbon, which should be the thickness of the plug neglecting range straggling.

For a 1 cm high proton beam at the production target, the resulting pion distribution in the transverse plane at the focus, calculated to second order, is shown in Fig. 4.10 (see Section 4.3.1) for a momentum interval of $\pm 10\%$. It is seen that 97% of the pions are contained within a strip 18 cm x 4 cm and 99% are contained in a

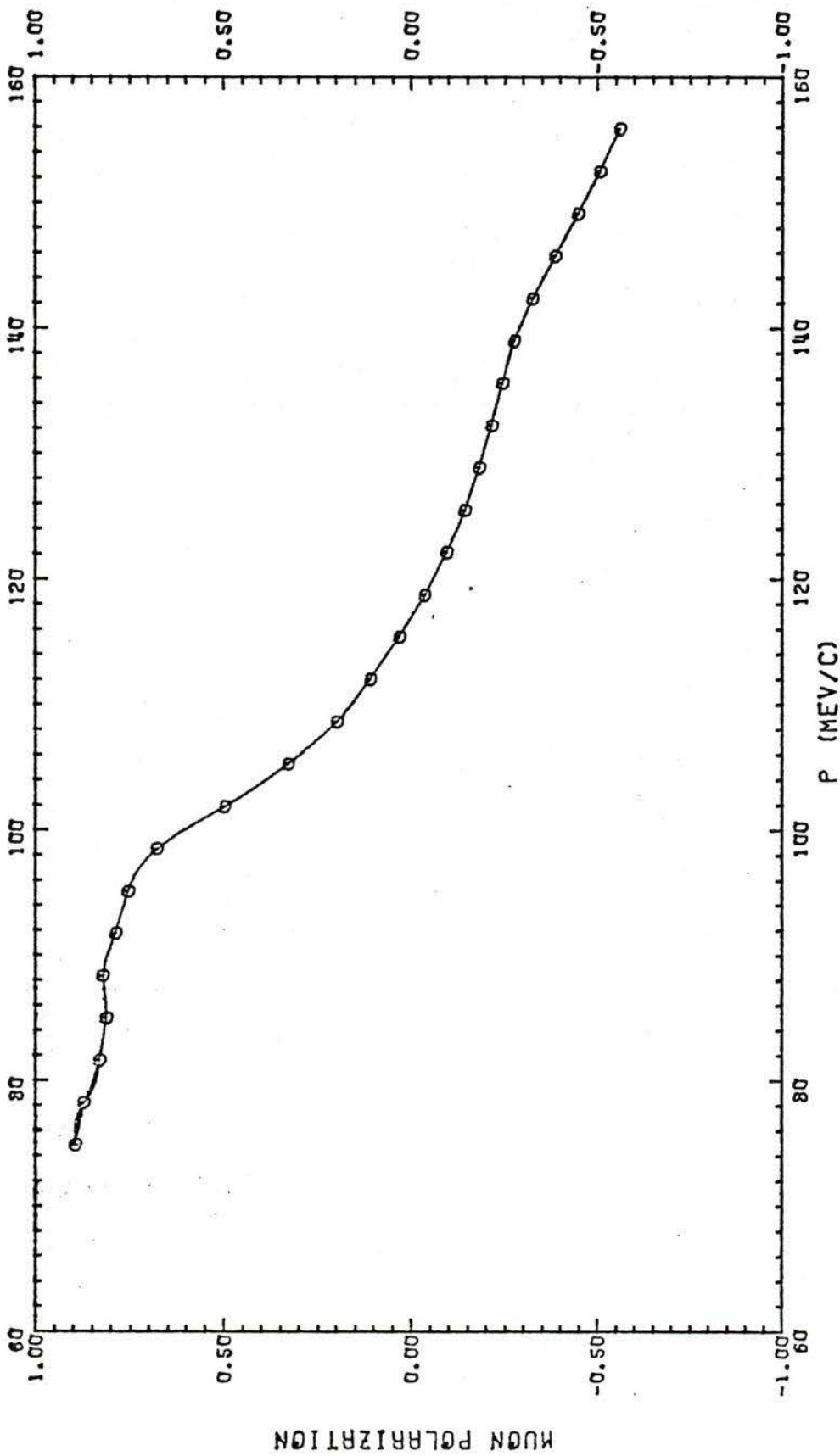


Fig. 4.28 Muon polarization as a function of momentum with the channel as set up for Fig. 4.26.

22 cm x 4 cm strip. If the proton beam height could be reduced to 0.5 cm, the height of the strip will be reduced accordingly. A calculation with MBEND using a transverse area of 25 cm x 25 cm and a similar calculation using an area of 25 cm x 4 cm gave the difference in the muon total flux as $1.6 \times 10^7 \mu^-/\text{sec}$. This is the intensity of the muons forming the halo. These muons, though, are contaminated with pions. The pion content is 77%. If the plug size is increased to 25 cm x 6 cm, the total muon flux transmitted is reduced to $1.2 \times 10^7/\text{sec}$ but the pion contamination is also reduced to only 1.5%.

The muons in the halo are transmitted above and below the pion plug. The momentum and range spectra are shown in Fig. 4.29 and Fig. 4.30 respectively. These are obtained by subtracting the spectrum for the 25 cm x 6 cm case from the spectrum shown in Fig. 4.7 for the case of no plug where the area at the exit is 25 cm x 25 cm. Fig. 4.29 indicates that the forward muon peak has shifted upwards to 109 MeV/c from about 100 MeV/c and the backwards muons to 45 from 42 MeV/c.

The muons passing through the plug will be degraded in energy and will, therefore, not contribute to the useful muon intensity. If a 9 g/cm^2 carbon degrader is used, about $5.4 \times 10^6 \mu^-/\text{sec}$ may be stopped in a 1 g/cm^2 target, using the forward muons. Using the backward muon peak, about $1.2 \times 10^6/\text{sec}$ may be stopped in 1 g/cm^2 carbon target after a 0.25 g/cm^2 C degrader. The disadvantage of this method is the large background flux of neutrons and electrons generated by pions and muons stopping in the plug.

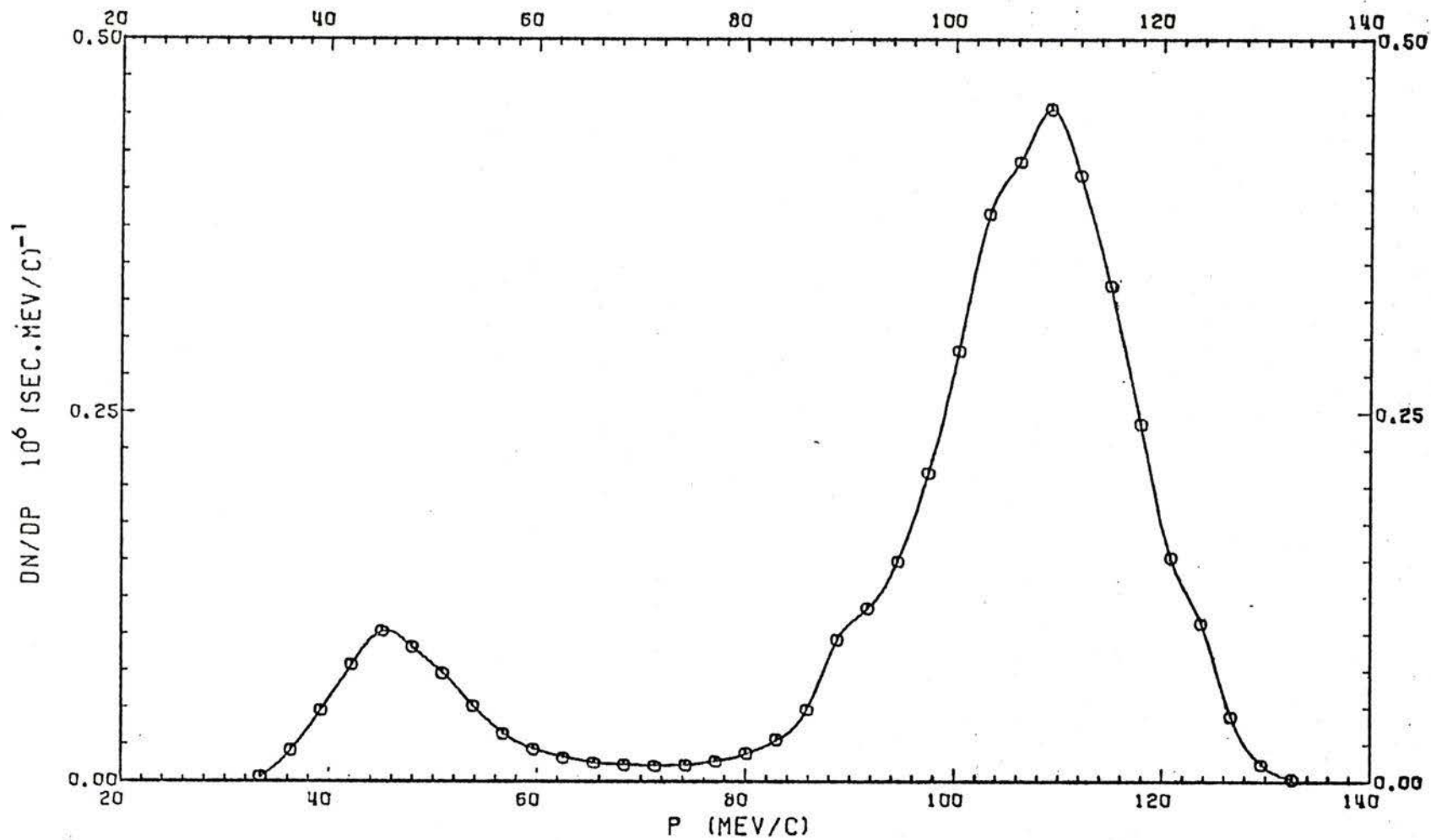


Fig. 4.29 Momentum spectrum of the muon halo when a 6 cm high plug is used to stop the pions. Flux integrated over a 25 cm x 25 cm area with $p_0 = 100$ MeV/c.

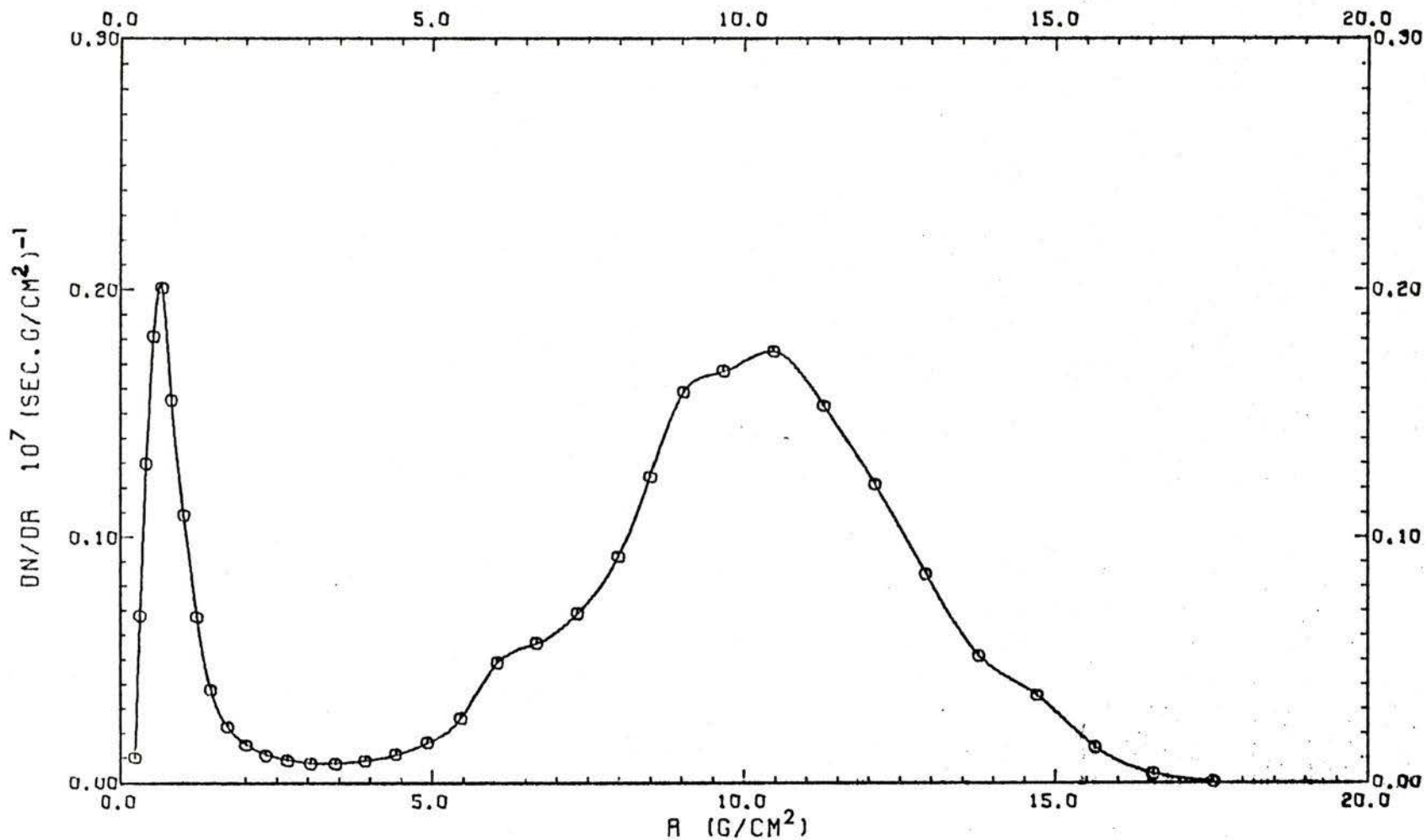


Fig. 4.30 Range spectrum of the muon halo when a 6 cm high plug is used to stop the pions. Flux integrated over a 25 cm x 25 cm area with $p_0 = 100$ MeV/c.

(c) Using an Absorber to Stop the Pions and Degrade the Muons

In this mode, a large absorber filling the beam pipe is placed at the pion focus. The thickness is chosen according to the pion energy so that all the pions (and, incidentally, the backward low energy muons) are stopped because of their lower range compared to the forward muons which are degraded to a lower energy and collected behind the absorber. For the case considered here, the channel central momentum is 100 MeV/c as in the previous case considered in (b) above. The absorber thickness required to stop all pions is 8.25 g/cm² of carbon. It will also stop all muons with momenta lower than 100 MeV/c. Muons of higher momenta, including those in the peak at 103 MeV/c (see Fig. 4.7), are transmitted. The momentum spectrum of the transmitted muons is shown in Fig. 4.31, indicating a shift of the peak to the lower momentum of 47 MeV/c and the disappearance of the low energy side of the forward peak. The corresponding range spectrum is shown in Fig. 4.32.

The total muon flux before the beam enters the absorber is 4.8×10^7 μ^- /sec (see Section 4.3.1). The total flux transmitted through the absorber is 3.4×10^7 /sec neglecting losses due to multiple scattering. An estimate of multiple scattering losses was made using calculated curves (Sternheimer, 1954) of the fraction of particles traversing a counter of a given area placed a given distance from the absorber. For a target 25 cm x 25 cm in area, for which the above fluxes are quoted, placed 20 cm downstream from the absorber, the loss due to

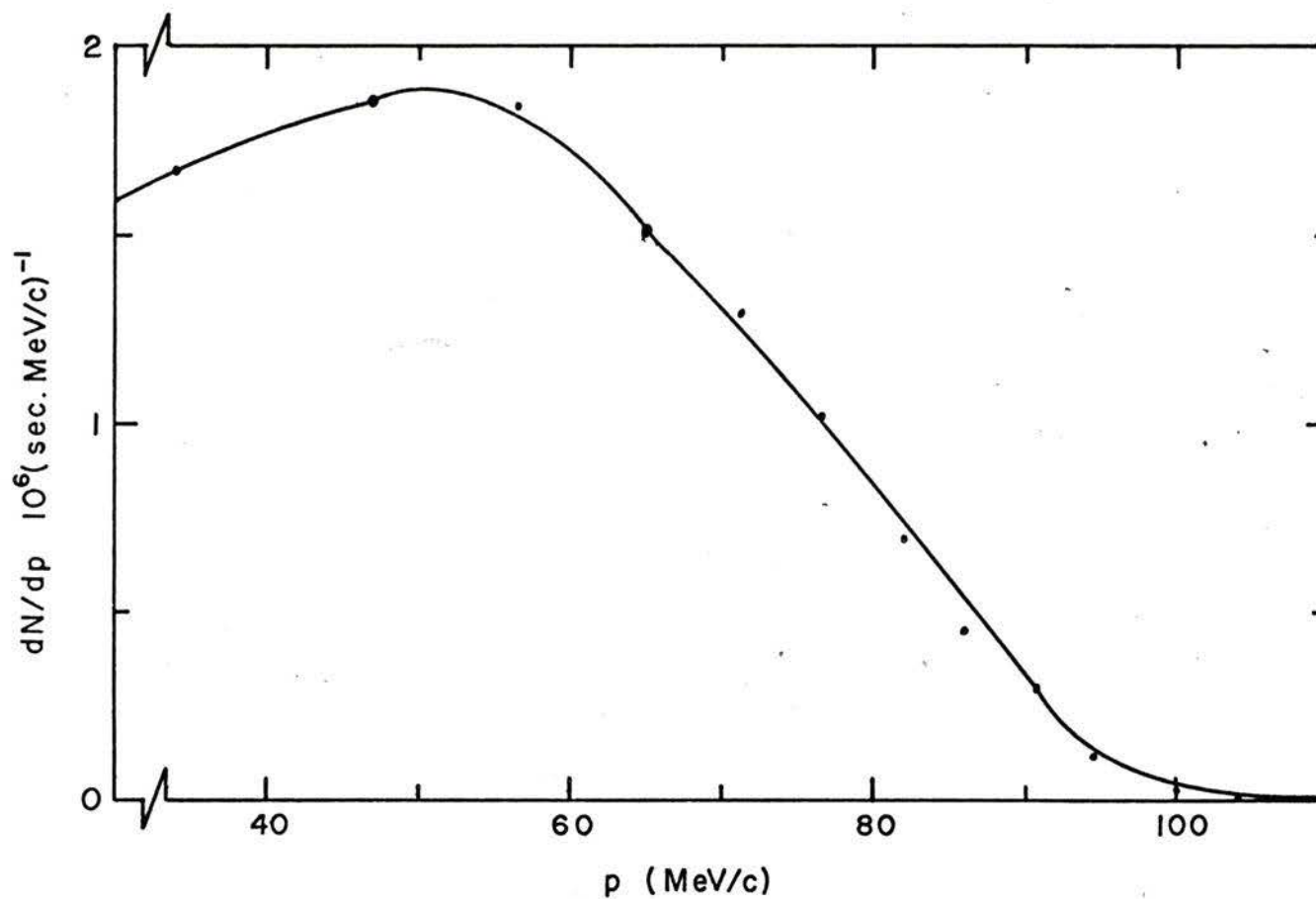


Fig. 4.31 Muon momentum spectrum transmitted through an absorber that stops all the pions. Flux integrated over an area of 25 cm x 25 cm for $p_0 = 100$ MeV/c.

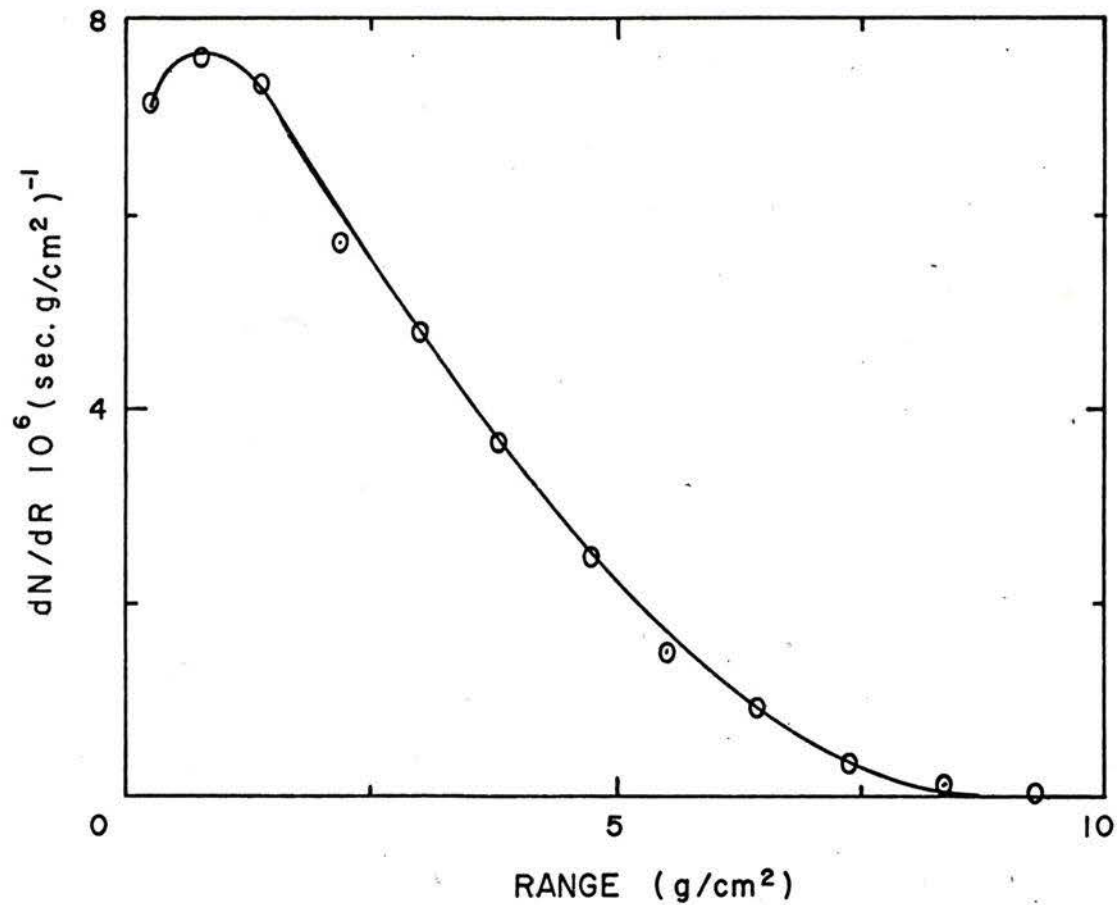


Fig. 4.32 Muon range spectrum transmitted through an absorber that stops all the pions. Flux integrated over an area of 25 cm x 25 cm for $p_0 = 100 \text{ MeV/c}$.

multiple scattering is 15%. Therefore, the total muon flux available at the target is $2.9 \times 10^7 \mu^-/\text{sec}$. This is much larger than that obtained from the muon halo discussed above. However, as in the previous case, a large background of neutrons and electrons is generated as a result of the pions and muons stopped in the absorber, which is a distinct disadvantage.

(d) Collecting 4 MeV μ^+ from Pions Decaying at Rest in the Production Target

Pions of very low energy may stop close to the surface of the production target. Negative pions will be captured by the target material but positive pions may decay into muons which escape the target. The energy of these muons will range between 4.12 MeV for those produced from pions stopped at the surface of the production target to zero for muons coming from pions stopped far enough inside the target for the muons to lose all their kinetic energy by degradation in the target material.

To collect these muons the channel should be tuned to a central momentum of 27.5 MeV/c. The momentum acceptance of the channel is $\pm 10\%$, which means that muons with momenta between about 25 MeV/c and 30 MeV/c will be transmitted, covering the peak indicated by the Arizona experimental results (Pifer *et al.*, 1971). If the Arizona experimental results are scaled to the TRIUMF energy, current and production target, the curve shown in Fig. 4.33 is obtained, indicating a maximum flux of $5 \times 10^5 \mu^+/\text{sec}$ in a 100 cm^2 target.

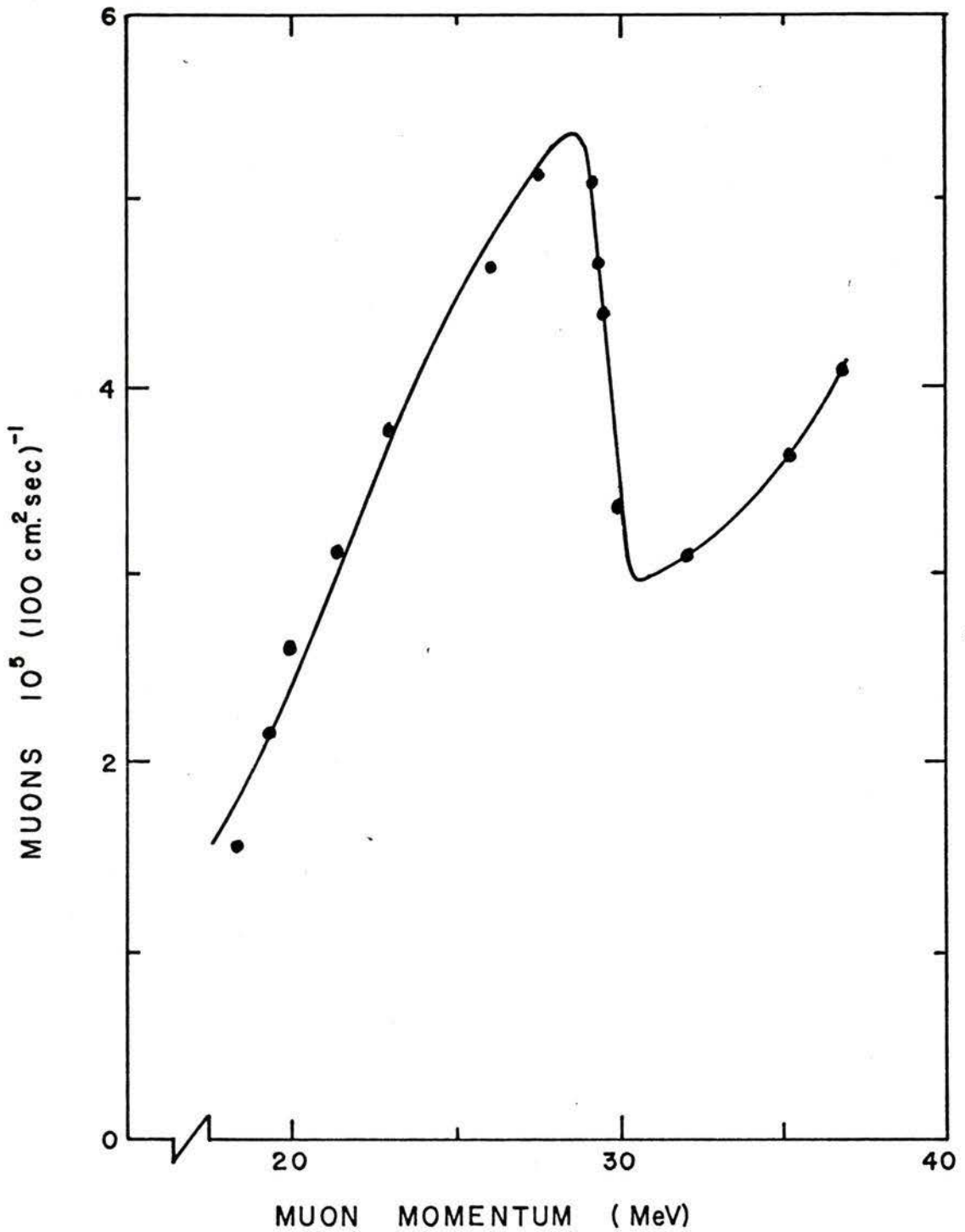


Fig. 4.33 Total muon flux as a function of channel momentum when the channel is operated in the Arizona mode to collect 4 MeV muons generated in the pion production target.

4.4.3 Operation of the Channel with the Analyzing Magnet

Although the momentum analyzing system will be discussed in Chapter 5, results are given here for the 90° analyzing magnet when used to separate the pions from the muons after the first section of the channel (the pion collection system) in the absence of the straight section. To match the magnet to the channel, Q_4 and Q_5 are adjusted to a pole-tip field of 1.76 and -2.37 kGauss respectively, and d_8 is increased to 24". Other elements of the system are unchanged as listed in Table 4.2.

(a) Using the Analyzing Magnet for Collecting Backward Muons

With the channel tuned to a central momentum of 160 MeV/c, the backward muon peak is at 85 MeV/c. The analyzing magnet is tuned to this momentum which is the optimum setting for maximum stopped flux. The pion-free momentum spectrum is shown in Fig. 4.34 and the corresponding range spectrum in Fig. 4.35. The muon polarization as a function of momentum is shown in Fig. 4.36. The total muon flux for this case is $1.0 \times 10^7 \mu^-/\text{sec}$ integrated over an area of 25 cm x 25 cm. From Fig. 4.35 it is seen that, if a carbon degrader of 5.0 g/cm^2 is used, $3.8 \times 10^6 \mu^-/\text{sec}$ may be stopped in a 1 g/cm^2 carbon target. If the channel is operated at a central momentum of 100 MeV/c, the backward muon peak is at 45 MeV/c. The analyzing magnet is tuned to this momentum and the corresponding spectra are shown in Fig. 4.37 and Fig. 4.38. The muon polarization is shown in Fig. 4.39. The total muon flux is $1 \times 10^6 \mu^-/\text{sec}$ for a 25 cm x 25 cm area. For this case, $0.7 \times 10^6 \mu^-/\text{sec}$ may be stopped in a 1 g/cm^2 carbon target without using a degrader.

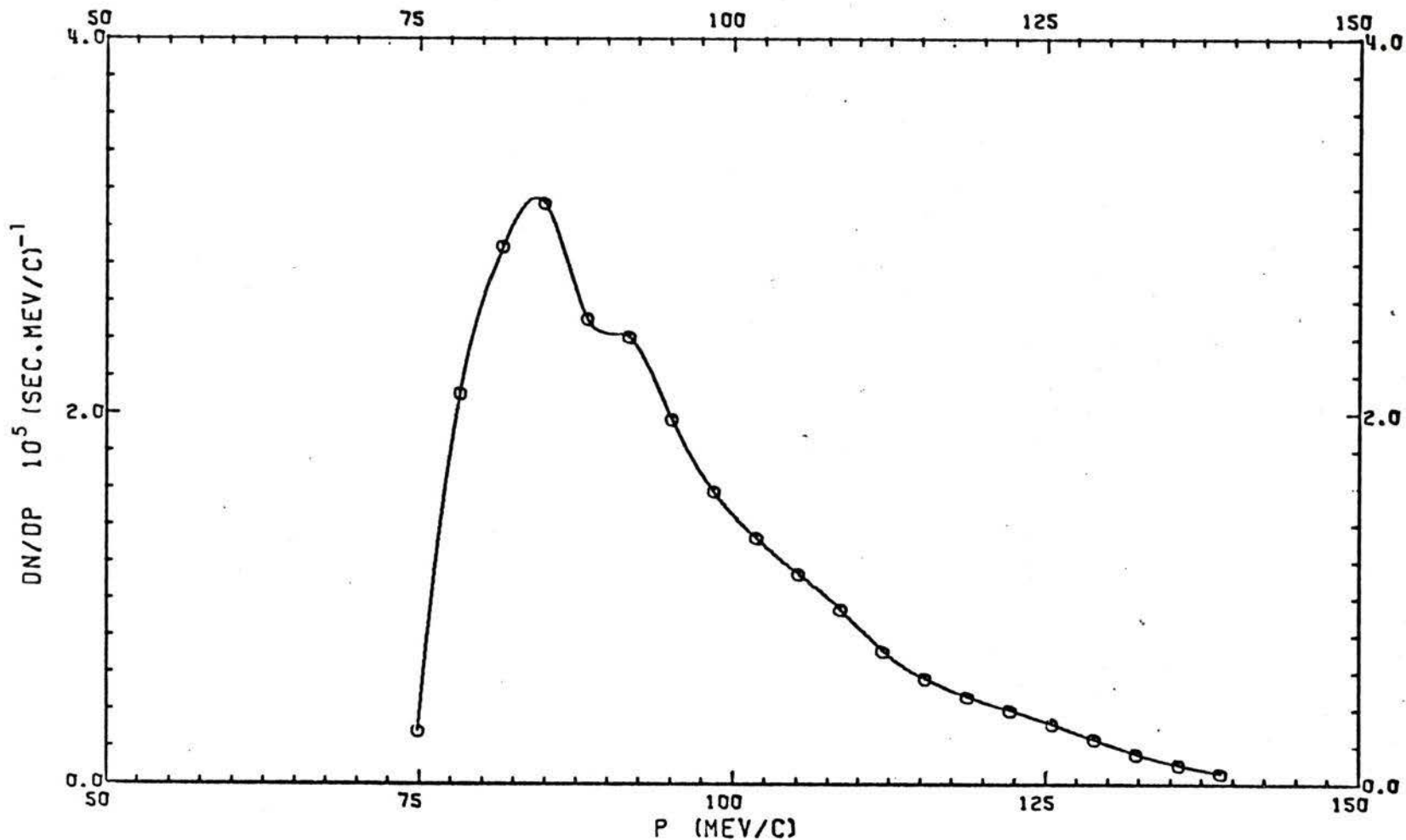


Fig. 4.34 Muon momentum spectrum at the end of the 90° analyzing magnet placed after the channel shown in Fig. 4.5. The magnet is tuned to 85 MeV/c for backward muons from the channel when operated with $p_0 = 160$ MeV/c. Flux is integrated over a 25 cm x 25 cm area.

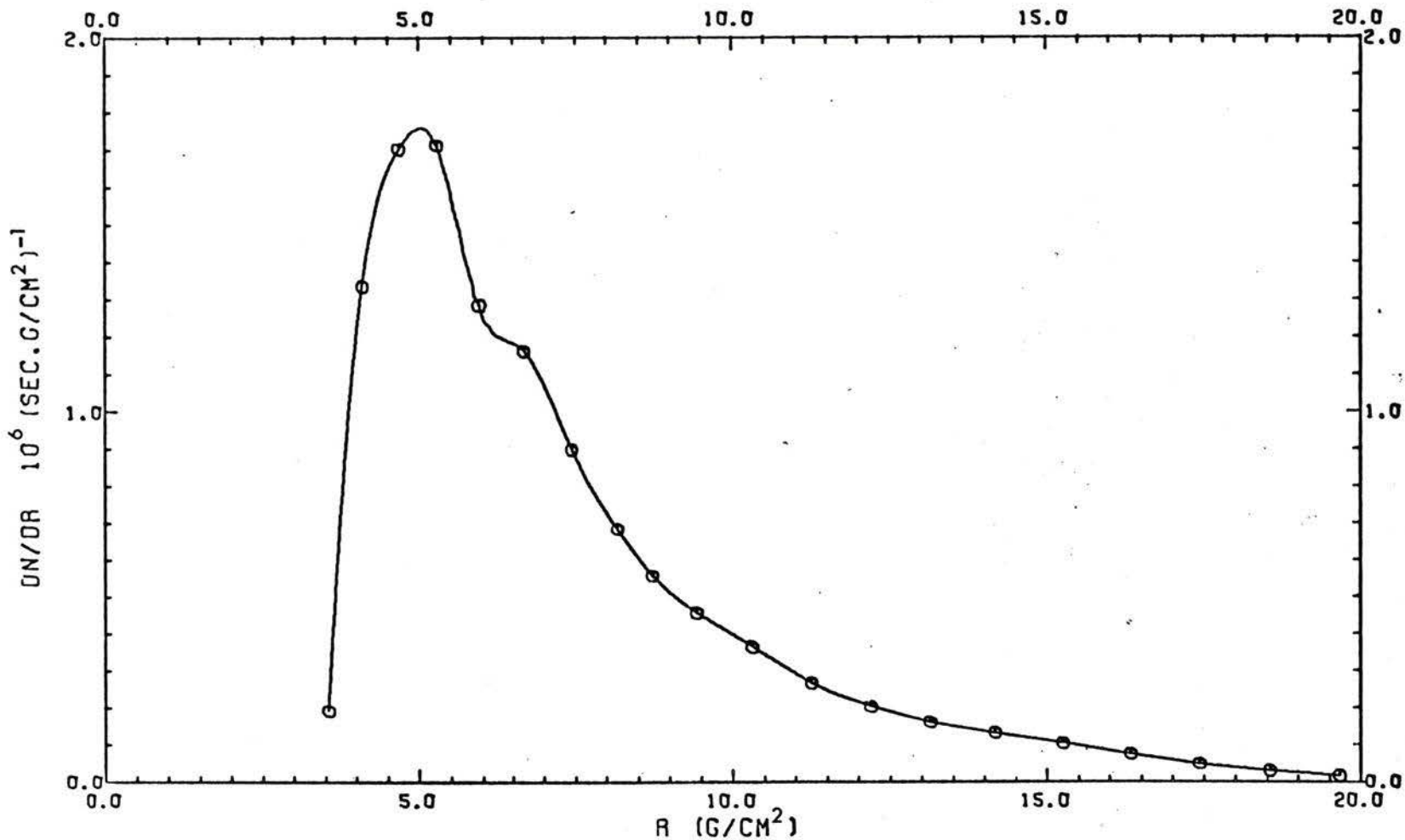


Fig. 4.35 Muon range spectrum at the end of the 90° analyzing magnet placed after the channel shown in Fig. 4.5. The magnet is tuned to 85 MeV/c for backward muons from the channel when operated with $p_0 = 160$ MeV/c. Flux is integrated over a 25 cm x 25 cm area.

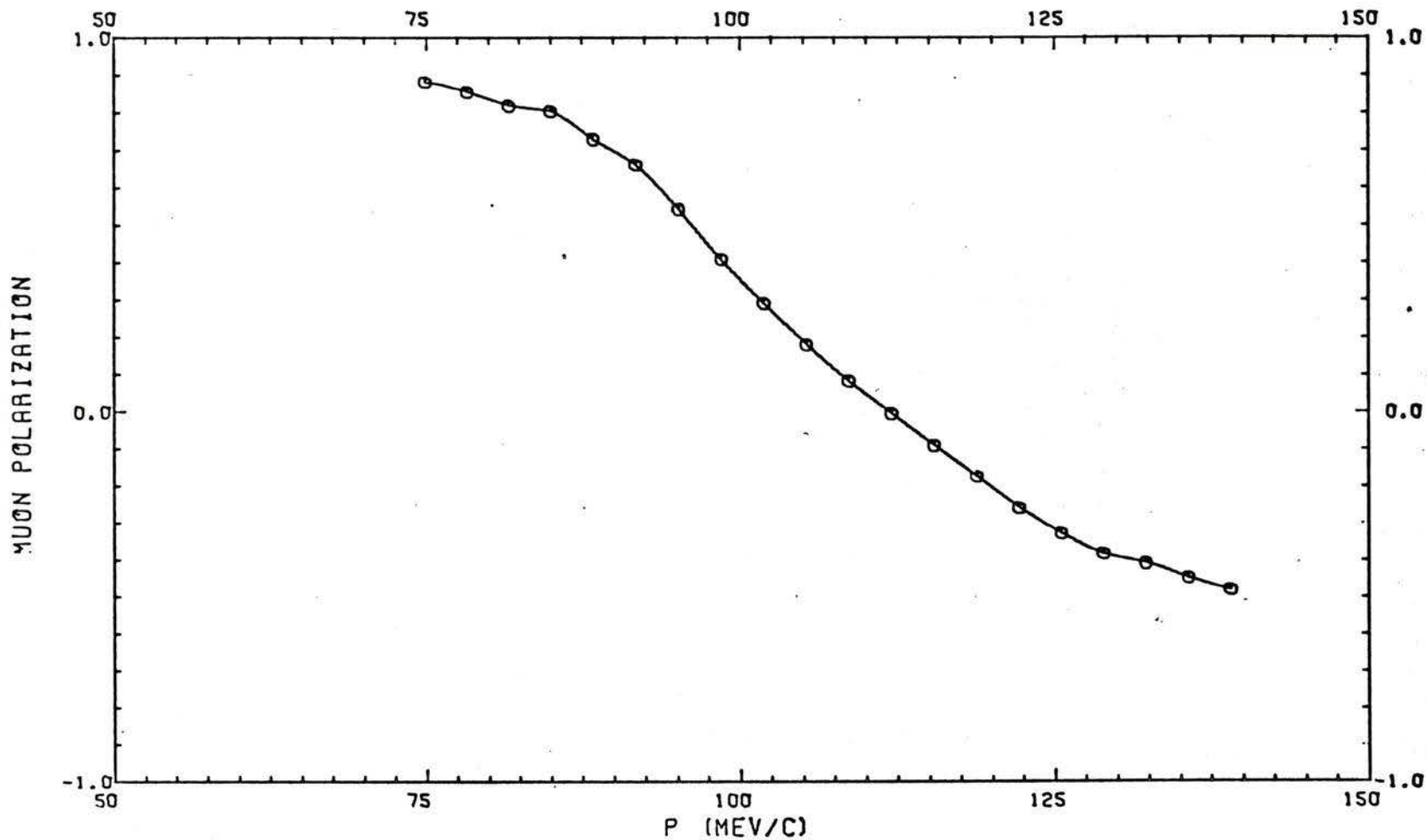


Fig. 4.36 Muon polarization as a function of momentum at the end of the 90° analyzing magnet with the setup described for Fig. 4.34.

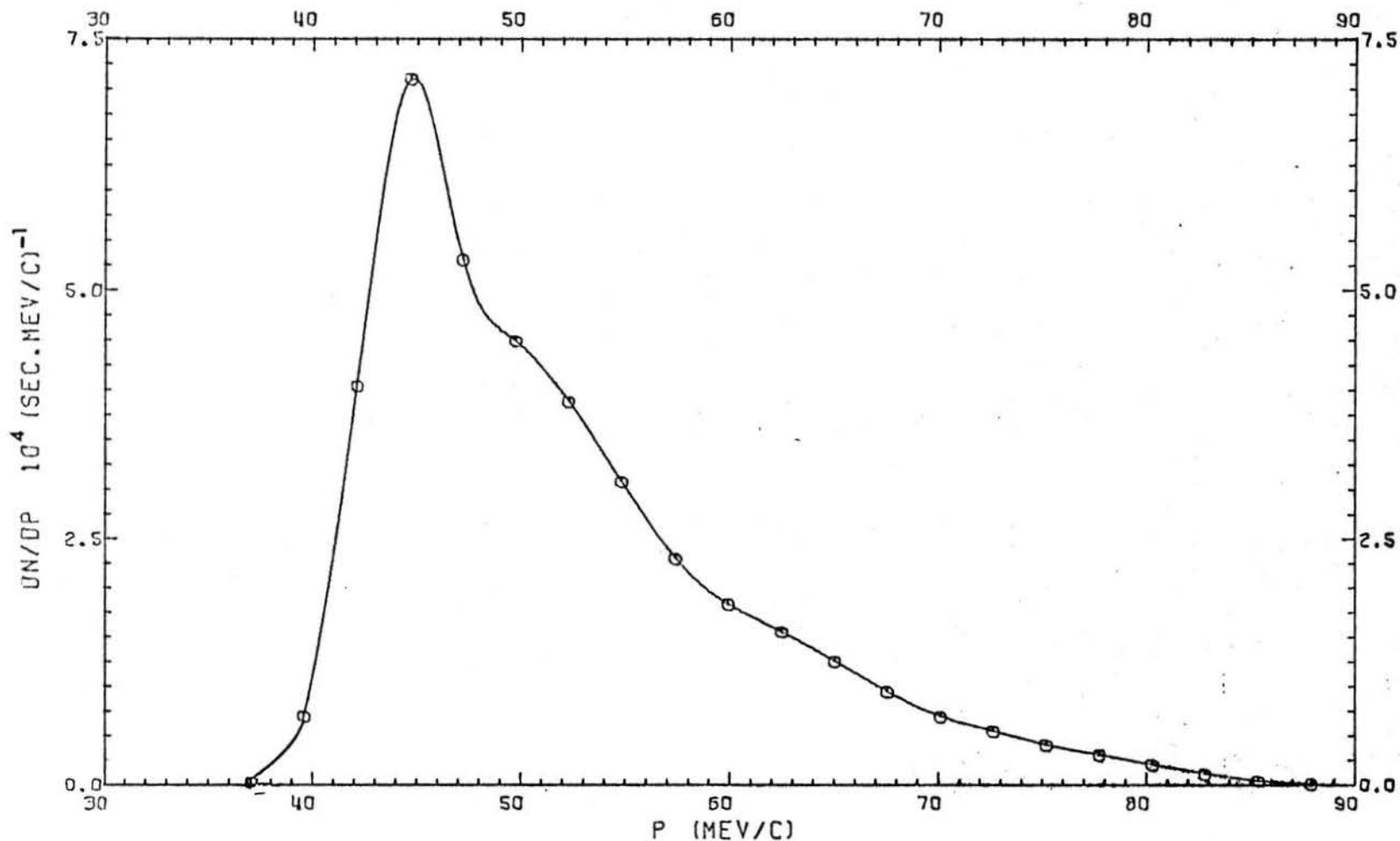


Fig. 4.37 Muon momentum spectrum at the end of the 90° analyzing magnet placed after the channel shown in Fig. 4.5. The magnet is tuned to 45 MeV/c for backward muons from the channel when operated with $p_0 = 100 \text{ MeV}/c$. Flux is integrated over a $25 \text{ cm} \times 25 \text{ cm}$ area.

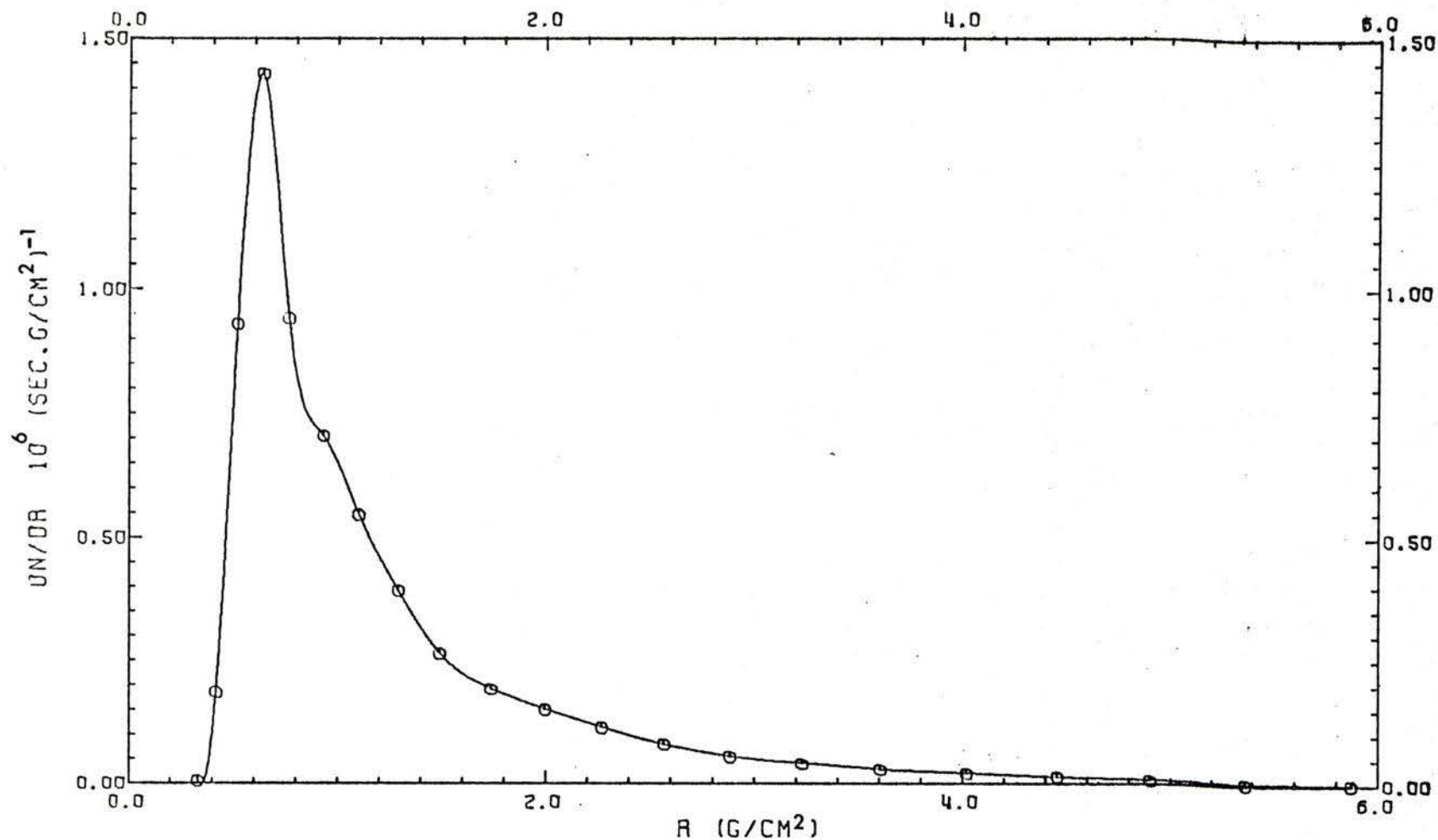


Fig. 4.38 Muon range spectrum at the end of the 90° analyzing magnet placed after the channel shown in Fig. 4.5. The magnet is tuned to 45 MeV/c for backward muons from the channel when operated with $p_0 = 100$ MeV/c. Flux is integrated over a 25 cm x 25 cm area.

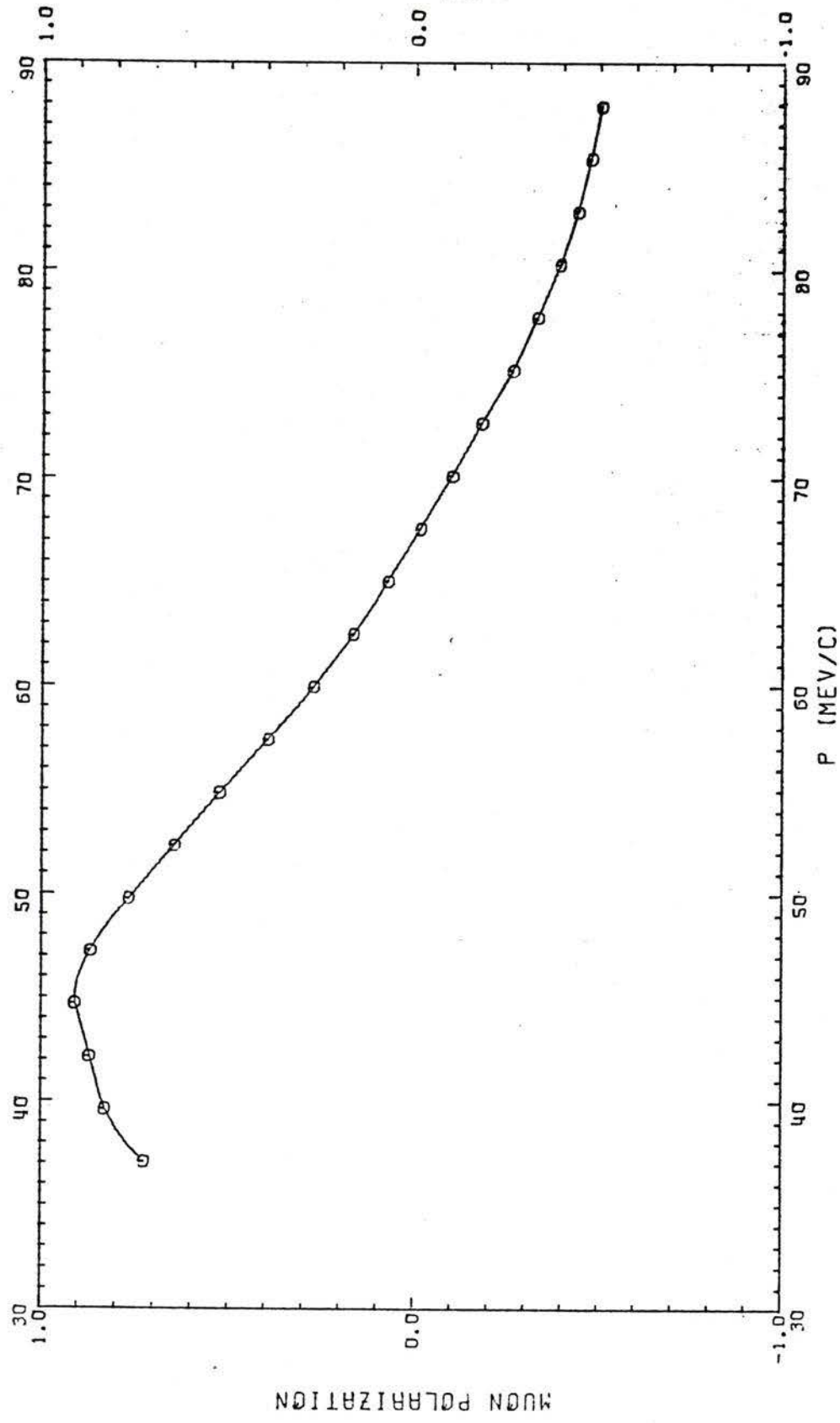


Fig. 4.39 Muon polarization as a function of momentum with the channel as set up for Fig. 4.37.

(b) Using the Analyzing Magnet for Forward Muons

With the channel tuned to a central momentum of 100 MeV/c, the pion cut-off occurs at 120 MeV/c and a pion-free forward muon beam is obtained when the analyzer is tuned to 132.5 MeV/c. The muon momentum spectrum for this case is shown in Fig. 4.40 and the range spectrum in Fig. 4.41. The total flux is $2.7 \times 10^6 \mu^-/\text{sec}$ for an area of 25 cm x 25 cm and the maximum stopping density is $1.1 \times 10^6 (\text{sec} \cdot \text{g}/\text{cm}^2)^{-1}$. If the analyzer is tuned to 130 MeV/c, a pion contamination of 0.5% is obtained but the total muon flux is almost 50% higher at $4 \times 10^6/\text{sec}$. The analyzing magnet may also be used to collect forward muons in conjunction with the methods outlined in Section 4.4.2 (b) and (c) where absorbers are used to stop the pions. The analyzer, in this case, will serve to reduce the background particles generated in the absorber.

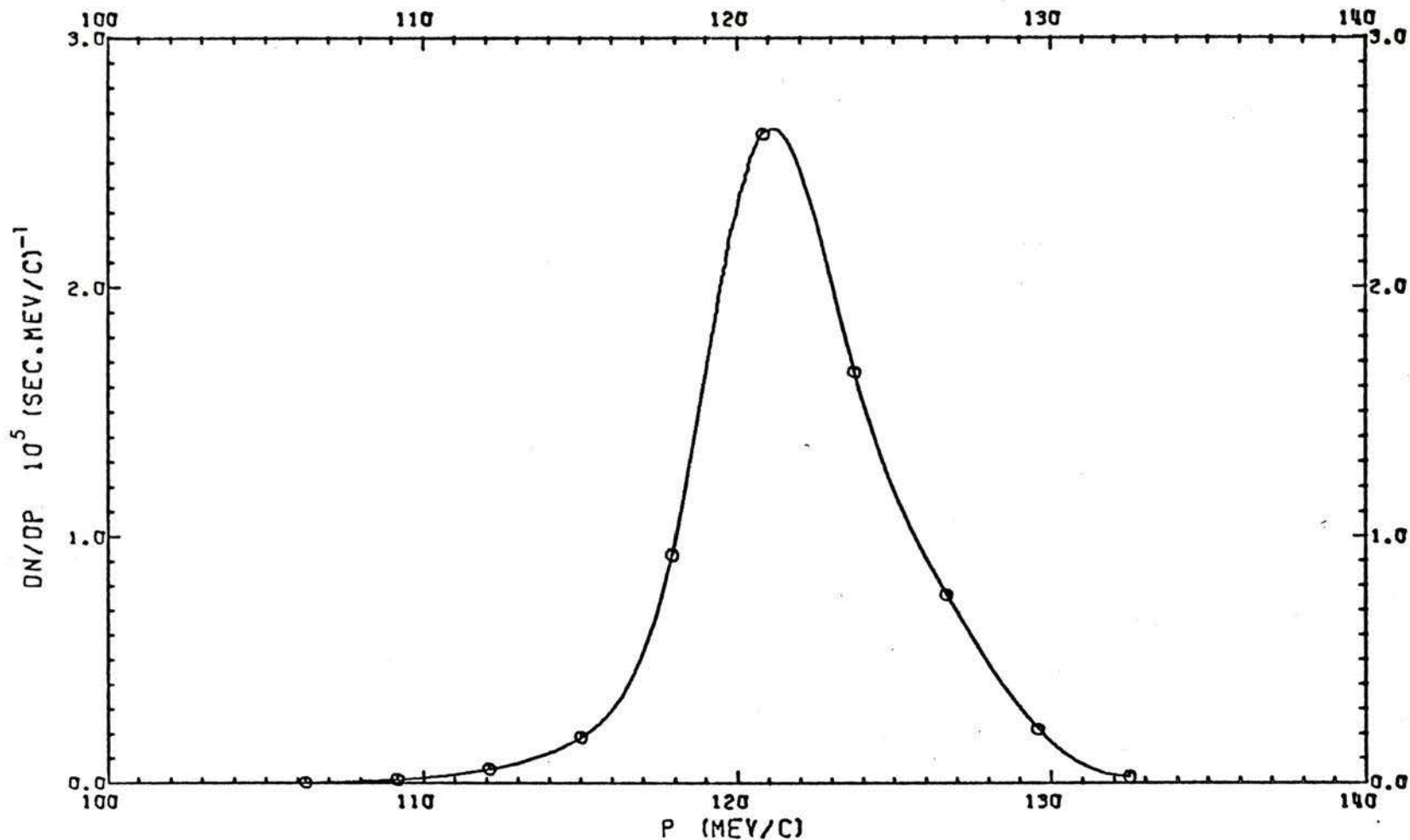


Fig. 4.40 Muon momentum spectrum at the end of the 90° analyzing magnet. The magnet is tuned to 132.5 MeV/c for forward muons from the channel when operated with $p_0 = 100$ MeV/c. Flux is integrated over a 25 cm x 25 cm area. (The magnet placed after the system shown in Fig. 4.5).

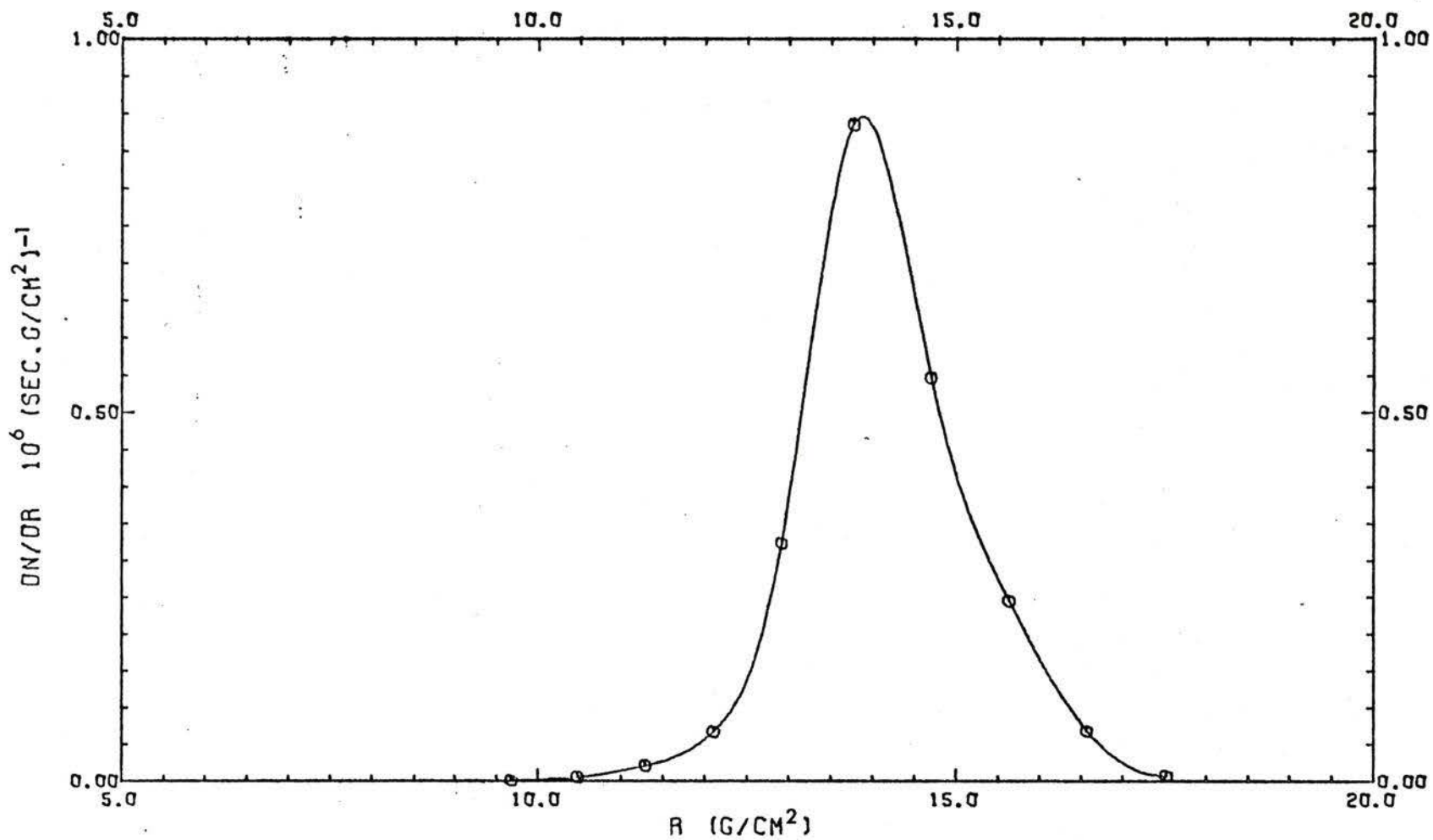


Fig. 4.41 Muon range spectrum at the end of the 90° analyzing magnet. The magnet is tuned to 132.5 MeV/c for forward muons from the channel when operated with $p_0 = 100$ MeV/c. Flux is integrated over a 25 cm x 25 cm area.

(The magnet placed after the system shown in Fig. 4.5).

CHAPTER 5

PROPOSED TRIUMF STOPPED PION/MUON CHANNEL

PHASE TWO

5.1 Choice of Straight Section

Four types of channels were considered, in more or less detail, for the design of the straight section: a helical quadrupole, a coaxial beam guide, a superconducting solenoid, and an alternating gradient quadrupole. The latter is chosen. The reasoning behind this choice, which is based on performance, cost and flexibility, is summarized in the following paragraphs, outlining the arguments for each type.

The helical quadrupole magnet was considered and not found suitable. The basic concept and the advantages and disadvantages of this type of channel were discussed in Section 3.4, which indicates no clear advantages as a straight section. Although it may offer a cost advantage, it is a single purpose device and has a lower acceptance than the alternating gradient quadrupole channel.

The coaxial beam guide was also considered and found unsuitable. This device was discussed in Section 3.3 and its main advantage as a straight section is its low cost. However, the disadvantages discussed in Section 3.3, in particular its low acceptance and lack of flexibility, makes it unsuitable even at a relatively low cost. The lack of published performance data for the only existing guide at Carnegie-Mellon make it difficult to evaluate its performance in practice.

The superconducting solenoid was discussed in Section 3.2, where the merits and disadvantages of the device are considered. Its very high capture efficiency for muons, 100% for low energy muons, makes it suitable as a straight section. However, the disadvantages discussed in Section 3.2, in particular the divergence of the beam at the exit, and the relatively large development and design program that would be involved (requiring funds and manpower not available at TRIUMF) made it less attractive, at least at the present time.

The alternating gradient quadrupole channel was discussed in Section 3.1. This type of channel is most suitable as a straight section because of its flexibility and proven performance in existing channels. An obvious advantage is that it can be built in stages as funds become available. In addition, there are several manufacturers experienced in making quadrupoles, thus avoiding in-house design and development which require unavailable manpower. It has, therefore, been chosen for the straight section of the stopped pion/muon channel.

5.2 Design of the Straight Section

5.2.1 Design Aims and Procedure

The aim is to maximize muon stopping density within the limits of available funds. To realize this aim, phase space and momentum acceptance and capture efficiency must be maximized. These quantities are functions of quadrupole apertures, length, spacing and magnetic fields. The procedure was to adjust quadrupoles Q4 and Q5 of the pion collection section (see Fig. 4.5) to form a waist in both transverse planes at the centre of the first quadrupole of the alternating gradient channel. Initial channel parameters are then chosen for which the stability condition (Citron *et al.*, 1963)

$$|\cos \mu| < 1$$

is satisfied. $\cos \mu$ is half the trace of the transfer matrix through one period. (A period is the system between the centres of two successive focussing quadrupoles.) $\cos \mu$ is related to the channel parameters length, spacing and gradient through the parameter η defined in Appendix F.

The parameters are then optimized using the linear optics of TRANSPORT so that the beam waist repeats itself periodically, keeping transverse displacements within the aperture of the quadrupoles. Further optimization was then carried out for the individual parameters using MBEND.

5.2.2 Parameter Optimization

The following channel parameters are optimized for maximum stopped muon rates from the backward decay of pions with a central momentum of 160 MeV/c:

- (a) field gradient of the channel quadrupoles,
- (b) quadrupole apertures, and
- (c) number of quadrupoles (length of the straight section).

Although quadrupole spacing is an important parameter, the optimum value for maximum channel acceptance is zero (Yale Staff, 1964). Therefore, in practice, this separation should be given the minimum value consistent with clearances on the quadrupole ends. 160 MeV/c is the optimum momentum for operating the pion collection section to inject the maximum pion flux into the straight section (see Table 4.4).

(a) Field Gradient

With other parameters fixed, the field gradient of the channel quadrupoles is varied and the change in the stopped muon flux is noted. The results are summarized in Fig. 5.1 which shows the change in the backward stopped muon peak and the total backward muons as functions of field gradient. These results are for a system consisting of the pion injection section plus six alternating gradient quadrupoles with zero spacing. This choice of number and spacing is made in order to reduce computing time and it is considered sufficient for the purpose of these calculations. An exit window of 25 cm x 25 cm is used for estimating fluxes at the end of the system. The total backward muons are obtained by integrating the differential flux over the range of momenta covered by the backward peak.

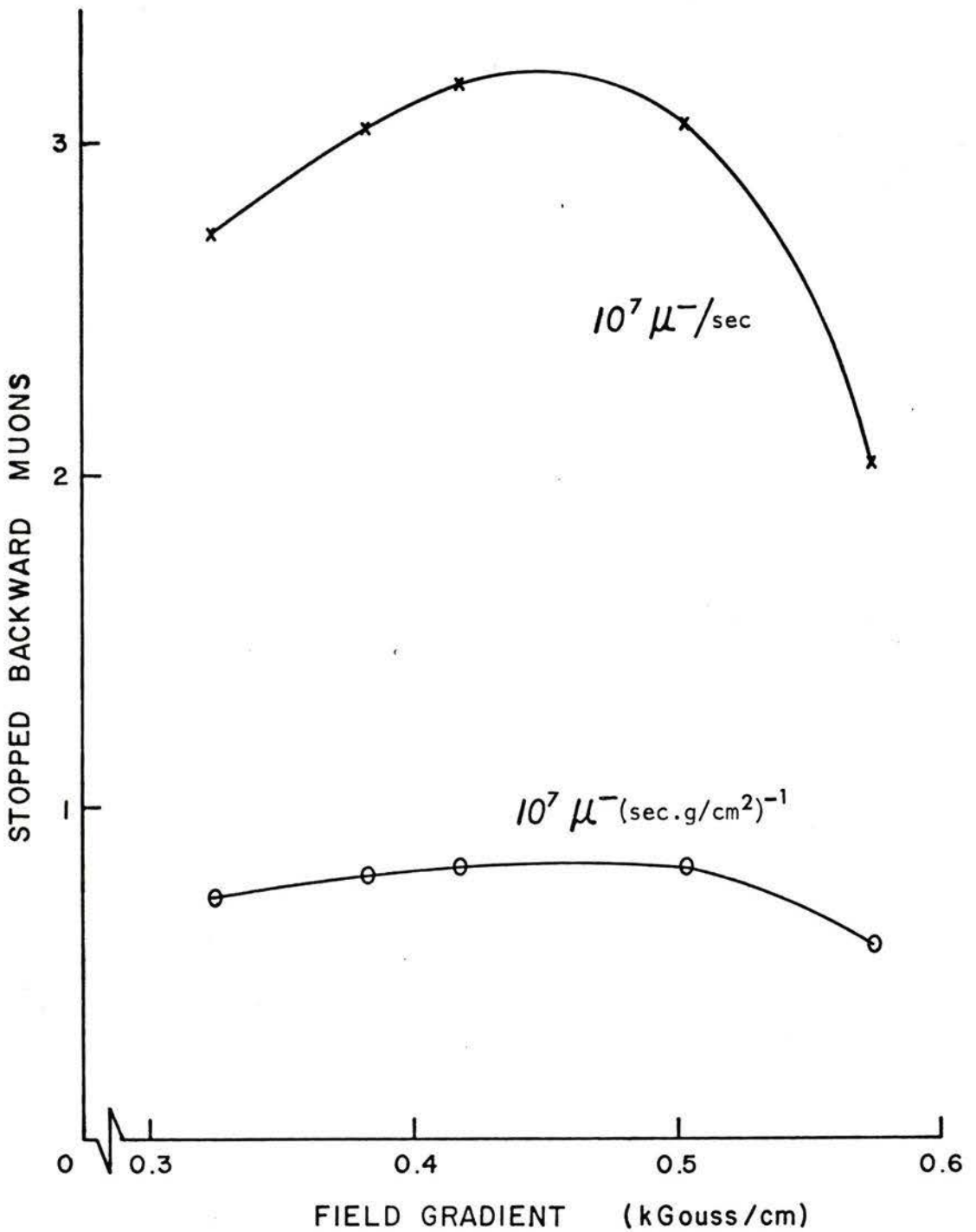


Fig. 5.1 Variation of backward muon flux with the A.G. field gradient of the straight section. Yields are quoted for an area of 25 cm x 25 cm at the end of the straight section and for $p_0 = 160 \text{ MeV/c}$.

It is seen from Fig. 5.1 that the total backward flux and the backward muon peak are maximum at a field gradient of about 0.45 kGauss/cm. However, it changes very little between 0.4 and 0.5 kGauss/cm. The backward muon peak follows the same pattern as the total muons but the variation with the field gradient is less significant.

(b) Aperture

With the optimum field gradient calculated in (a) but with twelve quadrupoles after the injection section, the variation of the backward muon fluxes with the change of the aperture of the straight section is calculated. Again, the drift length between quadrupoles is assumed zero and an exit window of 25 cm x 25 cm is used. The results are shown in Fig. 5.2 which indicate a rise in both backward total flux and muon peak with larger aperture. However, only a marginal increase in flux is obtained when the aperture increases from 10" to 12". Thus, the optimum aperture would be approximately 10" if one considers cost.

(c) Length

Using the optimum field and 10" aperture, the backward muon flux as a function of channel length is investigated. Assuming zero quadrupole spacing and an exit window area of 25 cm x 25 cm, the calculation results are displayed in Fig. 5.3 which also shows the corresponding pion-to-muon ratio for each case. It is to be noted that, after 10 or 12 quadrupoles, increasing the length does not result in significant increase in flux. Therefore, it is suggested that the optimum number of quadrupoles, bearing in mind the cost factor, is 12

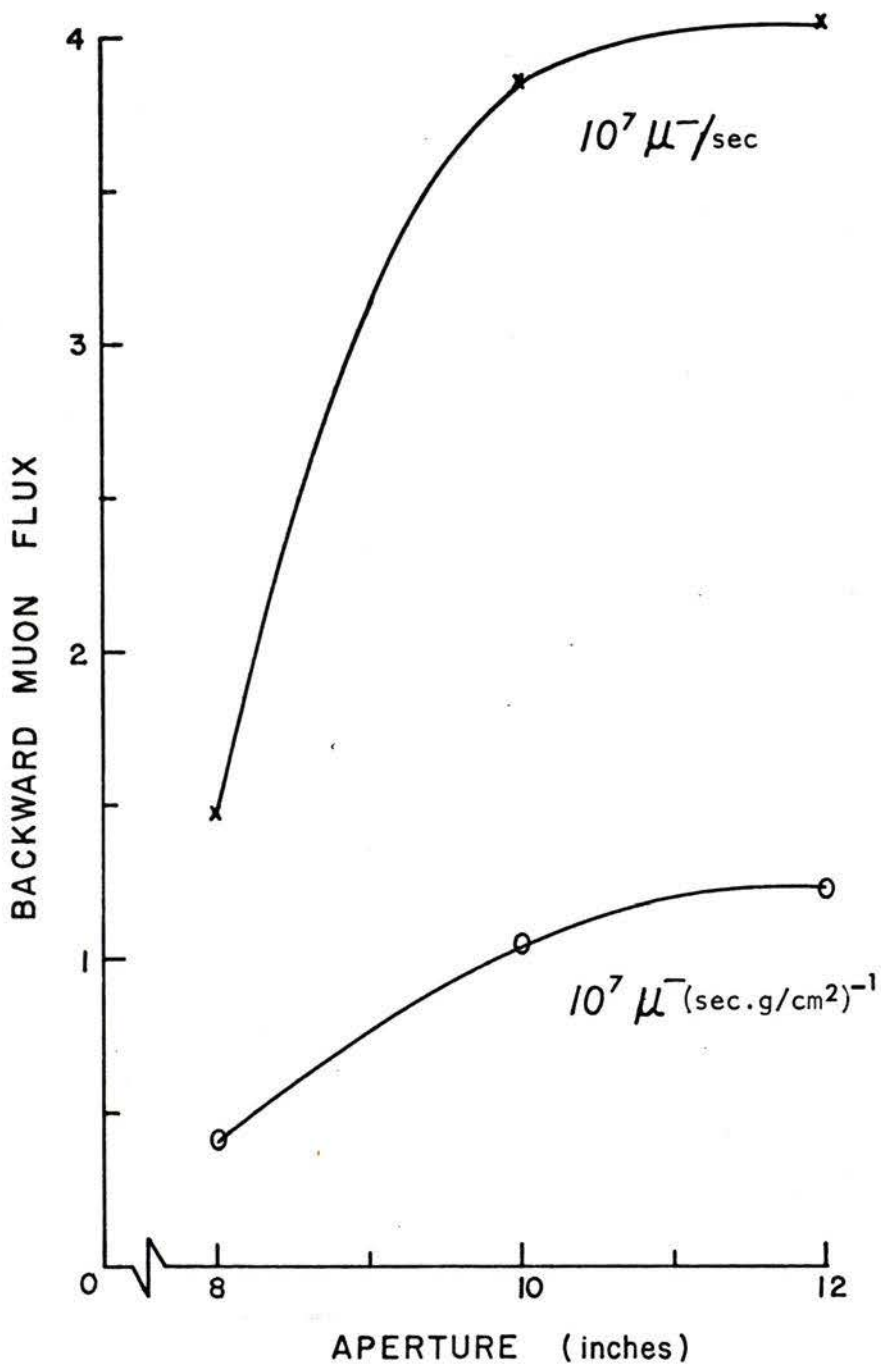


Fig. 5.2 Variation of backward muon flux with the quadrupoles aperture of the straight section. Yields are quoted for an area of 25 cm x 25 cm at the end of the straight section and for $p_0 = 160 \text{ MeV/c}$.

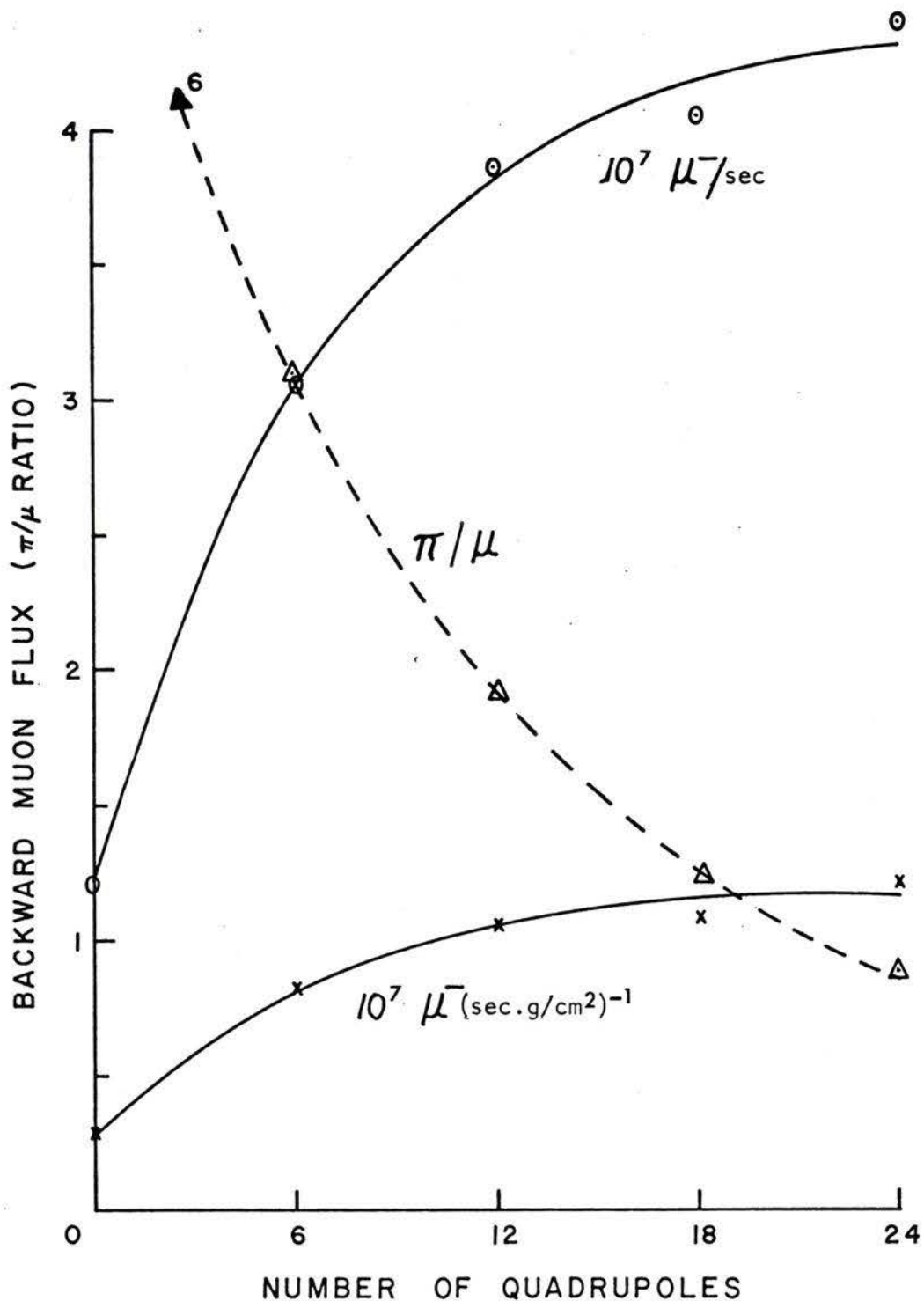


Fig. 5.3 Variation of backward muon flux with the total length of the straight section. Yields are quoted for an area of 25 cm x 25 cm at the end of the straight section and for $p_0 = 160 \text{ MeV}/c$.

corresponding to a 5 meter long straight section. However, since in practice a drift length of about 10 cm (depending on quadrupole design) is unavoidable, the length of the straight section is slightly over 6 meters. However, the pion-to-muon ratio continues to decrease, although at a slower rate, after 12 quadrupoles until it is less than 1 after 24 quadrupoles. When the channel is operated for collecting backward muons, this decrease in the ratio is not significant since the pion separation is almost complete.

When the channel is operated for forward muons, this factor is important since pion separation is more difficult and the muon flux diminishes as the pion contamination is reduced. The lower the pion-to-muon ratio, the smaller the reduction in the muon flux for a given contamination level.

5.3 Design of the Momentum Analyzing Section

The purpose of the analyzing system is to separate the pions, arriving at the end of the straight section, from the muons. The main criterion for the design, therefore, is to produce maximum spatial separation of the pions and the muons. This implies maximum momentum resolution and, consequently, maximum dispersion, which is determined mainly by the angle of bend and magnet length. The dispersion, produced by a single bending magnet, as a function of bending angle was calculated for three values of the magnet length. The results are shown in Fig. 5.4.

Separation of muons from the backward decay of pions does not require an elaborate analyzing system because the backward muon peak is well separated in momentum from the pion peak. On the other hand, the forward muon peak is almost coincident with the pion peak (see Fig. 5.6 and Fig. 5.10) and the pion cut-off is at 120 MeV/c for a central momentum of 100 MeV/c. Thus, the separation of forward muons is more difficult and requires a magnet with good resolution. Therefore, a 90° magnet, having an effective length of 1.0 m, is chosen providing a dispersion of about 1.8 cm per %. This is adequate for separating the forward muons (see Section 5.4.2).

Further calculation, however, indicates that if two 45° bends (with a length of 0.5 m each) are used instead of the single 90° bend, the dispersion increases with the separation of the two bends and is 2.14 cm per % for 0.6 m separation. If these two 45° magnets are made similar to those in the pion collection section (magnets M1 and M2 in Fig. 4.5), the total cost may be reduced because a single design is used.

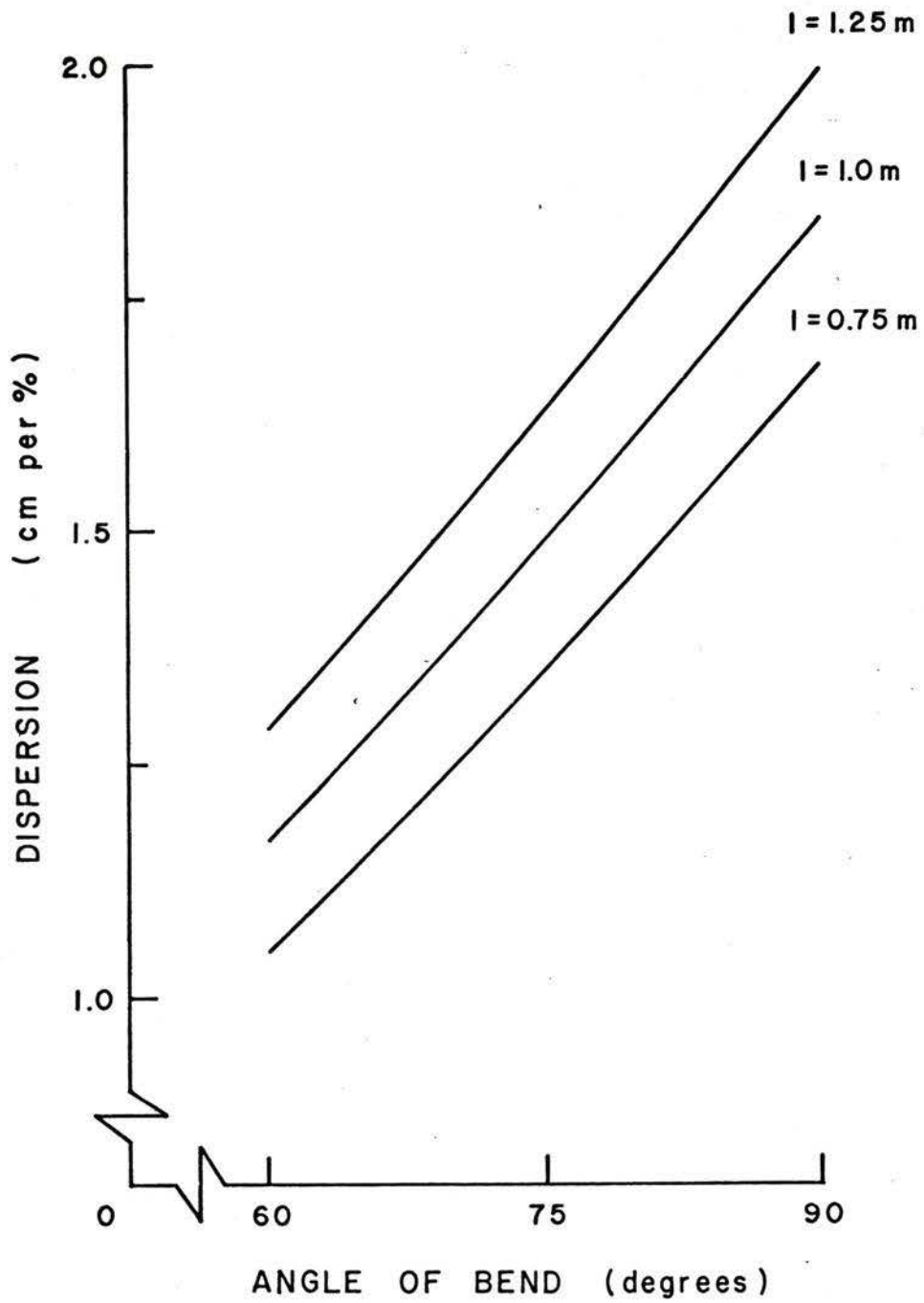


Fig. 5.4 Dispersion as a function of angle of bend for three values of the effective length l .

The gap of the analyzing magnet has been assumed to be 10" for the calculations presented in the next few sections. If this gap is reduced to 8", the reduction in the total muon flux is about 20% when the target area is assumed 25 cm x 25 cm and it is about 7% if the target area is assumed to be 10 cm x 10 cm. The reduction in the maximum stopping rate is 30% for the former and 40% for the latter case. The corresponding reduction in the magnet cost is 17%. Although a magnet with a 10" gap is preferable, the choice will depend on the availability of funds.

To focus the muon beam onto the stopping target, a quadrupole triplet is chosen. An x-focus can be obtained with a doublet but the beam size in the vertical plane becomes too large. A 10" aperture is selected for the quadrupoles in the triplet. A 12" aperture added only about 8% to the flux at the target which is insignificant. On the other hand, the cost of the 12" aperture triplet is about 30% higher than that for the 10" aperture triplet. The first element of the triplet should, however, be a narrow-type quadrupole so that it may be brought very close to the analyzing magnet to increase the acceptance.

5.4 Calculated Performance

The layout of the optimized system is shown in Fig. 5.5 indicating the three main sections. The yields quoted in this section are for a 100 μ A, 500 MeV proton beam on a 10 cm Be target and for an output beam cross section area of 25 cm x 25 cm unless stated otherwise.

5.4.1 Output Beam at the End of the Straight Section

With the pion collection section tuned for 160 MeV/c pions, the straight section was optimized to maximize the backward decay muons. The output momentum spectrum at the end of the straight section is shown in Fig. 5.6 indicating a backward muon peak at 82 MeV/c. The range spectrum is shown in Fig. 5.7 and the muon polarization in Fig. 5.8 and Fig. 5.9. The muon capture efficiency

$$\eta \equiv \frac{\text{total muon flux at channel exit}}{\text{total pion flux accepted by and decayed in the channel}}$$

is 11% for the combined pion collection and straight sections.

With the pion collection section tuned for 100 MeV/c, the straight section was optimized for forward muons. The output momentum spectrum is shown in Fig. 5.10, indicating a forward muon peak at about 100 MeV/c almost at the same position of the pions. The pion high momentum cut-off is at 120 MeV/c and pion-free muons with momenta above this value may be extracted. The range spectrum is shown in Fig. 5.11 which indicates that an 8.2 g/cm² thick C absorber may be placed here to

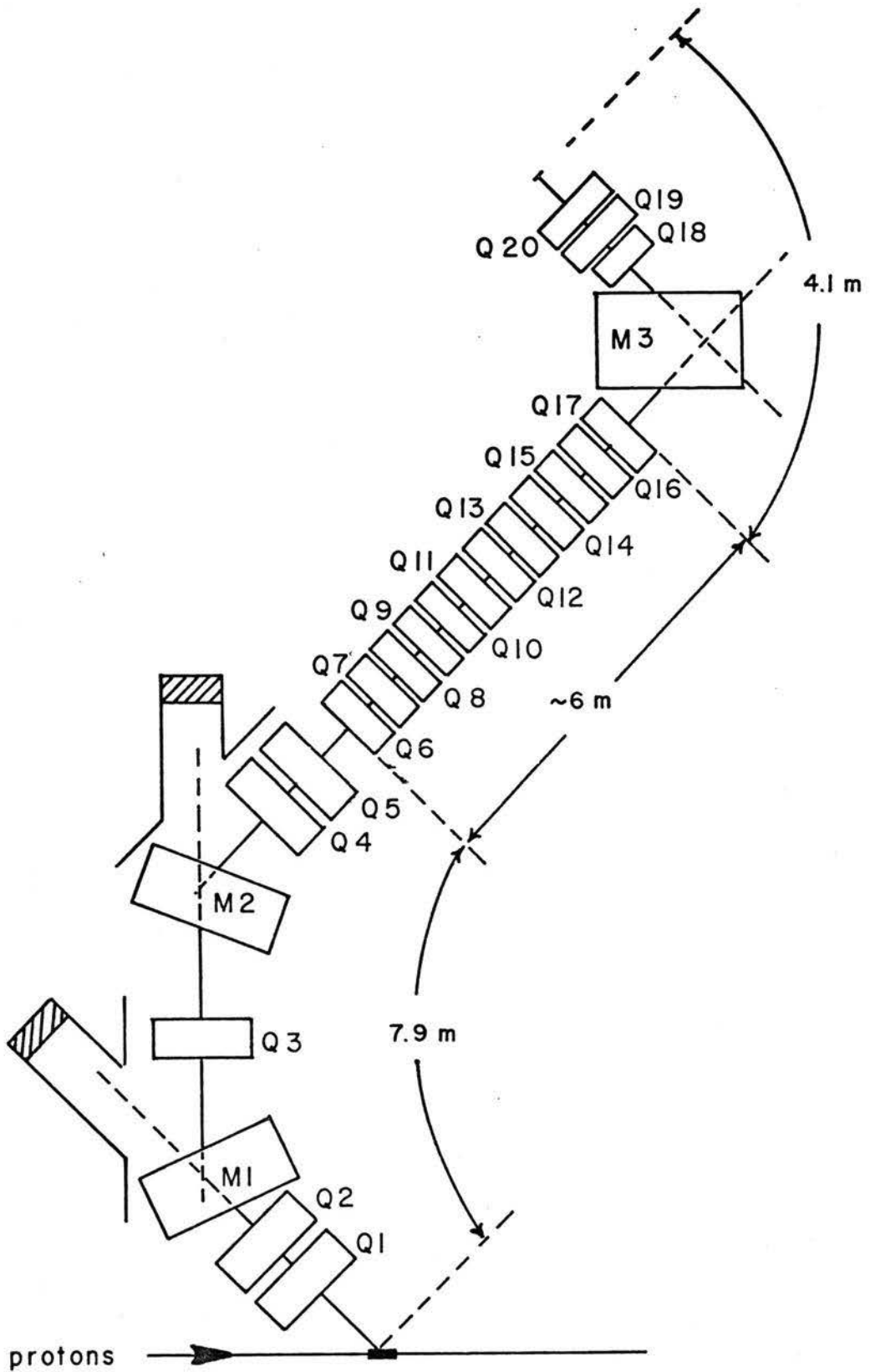


Fig. 5.5 Schematic layout of the complete muon channel (Phase One and Phase Two).

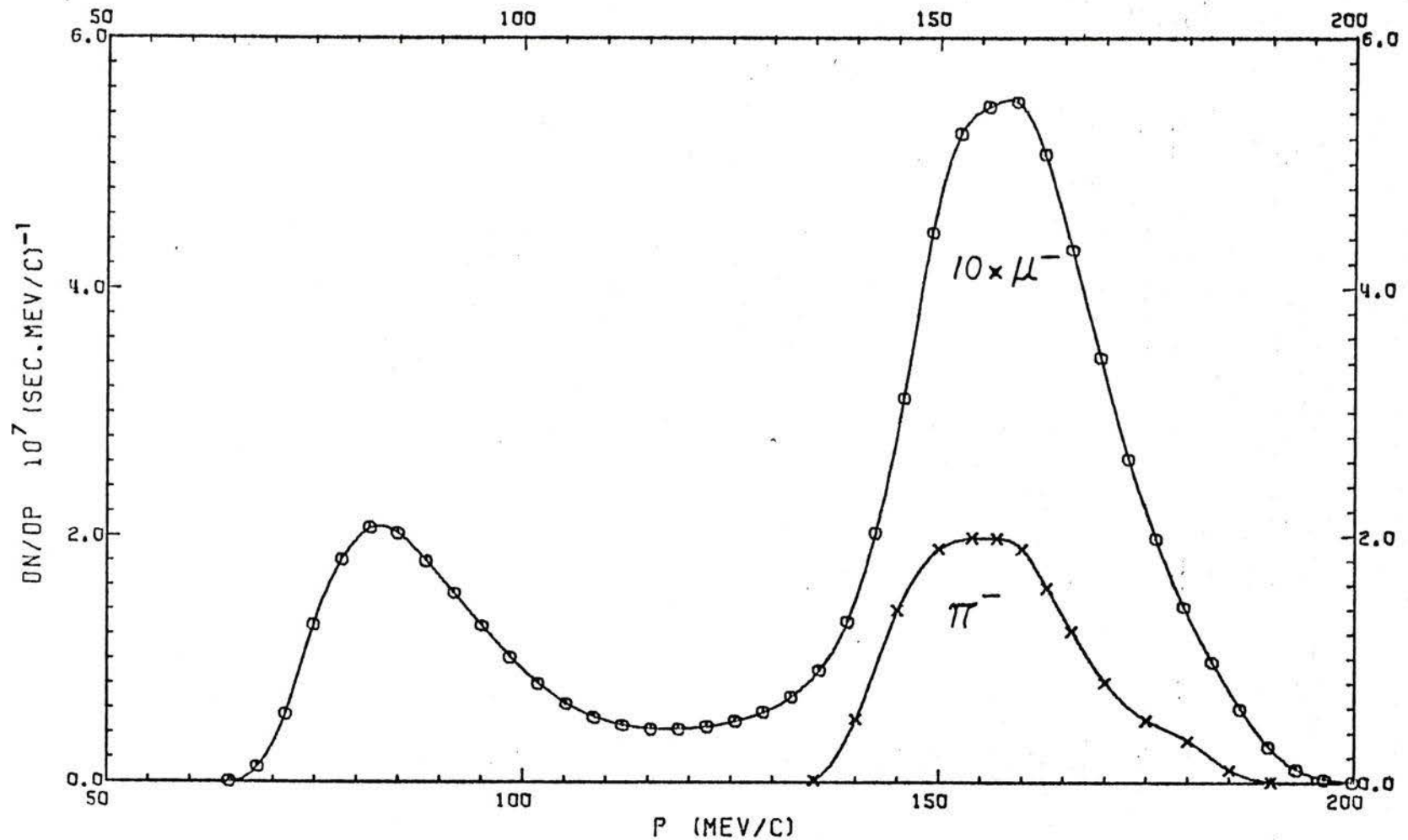


Fig. 5.6 Pion and muon momentum spectra at the end of the straight section for $p_0 = 160$ MeV/c and an area of 25 cm x 25 cm. The field gradient for the A.G. quadrupoles is 0.38 kGauss/cm.

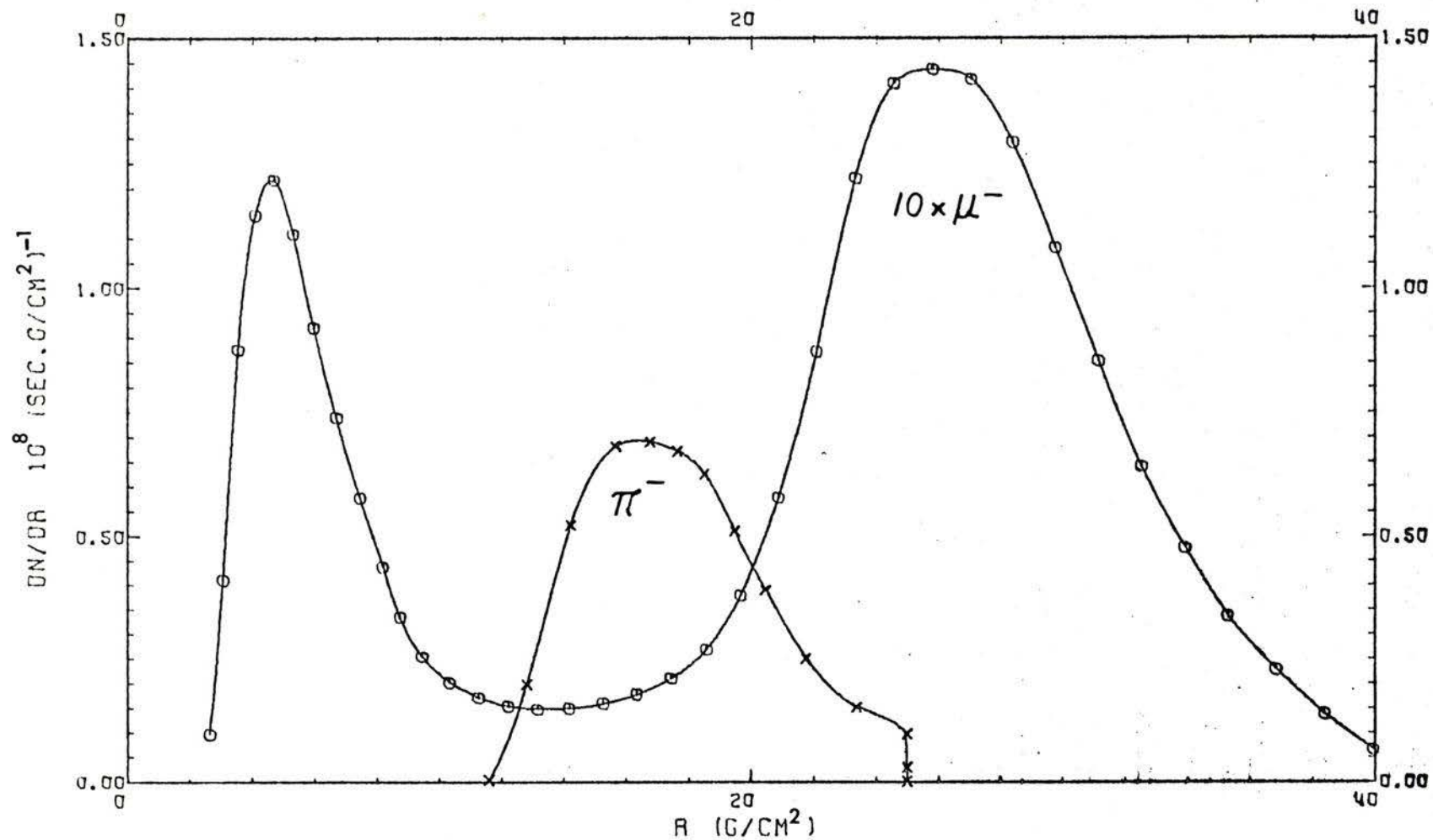


Fig. 5.7 Pion and muon range spectra at the end of the straight section for $p_0 = 160 \text{ MeV}/c$ and an area of $25 \text{ cm} \times 25 \text{ cm}$. The field gradient for the A.G. quadrupoles is $0.38 \text{ kGauss}/\text{cm}$.

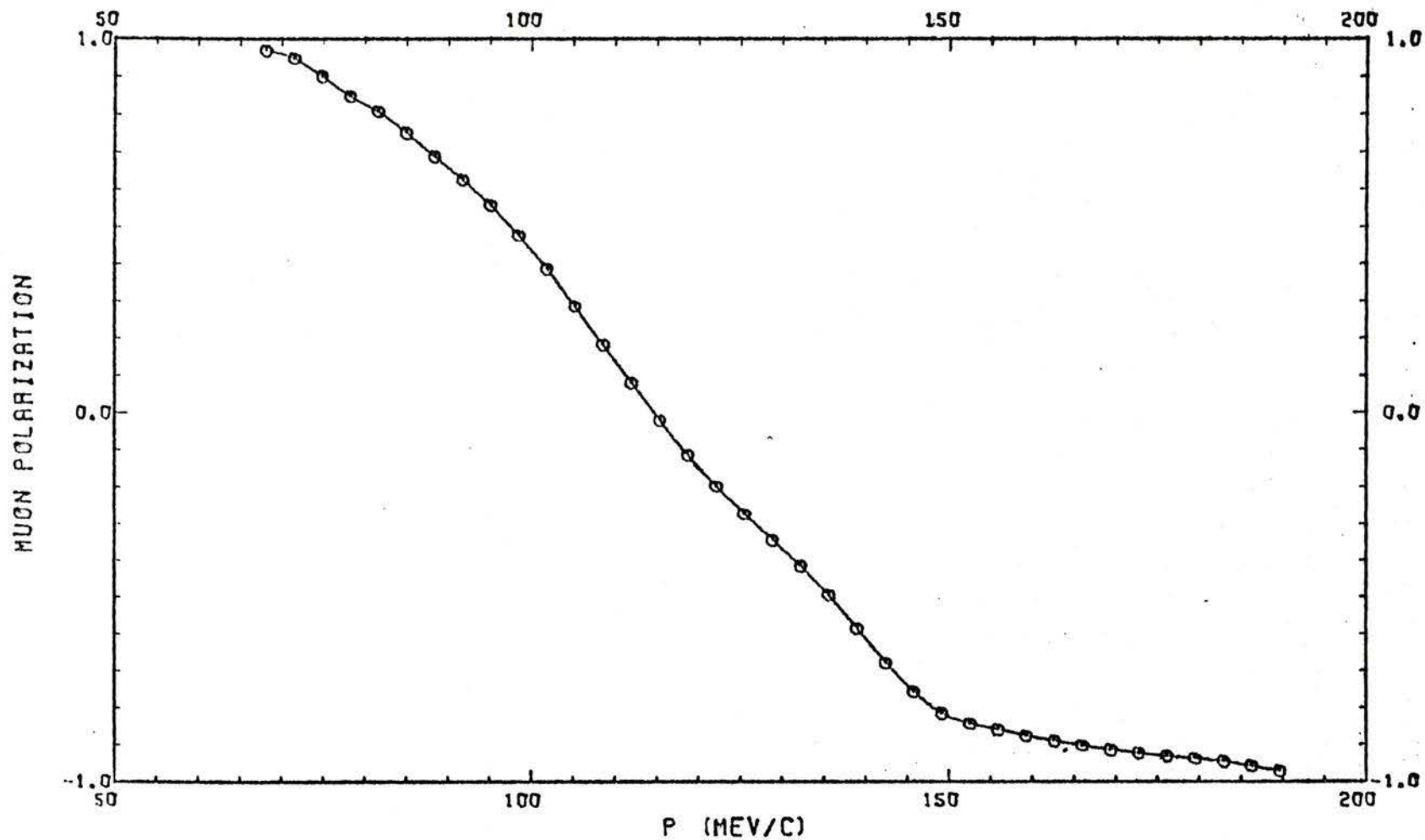


Fig. 5.8 Muon polarization at the end of the straight section as a function of momentum for $p_0 = 160$ MeV/c with the channel set up as for Fig. 5.6.

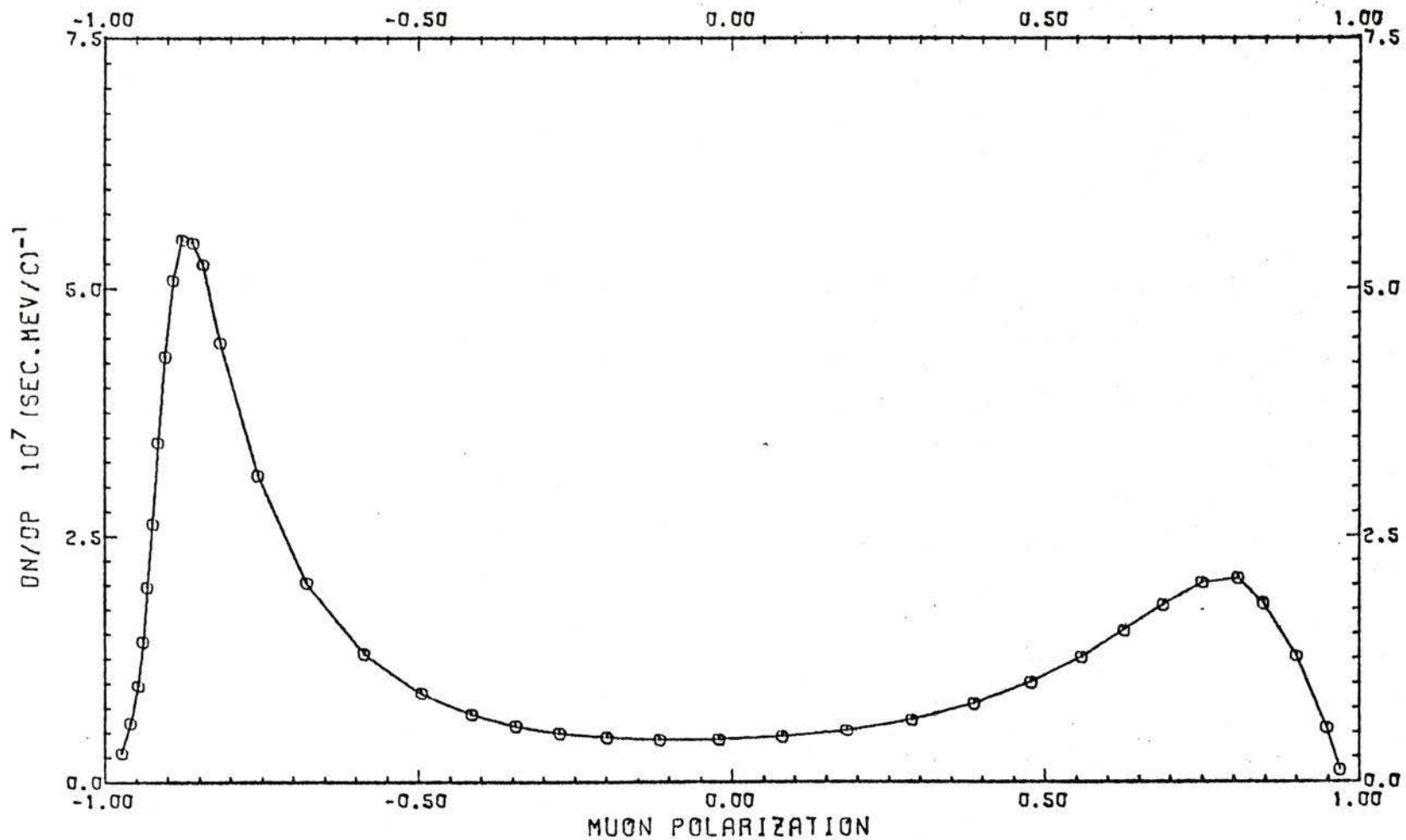


Fig. 5.9 Muon flux of a given polarization versus polarization at the end of the straight section for $p_0 = 160$ MeV/c and an A.G. field gradient of 0.38 kGauss/cm. Fluxes are quoted for an area of 25 cm x 25 cm.

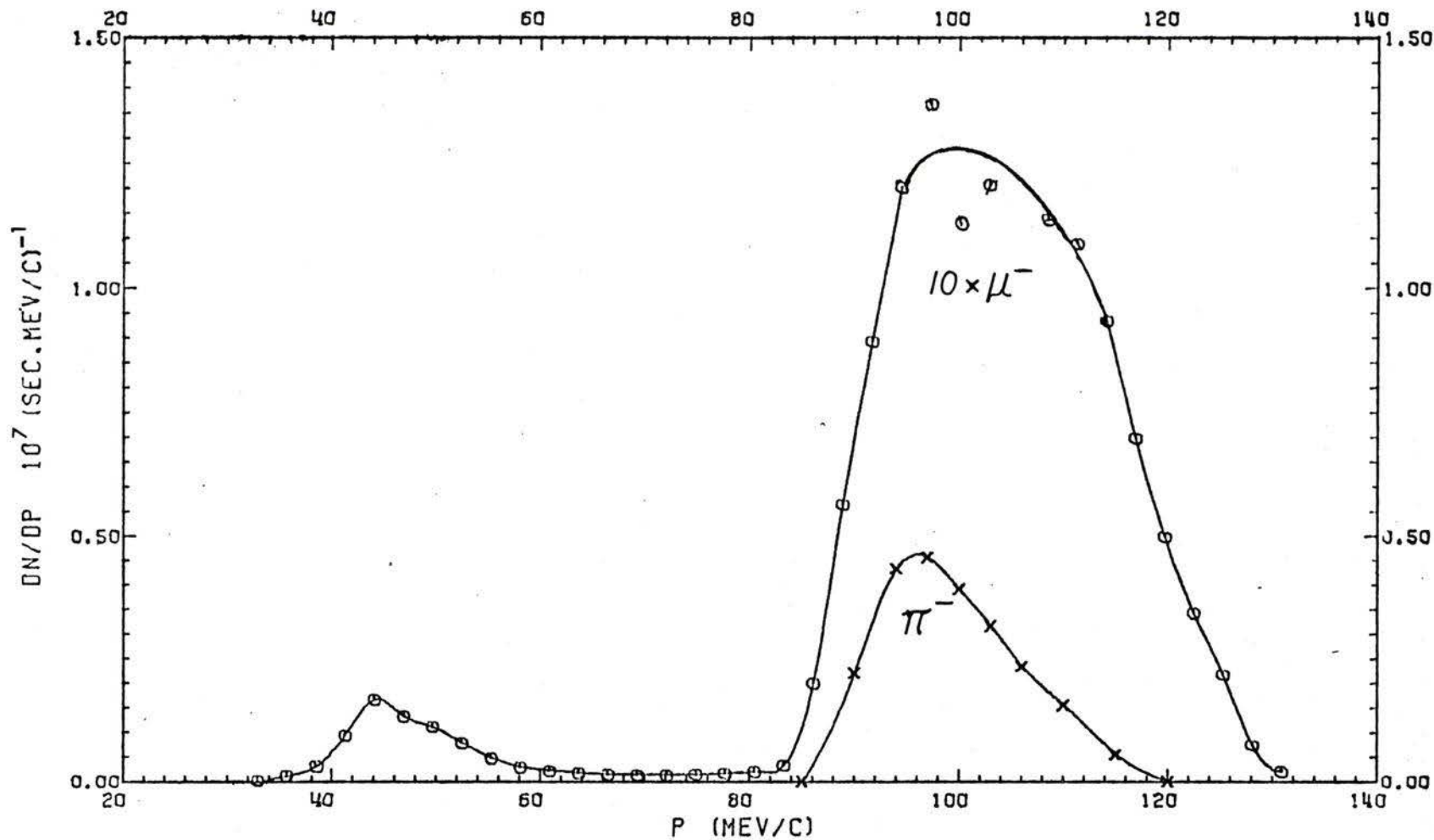


Fig. 5.10 Pion and muon momentum spectra at the end of the straight section for $p_0 = 100$ MeV/c and an area of 25 cm x 25 cm. The field gradient for the A.G. quadrupoles is 0.24 kGauss/cm.

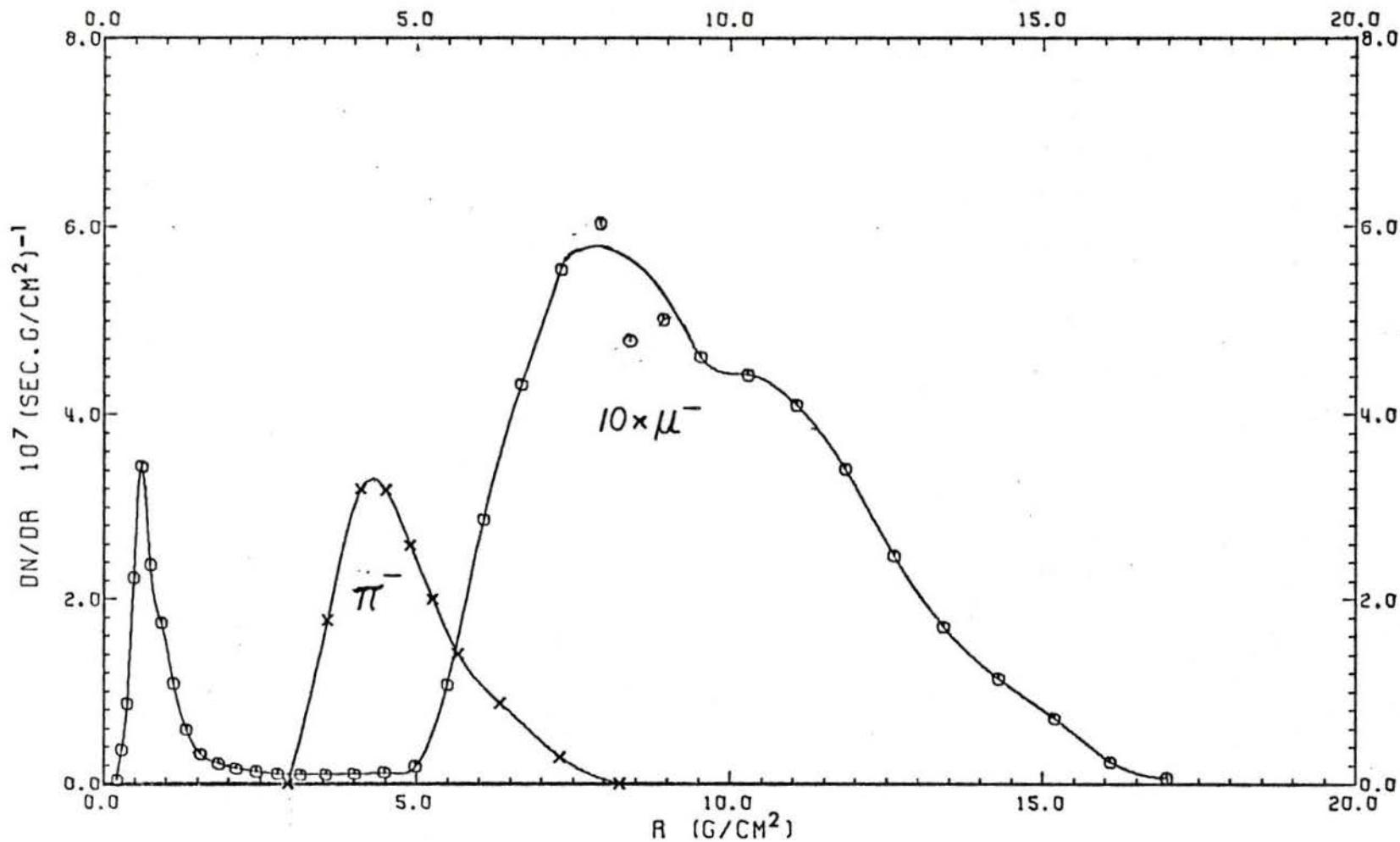


Fig. 5.11 Pion and muon range spectra at the end of the straight section for $p_0 = 100$ MeV/c and an area of 25 cm x 25 cm. The field gradient for the A.G. quadrupoles is 0.24 kGauss/cm.

stop almost all the pions and all the backward muons. The resulting muon beam may then be transported through the analyzing section to reduce background from the absorber. The muon polarization as a function of muon momentum is shown in Fig. 5.12.

The yields for the cases discussed above are summarized in Table 5.1 together with estimated polarization. These yields are for negative muons; positive muon yields are about three to four times larger.

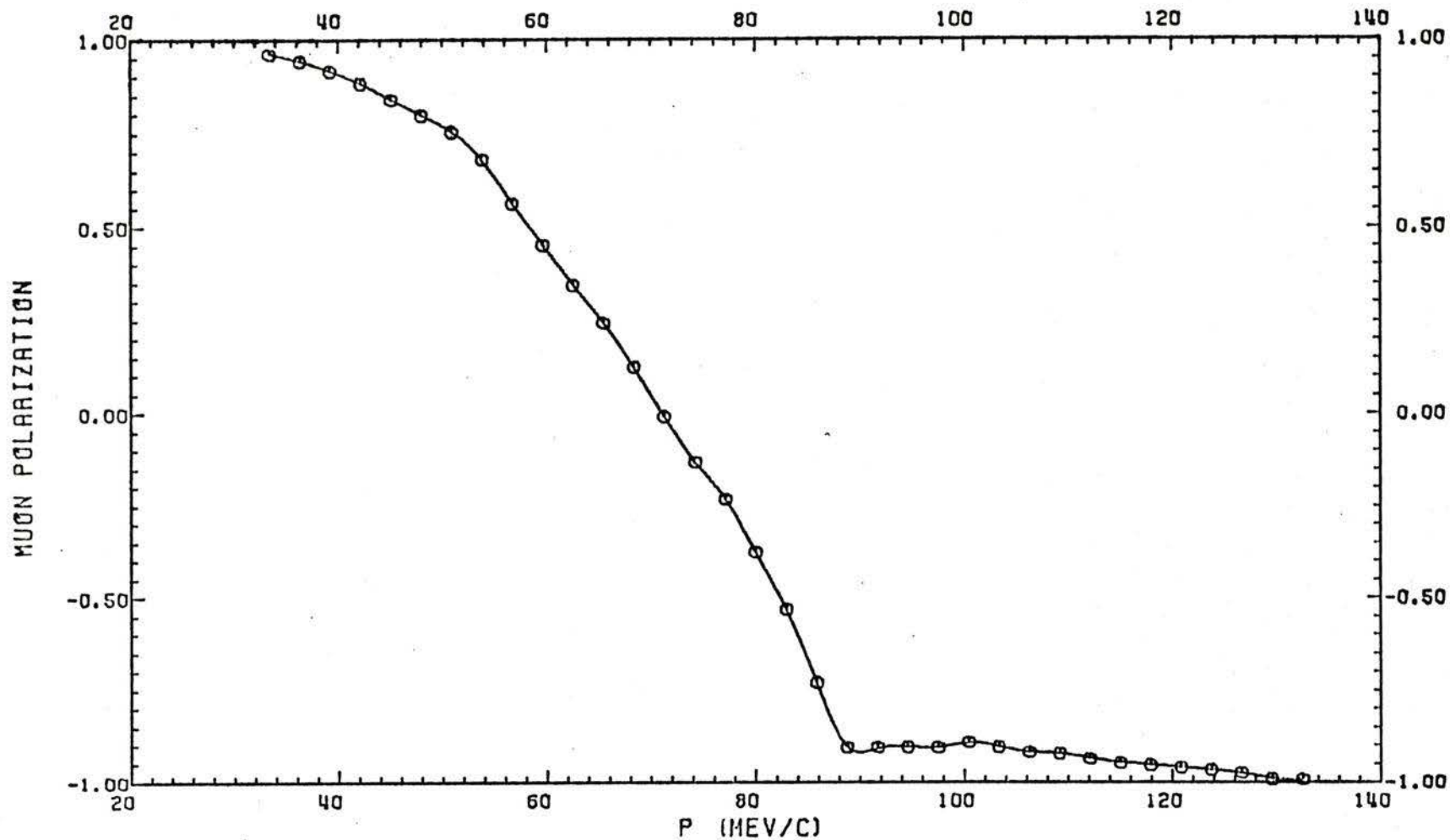


Fig. 5.12 Muon polarization at the end of the straight section as a function of momentum for $p_0 = 100$ MeV/c with the channel set up as for Fig. 5.10.

Table 5.1

Muon Beam Characteristics at the End of the Straight Section

	<u>$p_o = 160 \text{ MeV/c}$</u>	<u>$p_o = 100 \text{ MeV/c}$</u>
	Backward Decay:	Forward Decay:
Total flux μ^-/sec in 25 cm x 25 cm	2.3×10^8	3.8×10^7
Maximum flux $\mu^- (\text{sec} \cdot \text{MeV/c})^{-1}$	2.1×10^6 at 82 MeV/c	1.4×10^6 at 97 MeV/c
Stopping density $\mu^- (\text{sec} \cdot \text{g/cm}^2)^{-1}$	1.2×10^7 at 82 MeV/c	6.0×10^6 at 97 MeV/c
Muon polarization	> 65% for muons with momenta less than 92 MeV/c	> 97% for muons with momenta greater than 120 MeV/c

5.4.2 Output Beam After the Analyzing Magnet

As shown in Fig. 5.6, the backward muon peak is at 82 MeV/c. The analyzing magnet is tuned to this momentum. The field gradient of the A.G. quadrupoles is 0.38 kGauss/cm in order to improve the match. The output momentum spectrum is shown in Fig. 5.13 and the range spectrum in Fig. 5.14. The muon polarization is shown in Fig. 5.15 as a function of momentum. The total muon flux integrated over a 25 cm x 25 cm area is $1.3 \times 10^7 \mu^-/\text{sec}$.

For forward muons, the analyzing magnet is tuned to 132 MeV/c to accept the pion-free muons with momenta higher than 120 MeV/c as indicated in Fig. 5.10. The field gradient of the A.G. section is set to 0.24 kGauss/cm. The output momentum spectrum is shown in Fig. 5.16 and the range spectrum in Fig. 5.17. The muon polarization as a function of momentum is shown in Fig. 5.18. The total muon flux integrated over a 25 cm x 25 cm area is $1.4 \times 10^6 \mu^-/\text{sec}$. If some degree of pion contamination is permitted, a higher muon flux can be obtained. Thus if the analyzing magnet is tuned to 130 MeV/c, $2.1 \times 10^6 \mu^-/\text{sec}$ are obtained with a pion contamination of 2.5%. An even higher flux can be obtained if the pions are separated by ranging. Thus, as seen from Fig. 5.11, if an 8.2 g/cm² carbon absorber is placed at the end of the straight section, all the pions will be stopped but $2.4 \times 10^7 \mu^-/\text{sec}$ will pass through the absorber. The peak of the transmitted muons will have a momentum of about 45 MeV/c.

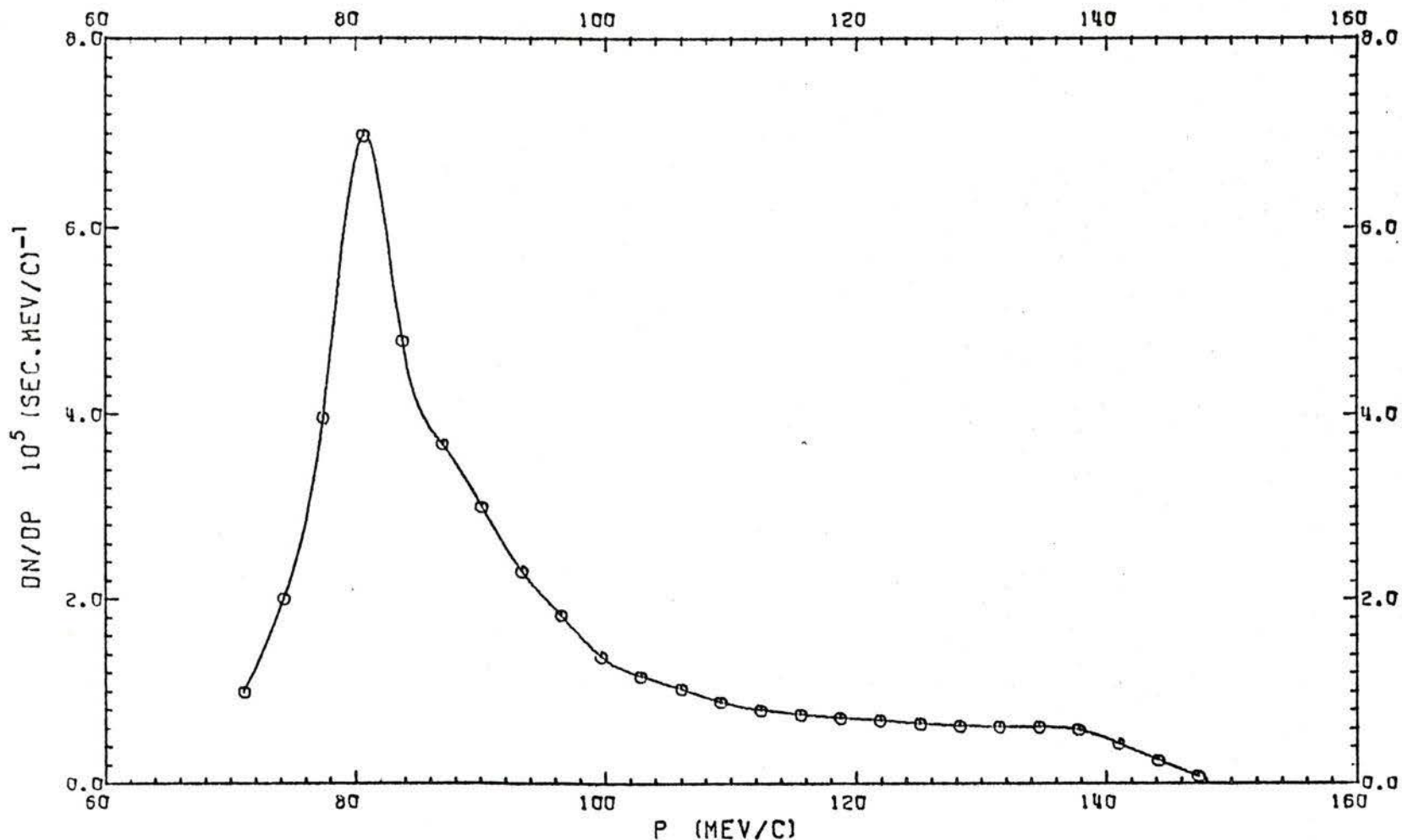


Fig. 5.13 Muon momentum spectrum after the straight section and the 90° analyzing magnet. The magnet is tuned to 82 MeV/c for backward muons. The pion collection section is tuned to 160 MeV/c and the gradient of the straight section is 0.38 kGauss/cm with the gradient of the last two quadrupoles reduced to 0.32 kGauss/cm. Fluxes are integrated over an area of 25 cm x 25 cm.

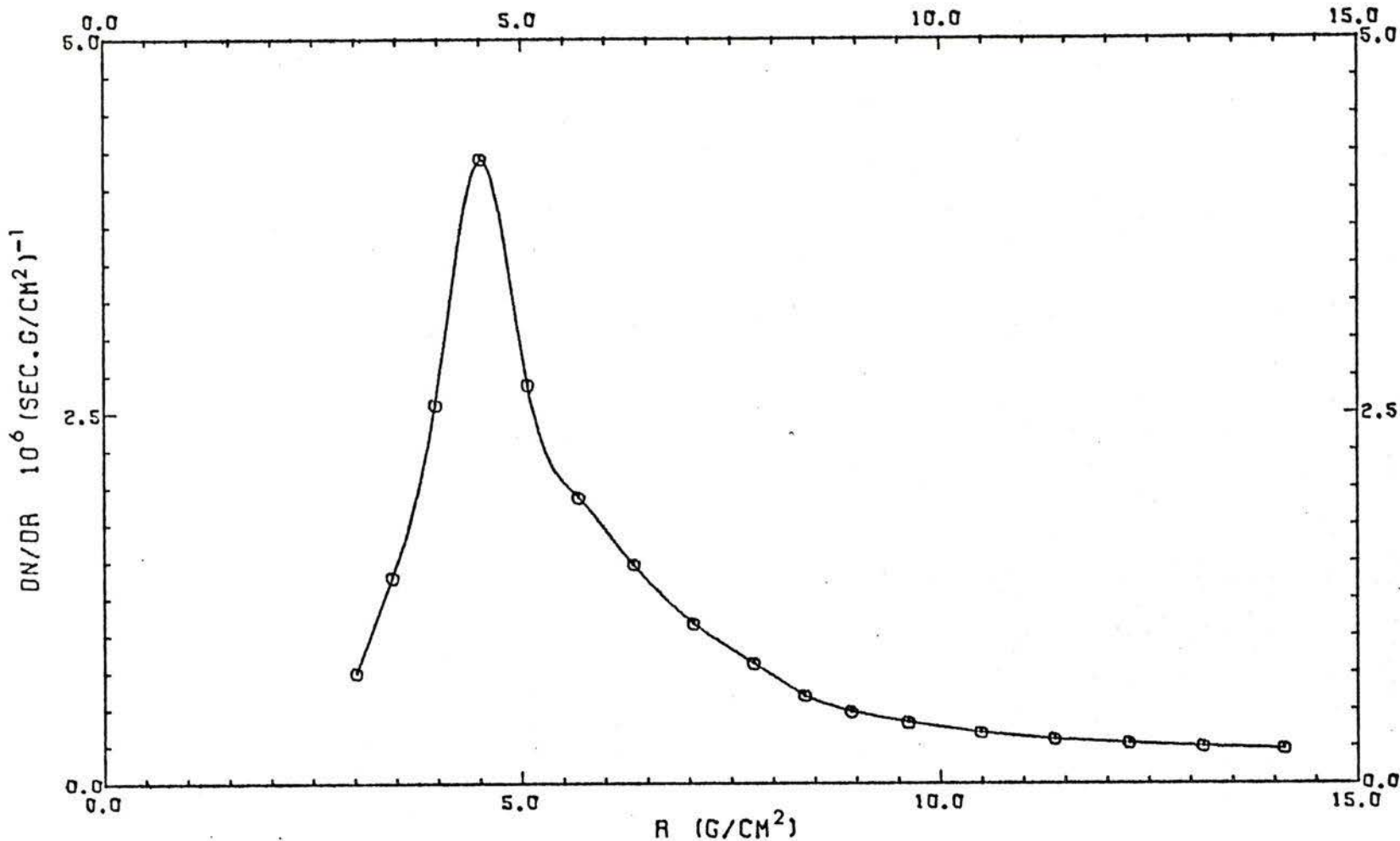
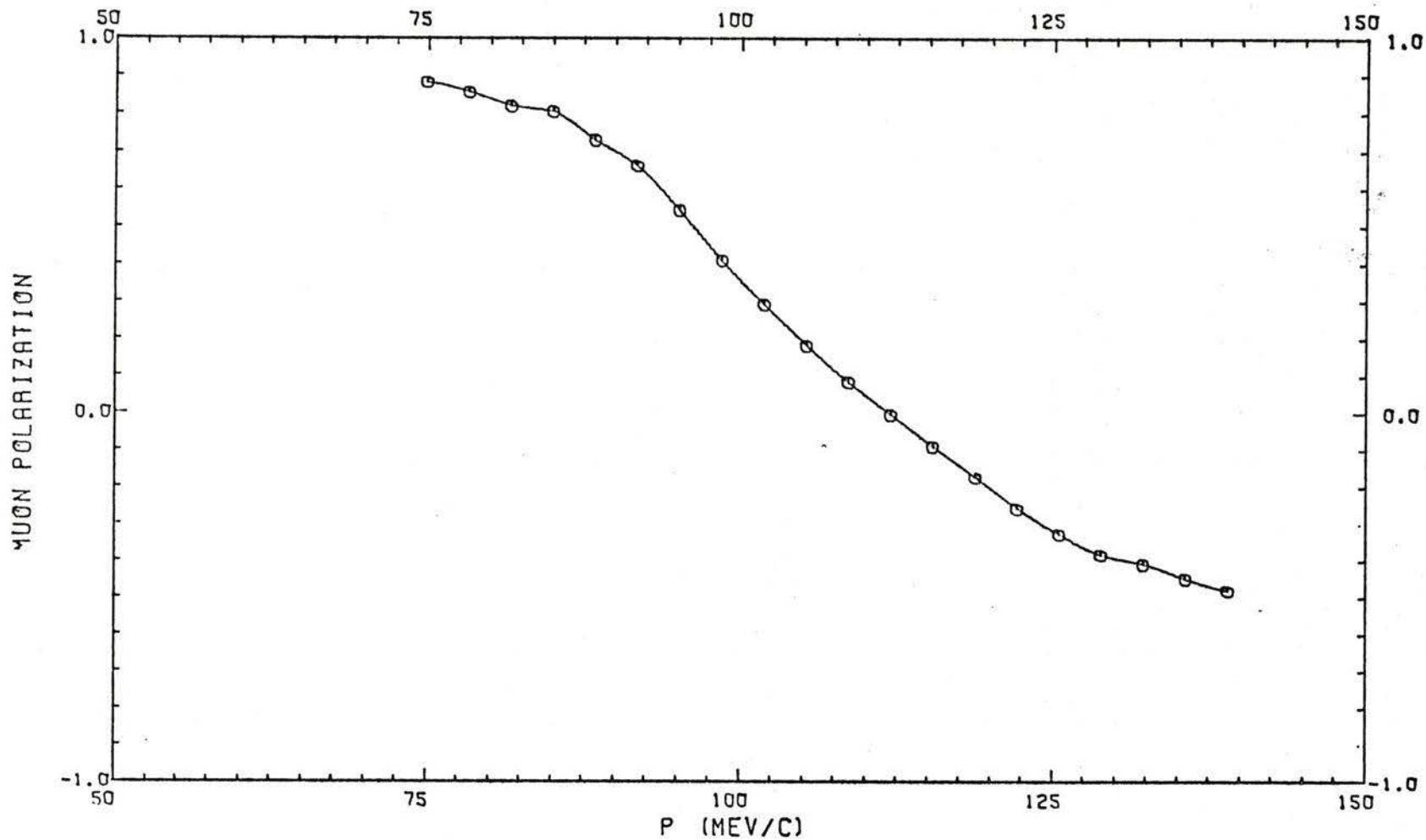


Fig. 5.14 Muon range spectrum after the straight section and the 90° analyzing magnet. The magnet is tuned to 82 MeV/c for backward muons. The pion collection section is tuned to 160 MeV/c and the gradient of the straight section is 0.38 kGauss/cm with the gradient of the last two quadrupoles reduced to 0.32 kGauss/cm. Fluxes are integrated over an area of 25 cm x 25 cm.



- 156 -

Fig. 5.15 Muon polarization as a function of momentum after the straight section and the 90° analyzing magnet with the channel set up as for Fig. 5.13.

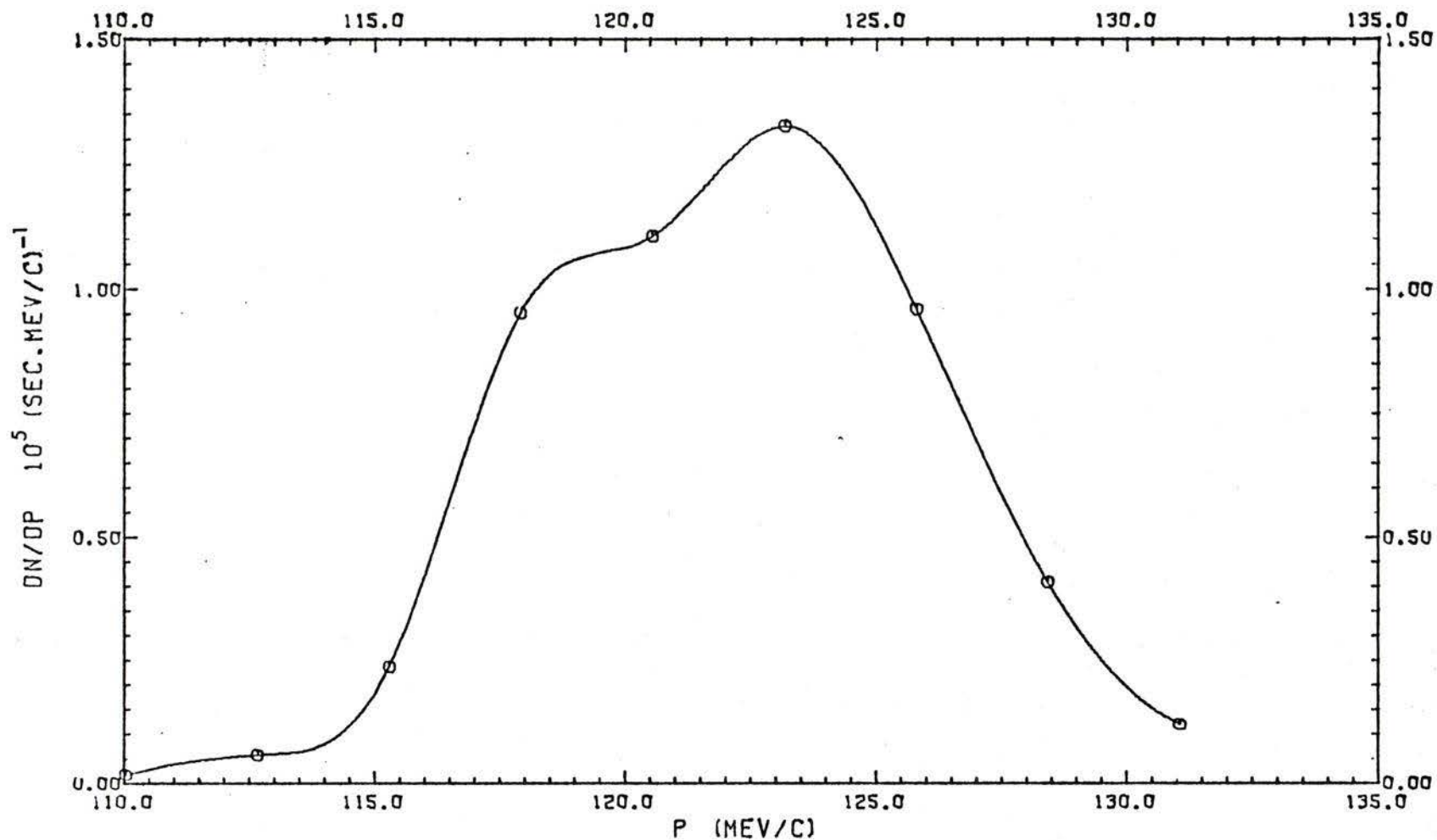


Fig. 5.16 Muon momentum spectrum after the straight section and the 90° analyzing magnet. The magnet is tuned to 132 MeV/c for forward muons. The pion collection section is tuned to 100 MeV/c and the gradient of the straight section is 0.24 kGauss/cm.

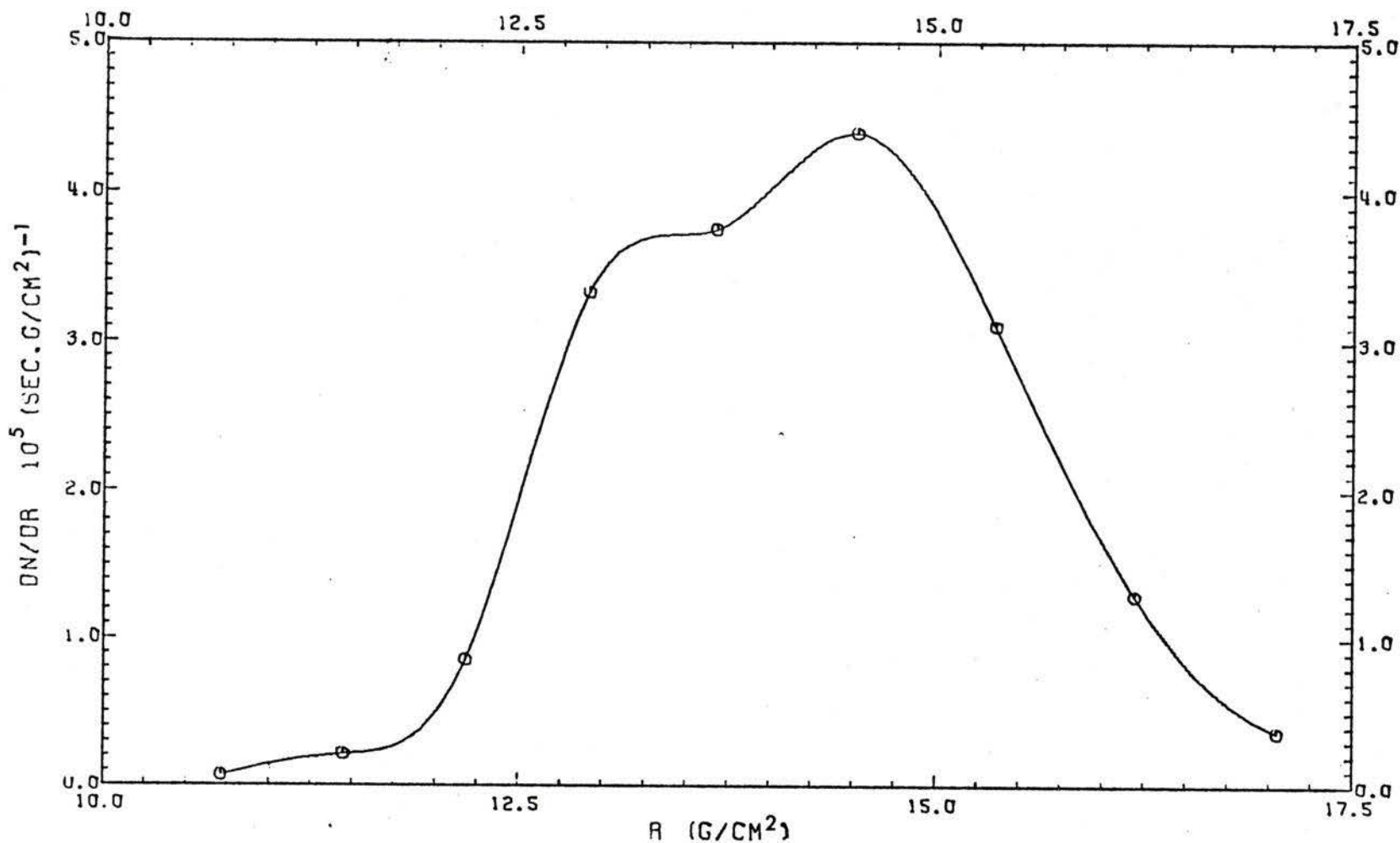


Fig. 5.17 Muon range spectrum after the straight section and the 90° analyzing magnet. The magnet is tuned to 132 MeV/c for forward muons. The pion collection section is tuned to 100 MeV/c and the gradient of the straight section is 0.24 kGauss/cm.

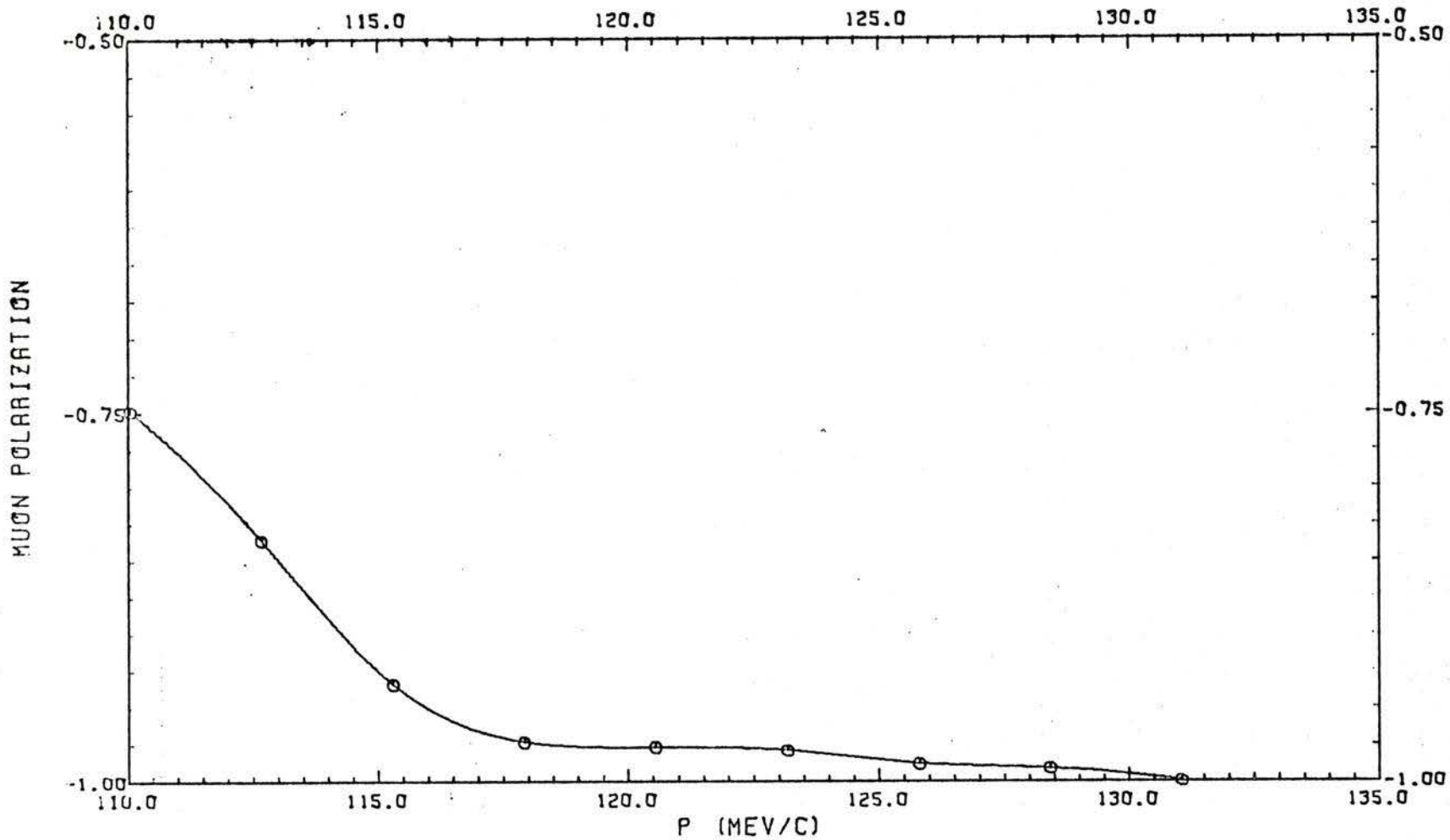


Fig. 5.18 Muon polarization as a function of momentum after the straight section and the 90° analyzing magnet with the channel set up as for Fig. 5.16.

5.4.3 Output Beam at the Stopping Target

The gradients of the quadrupoles in the triplet following the analyzing magnet are optimized to focus the muons onto the stopping target. However, because of the excessive computing time required for the calculation of fluxes for the complete channel, the optimization is rather crude and the fluxes reported here can be improved upon with further optimization.

With the pion collection section tuned for 160 MeV/c pions and the A.G. and analyzing sections set to collect backward muons, the momentum spectrum, range spectrum, and muon polarization are shown in Fig. 5.19, Fig. 5.20 and Fig. 5.21 respectively. With the pion collection section tuned for 100 MeV/c muons and the rest of the channel set to collect forward muons, the corresponding spectra are shown in Fig. 5.22 and Fig. 5.23, and the muon polarization is shown in Fig. 5.24. A summary of the fluxes and average polarization for the various cases is given in Table 5.2. The flux for the forward muons is small but an average polarization greater than 95% is obtained. To obtain higher flux of high energy muons, if required at all, the pions should be separated by ranging at the end of the straight section and the analyzing section used to reduce background particles generated in the pion absorber.

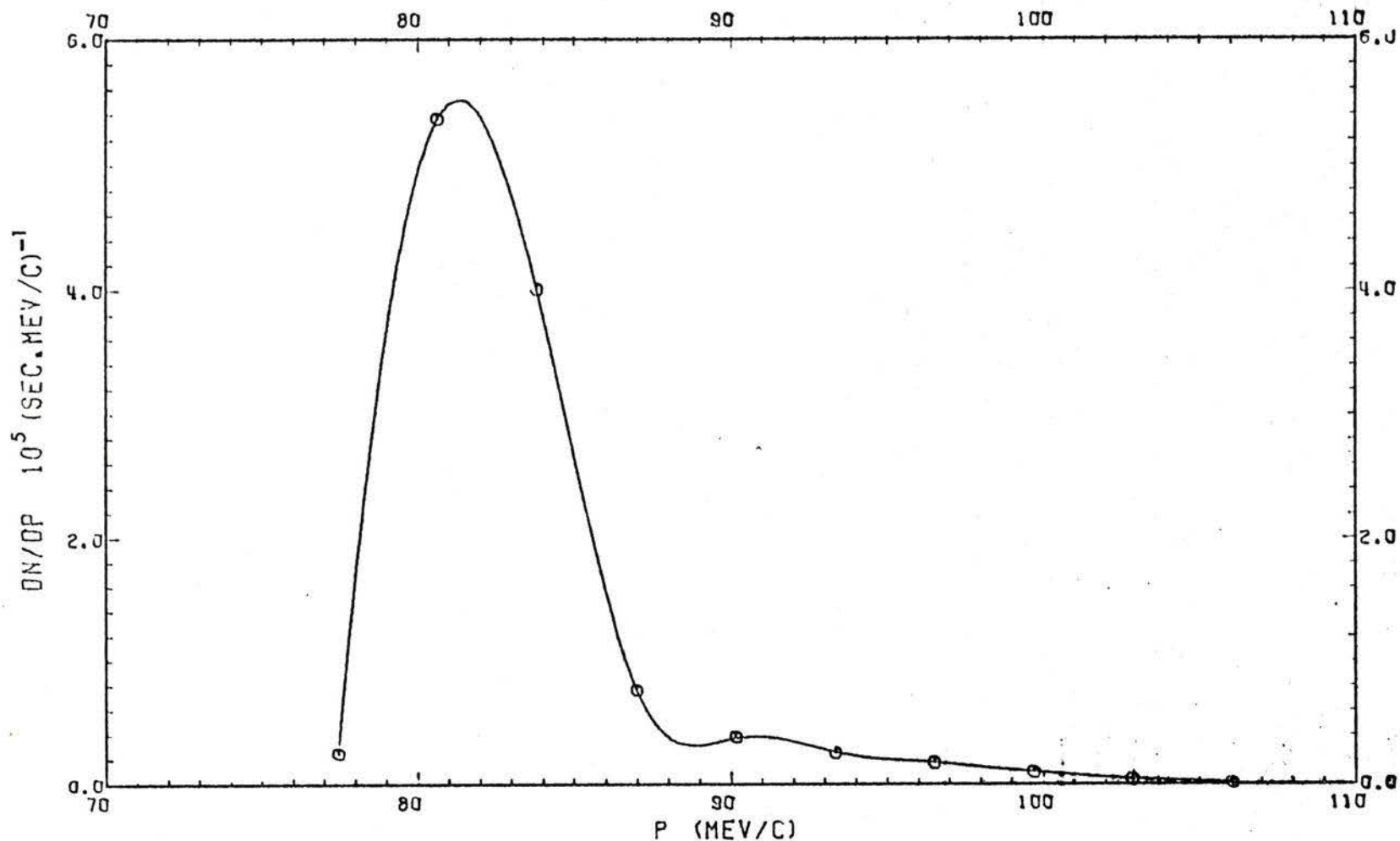


Fig. 5.19 Muon momentum spectrum at the stopping target. The magnet is tuned to 82 MeV/c for backward muons. The pion collection section is tuned to 160 MeV/c and the gradient of the straight section is 0.38 kGauss/cm except for Q16 and Q17 which have a gradient of 0.32 kGauss/cm. The gradients of final triplet were 0.164, 0.182, and 0.173 for Q18, Q19 and Q20 respectively. Fluxes are integrated over a 25 cm x 25 cm area.

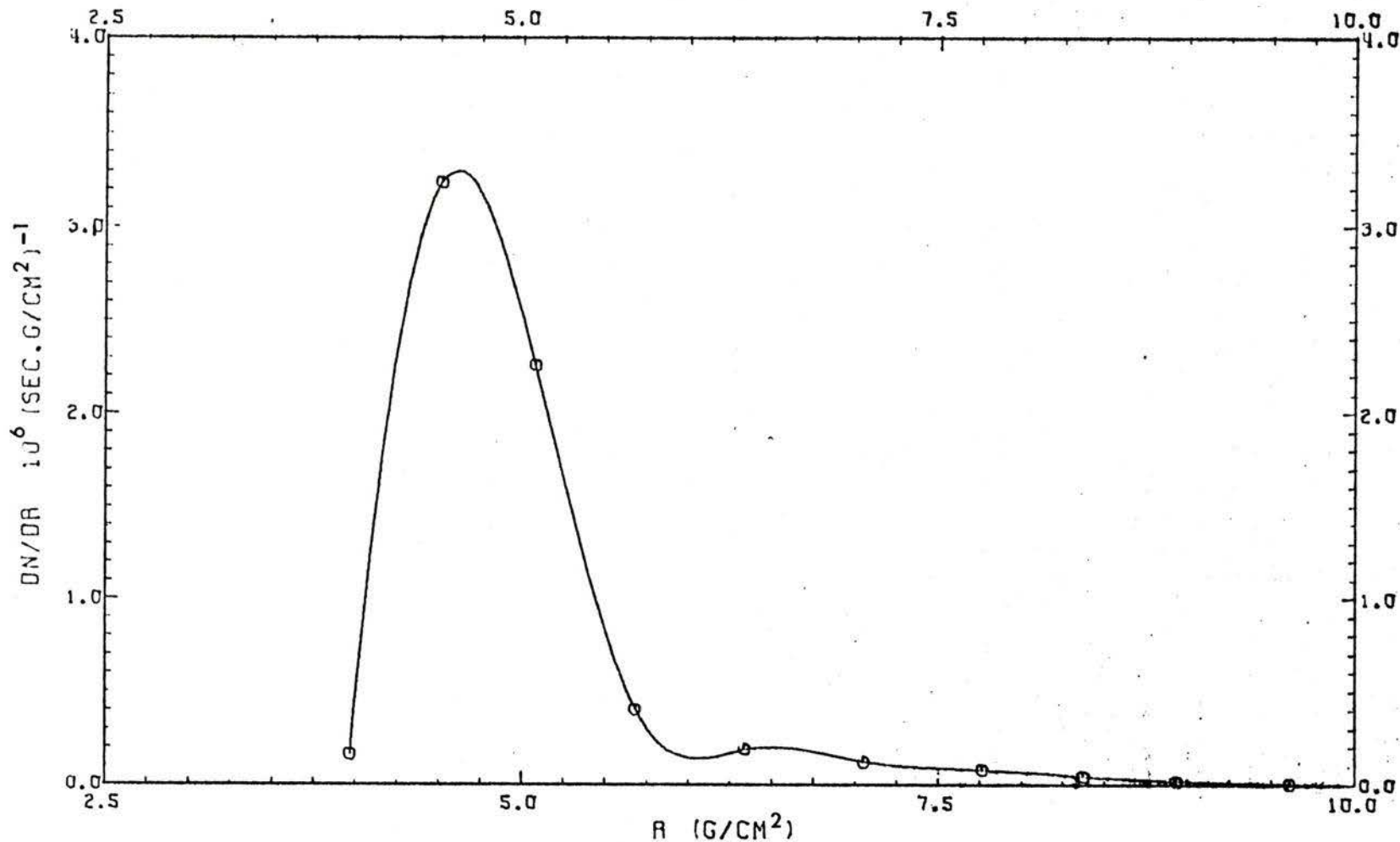


Fig. 5.20 Muon range spectrum at the stopping target. The magnet is tuned to 82 MeV/c for backward muons. The pion collection section is tuned to 160 MeV/c and the gradient of the straight section is 0.38 kGauss/cm except for Q16 and Q17 which have a gradient of 0.32 kGauss/cm. The gradients of final triplet were 0.164, 0.182, and 0.173 for Q18, Q19 and Q20 respectively. Fluxes are integrated over a 25 cm x 25 cm area.

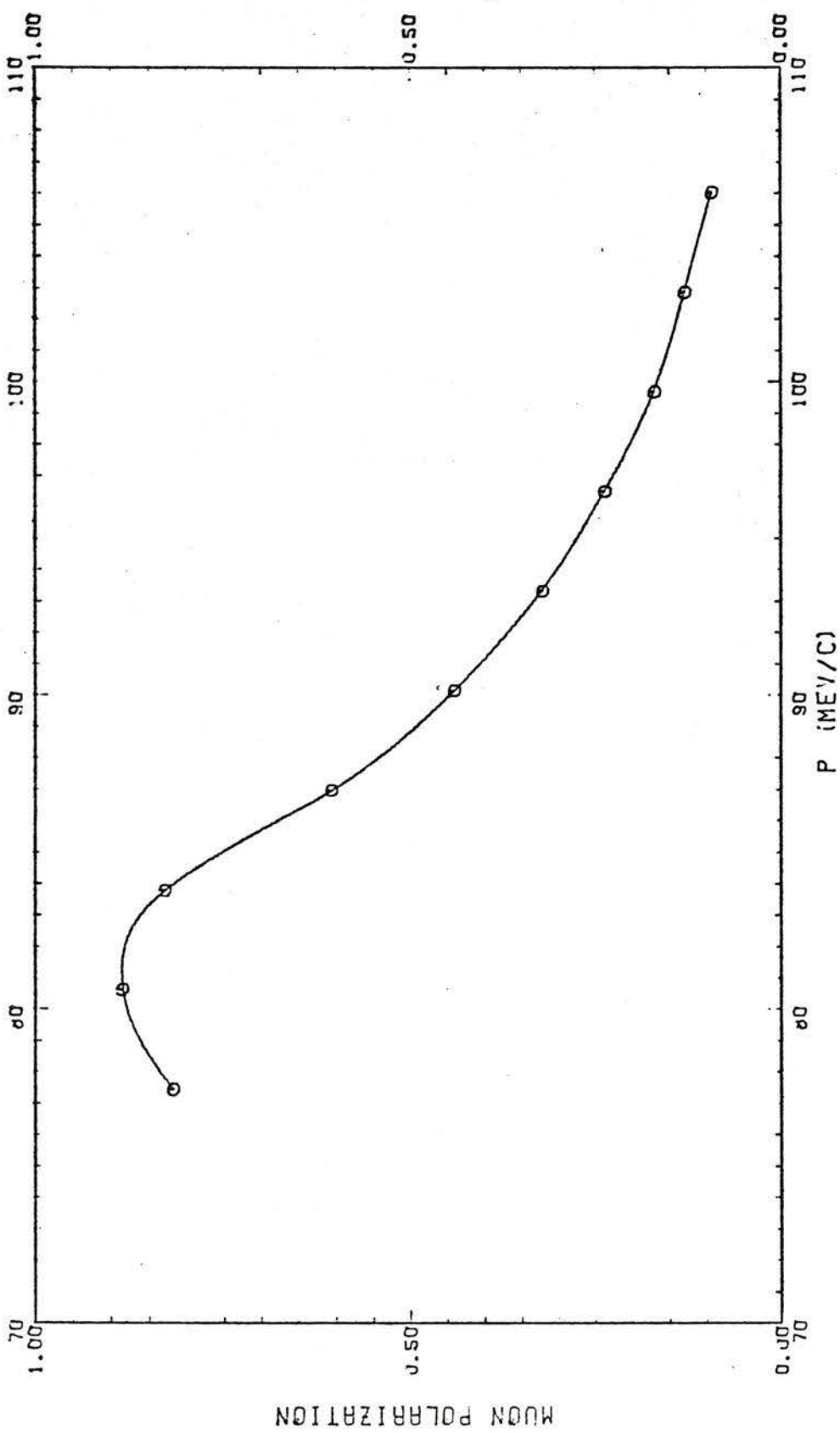


Fig. 5.21 Muon polarization as a function of momentum at the stopping target with the channel set as for Fig. 5.19.

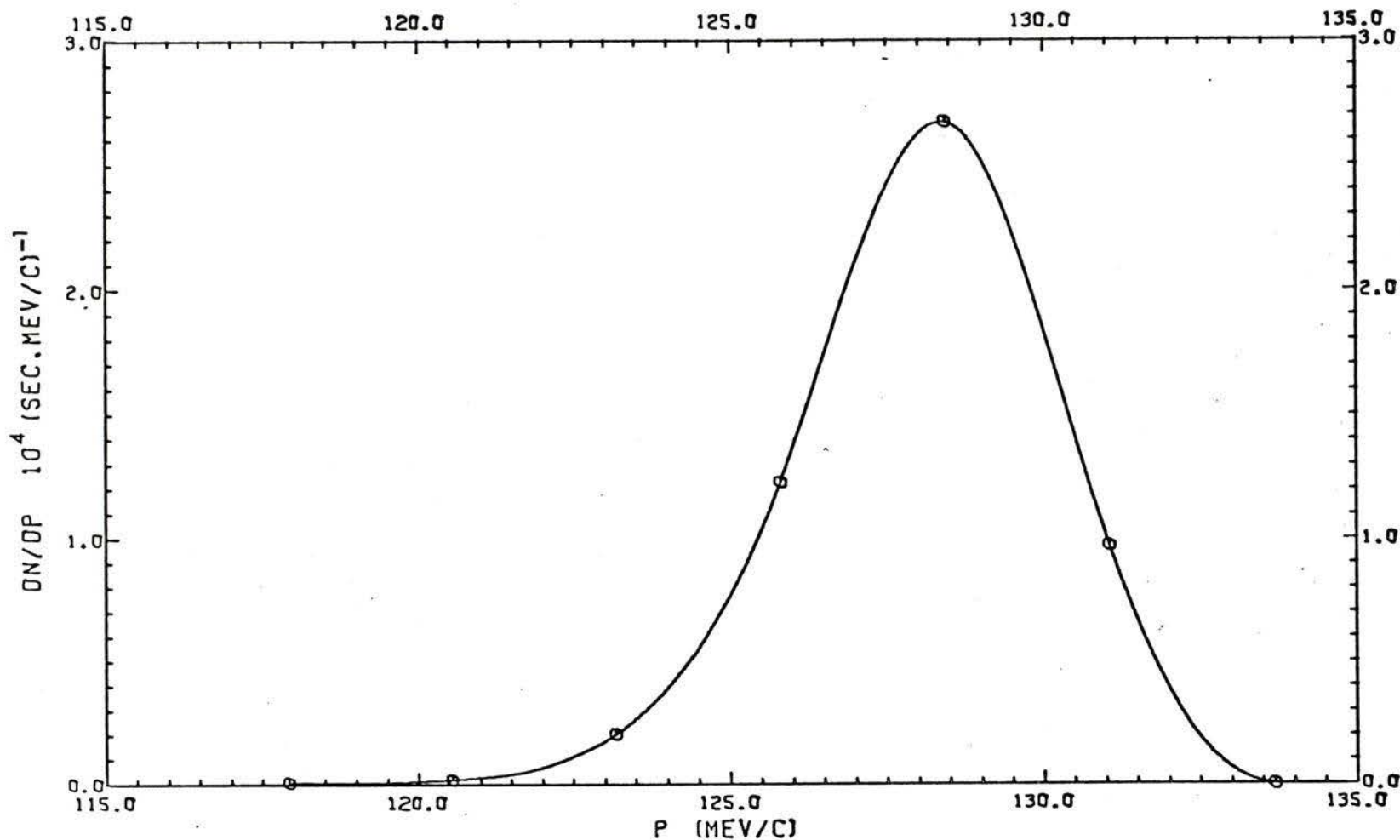


Fig. 5.22 Muon momentum spectrum at the stopping target. The magnet is tuned to 132 MeV/c for forward muons. The pion collection section is tuned to 100 MeV/c and the gradient of the straight section is 0.24 kGauss/cm.

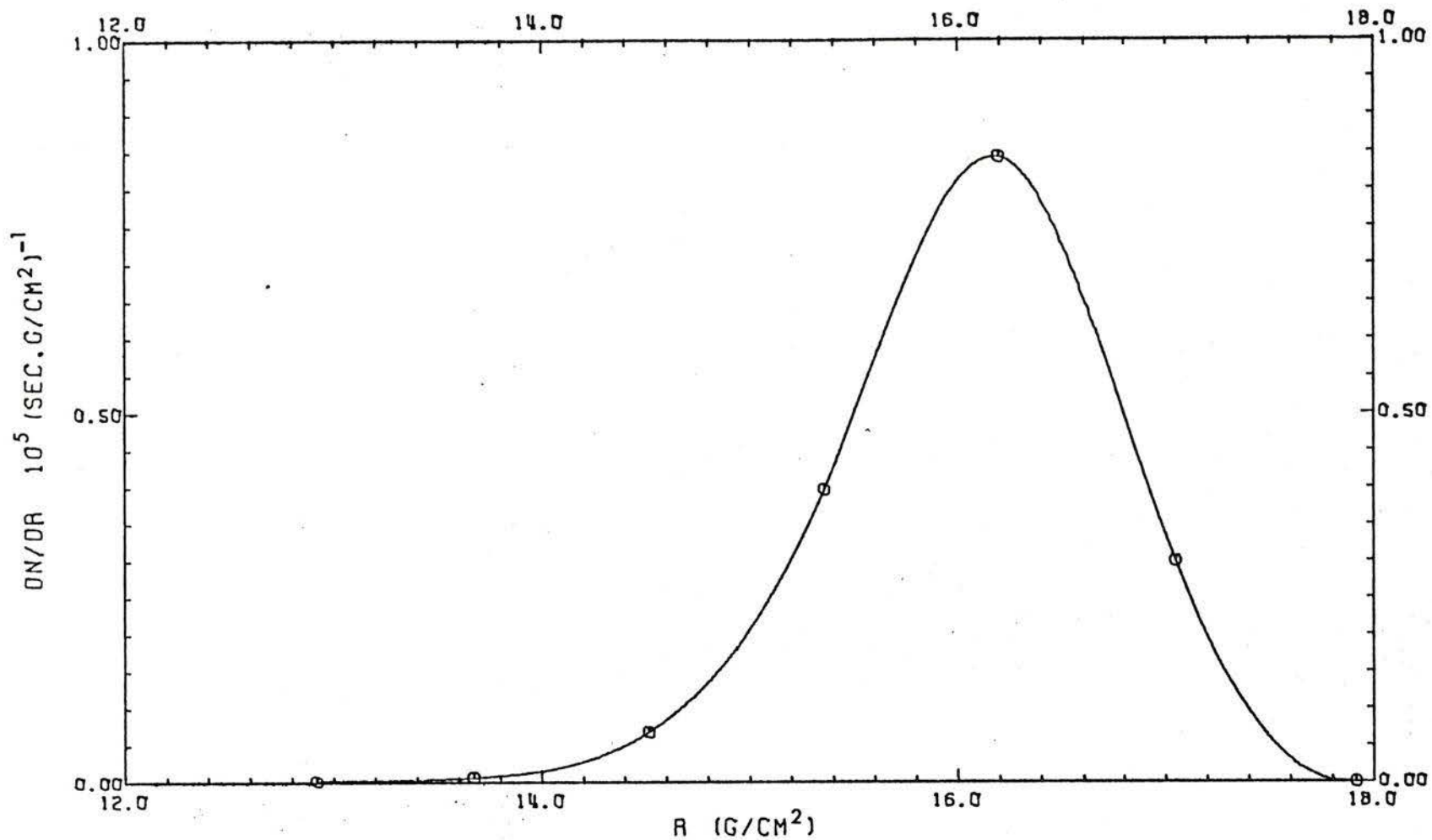


Fig. 5.23 Muon range spectrum at the stopping target. The magnet is tuned to 132 MeV/c for forward muons. The pion collection section is tuned to 100 MeV/c and the gradient of the straight section is 0.24 kGauss/cm.

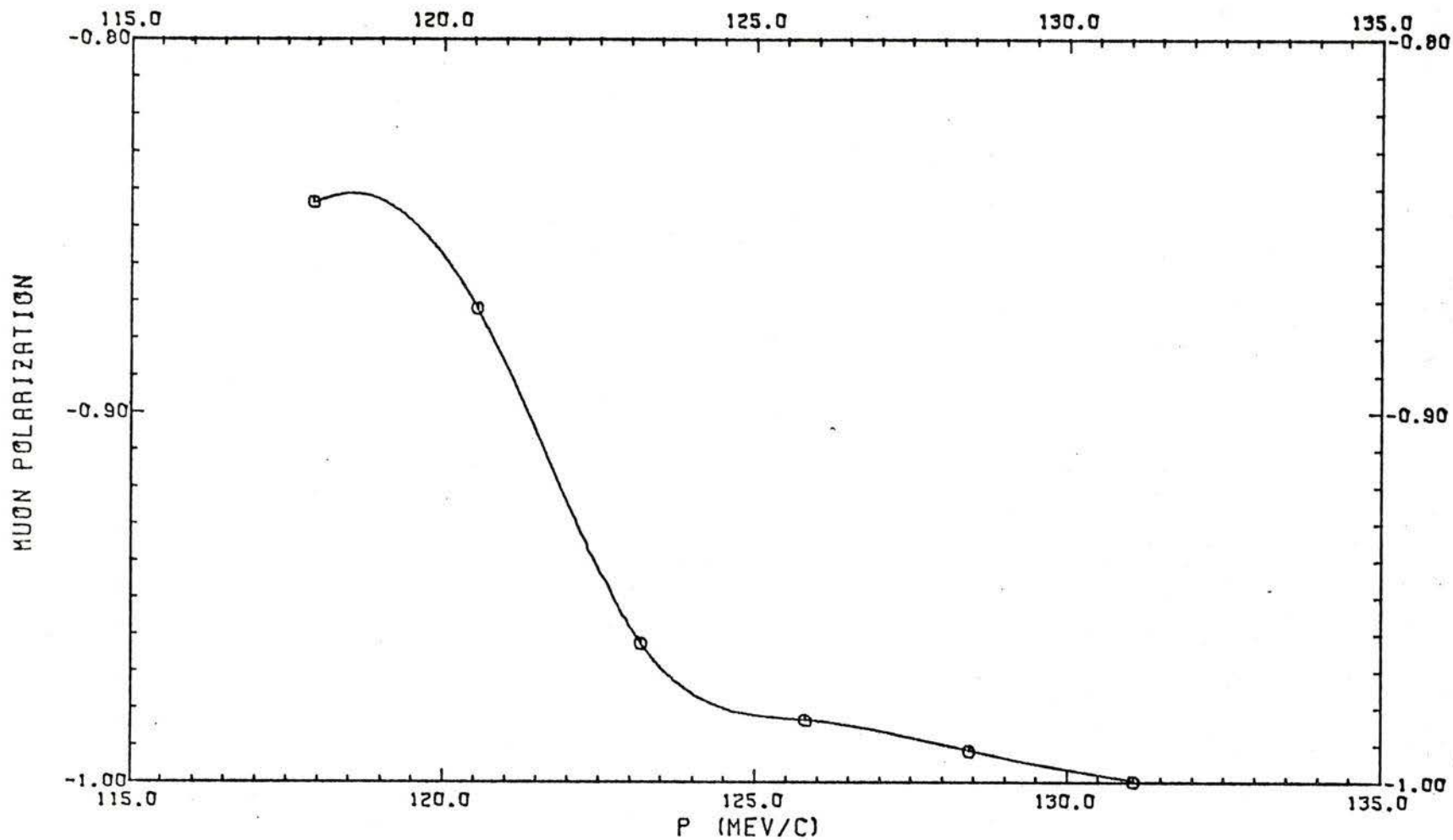


Fig. 5.24 Muon polarization as a function of momentum at the stopping target with the channel set as for Fig. 5.22.

Table 5.2

Muon Beam Characteristics at the Stopping Target

	<u>$p_0 = 160 \text{ MeV/c}$</u>		<u>$p_0 = 100 \text{ MeV/c}$</u>	
	<u>25 cm x 25 cm</u>	<u>10 cm x 10 cm</u>	<u>25 cm x 25 cm</u>	<u>10 cm x 10 cm</u>
Total flux μ^-/sec	3.6×10^6	1.3×10^6	1.4×10^5	5×10^4
Maximum flux $\mu^- (\text{sec} \cdot \text{MeV/c})^{-1}$	5.4×10^5	2.0×10^5 at 82 MeV/c	2.7×10^4	0.9×10^4
Stopping density $\mu^- (\text{sec} \cdot \text{g/cm}^2)^{-1}$	3.2×10^6	1.1×10^6 at 82 MeV/c	0.8×10^5	2.9×10^4
Muon polarization	44% < P_μ < 90% in the momentum range between 77 and 90 MeV/c		$P_\mu > 90\%$ for muons with momenta greater than 120 MeV/c	

CHAPTER 6

COMPARISON OF PREDICTION WITH EXPERIENCE

ON A CHANNEL AT BERKELEY

6.1 Introduction

A pion-deuteron elastic scattering experiment (Auld *et al.*, 1971) was carried out at the Lawrence Laboratory, Berkeley, by a team from the Universities of British Columbia and Victoria primarily to investigate the role of absorption effects in the pion-nucleus interaction. The design, setting up and testing of a pion channel* for this purpose provided an opportunity for evaluating procedures used in the design of the TRIUMF stopped pion/muon channel and for gaining experience in designing and setting up practical channels. This chapter will discuss the design and setting up of the channel and the testing of channel performance, but not the scattering experiment itself.

Measurements were to be made for several values of energy in the range 40 - 100 MeV and the energy resolution was to be better than 2 MeV in order to separate inelastic from elastic scattering. The 184" cyclotron at Berkeley provides a 740 MeV external proton beam. The beam size at the pion production target was about 1" in the horizontal and 2.5" in the vertical plane. Although the nominal value of the beam current was 25 nA, there was uncertainty as to the true

* This work was carried out in collaboration with P.A. Reeve, L.P. Robertson and Q. Ingram.

value at the time of the experiment. This makes any comparison between calculated and measured fluxes rather unreliable. Beam optics, however, were determined accurately and compare reasonably well with calculated values as seen in Section 6.4. The principal error in the calculated values is due to the assumption of a hard-edge model. This error is of the order of 10% for the type of magnets used in this experiment (Alexander and Reeve, 1971).

6.2 Channel Design

6.2.1 Design Criteria

For an experiment of this nature a medium resolution beam of pions is required and, in this case, a resolution of $.8\% \delta p/p_0$ was to be obtained. The pion beam intensity should be as large as possible; thus the production target should be chosen accordingly and the channel should be as short as possible in order to minimize losses from pion decay.

At or near the mid-plane a horizontal focus and a hodoscope are required for momentum definition. An achromatic beam at the scattering target is required and the beam size there should be as small as possible. Preferably, a double focus at the scattering target is to be obtained. Minimization of contaminants, namely, protons, neutrons, electrons and muons should be aimed at. Variable energy between 40 and 80 MeV is required.

6.2.2 Parameter Optimization

The production angle for the pion beam with respect to the proton beam was chosen to be large in order to minimize proton and neutron contamination. The choice of an angle of 129° was determined by the geometry of the experimental area at the Lawrence Laboratory. Also, because of space restriction in the target area, the channel begins with a bending magnet M1 (HP 18 x 36) as shown in Fig. 6.1, which indicates the designation of the various elements. The first drift length was determined by placing M1 as close as physically possible to the target to increase acceptance.

Since the magnets and quadrupoles were already available, their lengths were fixed and could not be used as a design parameter, but their strengths and spacings were variable parameters.

A 60° bending angle was used for M1 and M2 (LP 18 x 36) to obtain a large enough dispersion at the mid-plane horizontal focus where a hodoscope is placed. A larger angle could not have been used because of the geometry of the area available.

The first quadrupole doublet Q1 and Q2 is placed as close as possible to M1 in order to increase acceptance. The strengths of Q1 and Q2 and the drift length to the mid-plane were optimized so that:

- 1) a horizontal focus is obtained at the mid-plane for placing the hodoscope for momentum analysis;
- 2) vertical size of the beam will not be too large so the hodoscope elements will have reasonable lengths, say about 5";

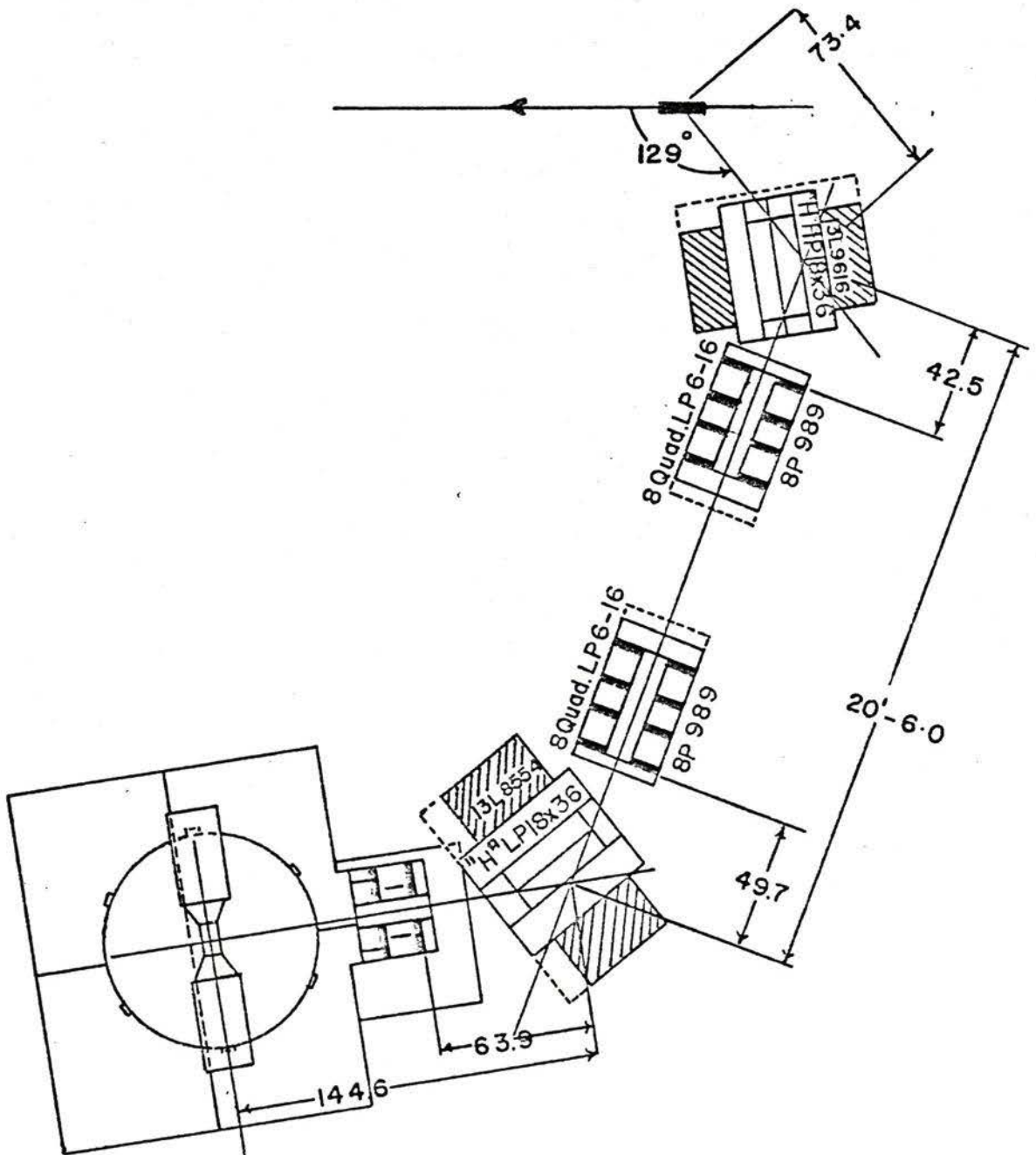


Fig. 6.1 A layout diagram of the pion channel for the π, d experiment at Berkeley.

- 3) the dispersion D is maximized; and
- 4) acceptance should be as large as possible.

Actually one cannot do very much about the dispersion by varying $Q1$ and $Q2$ since it is determined mainly by $M1$ before the doublet. The drift to $Q3$, the strengths of $Q3$, $Q4$ and $Q5$ and the spacing with respect to the mid-plane and to each other, were set to obtain, at the scattering target:

- 1) an achromatic beam ($R_{16} = 0$), and
- 2) a double focus (in both the horizontal and vertical planes).

It was necessary to add $Q5$ to obtain conditions 1) and 2) above, since the channel was not symmetric about the mid-plane. If the channel was made symmetric, a loss in acceptance would have resulted.

In the optimized channel (shown in Fig. 6.1) pions are extracted at an angle of 129° to the proton beam and bent through 60° into a quadrupole doublet that brings the pions to a focus in the horizontal plane. This is followed by another doublet, a 60° bending magnet and a quadrupole singlet forming an achromatic system and bringing the pions to a double focus (in both the horizontal and vertical planes). Table 6.1 gives the parameters of the elements chosen for the channel.

Table 6.1

Optimized Berkeley Channel Parameters

Element*	Effective Length (inches)	Pole-tip Field* (kG)	Quadrupole Aperture (inches)	Magnet Gap (inches)	Magnet Width (inches)
Drift	47.2	-	-	-	-
B.M.	47.2	3.735	-	8	18
Drift	14.6	-	-	-	-
QFH	20.0	1.207	8	-	-
Drift	4.0	-	-	-	-
QDH	20.0	-1.100	8	-	-
Drift	68.6	-	-	-	-
QFH	20.0	0.975	8	-	-
Drift	4.0	-	-	-	-
QDH	20.0	-0.609	8	-	-
Drift	21.6	-	-	-	-
B.M.	47.2	3.735	-	8	18
Drift	36.0	-	-	-	-
QFH	20.0	0.698	8	-	-
Drift	63.0	-	-	-	-

* See Fig. 6.1 and Fig. 6.6 for general layout of channel B.M. designate a bending magnet, QFH a quadrupole focussing in the horizontal plane and QDH a quadrupole defocussing in the horizontal plane (negative pole-tip field).

6.3 Calculated Performance

6.3.1 Channel Characteristics

The channel was designed for a central momentum of 128 MeV/c (50 MeV) and a momentum acceptance of $\pm 3\% p_0$. The solid angle of acceptance was calculated as a function of $\Delta p/p_0$ using NPFLUX (Hutson, 1970). This is shown in Fig. 6.2. The FWHM of the curve indicated a momentum acceptance of $\pm 2.75\% p_0$. However, particles with maximum momentum deviation of about $\pm 5\%$ may be transmitted if their initial divergences were small. The maximum acceptance solid angle of 6 msr is obtained for particles in the momentum range $p_0 \pm 1\% p_0$.

At the x-focus near the channel mid-plane, the first order cumulative matrix is (see Appendix K for the meaning of the various elements and their units):

$$\begin{pmatrix} -1.14 & 0 & 0 & 0 & 0 & 2.23 \\ -9.92 & -0.877 & 0 & 0 & 0 & 9.30 \\ 0 & 0 & -0.728 & 0.0955 & 0 & 0 \\ 0 & 0 & -1.55 & -1.17 & 0 & 0 \\ -1.16 & -.196 & 0 & 0 & 1.0 & -.208 \\ 0 & 0 & 0 & 0 & 0 & 1.00 \end{pmatrix}$$

indicating a focus in the horizontal plane. The magnification (R_{11}) is -1.14 and the dispersion (R_{16}) is 2.23 cm per $\% p_0$. The first order resolution is calculated as $\delta p = 2\% p_0$ for a projected source length of 3.9 cm. Second order effects, discussed below, raises this to $3.5\% p_0$.

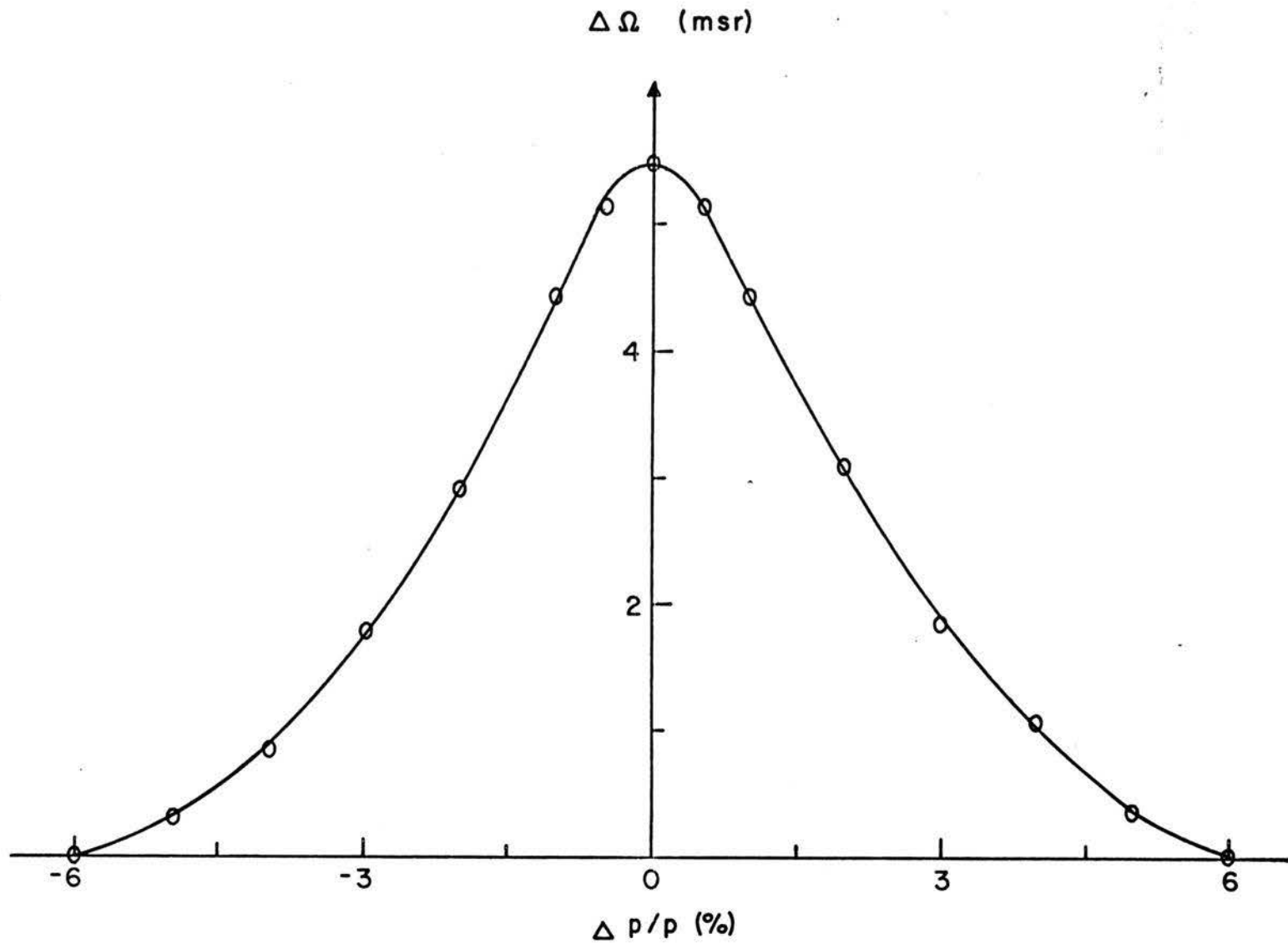


Fig. 6.2 Solid angle of acceptance as a function of $\Delta p/p$ for the pion channel at Berkeley.

At the scattering target, the cumulative first order matrix is:

$$\begin{pmatrix} 0.660 & 0 & 0 & 0 & 0 & 0 \\ 8.18 & 1.51 & 0 & 0 & 0 & -1.97 \\ 0 & 0 & 3.59 & 0 & 0 & 0 \\ 0 & 0 & 16.6 & 0.281 & 0 & 0 \\ 0.129 & 0 & 0 & 0 & 1.00 & -0.670 \\ 0 & 0 & 0 & 0 & 0 & 1.00 \end{pmatrix}$$

This indicates a magnification of 0.66 in the horizontal plane and 3.59 in the vertical plane. The beam is achromatic in displacement ($R_{16} = 0$) and approximately so in angular displacement (R_{26} small). A double focus is obtained.

The cumulative matrix from the mid-plane to the scattering target needed for the procedure to calculate the required channel characteristics is given below:

$$\begin{pmatrix} 0.58 & 0 & 0 & 0 & 0 & 1.29 \\ 7.83 & -1.73 & 0 & 0 & 0 & -3.41 \\ 0 & 0 & -4.21 & -0.34 & 0 & 0 \\ 0 & 0 & -19.0 & -1.79 & 0 & 0 \\ 0.82 & -0.22 & 0 & 0 & 1.00 & -0.21 \\ 0 & 0 & 0 & 0 & 0 & 1.00 \end{pmatrix}$$

The horizontal magnification is 0.58 and the dispersion of the second half is 1.29 cm per % p_0 .

First order beam envelopes for the horizontal and vertical planes and the dispersion trajectory are shown in Fig. 6.3, which was obtained using the program TRANS (Chan, Hunt and Lobb, 1972). This program also calculates derivative matrices (Reeve, 1970) which were used to determine the most sensitive quadrupoles. This calculation indicated that Q1 and Q5 are the critical elements in the system.

From the second order matrix coefficients, calculated by TRANSPORT (see Appendix K), some of the second order effects were estimated. The coefficient T_{122} (see Appendix K for TRANSPORT notation) is 0.1 cm at the end with respect to the mid-plane. The chromatic aberrations (see the note at the bottom of page 76) at the same position were calculated to be ± 0.6 cm, using the coefficients T_{116} , T_{126} and T_{166} . The angle of rotation of the focal plane with respect to the pion beam axis is given (Brown, 1967)

$$\phi = \tan^{-1} \frac{T_{126}}{R_{16}R_{22}}$$

where the matrix coefficients were evaluated at the mid-plane focus with respect to the production target. Using the values of these coefficients from the first and second order matrices, the focal plane angle was estimated to be 65.5° .

PION CHANNEL FOR THE BERKELEY PI, D EXPER

MOMENTUM = 0.120 (GEV/C)

- ▲ HORIZONTAL PLANE ENVELOPE (CM)
- ◆ VERTICAL PLANE ENVELOPE (CM)
- DISPERSION TRAJECTORY (CM/Z)

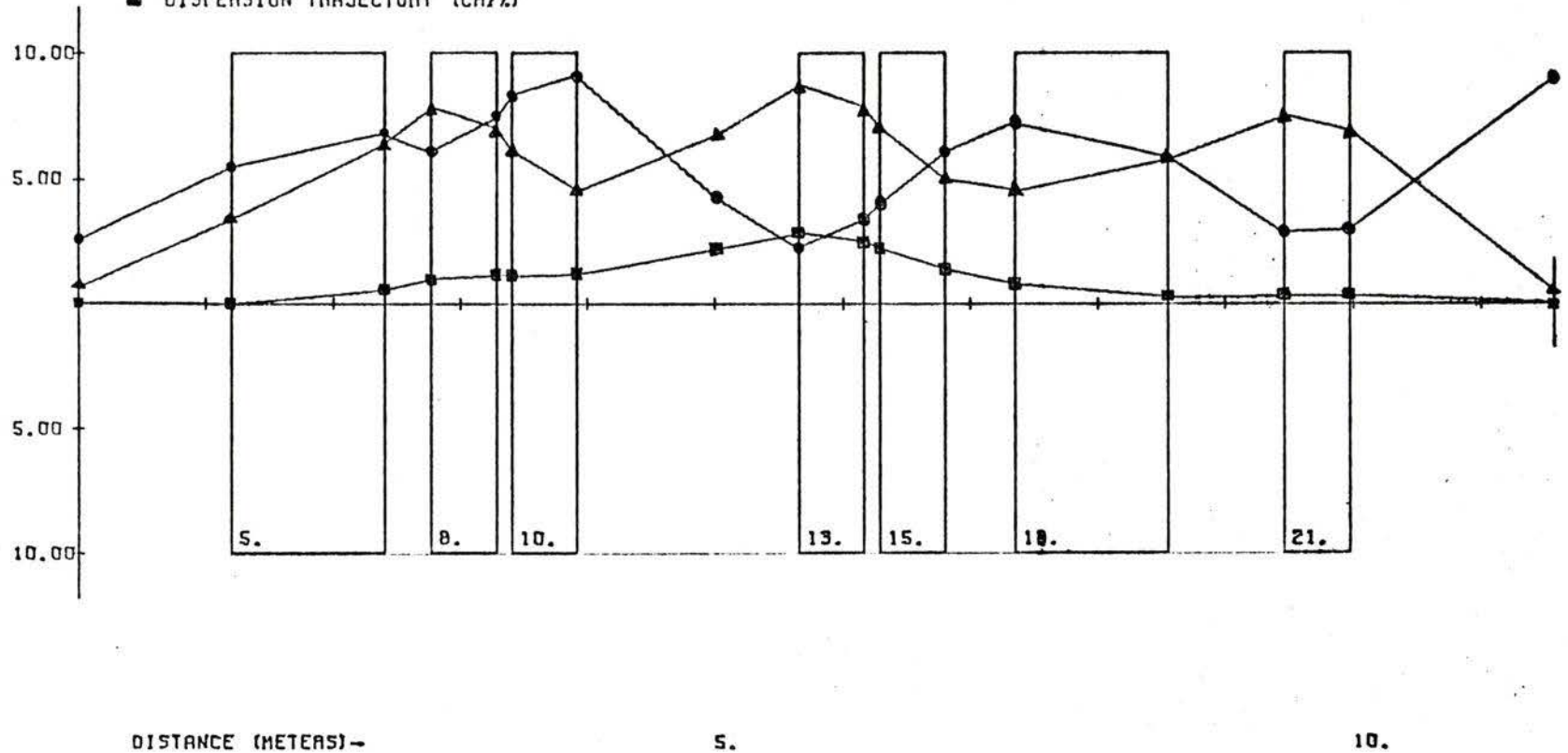


Fig. 6.3 Horizontal and vertical envelopes and the dispersion trajectory for the pion channel at Berkeley.

6.3.2 Expected Flux

The pion flux at the end of the channel is given by the relation

$$N_{\pi} = \frac{d^2 \sigma}{dE d\Omega} \cdot I_p \cdot N_t \Delta\Omega \cdot \Delta E$$

The production cross section $\frac{d^2 \sigma}{dE d\Omega}$ was assumed to be $10.6 \mu\text{b} (\text{MeV} \cdot \text{Steradian})^{-1}$. This value was obtained from the results of the Los Alamos experiment (Nagle *et al.*, 1969) for 46 MeV pions from Be at an angle of 135° . The proton current I_p was assumed as 25 nA and the number of target nuclei N_t was 1.875×10^{24} for the $6'' \times 3'' \times 2''$ Be target. (In fact, $5''$ Be and $1''$ C were in the line.)

The flux at the end of the channel was estimated using two different methods.

- (a) By using the solid angle of acceptance $\Delta\Omega$ calculated by using the program NPFLUX (see Appendix K) and allowing for pion decay in flight. This method yielded $4.5 \times 10^3 \pi^+$ per sec for the total flux. A pion beam distribution is also obtained as shown in Fig. 6.4.
- (b) By using the program MBEND (see Appendix L) which takes account of pion decay in flight. This method yielded $5.6 \times 10^3 \pi^+$ per sec for the total flux and provided the pion energy spectrum shown in Fig. 6.5. The maximum differential flux was $7.2 \times 10^2 \pi^+$ $(\text{sec} \cdot \text{MeV}/c)^{-1}$, occurring at a momentum of 130 MeV/c.

0	1	1	2	2	1	2	0
5	8	9	2	4	8	7	1
4	11	12	9	6	10	10	3
5	7	10	9	11	9	13	5
11	7	11	6	12	6	9	8
6	8	10	20	19	12	14	10
3	12	17	9	16	11	5	12
5	12	27	11	14	10	12	6
5	15	12	12	11	16	17	8
6	7	19	14	16	12	11	12
6	16	18	11	16	22	13	9
6	15	24	14	11	15	26	13
6	17	12	20	15	16	10	6
2	10	3	7	1	5	4	2

Fig. 6.4 Calculated pion distribution in the transverse plane at the end of the Berkeley channel for $\Delta p/p = 0$. The grid mesh is 1.0 cm in the horizontal and 1.0 cm in the vertical plane.

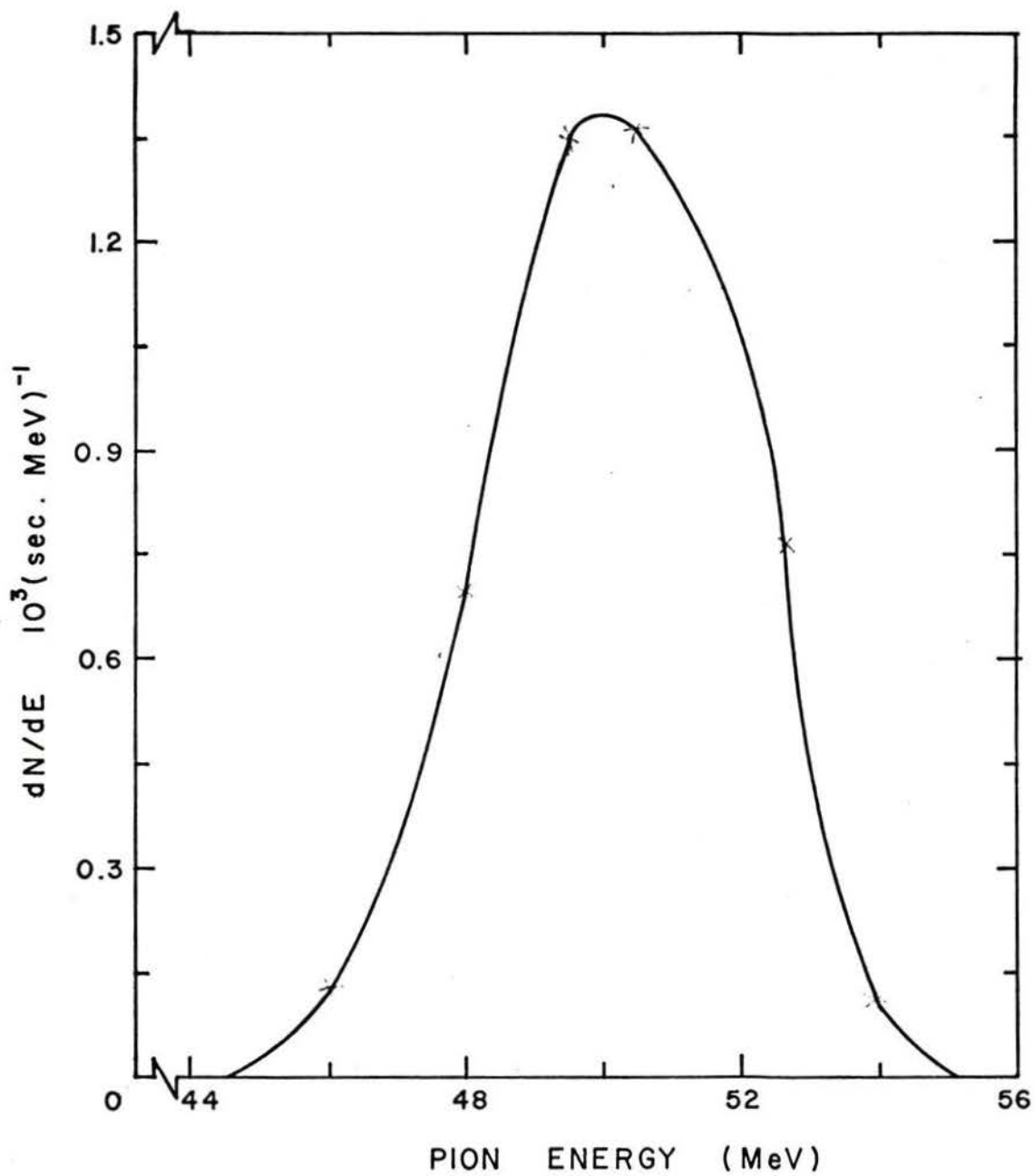


Fig. 6.5 Calculated pion energy spectrum for the Berkeley channel, assuming a 25 nA proton current incident on a 6" Be target.

6.4 Procedure and Data Analysis for Setting up and Testing the Channel

The channel was considered as made up of two regions: Region I, from the pion production target to the horizontal focus near the centre of the channel where a hodoscope is placed, as seen in Fig. 6.6. Region II extends from the hodoscope to the end of the channel where a total energy counter (TEC) is placed. After setting up Region I and Region II, as described in Sections 6.4.3 and 6.4.4 respectively, the test for achromaticity is described in Section 6.4.5. The measurement of dispersion by two different methods is described in Section 6.4.6 and the ratio of dispersion to magnification in Section 6.4.7. The measurement of magnification is described in Section 6.4.8 and resolution in Section 6.4.9. Miscellaneous effects are discussed in Section 6.4.10 and second order effects are examined in Section 6.4.11. Finally, measured and calculated pion fluxes are compared in Section 6.4.12.

6.4.1 Counter Arrangement

Fig. 6.6 shows the counter arrangement used for setting up the channel. The hodoscope consisted of twelve elements designated A1 through A12. Each element is 12 mm wide overlapping 1 mm on either side with its neighbours. B1 and B2 are two 5" x 5" NE 102 plastic scintillation counters used for timing and to define the usable particle flux. Finger counters B3 and B4 form a cross in front of the total energy counter (TEC). Another finger counter F was used during the setting up of the focus at the mid-plane. Spark chambers SC1 and SC2, separated by 20 cm, were placed 1/2 m upstream of the channel end.

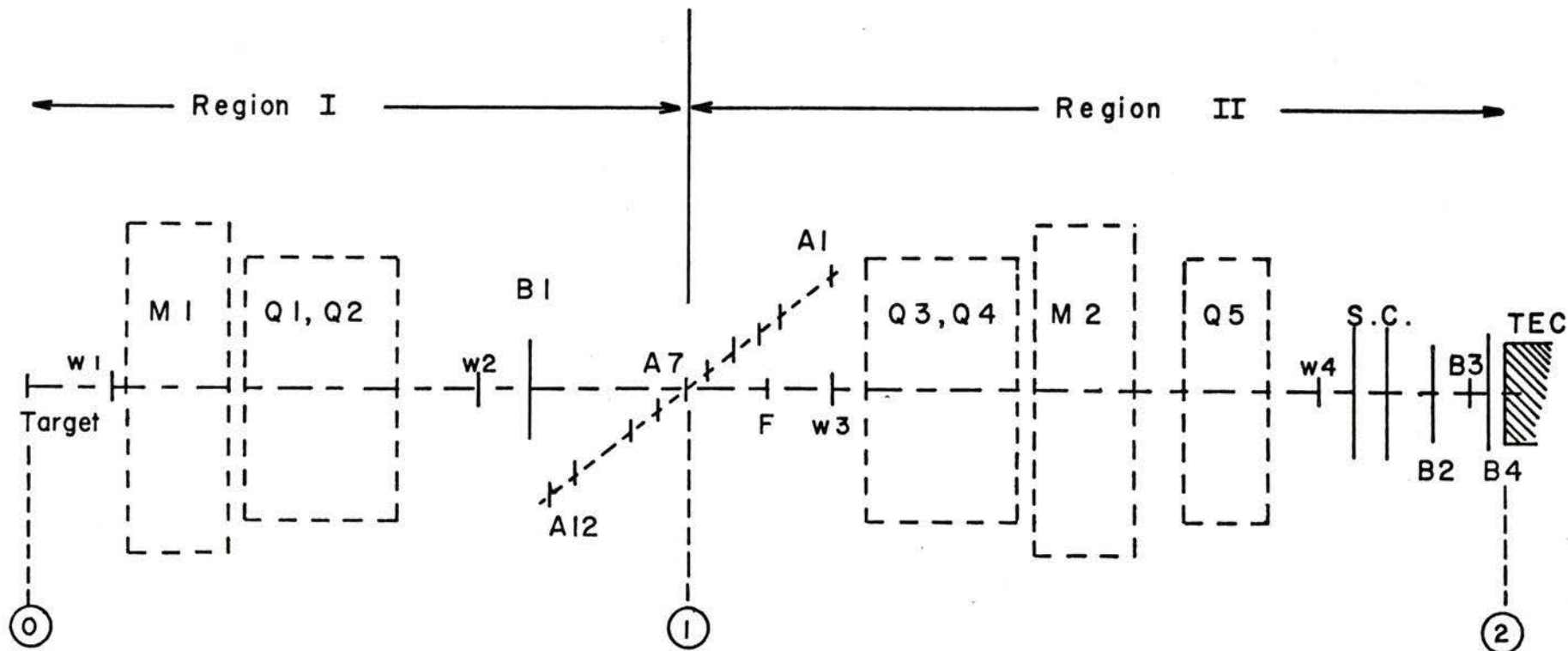


Fig. 6.6 Counter arrangement used in setting up and testing the pion channel at Berkeley.

6.4.2 Multiple Scattering at 50 MeV

There are three sources of multiple scattering: the air in the free spaces where the vacuum tube does not extend, the material of the several counters and vacuum windows in the beam line, and the wires of the spark chamber planes. However, the effect of multiple scattering on the beam size depends on the location of the scattering materials. Since all the counters are at or near a focus, their contribution is negligible. Also, the contribution from the windows W2 and W3 (0.003" thick mylar) may be neglected because of their proximity to the focus at the mid-plane.

For the purpose of setting up the focus at the mid-plane, the contributions to multiple scattering from the air space between the production target and the first bending magnet and the window W1 were included, as well as the contributions from Region II which was used as a telescope to set up Region I. For the cases in which the spark chamber was used, the contribution to multiple scattering from the air space between the spark chamber and the end of the channel was not included because the particles' positions were determined by the spark chamber and projected to the end of the channel by calculation. But scattering by the wires of the first spark chamber plane was included. Scattering by the wires of the second plane and by the air in the final section from the spark chamber to the end were included for the cases when the total energy counter was used to determine the pion peak position and width.

The calculation was carried out (Robertson, 1971) using the relation

$$\sigma_{\text{rms}}(\text{Projected}) = \frac{15}{p\beta} \left(\frac{L}{L_{\text{rad}}} \right)^{\frac{1}{2}} \quad (6.4.1)$$

where: σ_{rms} is the projected root mean square scattering angle,
p is the pion momentum in MeV/c,
 β is the pion velocity relative to velocity of light,
L is the thickness of the material traversed, and
 L_{rad} is the radiation length of the material,
together with the transformation matrices at the various positions in the system where multiple scattering occurs. The rms displacement at 50 MeV and 100 MeV was estimated to be

	rms displacement (cm)	
	<u>50 MeV</u>	<u>100 MeV</u>
Scattering in Region I	0.85	0.47
Scattering in Region II (spark chamber used)	1.04	0.57
Scattering in Region II (TEC used)	1.16	0.64

6.4.3 Setting up Region I

The first part of the channel was set up using Region II as a telescope. In order to reduce the contribution of the angular divergence, a finger counter F is placed in coincidence with the centre hodoscope element (Fig. 6.6) and 25.5 cm downstream from it to define a beam with small angular divergence at the mid-plane. To determine whether a focus has been obtained ($R_{12} = 0$) the spark chamber planes were considered as being divided into two halves by a vertical line through the optic axis. This was incorporated in the software of the data acquisition system. A focus is indicated when the peaks of the horizontal pion distribution from the two halves of the spark chamber overlap. This is because if magnets and lenses were set correctly and a focus is obtained, particles will come to the same focal plane irrespective of which half of the spark chamber plane they have passed through. The most sensitive lenses in the system were determined quickly by detuning the various quads in turn and examining the effect on the pion peak position. It was found that Q1 was the most critical in agreement with the calculated results indicated in Section 6.3.1.

The precision obtainable with this procedure can be determined by estimating the uncertainties in the system coordinates. Thus, the displacement at the horizontal focus near the channel centre is given by:

$$x_1 = I_{R_{11}x_0} + I_{R_{12}x_0} + I_{R_{16}} \frac{\Delta p}{p} \quad (6.4.2)$$

where I_{R11} , I_{R12} and I_{R16} are the matrix coefficients evaluated for Region I, x_0 and x_0^i are the displacement and divergence at the pion production target, and $\Delta p/p$ is the momentum deviation. It is assumed that the errors are random and the terms are added in quadrature to obtain a likely error. The following uncertainties contribute to the error in setting up Region I:

- ± 0.6 cm due to the finite target length as seen by the channel,
- ± 35 mrad being the channel acceptance for $\frac{\Delta p}{p} = 0$,
- ± 0.5 cm the uncertainty introduced by the finite width of the hodoscope element,
- ± 29 mrad the uncertainty in the angular divergence of Region II introduced by the finite sizes of A7 and the finger counter F added in quadrature,
- ± 0.4 cm determined by the spark chamber resolution for the two planes added in quadrature and projected to the channel end.

Using these uncertainties, and the calculated transfer matrix coefficients (see Section 6.3.1), the error in calculating x_2 is

$$x_2 = 20.3 I_{R12} + 29 I_{R12}^{II} \pm 0.66 .$$

This represents the error expected in setting the focus of both regions. An upper limit on the value of the second term was obtained experimentally by detuning Q5 by 10% from the calculated value which, as will be

seen in the next section, is bigger than the error in its setting. This detuning resulted in a splitting of the pion peaks by two channels, corresponding to $\pm .23$ cm. Therefore, the calculated uncertainty in setting up Region I is given by:

$$x_2 = 20.3 I_{R_{12}} + 0.23 \pm 0.66 .$$

Experimentally, when Q1 was detuned from its calculated value, the pion peaks were split apart depending on how far it was detuned. A minimum full-width-at-half-maximum (FWHM) of ten channels was obtained when Q1 was set at its calculated value. Thus, the measured value of x_2 is ± 1.15 cm. This represents the spread due to the errors in focussing Regions I and II, multiple scattering in the channel, and second order effects if any. The multiple scattering contribution from both Region I and Region II at 100 MeV, added in quadrature, is 0.74 cm. When this is subtracted out, in quadrature, from the above error, the error due to the channel optics only is ± 0.88 cm.

The equivalent resolution of setting Region I is equal to the error in determining that the two pion peaks overlap plus the error in setting the focus in Region II . Experimental results indicated that the two peaks overlap to within ± 1 channel, corresponding to ± 0.23 cm. An upper limit on setting the focus for Region II was, as indicated earlier, 2 channels or ± 0.23 cm. The total error is obtained by adding the two errors giving $\pm .46$ cm. This error will produce an equivalent momentum spread given by

$$\delta p = \pm \frac{0.46}{D/M} = \pm \frac{0.46}{2.2} x = \pm 0.2\% p_0$$

where D is the dispersion and M is the magnification.

6.4.4 Setting up Region II

For the second region, the finger counter F (see Fig. 6.6) was removed. The procedure was to detune Q5 (which is more critical than Q3 and Q4) and observe any splitting in the pion peaks from the two halves of the spark chamber.

To estimate the uncertainties expected in setting up the second region, the displacement at the channel end x_2 for a central trajectory where

$$x_1 = x_1^i = \frac{\Delta p}{p} = 0 \quad ,$$

is

$$x_2 = \pm {}^{II}R_{12}\Delta x_1^i \pm {}^{II}R_{11}\Delta x_1 \pm {}^{II}R_{16}\Delta \frac{\Delta p}{p} \pm \Delta x_2 \quad (6.4.3)$$

The values of these terms were evaluated in the previous section except for Δx_1^i which now represents the full beam divergence at the mid-plane (since the finger counter F is now removed). Thus, adding the random uncertainties in quadrature give

$$x_2 = 50 {}^{II}R_{12} + 0.21 \quad 0.53 \quad .$$

The experimental results are summarized in Fig. 6.7 which shows the pion peak separation plotted against the percentage detuning of Q5. This indicated that the calculated value was 4% low. Q5 was then set 4% higher than the calculated value. At this setting, the FWHM of the pion peak was 11 ± 1 channels which is equivalent to a spread of ± 1.26 cm. If the multiple scattering effect of ± 0.57 cm is subtracted out in quadrature, then the width due to optics only is ± 1.12 cm.

The equivalent resolution of setting Region II is determined by the error in the overlap of the two peaks, which is ± 0.23 cm, the systematic error in setting up Region I, which is equivalent to 0.21 cm. The momentum spread caused by these errors is calculated using the ratio of the dispersion to the magnification and is $\pm 0.5\% p_0$.

6.4.5 Achromaticity

A system is achromatic if particles of differing momenta are brought to the same focus. The procedure to check achromaticity was to observe with the spark chamber the dependence of the pion peak position on several hodoscope elements which represent sources of pions of different momenta. The central wire of the spark chamber was numbered 50. Experimental results for 5 hodoscope elements, including the extreme elements A1 and A12, indicated that the pion peak position was within the limits 11.14 cm and 11.85 cm; that is, the channel is achromatic to within ± 0.35 cm. This corresponds to a momentum spread of $\pm 0.16\% p_0$.

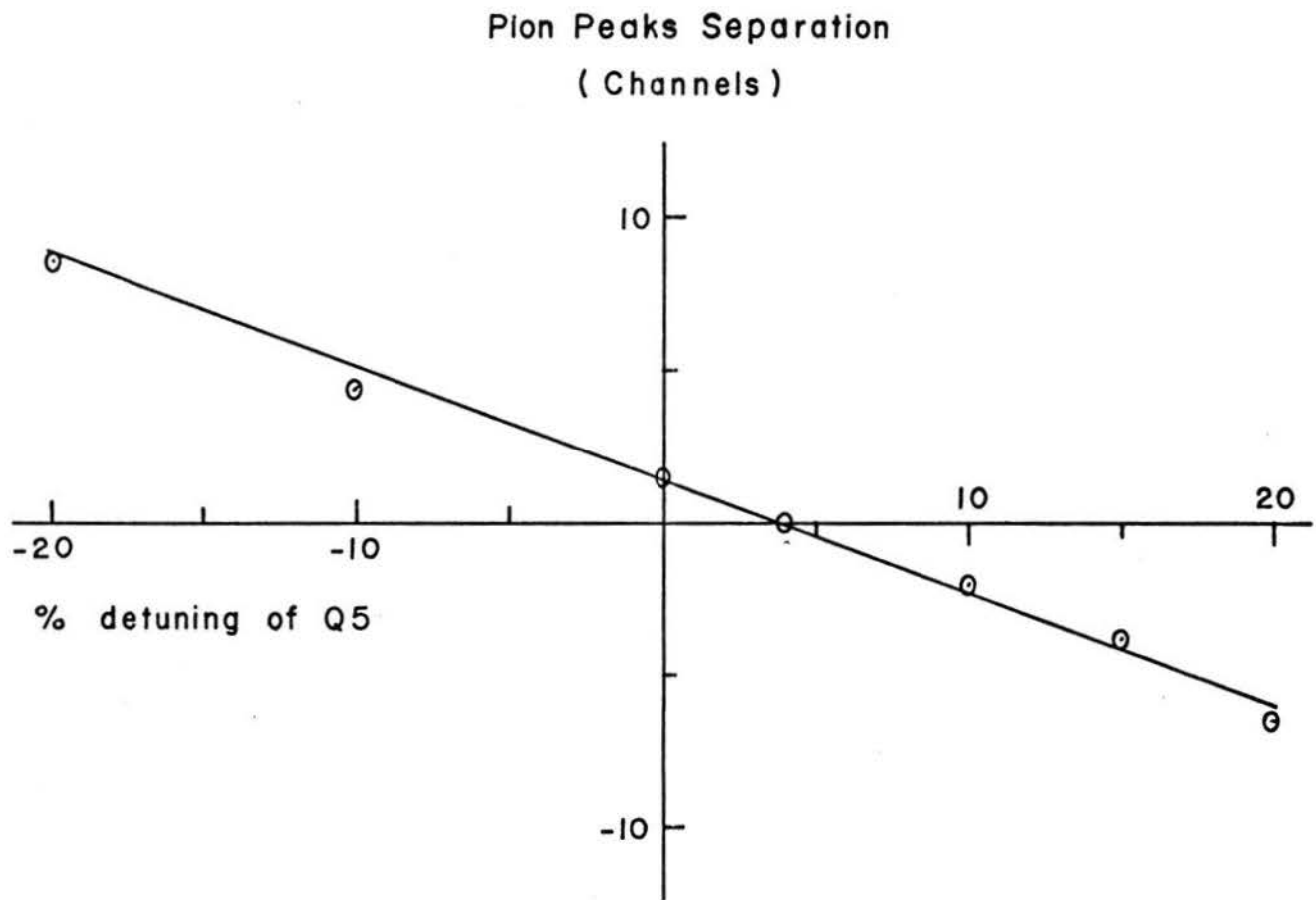


Fig. 6.7 Effect of detuning Q5 from the calculated value on the focus at the channel end.

6.4.6 Dispersion in Region II

Two independent methods were used to measure the dispersion. Method (a) was carried out at 100 MeV and Method (b) at 50 MeV.

Method (a) For a rectangular bending magnet the first order matrix has no focussing in the bend plane and $\frac{dB}{B} \equiv \frac{dp}{p}$ appears to first order in the R_{16} and R_{26} terms. The position at the channel end (scattering target) x_2 is related to the momentum $\frac{\Delta p}{p}$ and the position x_1 at the mid-plane by

$$x_2 = {}^{II}R_{11}x_1 + {}^{II}R_{16} \frac{\Delta p}{p} \quad . \quad (6.4.4)$$

With a source target of ± 0.6 cm projected length, the position x_1 at the mid-plane is defined by the hodoscope so that the momentum bite $\frac{\Delta p}{p}$ is defined. In Fig. 6.8 is plotted the centroid position of the pion distribution, measured at the channel end using the spark chambers, versus the % change in the magnet current (the hysteresis has been measured to be negligible at the excitation level used). The central ray is defined by the middle hodoscope element (for which $x_1 = 0$), so that

$$x_2 = {}^{II}R_{16} \frac{\Delta p}{p}$$

where

$$\frac{\Delta p}{p} \equiv \frac{\Delta B}{B} \quad .$$

The slope of the x_2 versus $\frac{dB}{B}$ curve of Fig. 6.8 gives the value of ${}^{II}R_{16}$ which is equivalent to the dispersion of the second half of the channel (Region II). This value is 1.15 ± 0.02 cm per % .

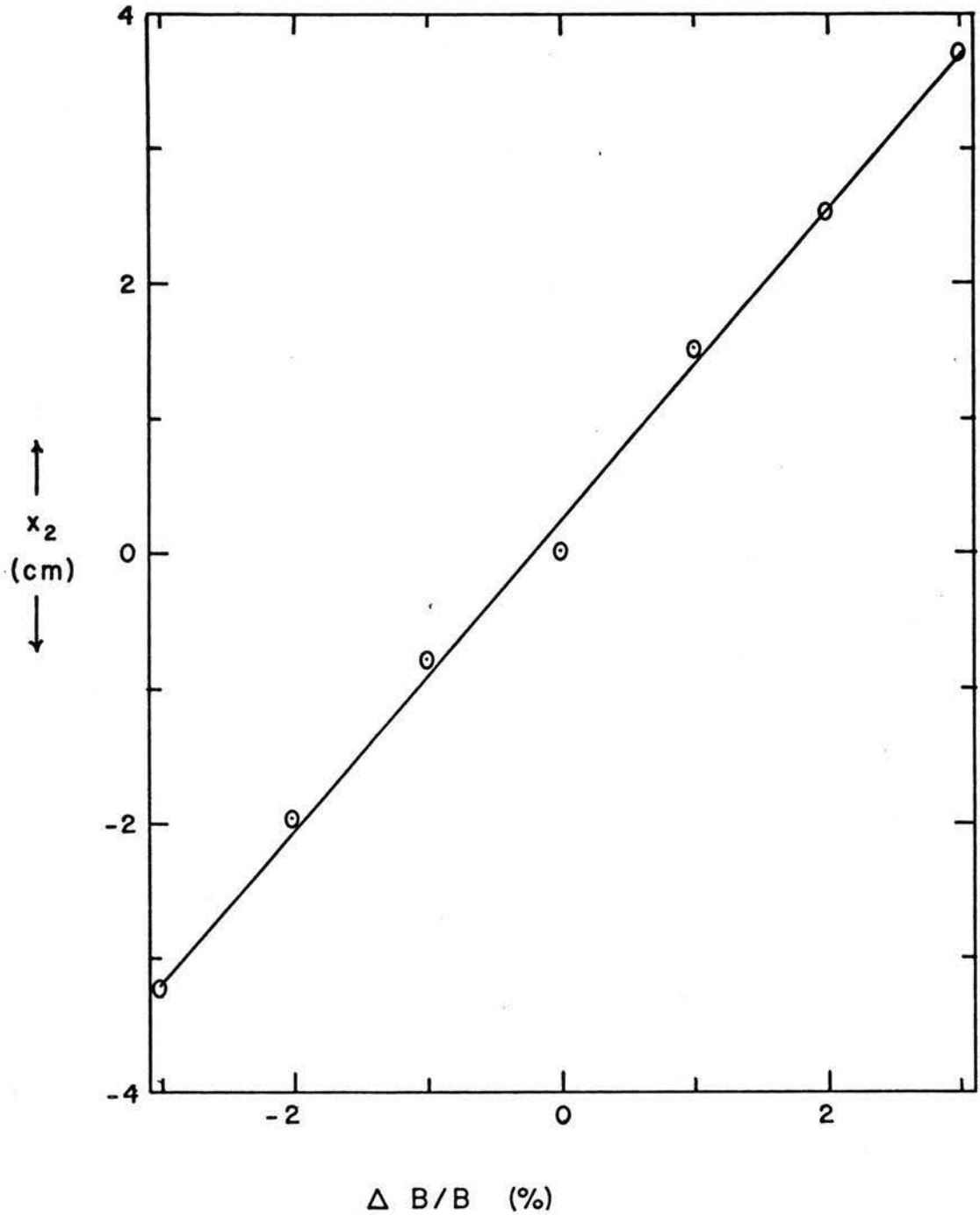


Fig. 6.8 Centroid position of the pion distribution x_2 , measured at the channel end, versus the % change in the field of the second bending magnet $\Delta B/B$.

The accuracy of this method depends on the accuracy with which the centroid of the pion distribution can be determined. The uncertainty with which this centroid can be determined is given by

$$x_2 \pm \Delta x_2 = \text{II}_{R16} \frac{\Delta p}{p} \pm \text{II}_{R12} \Delta x_1' + \text{II}_{R16} \Delta \frac{\Delta p}{p} \pm \text{II}_{R11} \Delta x_1 \quad (6.4.5)$$

which, on using the values determined previously (Section 6.4.3), give

$$x_2 = \text{II}_{R16} \frac{\Delta p}{p} \pm 0.5 \text{ cm.}$$

At 100 MeV, the maximum value for x_2 as indicated by the FWHM of the pion distribution was 2.53 cm, which sets the expected error in measuring the dispersion as ± 0.09 cm using the calculated value of $D/M = 2.2$ cm per %.

Method (b) In this method, carried out at 50 MeV central energy, the position of the cross (the two finger counters B3 and B4 at right angles to each other) and the total energy counter across the beam and the corresponding position of the pion peak in the total energy counter were measured for each hodoscope counter. These quantities are also related by equation (6.4.4). The spark chambers were not used for this case.

For method (b) the total energy counter was first calibrated by plotting the pion peak channel number for each hodoscope element against percentage change in momentum ($\% \Delta B/B$). The slope for each curve was calculated and the average was 0.46% per channel with a standard deviation of $\pm 0.03\%$ per channel.

The experimental results for method (b) are shown in Fig. 6.9 in which the pion peak position (channel number) is plotted as a function of the position of the cross counters (and the TEC) in centimeters for each hodoscope element. The curves are displayed in two groups for clarity. These curves also provide data for the calculation of the magnification discussed in Section 6.4.8. The average of the slopes of these curves was 0.55 cm per channel with a standard deviation of ± 0.04 cm per channel. Using the calibration factor of 0.46% per channel, the dispersion coefficient is 1.20 ± 0.05 cm per %.

Thus, the results for the dispersion values may be summarized as follows:

Method (a): $D = 1.15 \pm 0.09$ cm per %;

Method (b): $D = 1.20 \pm 0.06$ cm per %;

TRANSPORT Calculation: $D = 1.29$ cm per %.

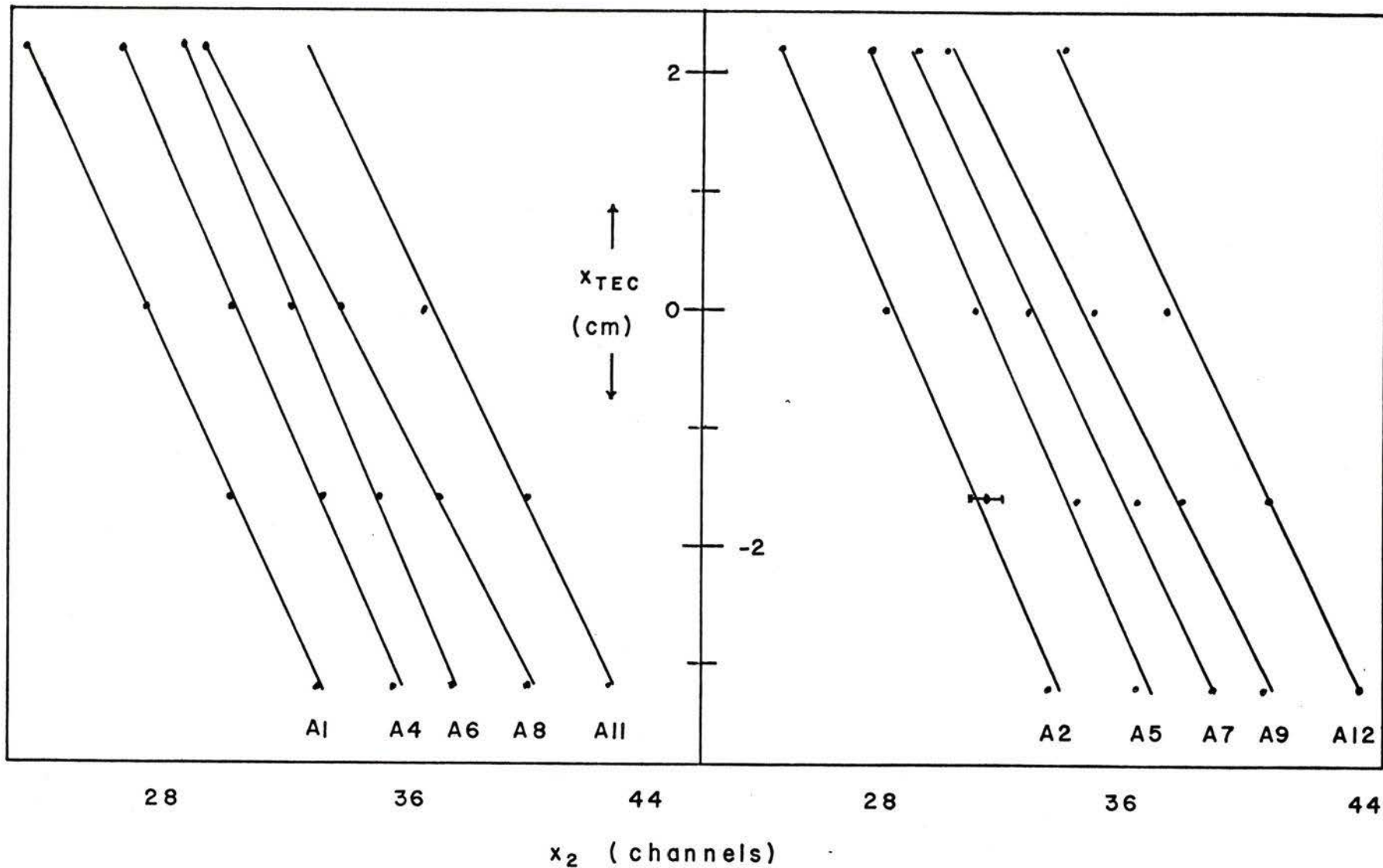


Fig. 6.9 Centroid position of the pion distribution x_2 (in channels) versus the position x_{TEC} of the cross (counters B3 and B4) and the TEC (in cm) for each hodoscope element.

6.4.7 D/M Ratio

The ratio of the dispersion to the magnification was measured using two different methods, using the total energy counter.

Method (a) The ratio D/M was determined directly from a plot of the position of hodoscope elements x_1 against the shift in energy spectrum of the pion peak as given by the TEC for a given fixed position of the cross counters and the TEC (that is for $x_2 = 0$, as the system is achromatic). This can be seen by letting $x_2 = 0$ in the relation (6.4.4) which gives

$$\frac{II_{R16}}{II_{R11}} = \frac{D}{M} = \frac{x_1}{\Delta p/p}$$

$\Delta p/p$ was determined from the pion peak shift due to the various hodoscope elements. Fig. 6.10 shows the results for this method. The slope of the curve gives the ratio D/M after using the calibration coefficient $0.46 \pm .03$ channel per % for the TEC. This ratio is 2.33 ± 0.03 cm per %.

Method (b) In this method, the position of the hodoscope elements x_1 was plotted against the shift in pion peak channel for each of five values of $\Delta B/B$. Fig. 6.11 shows these curves, whose slopes give the D/M values as can be seen from the relation (6.4.4). The average value of the slopes was 1.09 ± 0.16 cm/channel. Using the calibration coefficient 0.46 ± 0.03 channel per %, the D/M ratio is 2.37 ± 0.16 cm per %.

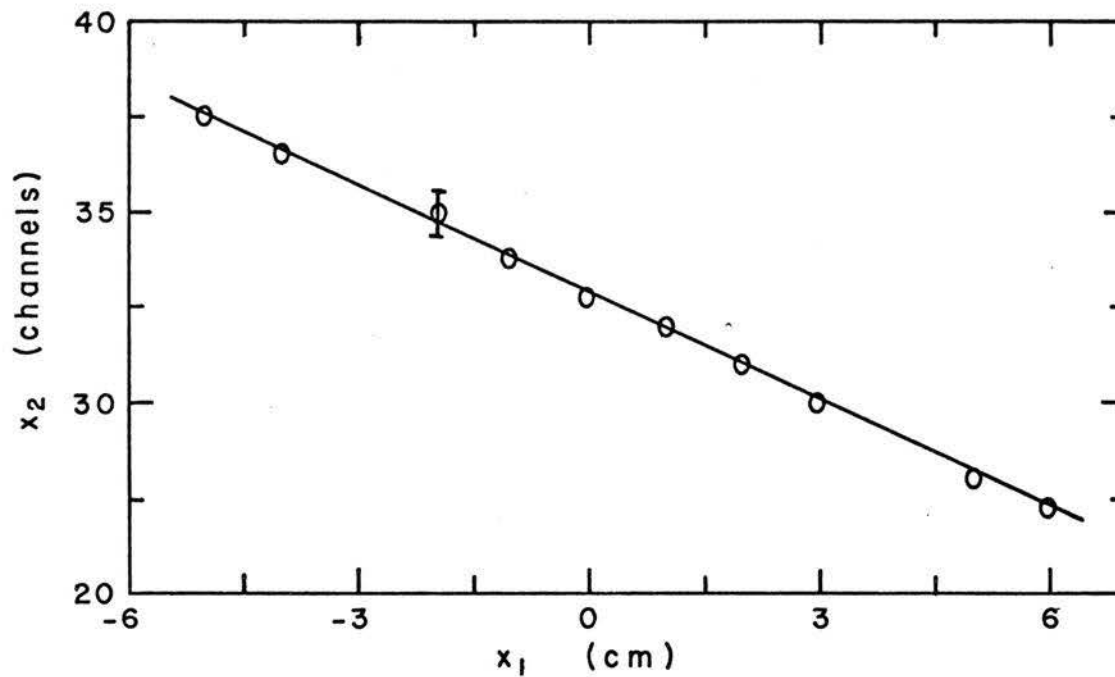


Fig. 6.10 Centroid position of the pion distribution x_2 (in channels) versus the position of the hodoscope counters (in cm) for a fixed position of the TEC.

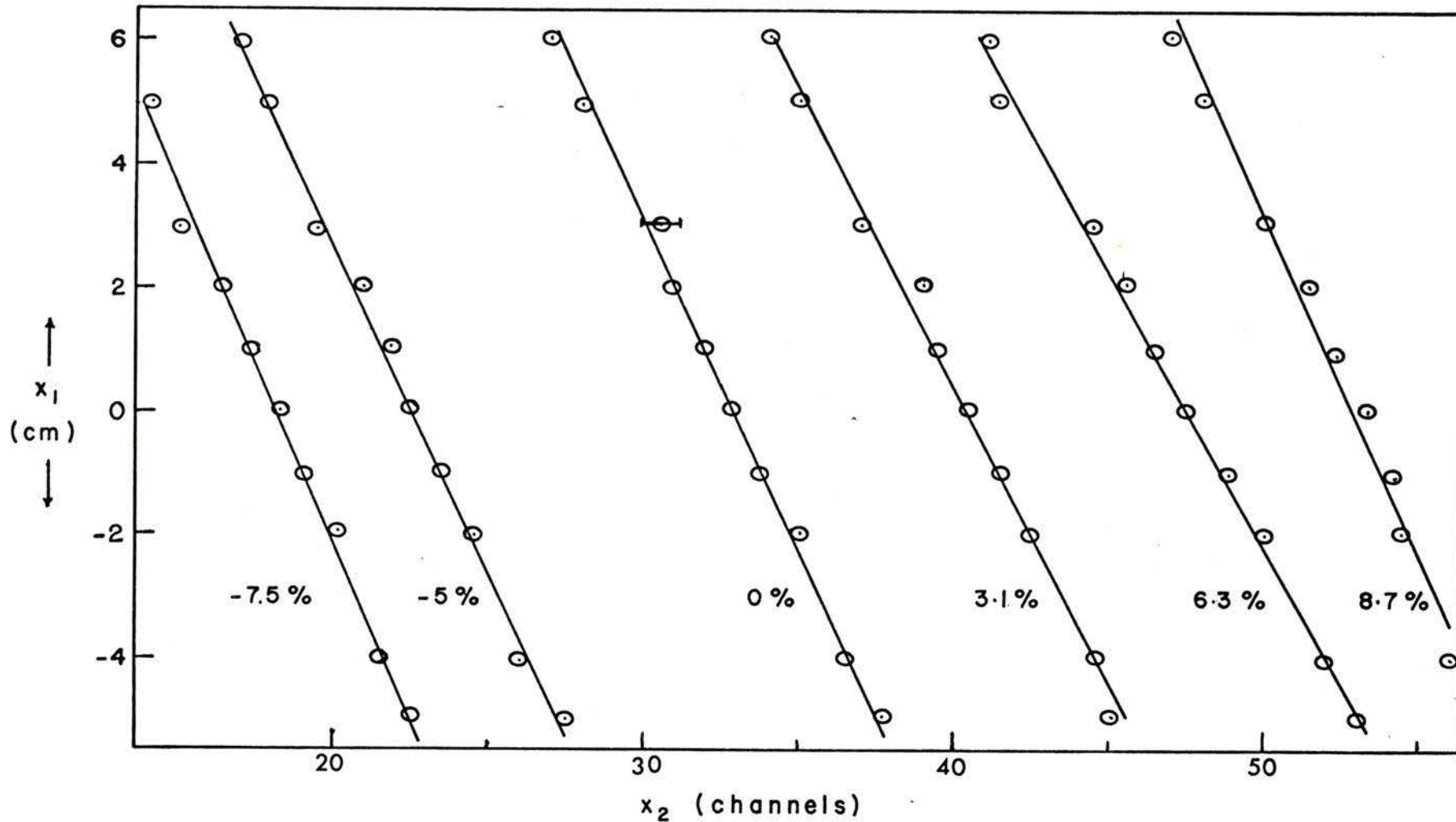


Fig. 6.11 Centroid position of the pion distribution x_2 (in channels) versus hodoscope positions (in cm) for the five values of $\Delta B/B$ indicated on the individual curves.

The large uncertainty in this last figure for D/M is due to the rather crude method used in moving the TEC and cross counters and measuring this motion. Thus the D/M values from the two methods are:

Method (a): 2.33 ± 0.03 cm per %,

Method (b): 2.37 ± 0.16 cm per %,

Calculated: 2.23 cm per %.

6.4.8 Magnification of Region II

The magnification $M = {}^{\text{II}}R_{11}$ was measured directly using the previous results indicated in Fig. 6.9. The intercept of a curve for any of the hodoscope elements on the line (shown dashed) which passes through the intersection of A7 and the axis (for which $x_2 = 0$) is a measure of the size of the displacement at the TEC, namely x_2 . The distance between this particular element and A7 is a measure of the displacement at the mid-plane x_1 . The magnification is, therefore, obtained by dividing the first by the latter. This can be seen clearly by letting $\Delta p/p = 0$ in the relation (6.4.4). The experimental results give 9 values of M which has a mean value of 0.48 with a standard deviation of ± 0.06 , compared to 0.58 from TRANSPORT calculation and 0.5 derived from measured D/M and D.

6.4.9 Resolution

Writing the relation (6.4.4) in the equivalent form

$$x_2 = Mx_1 + D(\Delta p/p_0)$$

where M and D refer to the magnification and dispersion for Region II, then the momentum resolution is

$$\frac{\delta p}{p_0} = \frac{1}{D} (x_2 - Mx_1) \quad (6.4.6)$$

x_2 is the full width at half the pion peak maximum (FWHM); x_1 is the width of a hodoscope element.

An estimate of the uncertainty expected in determining the resolution can be made by estimating the uncertainties in the various terms. Thus

$$\Delta \frac{\Delta p}{p_0} = \Delta \frac{x_2}{D} - \Delta \frac{M}{D} x_1$$

The uncertainties in x_2 and x_1 are ± 0.4 cm and ± 0.6 cm respectively. If the experimental results are used, then the uncertainties in M and D are ± 0.06 and ± 0.05 cm per % respectively. Substituting in the above expression one obtains

$$\Delta \frac{\delta p}{p_0} = \pm 0.73\%$$

for the uncertainty expected in determining the resolution.

The experimental results using A7, B1, B2 and the spark chamber in coincidence gave

$$\text{FWHM} = 2.3 \pm 0.35 \text{ cm at } 100 \text{ MeV and}$$

$$\text{FWHM} = 3.9 \pm 0.35 \text{ cm at } 50 \text{ MeV.}$$

Using these values and the average measured values for M and D, the resolution was calculated to be

$$\begin{aligned} \frac{\delta p}{p_0} &= 1.52 \pm 0.36\% p_0 \text{ at } 100 \text{ MeV and} \\ &= 2.83 \pm 0.36\% p_0 \text{ at } 50 \text{ MeV.} \end{aligned}$$

Although the finite size of the hodoscope element (which is the pion source as far as the experimenter is concerned) was considered in obtaining these results, multiple scattering was not taken into account. This explains the difference in resolution at the two operating energies. The calculated ratio of multiple scattering at 100 MeV to that at 50 MeV was 0.55; the ratio of the measured values above is 0.54 in very good agreement.

The multiple scattering effects due to Region II were calculated to be ± 1.16 cm at 50 MeV, which is equivalent to a resolution of $\pm 1.0\% p_0$. If this is subtracted out, in quadrature, from the resolution at 50 MeV obtained above, then the channel resolution is $2.0\% p_0$ or $\pm 1.0\% p_0$.

6.4.10 Other Effects

Apart from the measurements discussed in the previous sections some observations were made concerning the channel characteristics. These included the following.

Resolution for Various Hodoscope Elements, as measured by the FWHM for pion peaks, is plotted in Fig. 6.12 for each of three settings of the last quadrupole Q5. A slight tendency for the FWHM to show a minimum near the centre element A7 can be seen. However, this is within the error in determining the FWHM. This curve also indicates that the FWHM is independent of the Q5 setting to within error.

The Possible Dependence of Resolution on $\Delta p/p$ was examined and, as seen in Fig. 6.13, where the FWHM is plotted against $\Delta B/B (= \Delta p/p)$ for each hodoscope element; no such dependence exists to within the experimental errors in measuring the FWHM for the pion peaks.

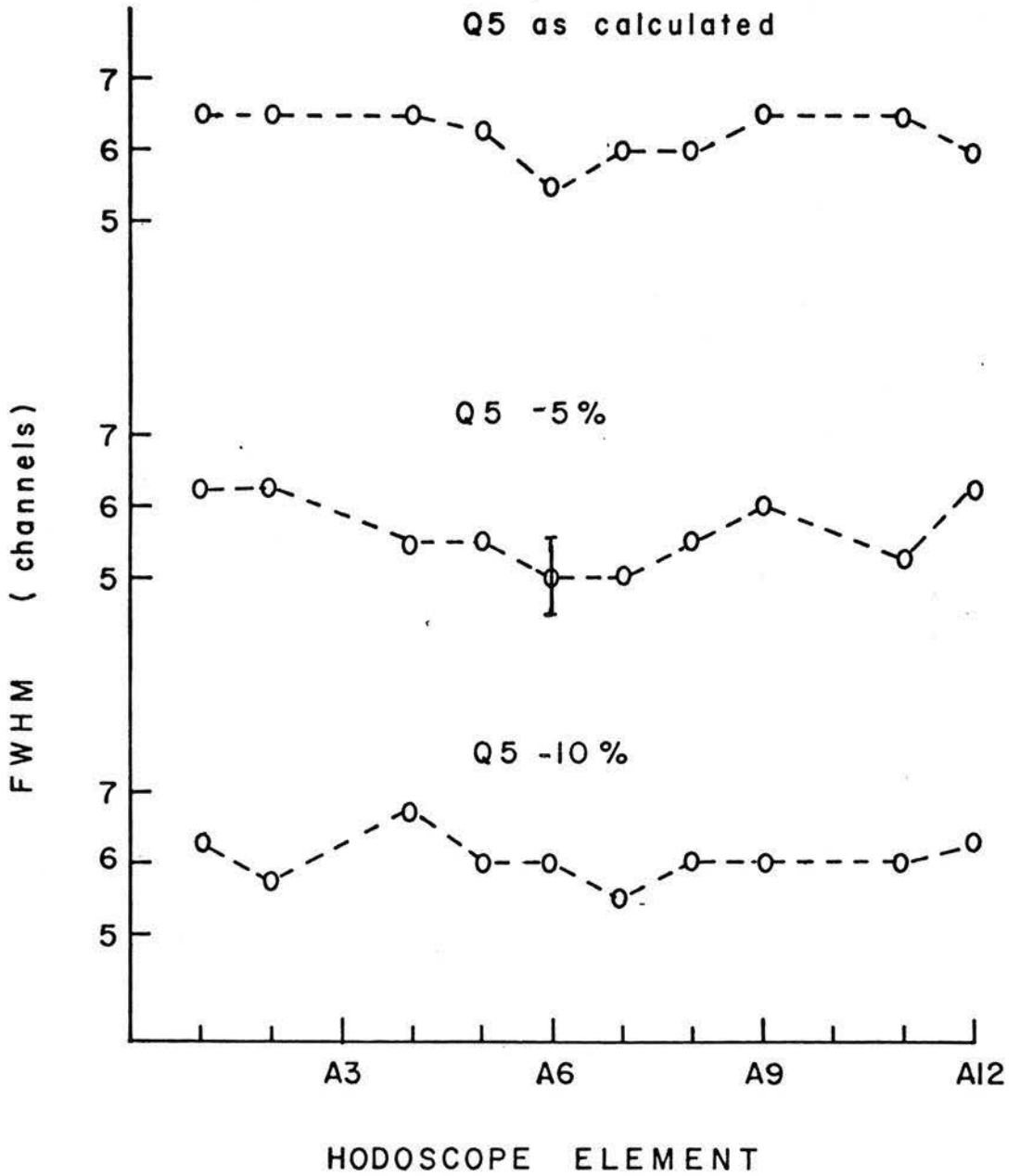


Fig. 6.12 Resolution (as measured by the FWHM) versus the hodoscope counters for three settings of Q5.

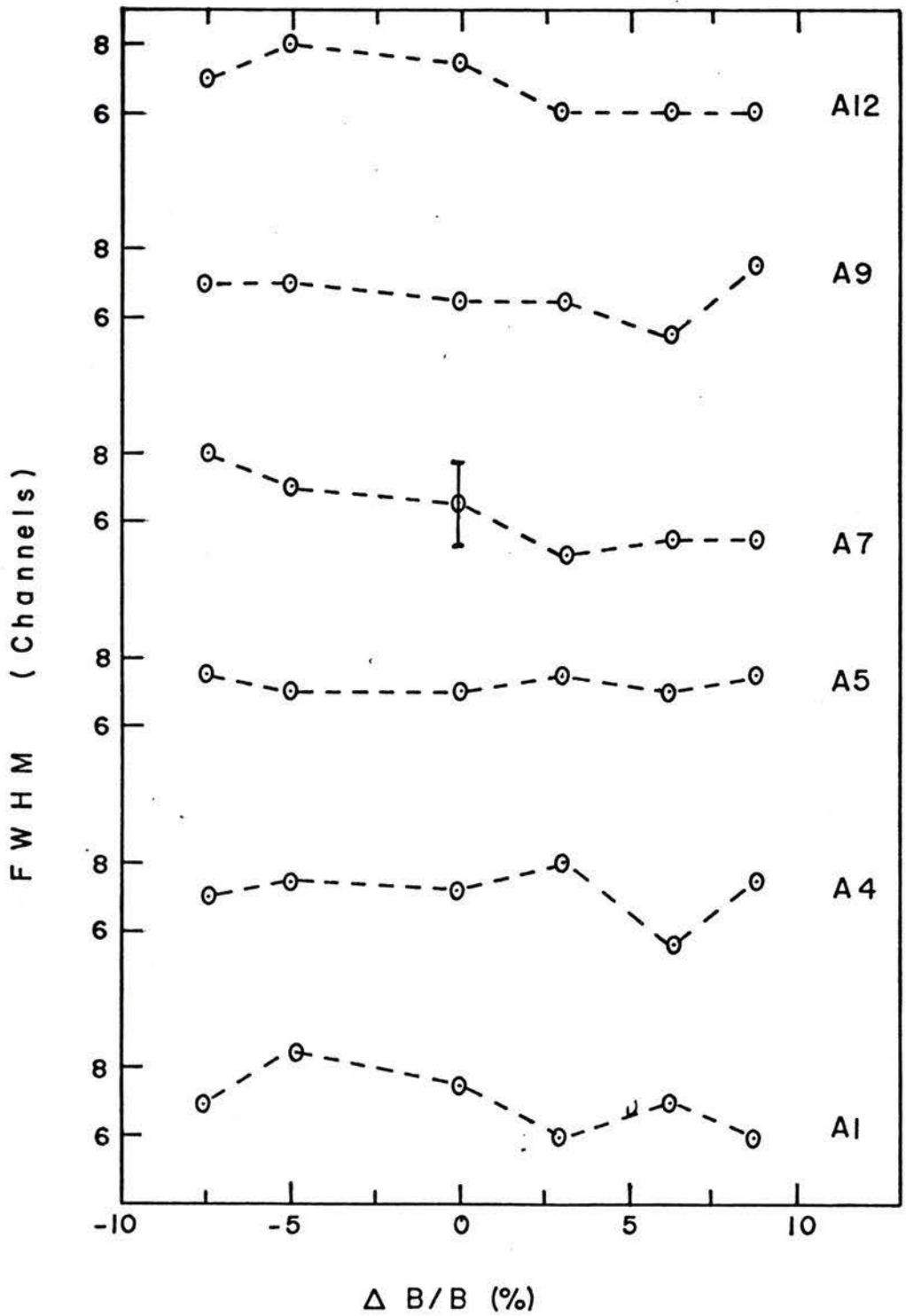


Fig. 6.13 Dependence of resolution (FWHM) on $\Delta p/p$ ($= \Delta B/B$) for several hodoscope elements.

6.4.11 Second Order Effects

An upper limit on some of the second order effects can be obtained.

Chromatic aberrations were estimated from data obtained from the spark chamber which, as explained in Section 6.4.3, provide two pion distributions, one projected from the left and the second from the right hand side of the spark chamber. The two distributions would normally coincide if the channel were set up correctly. If chromatic aberrations were significant, a split of the two distributions would have been observed for the different hodoscope elements. As it is, experimental results show a split well within the experimental error. The conclusion is that chromatic aberrations are zero to within ± 2 wires or ± 0.46 cm corresponding to a momentum spread of $\pm 0.4\%$ p_0 . This compares with a calculated value of ± 0.6 cm.

Geometric aberrations were estimated by placing a software hole in the spark chamber separating the two halves; i.e., pions passing through the centre were vetoed by an anti-coincidence arrangement. The hole was ± 7 wires around the centre wire. This arrangement gives more weight to pions away from the axis which results in an exaggeration of any spherical aberrations which are present. The experimental results, using five hodoscope elements including the two extreme elements on either side, indicated no separation to within ± 3 wires or ± 0.7 cm of the pion peaks. This corresponds to a momentum spread of $\pm 0.6\%$ p_0 , which compares with a calculated value of ± 0.1 cm.

6.4.12 Comparison of Calculated and Measured Pion Flux

For the same target used in estimating the pion flux in Section 6.3.2, the total measured flux was $5.1 \times 10^3 \pi^+$ /sec. The measurement was carried out with the scintillation counters B1 and B2 in coincidence. B2 time delay with respect to B1 was set to discriminate against electrons and muons. The energy spectrum, shown in Fig. 6.14, was obtained with the total energy counter and a 256 channel pulse height analyzer.

Comparison of the calculated and measured pion fluxes, which are

calculated using NPFLUX	$4.5 \times 10^3,$
calculated using MBEND	$5.6 \times 10^3,$
measured	$5.1 \times 10^3,$

indicates that the calculated and measured values differ by about 10%. However, because of the uncertainty in the value of the proton current (assumed 25 nA for the purpose of the calculation), this rather good agreement must be considered fortuitous.

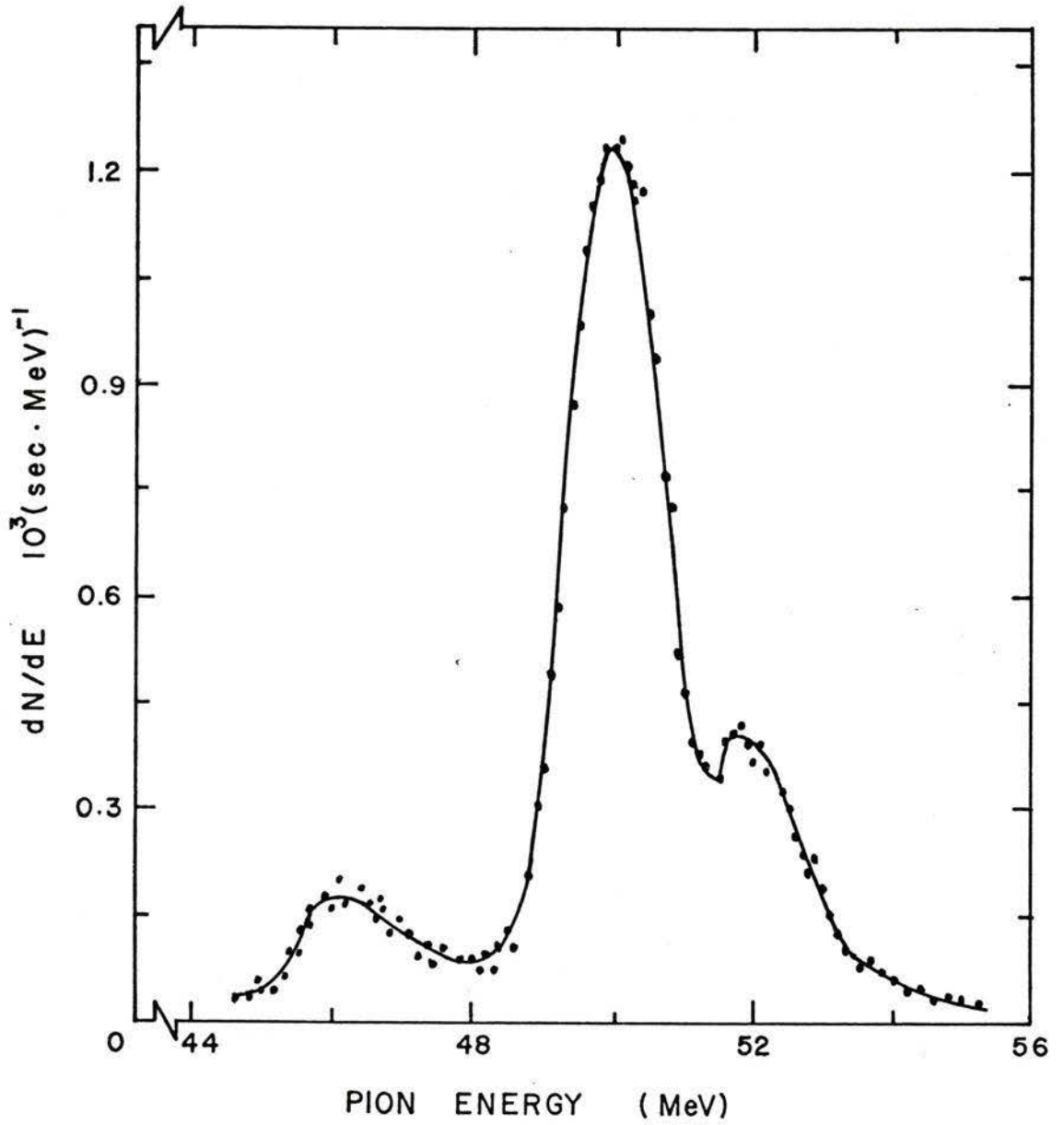


Fig. 6.14 Experimental pion energy spectrum for the Berkeley Channel using 6" Be target.

CHAPTER 7

MISCELLANEOUS TOPICS

7.1 Comparison with Other Channels

The dual purpose character of the TRIUMF channel, being designed specifically to provide both pions and muons, makes it difficult to compare with the other high intensity muon channels, namely the proposed SIN and LAMPF channels. Although this channel appears similar to the LAMPF channel, it is different in at least two respects. First, the pion collection section is also a stopped pion channel and is designed as such. Secondly, pion extraction is made at a backward angle of 135° (compared to LAMPF forward angle of 60°) in order to minimize high energy neutrons and protons. It is a lower cost channel compared to LAMPF since it is simpler and employs fewer quadrupoles and magnets.

The greater sophistication of the LAMPF channel and analyzing system is rewarded by a muon beam of high purity. But this has been achieved at a large cost. The main characteristics of the TRIUMF and other channels are summarized in Table 7.1 for comparison. Since the proton current available to the LAMPF channel is 1 mA compared to the 100 μA for TRIUMF, yields should be compared at the same current. Therefore, the TRIUMF channel performance, as far as fluxes are concerned, is comparable to that of LAMPF, $2.1 \times 10^4 \mu^- (1 \mu\text{A} \cdot \text{sec} \cdot \text{MeV}/c)^{-1}$ for TRIUMF, and $0.7 \times 10^4 \mu^- (1 \mu\text{A} \cdot \text{sec} \cdot \text{MeV}/c)^{-1}$ for LAMPF.

Table 7.1

Comparison of the TRIUMF, LAMPF, and SIN Channels

	E_p MeV	I_p mA	Angle of extraction	p_π MeV/c	$\frac{\Delta p_\pi}{p_0}$ full	μ^- Flux at Exit of Straight Section $10^6 (\text{sec} \cdot \text{MeV}/c)^{-1}$	
						forward	backward
TRIUMF	500	0.1	135°	160	0.55	-	2.1
				100	0.30	1.4	-
LAMPF	800	1.0	60°	180	0.45	-	7.0
				90	0.15	9.0	1.0
SIN	590	0.1	0°	200	0.27	21	21

These values are for backward muons from pions having central momenta of 160 and 180 MeV/c respectively. Furthermore, since the LAMPF beam peaks at 112 MeV/c and the TRIUMF beam at 82 MeV/c, the stopping rate for TRIUMF is 30% better. However, for forward muons, the LAMPF analyzing system is superior to that of TRIUMF.

The SIN channel has the advantage of a large solid angle of acceptance (75 msr for SIN vs. 26 msr for TRIUMF) made possible by extracting pions at 0° with the channel entrance only 30 cm from the production target. The other factor is the large capture fraction of the solenoid. Different calculation procedures may account for some of the differences between the three machines.

7.2 Possible Use of the Pion Collection System for Scattering Experiments

The use of the first section of the channel for scattering was not considered as a design criteria. However, interest in this mode of operation led to an investigation (Reeve, 1972) of the possible use of the channel for scattering experiments. It was shown by Reeve that an improvement in resolution is obtained if a focus is obtained and slits are placed downstream from Q3 (see Fig. 4.5). On the other hand, in the pion mode of operation discussed in Section 4.1.1, a focus is obtained and slits are placed upstream from Q3. This is because placing the focus downstream reduces the solid angle of acceptance, as calculated by NPFLUX, from 28 to 19 msr. For pion scattering experiments, this reduction is not serious.

Whether the slits are placed upstream or downstream from Q3 does not affect the operation of the channel for stopped muons, since the slits are kept fully open in this case. It should be noted, though, that the improvement in resolution, obtained by placing the slits downstream, is not very large. The re-optimized channel, as reported by Reeve, has a first order resolution of $\pm 1.7\% p_0$ for a projected source size of ± 3.5 cm, compared to $\pm 2.5\% p_0$ for the reference channel described in Section 4.3 and 3.0% for the channel with slits upstream of Q3 described in Section 4.4.1 for the same source size.

7.3 Beam Switching

The method adopted (Al-Qazzaz and Pearce, 1971) for switching the beam between two users is illustrated in Fig. 7.1 where the quadrupole triplet after the analyzing magnet is mounted on a platform that can be turned through a small angle. To switch between the main user and the parasite experiment, the current of the bending magnet is changed slightly to reduce the angle of bend, and the platform carrying the triplet is rotated accordingly. Thus, the switching should take only a few minutes.

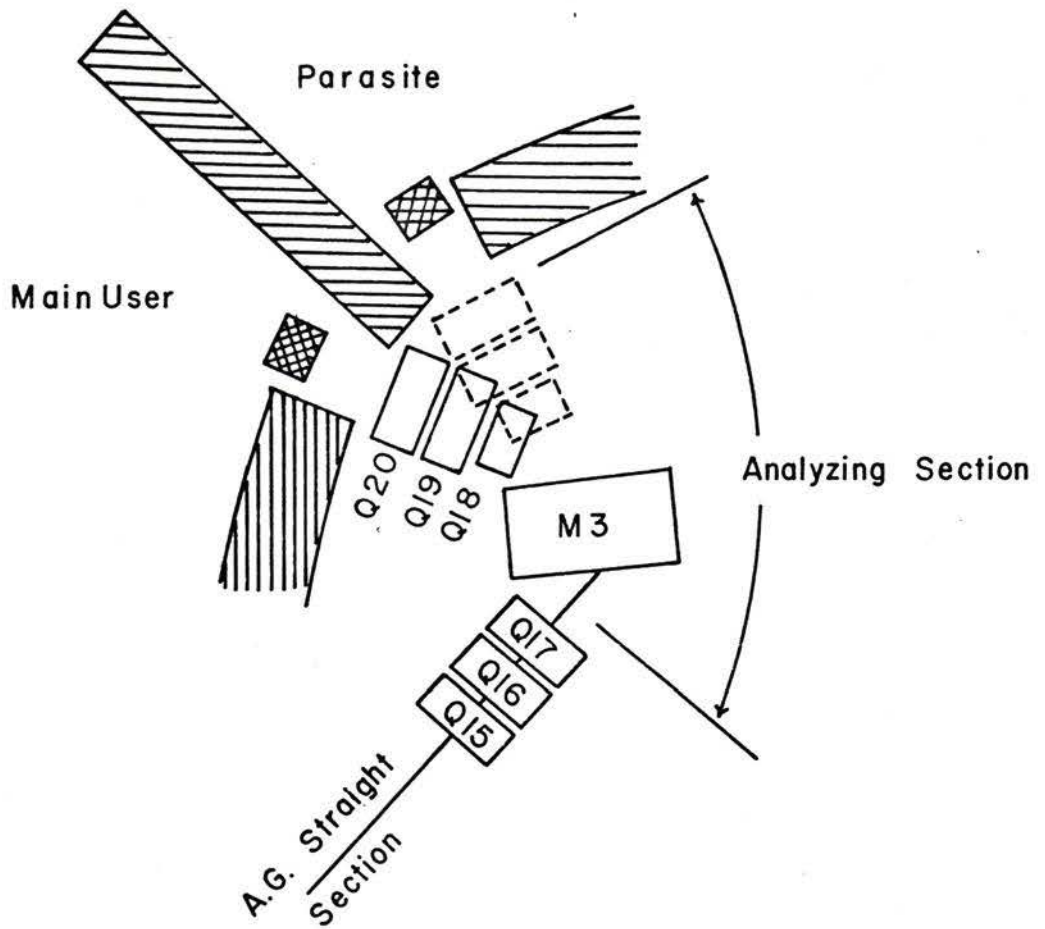


Fig. 7.1 Schematic diagram showing the arrangement for beam switching between two users.

7.4 Vacuum, He or Air

The question of whether to use vacuum, helium-filled bags, or air in the channel has been investigated (Pearce, 1968). As far as beam loss caused by multiple scattering by air or helium, it was concluded that air should be excluded because it caused an rms displacement four times larger than helium, resulting in an unacceptable beam loss.

The choice between helium or vacuum was based on cost consideration and it was concluded by Pearce that vacuum is probably cheaper. Also, when the channel is operated at a momentum of 100 MeV/c or lower, multiple scattering losses caused by helium become significant. Therefore, vacuum is recommended for the channel described in this work.

7.5 Some Comments on the Engineering Aspects of the Channel

7.5.1 Magnet Spacing

The actual dimensions of the quadrupoles and the bending magnets are not known yet except for the first radiation-hardened quadrupoles. Therefore, magnet spacing was based on estimates of the overall dimensions. Thus, the quadrupoles Q1 and Q2 (see Fig. 5.5) should be as close to each other as possible. Also, Q2 should be as close as possible to the first bending magnet M1. This is also true of the distance between Q4 and Q5. On the other hand, the distance between the second bending magnet M2 and Q4 was chosen to allow the undeflected neutral particles to pass through to the neutron trap without hitting the quadrupole. A narrow-type quadrupole for Q1 will be advantageous, but this was rejected for cost reasons.

For the A.G. section, as mentioned in Section 5.2.2, the separation between individual quadrupoles should be as small as possible. The analyzing magnet should be placed as close as possible to Q17. Similarly Q18, which should preferably be narrow-type, is placed as close as possible to the magnet. The last three quadrupoles also should have minimum spacings.

7.5.2 Magnet Length

Except for Q1, all the other quadrupoles are chosen to have 12" pole pieces. For the 12" aperture quadrupoles this corresponds to an effective length of 18" (46 cm). This is adequate for the calculations, which assume a hard-edge model (see Appendix B) of the field distribution, to be meaningful. Shorter quadrupoles are desirable for the pion collection system but the calculations, using the commonly available beam optics computer codes, will not be representative of the actual behaviour of the channel. For the 10" aperture quadrupoles of the A.G. section, shorter quadrupoles may be chosen. However, the choice of these lenses should be based, principally, on cost consideration. The Chicago-type thin lenses (Culligan *et al.*, 1964) should be considered for this purpose.

For the bending magnets M1 and M2, 20" long pole pieces are chosen because of the relatively large gaps used. With the 10" gaps, shorter magnets will result in a field distribution dominated by the fringe fields which makes the calculations based on the hard-edge model not very meaningful. Computer codes employing ray tracing techniques through any form of field configuration without the use of hard-edge models are available. But they are inefficient and not suitable for optimization because of the excessive computing time required.

7.5.3 Special Arrangement for Pion Experiments

In order to use the pion collection section for experiments requiring high pion fluxes and low muon content, the first three or four quadrupoles of the A.G. straight section (starting with Q6) have to be removed to make room for experimental equipment. Therefore, these lenses should be mounted together on a single table which may be removed and replaced quickly with the overhead crane.

CHAPTER 8

CONCLUSIONS

The channel design described in Chapters 4 and 5 satisfies the design criteria, and was selected after considering alternate concepts with due regard to costs.

In Phase One of the design (the pion collection system) the emphasis was on maximizing the number of stopped pions since this section of the channel was intended to serve as a stopped pion channel. The optimization of Phase Two was carried out to maximize the number of muons, particularly muons from the backward decay of pions. Although the emphasis was on negative particles, the channel is capable of providing particles of both polarity. The yields for positive particles are about three times higher than those for negative particles.

The operating energy of the channel is variable and expected yields for the Phase One design were calculated for several values of the central momentum between 60 MeV/c and 180 MeV/c and are given in Table 4.4. The calculations indicated that the optimum value for the maximum operating momentum is 160 MeV/c. Thus, the yields for the various modes of operation were calculated for this momentum as well as the design momentum of 100 MeV/c. Should the maximum channel momentum be restricted to 140 MeV/c because of lack of funds, the yields for 140 can readily be obtained by interpolating in Table 4.4.

In Table 8.1 some examples of the number of stops in targets 1 g/cm^2 and 50 mg/cm^2 and the appropriate degrader are given, together with the total flux available for several modes of operation and the target thickness required to stop at least 80% of the given flux. It is seen that the best mode of operation, as far as the number of stops is concerned, is that when an absorber is used to stop the pions and degrade the muon beam simultaneously. The values given for this case take account of losses due to multiple scattering. The only disadvantage is the background of particles produced in the absorber. However, the analyzing magnet may be used to reduce this background. This mode of operation should be examined experimentally when the Phase One channel is completed.

The accuracy of the calculated values quoted was estimated by comparing measured and calculated values at an experiment being performed at Berkeley. As far as the optics is concerned, the discrepancy is approximately equal to the experimental error as discussed in Chapter 6. Although the measured and calculated pion flux differ by only 10%, the agreement is probably fortuitous in view of the uncertainty in the value of the proton current.

The performance of the channel described in this work compares reasonably well with proposed channels in other facilities. Normalized to the same current, the LAMPF and the TRIUMF channels yield approximately the same flux of backward muons. The SIN channel provides a larger flux, as seen in Table 7.1, which is due to the high capture

rate of the solenoid. However, different calculation procedures may account for some of the differences in yields.

The present design is flexible, as can be seen from several possible modes of operation discussed in Chapters 4 and 5. The pion collection system alone can be used for providing muons as well as pions. The addition of a straight section can be made in stages over a period of time.

rate of the solenoid. However, different calculation procedures may account for some of the differences in yields.

The present design is flexible, as can be seen from several possible modes of operation discussed in Chapters 4 and 5. The pion collection system alone can be used for providing muons as well as pions. The addition of a straight section can be made in stages over a period of time.

Appendix A

FUNDEMENTAL PROPERTIES OF PIONS AND MUONS

Some fundamental properties of the pions and the muons are listed below:

	<u>Pions</u>	<u>Muons</u>
Charge states	+, -, 0	+, -
Mass	π^{\pm} 139.576 \pm 0.011 π^0 134.972 \pm 0.012	105.6594 \pm 0.0004
Intrinsic spin	0	1/2
Magnetic moment		1.00116616 μ_0^* \pm .00000031
Parity	-1	+1
Helicity		μ^- +1 μ^+ -1
Lepton number	0	μ^- +1 μ^+ -1
Mean Life (sec)	π^{\pm} (2.6024 \pm 0.0024) \times 10 ⁻⁸ π^0 (0.84 \pm 0.10) \times 10 ⁻¹⁶	(2.1994 \pm 0.0006) \times 10 ⁻⁶

* $\mu_0 = \frac{e\hbar}{2m_\mu c}$, the muonic Bohr magneton.

Appendix B

BASIC CONCEPTS OF BEAM TRANSPORT SYSTEMS

B.1 Definitions and Notation

In a beam transport system, a beam of particles is focussed and its direction controlled by a series of magnetic devices which are separated by field-free spaces called drift spaces. These devices and drift spaces are referred to as beam transport elements.

A charged particle in a magnetic field is subject to the Lorentz force

$$\vec{F} = e\vec{v} \times \vec{B} \quad (\text{B.1})$$

where e is the charge on the particle, v its velocity, and B the magnetic field. The Lorentz force acts in a plane orthogonal to the direction of motion and therefore causes the particle to be displaced from its initial path.

The path followed by the particle under the influence of the applied fields is called the particle "trajectory". The "optical axis" or central trajectory is defined for a given initial position and direction. Trajectory coordinates for particles with other initial conditions are referred to this central trajectory.

If, as is the case for many beams, the angular deviations from the optical axis, σ , are small, then the approximation $\sin \theta = \theta$ is valid. This is referred to as the paraxial approximation.

In developing the equations of motion, sufficient accuracy is often obtained if only the linear terms in the displacement and angle are retained. This will be referred to as the linear approximation and the resulting equations as the linearised equations of motion. The symmetry properties of the quadrupoles and magnets chosen as beam transport elements permit the assumption of independent equations for the x- and y-motions.

B.2 Beam Handling Devices

The most commonly used beam handling elements are the quadrupoles and bending magnets. Quadrupoles are used as "lenses" for containing the beam of particles transported between the source and the experimental area. A quadrupole magnet consists of four symmetrically placed iron pole pieces mounted on a common yoke and excited by current carrying coils. An ideal quadrupole would have a symmetric field as shown in Fig. B.1.

The components of the quadrupole field are (Banford, 1966)

$$B_x = gy,$$

$$B_y = gx,$$

and

$$B_z = 0,$$

(B.2)

where

$$g = \frac{\partial B_x}{\partial y} = \frac{\partial B_y}{\partial x} = \text{constant}.$$

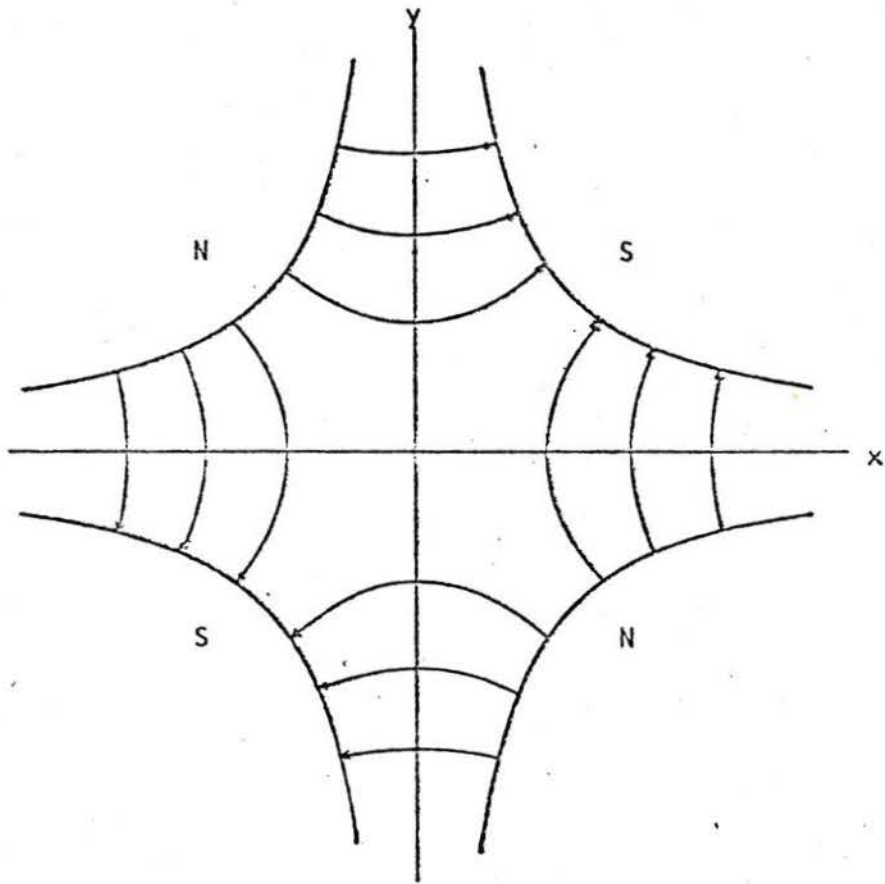


Fig. B.1 The Ideal Quadrupole Field

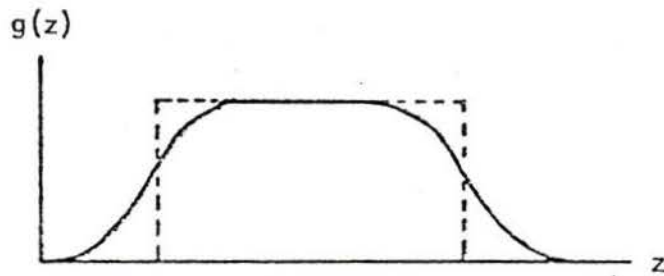


Fig. B.2 The Hard-Edge Model

g is known as the magnetic field gradient of the quadrupole. Then the components of the Lorentz force are

$$\begin{aligned} F_x &\approx +evB_y = +evgx \\ F_y &\approx -evB_x = -evgy \end{aligned} \tag{B.3}$$

by using (B.2).

Therefore
$$F_x = -F_y$$

i.e., if the force has a focussing effect in the xz -plane, it will have a defocussing effect in the yz -plane. This action can be reversed by rotating the quadrupole through 90° so that the north and south poles are interchanged. A net focussing effect in both planes can be obtained by using two quadrupoles, one of each type.

The first order equations of motion of a charged particle travelling through a quadrupole, assuming paraxial conditions, are obtained (Banford, 1966) from equations (B.1), (B.2), and (B.3); thus, from (B.1)

$$F_x = e(v_y B_z - v_z B_y) = -ev_z B_y$$

so
$$m \frac{d^2x}{dt^2} = -ev_z gx$$

from equation (B.3).

With the approximation
$$v = \frac{ds}{dt} \approx \frac{dz}{dt},$$

$$mv^2 \frac{d^2x}{dz^2} = -evgx.$$

Therefore
$$\frac{d^2x}{dz^2} = - \frac{e}{p} gx .$$

Similarly for the y-plane.

The equations of motion are

$$\frac{d^2x}{dz^2} + \frac{g}{(B\rho)} x = 0$$

(B.4)

in the focussing plane, and

$$\frac{d^2y}{dx^2} - \frac{g}{(B\rho)} y = 0$$

in the defocussing plane, where $(B\rho)$ is known as the "magnetic rigidity" and is related to the particle momentum by

$$(B\rho) = \frac{mv}{e} = \frac{p}{e} ,$$

m being the relativistic mass of the particle and v its instantaneous velocity.

For a practical quadrupole, the field gradient g varies along the z -axis as shown by the solid line of Fig. B.2. For purposes of computation, a "hard-edge model" (Steffen, 1964) is used, as shown by the dashed line of Fig. B.2. Consequently one defines an "effective length" L such that

$$L = \frac{\int_{-\infty}^{+\infty} g(z) dz}{g}$$

(B.5)

where $g(z)$ is the measured field gradient along the z -axis of the real quadrupole and g is the value of the gradient well inside the magnet.

This definition of L ensures that the actual field and the hard-edge model field are equivalent to first order of approximation insofar as their focussing (or defocussing) action on a charged particle is the same. The error introduced by assuming a hard-edge model ranges from a few percent for long, small-aperture quadrupoles to about 20% for short, large-aperture quadrupoles (Alexander and Reeve, 1971).

Bending magnets are used to deflect the optical axis of a beam of particles in the desired direction. A hard-edge model is also used here for the homogeneous or constant field magnet and the effective length is defined by

$$L = \frac{\int_{-\infty}^{+\infty} B(z) dz}{B} \quad (B.6)$$

where $B(z)$ is the measured field and B is the field well within the magnet.

The various parameters which describe a bending magnet are indicated in Fig. B.3. The magnetic field is related to the radius of curvature, r_0 , and the magnetic rigidity ($B\rho$) by

$$B = \frac{(B\rho)}{r_0} \quad (B.7)$$

The angle of bend θ is related to r_0 by

$$L = r_0\theta \quad (B.8)$$

If the pole faces of the bending magnet are normal to the beam axis, the entrance angle ϕ_1 and the exit angle ϕ_2 will each have a value of zero.

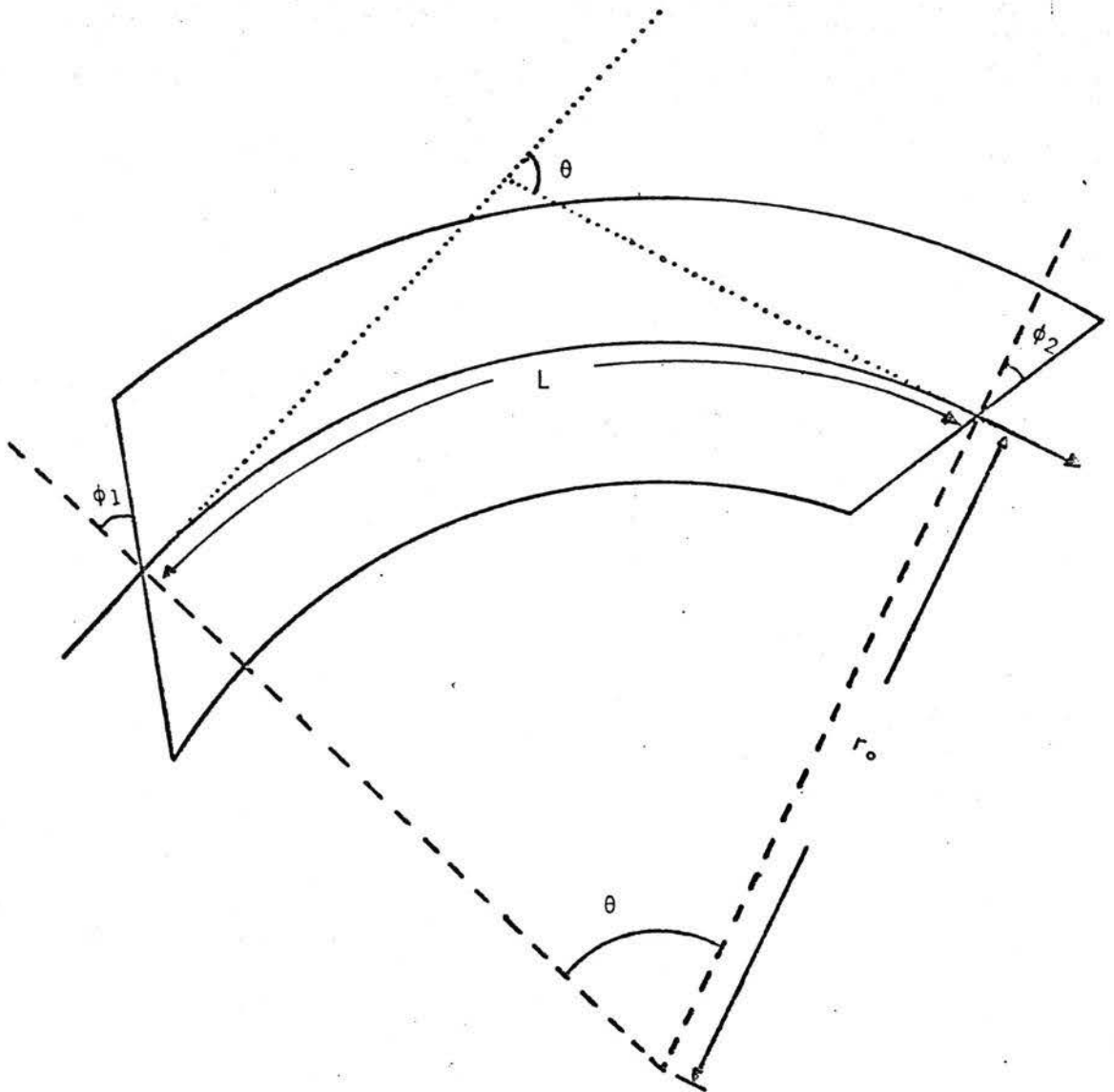


Fig.B.3 Bending Magnet, A Plan View
Showing Magnet Parameters.
As shown, θ and ϕ_1 are positive
and ϕ_2 is negative.

The first order equations of motion of a charged particle in the field of a normal bending magnet, assuming paraxial conditions, are (Hansford, 1965)

$$\frac{d^2x}{dz^2} + \frac{1-n}{r_o^2} - \frac{1}{r_o} \cdot \frac{\Delta p}{p} = 0 \quad (\text{B.9})$$

in the plane of bend, and

$$\frac{d^2y}{dz^2} + \frac{n}{r_o^2} = 0$$

in the non-bending plane, where n is the field index given by

$$n = - \frac{r_o}{B} \cdot \frac{\partial B}{\partial r}$$

and is zero for homogeneous (constant field) bending magnets. The third term represents the effect of beam momentum spread.

A wedge magnet ($\phi_1 = \phi_2 = 0$) focusses in the horizontal plane. A bending magnet with rotated pole faces has additional focussing properties on the edges which may strengthen or weaken the focussing effect of the normal magnet; it can be considered as a normal magnet and each of the pole face rotations can be represented by a thin lens or, as it is often called, a focussing (or defocussing) edge. Whether the thin lens is a focussing or a defocussing edge depends on the sign of the angles ϕ_1 and ϕ_2 . The convention used here (Penner, 1961) is that if the effect of the rotated pole face is to produce focussing in the vertical plane, the angle concerned is considered positive.

For the focussing effect of pole face rotations, we have

$$\frac{d^2x}{dz^2} + \frac{\tan \phi}{Lr_0} \cdot x = 0$$

and

(B.10)

$$\frac{d^2y}{dz^2} - \frac{\tan \phi}{Lr_0} \cdot y = 0$$

for the bending and non-bending planes respectively. ϕ represents either an entrance or an exit angle. This crude thin lens approximation for pole face rotations can be improved by replacing the angle ϕ by $(\phi - \psi)$ where ψ is given by (Brown, 1967)

$$\psi = ah \frac{1 + \sin^2 \phi}{r_0 \cos \phi}$$

where h is the magnet gap and a is evaluated for the fringing fields. Typical values of a for actual magnet may range from 0.3 to 1.0, depending on the geometry of the magnet. For the purpose of computation a value of 0.5 or 0.6 may be taken.

B.3 Particle Trajectories

The equations of motion through the various elements of a beam transport system can all be represented by a single trajectory equation

$$\frac{d^2u}{dz^2} + k(z)u - d = 0 \tag{B.11}$$

$$u = x \text{ or } y$$

where $k(z)$ takes the following forms for the various elements given by equations (B.4), (B.9), and (B.10):

$\frac{1}{Lf}$ for a thin lens

$\frac{g}{(B\rho)}$ for a quadrupole

$\frac{\tan \phi}{Lr_0}$ for a focussing or defocussing edge

$\frac{1-n}{r_0^2}$ for a bending magnet in the plane of bend

$\frac{n}{r_0^2}$ for bending magnet in the non-bending plane

and d has the form

$\frac{1}{r_0} \cdot \frac{\Delta p}{p}$ in the plane of bend for a beam of particles
with momentum spread.

The solutions to the linearised equation (B.11) are given in terms of the trigonometric sine and cosine functions when the element is focussing, $k(z) > 0$, and in terms of the hyperbolic functions when defocussing, $k(z) < 0$.

In matrix notation (Penner, 1961), the solutions can be represented by

$$\begin{pmatrix} u \\ u' \\ \frac{\Delta p}{p} \end{pmatrix} = \begin{pmatrix} R_{11} & R_{12} & R_{13} \\ R_{21} & R_{22} & R_{23} \\ 0 & 0 & 1 \end{pmatrix} \begin{pmatrix} u_0 \\ u'_0 \\ \frac{\Delta p}{p} \end{pmatrix} \quad (\text{B.12})$$

where $u = x$ or y and the zero subscript refers to initial values of the displacement u , the slope $u' = \frac{du}{dz}$ and the momentum deviation $\frac{\Delta p}{p}$ which is constant. The matrix elements R_{ij} are functions of the trigonometric circular or hyperbolic sine and cosine functions.

When $u_0 = 1$, $u'_0 = 0$ and $\frac{\Delta p}{p} = 0$, u is called a sine-like trajectory.

When $u_0 = 0$, $u'_0 = 1$ and $\frac{\Delta p}{p} = 0$, u is called a cosine-like trajectory.

When $u_0 = u'_0 = 0$ and $\frac{\Delta p}{p} = 1$, u is called a dispersion trajectory.

The above three trajectories are called "principle trajectories"; all other trajectories can be expressed in terms of these principal trajectories. If the displacement and slope of the output trajectories after the final element are independent of the beam momentum, the system is called "dispersionless" or "achromatic". For such a system, the R_{13} and R_{23} components of the transfer matrix are zero. If $R_{12} = 0$, a focus is said to be obtained in which case R_{11} will represent the magnification of the system.

B.4 Phase Space and Ellipse Representation

Phase space is the six-dimensional space (x, y, z, p_x, p_y, p_z) where x, y and z are the position coordinates in three dimensional Cartesian space, and p_x, p_y and p_z are the three corresponding momentum coordinates for a point in this space. The motion of a particle in time in the three-dimensional position space is represented by the motion of a point in phase space; and a beam of particles is represented by a group of points in phase space, each point corresponding to one particle in the beam. The group of points will then fill a certain volume in phase space; the surface of this volume defines the boundaries of the beam.

On transformation of the phase space volume in time, the particle density in phase space obeys Liouville's Theorem. This theorem states that for motion in an external field, for which Hamiltonian equations can be written, the particle density in phase space remains constant. Thus the phase space volume containing a group of particles remains constant although the shape may change. A derivation of this theorem is given in Steffen (1964). If the particle motion along the three coordinates of real space is mutually independent, the theorem applies to the motion in each plane separately and the areas in the three hyper-planes (x, p_x) , (y, p_y) , and (z, p_z) remain constant. In paraxial beam optics one can assume in the linear approximation that the axial momentum p_z is constant; thus

$$p_x = m \frac{dx}{dt} = m \frac{dx}{dz} \cdot \frac{dz}{dt} = p_z x'.$$

Since $x' \propto p_x$, the area in phase plane (x, x') which is occupied by a beam of particle trajectories is also a constant of the motion.

Similarly the area in the phase plane (y, p_y) can be represented by an area in the plane (y, y') and its size remains constant.

The area of phase space divided by the constant π containing the trajectories of a beam of particles is called the emittance of the beam. The area in phase space enclosed by all particle trajectories transmitted by a beam handling device is referred to as the acceptance of the device.

The most common phase space contour of beam encountered in practice is a polygon. But this can be well approximated by an ellipse which contains a given fraction of the particle trajectories (e.g. 90% of them). The ellipse representation offers certain advantages; it can be described by three parameters only, it can conveniently be handled mathematically, and more important, it retains its elliptical shape on transforming through a linear beam transport system.

The equation of the phase space ellipse in the (u, u') space is (Steffen, 1964)

$$\gamma u^2 + 2\alpha u u' + \beta u'^2 = \epsilon \quad (\text{B.13})$$

with the normalizing condition

$$\beta\gamma - \alpha^2 = 1$$

where $u = x$ or y .

β is called the amplitude function; it is a function of z and it depends on the initial ellipse parameters β_0 , α_0 , and ϵ . Fig.B.4 shows the phase space ellipse of area F and its relation to the parameters α , β , γ , and ϵ .

The maximum displacement of the trajectories within the ellipse U_{\max} is given, in terms of the ellipse parameters, by

$$U_{\max} = (\epsilon\beta)^{\frac{1}{2}}.$$

The maximum slope, or angular deviation, is given by

$$U'_{\max} = (\epsilon\alpha)^{\frac{1}{2}}.$$

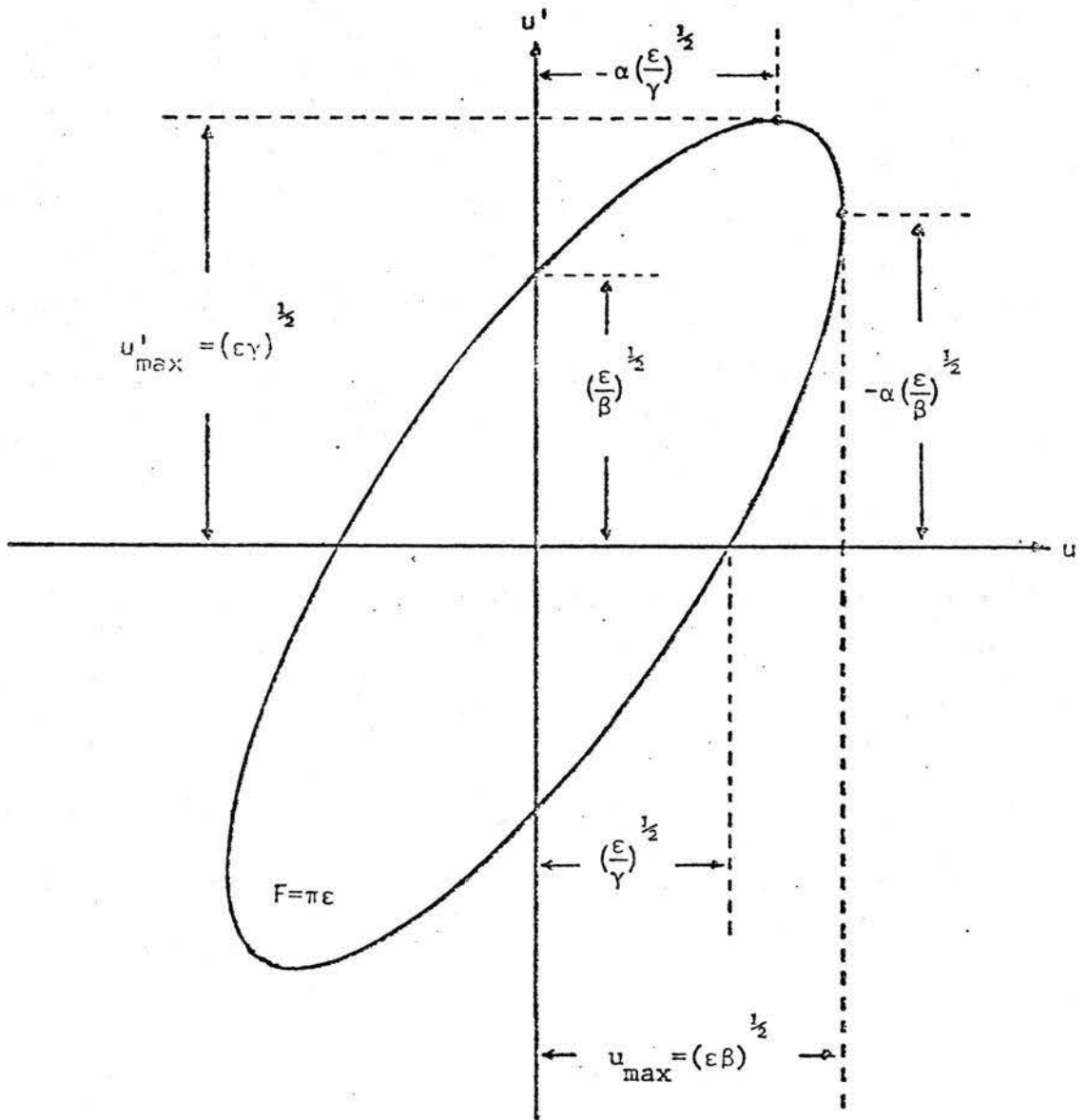


Fig .B.4 Phase Space Ellipse, Relation to Ellipse Parameters

The trajectories U_{\max} and U'_{\max} do not correspond to any single particle but represent, at any point along the beam axis, the maximum displacement and slope respectively. $U_{\max}(z)$ is called the beam envelope; it is useful to determine the apertures required to transmit a beam of a given emittance through a transport system.

B.5 Extension to Second Order

The trajectory equations in Section B.3 were obtained by retaining the first order terms only in the Taylor expansion of the solutions to the equations of motion. If the expansion is terminated with the second order terms, the solution may be written (Brown, 1967), in terms of the initial values of the coordinates, as

$$x_i = \sum_{j=1}^6 R_{ij} x_j(0) + \sum_{j=1}^6 \sum_{k=j}^6 T_{ijk} x_j(0) x_k(0) \quad (\text{B.14})$$

where x_i , $i=1$ to 6 are the elements of a column vector which stand for the coordinates x , x' , y , y' , ℓ , and $\Delta p/p$ respectively. R_{ij} are first order and T_{ijk} are second order matrix elements calculated by TRANSPORT (Brown and Howry, 1970). ℓ is the path length difference between an arbitrary ray and the central trajectory. Obviously, the 3 x 3 matrix representation, given in Section B.3, is not adequate in this case and a more general 6 x 6 matrix has been adopted where both the x-plane and y-plane first order solutions are represented (see Appendix K).

The first term of equation (B.14) is the first order solution discussed in Section B.3. The second order matrix elements of interest are the T_{116} , T_{126} , and T_{166} representing chromatic aberrations, and T_{122} representing geometric aberrations generated in dipole magnets. A comprehensive treatment of first and second order theory is given in the report SLAC-75 (Brown, 1967).

Appendix C

π - μ KINEMATICS

C.1 Pion Decay

The dominant decay mode of the pion is

$$\pi \rightarrow \mu + \nu . \quad (C.1)$$

Energy and momentum conservation in the rest frame of the pion leads to, with the usual notation,

$$m_{\pi} = E_{\mu}^{*} + E_{\nu}^{*} \quad (C.2)$$

and

$$p_{\mu}^{*} = p_{\nu}^{*} \quad (C.3)$$

with the stars indicating that the energy and momentum are evaluated in the rest frame of the pion. For the massless neutrino

$$p_{\nu}^{*} = E_{\nu}^{*} . \quad (C.4)$$

Therefore,

$$m_{\pi} = E_{\mu}^{*} + p_{\mu}^{*} . \quad (C.5)$$

C.2 Momentum Range of the Decay Muon

The energy of the decay muon in the laboratory frame is related to its energy in the pion frame by the Lorentz transformation of the energy-momentum four-vector and can readily be shown to be

$$E_{\mu} = \gamma_{\pi} (E_{\mu}^{*} + \beta_{\pi} p_{\mu}^{*} \cos \theta^{*}) , \quad (C.6)$$

where β and γ have their usual meaning in relativity.

The muon energy has a maximum value in the forward decay, when its decay angle $\theta = 0$ with respect to the direction of motion of the parent pion, and a minimum value in the backward decay, when $\theta = 180^{\circ}$. Thus, the upper and lower limits on the muon energy are given by

$$E_{\mu} = \gamma_{\pi} (E_{\mu}^{*} \pm \beta_{\pi} p_{\mu}^{*}) \quad (C.7)$$

It can readily be shown, by a simple application of the Lorentz transformation to a particle in its own rest frame, that

$$E = \gamma m \quad \text{and} \quad p = \beta E \quad (C.8)$$

where m is the rest mass of the particle. Therefore, the following relations are obtained:

$$E_{\mu}^{*} = \gamma_{\mu}^{*} m_{\mu} , \quad p_{\mu}^{*} = \beta_{\mu}^{*} \gamma_{\mu}^{*} m_{\mu} , \quad \text{and} \quad \gamma_{\pi} = \frac{p_{\pi}}{\beta_{\pi} m_{\pi}} \quad (C.9)$$

Using these relations (C.9) in equation (C.7), one obtains, after simplifying,

$$p_{\mu} = \frac{\beta_{\mu}}{\beta_{\pi}} \cdot \frac{\gamma_{\mu}^{*} m_{\mu}}{m_{\pi}} (1 \pm \beta_{\pi} \beta_{\mu}^{*}) p_{\pi} . \quad (C.10)$$

From equation (C.5), using the relations (C.9), one gets

$$\begin{aligned} m_{\pi} &= \gamma_{\mu}^{*} m_{\mu} + \beta_{\mu}^{*} \alpha_{\mu}^{*} m_{\mu} \\ &= \gamma_{\mu}^{*} m_{\mu} (1 + \beta_{\mu}^{*}) \end{aligned} \quad (C.11)$$

or

$$\frac{\gamma_{\mu}^* m_{\mu}}{m_{\pi}} = \frac{1}{1 + \beta_{\mu}^*} \quad (\text{C.12})$$

Substituting (C.12) in (C.10) gives

$$p_{\mu} = \frac{\beta_{\mu}}{\beta_{\pi}} \cdot \frac{1 \pm \beta_{\pi} \beta_{\mu}^*}{1 + \beta_{\mu}^*} \cdot p_{\pi} \quad (\text{C.13})$$

The relativistic addition of velocities (e.g. Landau and Lifshitz, 1962) yields for the laboratory velocity of the muon

$$\beta_{\mu} = \frac{\beta_{\pi} \pm \beta_{\mu}^*}{\beta_{\pi} \beta_{\mu}^*} \quad (\text{C.14})$$

Finally, substituting (C.14) in (C.13) gives the extreme values of the momentum of the decay muon, namely

$$p_{\mu} = \frac{\beta_{\pi} \pm \beta_{\mu}^*}{\beta_{\pi} (1 + \beta_{\mu}^*)} \cdot p_{\pi} \quad (\text{C.15})$$

The maximum and minimum momenta of the decay muon, together with the maximum decay angle discussed below, are given in Table C.1 for several pion momenta.

C.3 Maximum Decay Angle of the Muon

The Lorentz transformation of the energy-momentum four-vector yields the following relations

$$p \sin\theta = p^* \sin\theta^* \quad (C.16)$$

$$p \cos\theta = \gamma(\beta E^* + p^* \cos\theta^*) \quad (C.17)$$

Dividing (C.16) by (C.17) one gets

$$\tan\theta = \frac{\sin\theta^*}{\gamma(\beta E^*/p^* + \cos\theta^*)} \quad (C.19)$$

by using (C.8) and putting $g = \beta/\beta^*$. Equation (C.19) describes the transformation of angles from the pion rest frame to the laboratory frame.

For the pion decay in flight, no particle goes backwards in the laboratory, except for pions with extremely low momentum. Therefore, there will generally be a maximum decay angle θ_{\max} . This maximum angle is obtained by differentiating equation (C.19) with respect to θ^* , then setting $d\theta/d\theta^*$ equal to zero which gives $\cos\theta^* = -1/g$. Thus, using this in equation (C.19) with θ replaced by θ_{\max} , one gets

$$\theta_{\max} = \arctan[(1-\beta^2)/(g^2-1)]^{1/2} \quad (C.20)$$

The maximum decay angle of the muon is tabulated in Table C.1.

Table C.1

π - μ Decay Kinematics

p_{π} <u>MeV/c</u>	p_{μ} (min) <u>MeV/c</u>	p_{μ} (max) <u>MeV/c</u>	σ (max) <u>degrees</u>
40	0.46	62.5	79.8
45	4.08	66.7	61.0
50	7.67	71.0	51.9
55	11.2	75.3	45.7
60	14.8	79.6	41.0
65	18.3	84.0	37.3
70	21.7	88.4	34.2
75	25.2	92.8	31.7
80	28.6	97.3	29.5
85	32.0	102.7	27.6
90	35.3	106.2	25.9
95	38.7	110.8	24.5
100	42.0	115.3	23.2
105	45.3	119.9	22.0
110	48.6	124.6	21.0
115	51.8	129.1	20.0
120	55.1	133.7	19.2
125	58.3	138.3	18.4
130	61.5	143.0	17.6
135	64.7	147.6	17.0
140	67.9	152.3	16.3
145	71.1	157.0	15.8
150	74.2	161.7	15.2
155	77.4	166.4	14.7
160	80.5	171.2	14.2
165	83.6	175.9	13.8
170	86.8	180.7	13.4
175	89.9	185.4	13.0
180	93.0	190.2	12.6
185	96.0	195.0	12.3
190	99.1	200.0	12.0
195	102.2	204.6	11.7
200	105.2	209.4	11.4

C.4 Angular Distribution of the Decay Muons

Because of the isotropic decay in the pion frame, it can be assumed that the number of muons per unit solid angle is constant and is given by:

$$\frac{dN}{d\Omega^*} = \frac{1}{4\pi} \quad (C.21)$$

The angular distribution of the decay muons in the laboratory frame is

$$\frac{dN}{d\theta} = \frac{dN}{d\Omega} \cdot \frac{d\Omega}{d\theta} = \frac{dN}{d\Omega^*} \cdot \frac{d\Omega^*}{d\Omega} \cdot \frac{d\Omega}{d\theta} \quad (C.22)$$

The element of solid angle $d\Omega$ is given by

$$d\Omega = 2\pi \sin\theta \, d\theta \quad (C.23)$$

and a similar expression is obtained for $d\Omega^*$. Consequently, using (C.21), (C.22) and (C.23), one gets

$$\frac{dN}{d\theta} = \frac{1}{2} \sin\theta^* \frac{d\theta^*}{d\theta} \quad (C.24)$$

It can readily be shown, using (C.19), that

$$\frac{d\theta^*}{d\theta} = \frac{\gamma^2(g + \cos\theta^*) + \sin^2\theta^*}{\gamma(g + \cos\theta^*)} \quad (C.25)$$

Substituting (C.25) in (C.24) gives, for the angular distribution

$$\frac{dN}{d\theta} = \frac{\sin\theta^*}{2\gamma} \cdot \frac{\gamma^2(g + \cos\theta^*) + \sin^2\theta^*}{(G + \cos\theta^*)} \quad (C.26)$$

C.5 Useful Tables

The pion and muon kinematics are tabulated in Table C.2 and Table C.3 respectively, where for a given momentum, the energy, β , γ , the magnetic rigidity in Tesla-meters, the decay length in meters, and the surviving fractions in % Tabulated.

In Table C.4 and Table C.5, the range R in g/cm^2 and dp/dR in MeV/c per g/cm^2 are tabulated[†] for the given momenta. The momentum interval chosen is not uniform. A small interval is used when R and dp/dR are sensitive to small changes in momentum.

[†] Data obtained from the report UCRL-2426 Vol. IV.

Table C.2

Pion Kinematics

P_{π} MeV/c	T_{π} MeV	β_{π}	γ_{π}	Rigidity ($B\rho$) T · m	Decay length m	Surviving fraction at 8 m %
40	5.62	0.276	1.04	0.133	2.24	2.68
45	7.08	0.307	1.05	0.150	2.52	4.00
50	8.69	0.337	1.06	0.167	2.80	5.52
55	10.5	0.367	1.08	0.184	3.08	7.19
60	12.4	0.395	1.09	0.200	3.36	8.95
65	14.4	0.422	1.10	0.217	3.64	10.8
70	16.7	0.448	1.12	0.234	3.92	12.6
75	18.9	0.473	1.14	0.250	4.20	14.5
80	21.3	0.497	1.15	0.267	4.47	16.4
85	23.9	0.520	1.17	0.284	4.75	18.2
90	26.5	0.542	1.19	0.300	5.03	20.0
95	29.3	0.563	1.21	0.317	5.31	21.8
100	32.1	0.582	1.23	0.334	5.59	23.5
105	35.1	0.601	1.25	0.350	5.87	25.2
110	38.1	0.619	1.27	0.267	6.15	26.8
115	41.3	0.636	1.30	0.384	6.43	28.4
120	44.5	0.652	1.32	0.400	6.71	29.9
125	47.8	0.667	1.34	0.417	6.99	31.4
130	51.2	0.682	1.37	0.434	7.27	32.8
135	54.6	0.695	1.39	0.450	7.55	34.2
140	58.1	0.708	1.42	0.467	7.83	35.5
145	61.7	0.720	1.44	0.484	8.11	36.8
150	65.3	0.732	1.47	0.500	8.39	38.1
155	69.0	0.743	1.49	0.517	8.67	39.3
160	72.8	0.754	1.52	0.534	8.95	40.5
165	76.5	0.764	1.55	0.550	9.23	41.6
170	80.4	0.773	1.58	0.567	9.51	42.7
175	84.3	0.782	1.60	0.584	9.79	43.7
180	88.2	0.790	1.63	0.600	10.1	44.7
185	92.2	0.798	1.66	0.617	10.4	45.7
190	96.2	0.806	1.68	0.634	10.6	46.7
195	100.2	0.813	1.72	0.651	10.9	47.6
200	104.3	0.820	1.75	0.667	11.2	48.5

Table C.3
Muon Kinematics

P_{π} <u>MeV/c</u>	T_{π} <u>MeV</u>	β_{π} —	γ_{π} —	Rigidity ($B\rho$) <u>T · m</u>	Decay length <u>m</u>	Surviving fraction at 6.5 m <u>%</u>
20	1.88	0.186	1.02	0.067	126	95.05
30	4.18	0.273	1.04	0.100	189	96.67
40	7.32	0.354	1.07	0.133	252	97.49
50	11.2	0.428	1.11	0.167	315	97.99
60	15.9	0.494	1.15	0.200	378	98.32
70	21.1	0.552	1.20	0.234	441	98.56
80	26.9	0.604	1.25	0.267	504	98.74
90	33.1	0.648	1.31	0.300	567	98.88
100	39.8	0.687	1.38	0.334	630	98.99
110	46.9	0.721	1.44	0.367	693	99.08
120	54.2	0.751	1.51	0.400	756	99.16
130	61.9	0.776	1.59	0.434	819	99.22
140	67.7	0.798	1.66	0.467	882	99.28
150	77.8	0.818	1.74	0.500	945	99.32
160	86.1	0.835	1.82	0.534	1008	99.37

Table C.4

Range and dp/dR for Pions in Carbon

<u>P_π</u> <u>MeV/c</u>	<u>R</u> <u>g/cm²</u>	<u>dp/dR</u> <u>(MeV/c)/(g/cm²)</u>
40	0.22	50.7
42	0.26	45.0
44	0.32	40.5
46	0.36	36.0
48	0.42	32.5
50	0.49	29.3
52	0.56	26.7
54	0.63	24.4
56	0.71	22.5
58	0.81	20.7
60	0.92	19.0
65	1.18	15.9
70	1.54	13.5
75	1.96	11.7
80	2.42	10.2
85	2.95	9.00
90	3.58	8.00
95	4.25	7.20
100	4.90	6.6
105	5.50	6.1
110	6.33	5.62
120	8.25	4.88
130	10.4	4.34
140	12.8	3.90
160	18.5	3.30
180	25.0	2.92

Table C.5

Range and dp/dR for Muons in Carbon

P_{π} <u>MeV/c</u>	R <u>g/cm²</u>	dp/dR <u>(MeV/c)/(g/cm²)</u>
20	0.04	148
22	0.05	117
24	0.07	93.0
26	0.09	76.0
28	0.12	63.0
30	0.16	52.5
32	0.20	45.0
34	0.24	38.7
36	0.30	33.7
38	0.36	29.5
40	0.44	25.8
42	0.52	23.2
44	0.61	20.8
46	0.70	18.8
48	0.81	17.1
50	0.95	15.5
52	1.08	14.2
54	1.23	13.2
56	1.38	12.1
58	1.54	11.2
61	1.85	10.1
64	2.15	9.35
67	2.50	8.52
70	2.87	7.80
74	3.41	7.02
78	4.06	6.38
82	4.75	5.84
86	5.48	5.37
90	6.30	4.97
94	7.20	4.65
98	8.10	4.36
102	8.75	4.20
106	9.60	4.00
110	10.7	3.82
120	13.5	3.41
130	16.7	3.11
140	20.0	2.89
160	27.3	2.57
180	35.5	2.37
200	44.7	2.23

Appendix D

STOPPED PION CHANNELS

Some of the low energy pion channels which could be used for stopped pion experiments, as well as pion channels proposed or constructed specifically for stopped pion experiments, are reviewed in the following sections.

D.1 Proposed LAMPF Low Energy Pion Channel

The criteria for designing this channel (Amato *et al.*, 1970) were based on the requirements for low energy pion experiments proposed for LAMPF. The channel was to provide both positive and negative pions, have good resolution ($\pm 0.1\% \Delta p/p_0$ or better), be achromatic and isochronous, have minimum contaminations, have a variable spot size between 1 cm x 2 cm and 10 cm x 10 cm, and finally the channel was to be short and costs were to be minimized.

The proposed channel consists of four rectangular bending magnets preceded and followed by quadrupole doublets. A schematic diagram of the channel is shown in Fig. D.1. Each magnet bends the beam through 60° in the vertical plane with the channel exit at the same level as the entrance. It is symmetric about a plane midway between the second and third magnets.

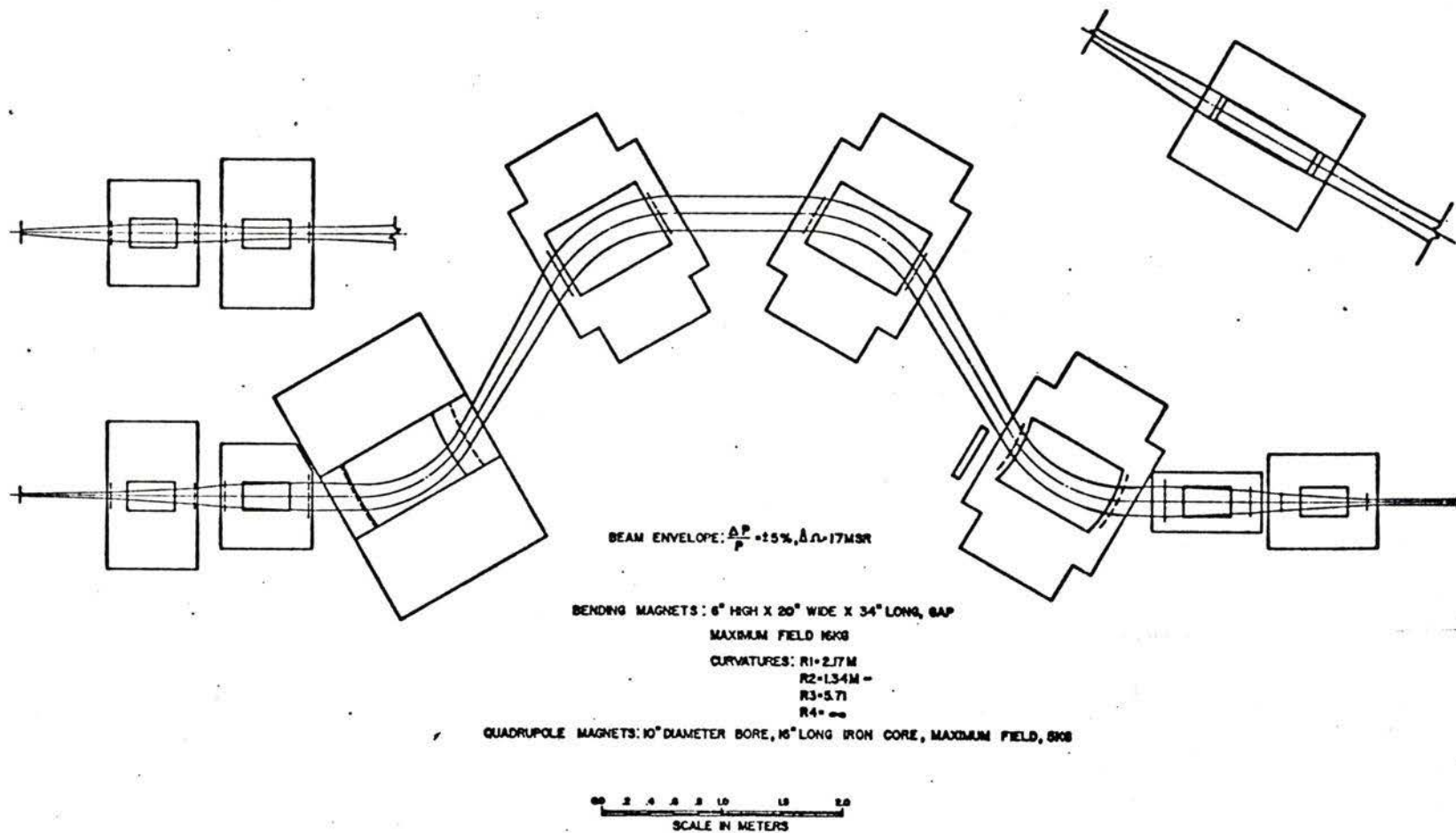


Fig. D.1 The proposed LAMPF low energy general purpose pion channel.
 Reproduced from the LASL report MP-7-10 (Amato *et al.*, 1970).

The calculated performance of the channel indicated that the channel is achromatic and essentially isochronous, transmitting a momentum interval varying between ± 0.05 and $\pm 5\% \Delta p/p_0$. It has a solid angle of acceptance of 17 msr for 10" aperture quadrupoles and 6" gap magnets. It is 14 m long and is capable of operating at high energy; 300 MeV was quoted although the maximum energy has not been decided. The beam size at the exit can be varied by changing the position and fields of the two exit quadrupoles. Calculated pion flux and beam spot sizes, for three values of $\Delta p/p_0$, are (Amato *et al.*, 1970):

$\Delta p/p_0$ (%)	0.05	1.0	5.0
Ω (msr)	10	20	15
x (cm)	1.5	1.5	1.5
x' (mr)	125	125	115
y (cm)	0.13	1.0	3.4
y' (mr)	40	40	45
T_π (MeV)	Fluxes $10^8 \pi^+$ /sec		
50	0.004	1.6	6.0
100	0.19	7.3	27.0
200	0.33	13.0	50.0

The quoted spot sizes were calculated to second order and contained at least 95% of the beam. The fluxes are quoted for a 3 cm carbon target and a pion production angle of 45° . A proton current of 1 mA (6×10^{15} protons per sec) at 800 MeV was assumed.

Beam contamination with protons, neutrons, muons and electrons was considered. Based on data from the LASL pion production experiment (Nagle *et al.*, 1969), 5 protons per π^+ at 50 MeV are assumed to reach the end of the channel. It was proposed to eliminate these protons by using a thin CH₂ absorber placed after the momentum selecting slits at the mid-plane of the channel. The effect of the absorber on the pion beam was shown to be negligible.

Neutrons produced by the target and in the target cell were calculated to be about 10^{14} per sec entering the first quadrupole of the channel. These are sufficiently attenuated by the four bend system. The remaining contamination of about 10^{-4} neutrons per pion is due mainly to neutrons generated from pions and protons stopping in the channel.

Muon contamination of about 9% for 50 MeV pions was calculated from both pion decay and muons from the target area. Electron contamination was estimated using the LASL pion production experiment data. For 50 MeV pions from carbon, the electron/pion ratio is 0.9 for the negative and 0.2 for the positive pions. It is suggested that these electrons are discriminated against by time of flight, except in certain experiments where an electron separator may become necessary.

The cost of the proposed channel was estimated at \$194,000 for a maximum energy of 300 MeV, a maximum acceptance solid angle of 17 msr, and a maximum momentum acceptance of $\pm 10\%$.

D.2 Nevis^{*} Low Energy Pion-muon Channel

As part of the Nevis synchrocyclotron conversion program, a channel intended primarily for stopped pion experiments has been proposed (Holland *et al.*, 1971). The criteria for the design were: the channel should provide both positive and negative pions, contamination with unwanted particles is minimized, flux is maximized, flexibility, cost minimization, variable central momentum and momentum bite, spot size are adjustable between 1" x 1" and 2.5" x 2.5", and small divergence (≤ 10 mr) in at least one plane. The channel should preferably be achromatic and capable of providing muons.

Three designs were considered. The first consists of two equal but opposite 50° bends separated by 40" free space, as shown in Fig. D.2 channel A, with quadrupole doublets preceding and following the bend system; total length is 6.75 m and acceptance solid angle is 38 msr; momentum bite of $\pm 10\%$ is obtainable when the slits are wide open giving a 1" x 1.8" spot, and of $\pm 1\%$ when the slits are ± 0.7 " wide. The second design consists of two 40° bends in the same direction with a quadrupole singlet between them and a doublet before and one after the bends. The third design is a three bend system with doublets preceding and following the bends as shown in Fig. D.2, channel B. Although the system has not been optimized, two 40° bends and an 80° bend in the centre satisfy the criteria.

* Nevis Cyclotron Laboratory, Columbia University, Irvington, New York 10533.

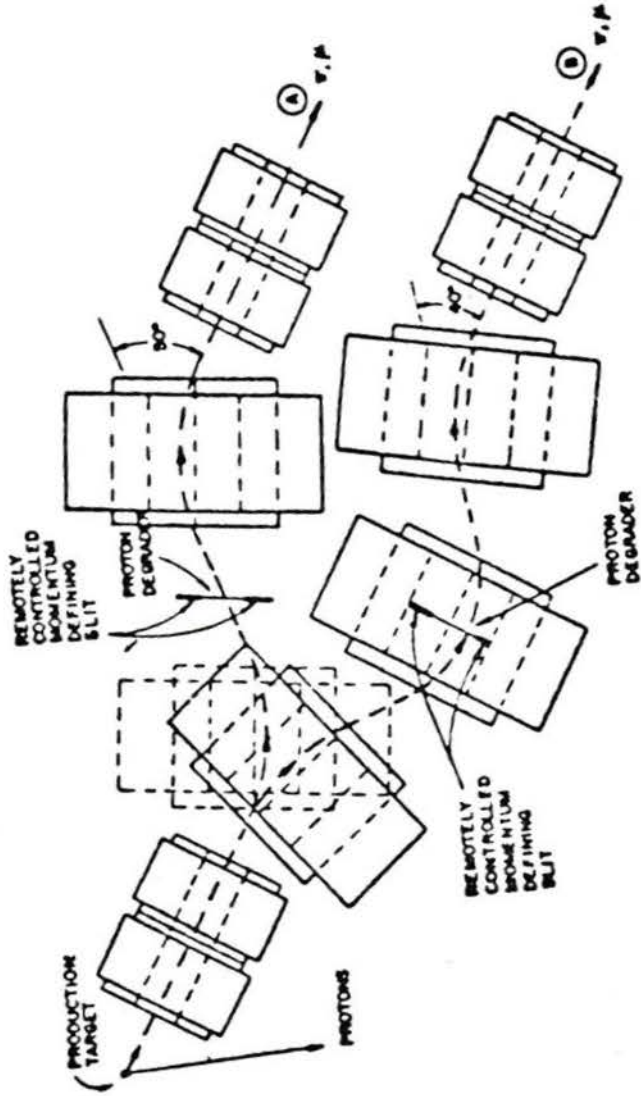


Fig. D.2 Proposed Nevis low energy pion-muon channel, two configurations.

The system is essentially achromatic with a slit system inside the centre bend allowing variable momentum bite between $\pm 1\%$ and $\pm 10\%$. Total length is 8.2 m and acceptance solid angle is 34 msr.

The calculated performance for the third design indicated that for operation with a large momentum bite, $\pm 10\%$, the integrated pion flux was $1 \times 10^8 \pi^+$ /sec or $2.5 \times 10^7 \pi^-$ /sec with 18% electron and 20% muon contamination. For operation with a small momentum bite, $\pm 1\%$, $2.5 \times 10^7 \pi^+$ and $0.7 \times 10^7 \pi^-$ per sec are obtained with the same electron but slightly higher muon contamination. These fluxes are quoted for operation with a central momentum of 100 MeV/c and a spot size of 1.2" x 1.2" for a 3 cm Be target and 20 μ A proton beam current. The contaminations quoted are those originating at the target.

12" aperture Danby type quadrupoles with pole pieces 18" in length were designed and completed. 30" long window frame magnets with 9" gaps and 27" in width were designed.

Appendix E

STOPPED PION/MUON CHANNELS

Examples of existing and proposed channels which are designed to be used for either stopped pions or stopped muons are reviewed in this Appendix.

E.1 SREL* Channel

The SREL pion/muon channel (Funston, 1971) was designed to transport the internally generated mesons from the NASA[†] 600 MeV synchrocyclotron. The criteria were maximum flux of both pions and muons, variable momentum, and the capability of producing both positive and negative mesons.

Four types of channels were considered: a conventional CERN-type channel, a Van der Meer coaxial line, a helical quadrupole channel, and a superconducting solenoid. The conventional CERN-type quadrupole channel was chosen and constructed. The channel consists of three main parts: an input section (to match the main channel to the emittance of mesons generated internally in the cyclotron) consisting of two quadrupoles of 15" and 12" aperture respectively, the main channel having 24 square shaped lenses, and an output section consisting of a single H-type bending magnet. The main channel lenses are all 9.19" long and 10.8" in aperture. The layout of the channel is shown in Fig. E.1.

* Space Radiation Effects Laboratory, Newport News, Virginia 23606

† National Aeronautic and Space Agency

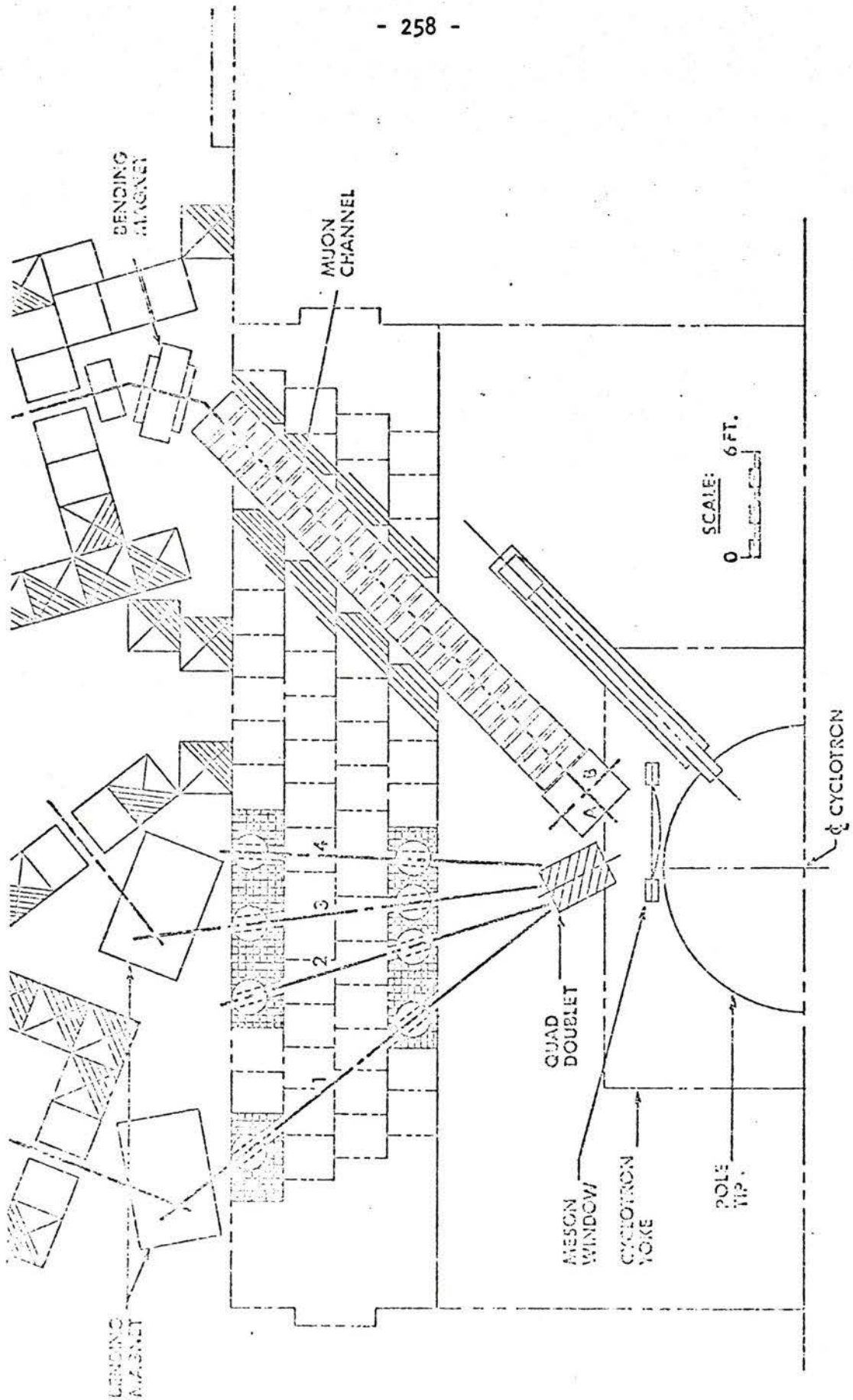


Fig. E.1 SREL pion/muon channel. Reproduced (Funston, 1971).

The channel was installed and tested in 1968. Total pion and muon yields were measured using a range telescope consisting of three scintillators in coincidence, a stopping counter, and a fourth scintillator in anticoincidence. The double wedge Fe degrader was placed between the second and third scintillators. The muon flux was $1.7 \times 10^6 \mu^-$ per sec in an area of $6'' \times 6'' \times 1/2''$ with a momentum spread equivalent to $21 \text{ g/cm}^2 \text{ Fe}$ (FWHM). The pion total flux was about the same but had a narrower peak; the momentum spread was $6 \text{ g/cm}^2 \text{ Fe}$ (FWHM). The stopping rate per gram was 1.5×10^3 . The range curves are reproduced in Fig. E.2. Elaborate beam profile and phase space measurements were made, but contamination was not considered.

E.2 Saclay Channel

Built to provide stopped pions and muons, the Saclay Channel (Duclos *et al.*, 1970) consists of a set of 9 quadrupoles placed between two 60° bending magnets. Two quadrupoles after the second bending magnet focus the beam onto the experimental target. A layout sketch is shown in Fig. E.3. Two sets of slits are indicated; the set F1 defines the angular acceptance and the set F2 defines the momentum acceptance.

The bending magnets have $12''$ wide pole pieces, $4.5''$ gaps, and $20''$ radius. A maximum field of 16 kGauss is obtainable. The 9 quadrupoles have $8''$ bore radius, $8''$ long pole pieces, a maximum gradient of 0.65 kGauss/cm and $6.25''$ spacing. The two quadrupoles after the second magnet also have $8''$ bore radius but $10.25''$ long pole pieces.

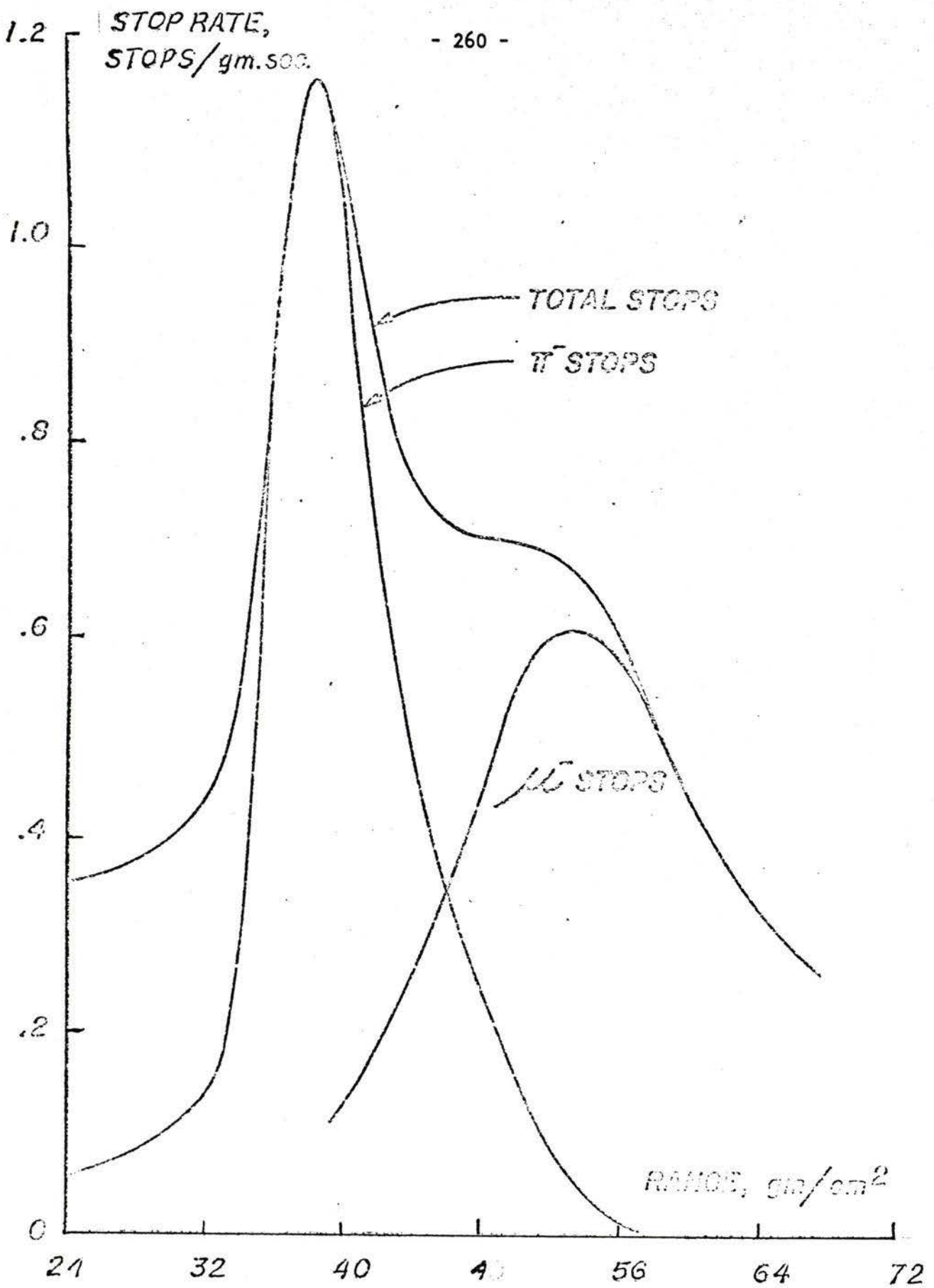


Fig. E.2 Range curves obtained with the SREL Channel. Reproduced (Funston, 1971).

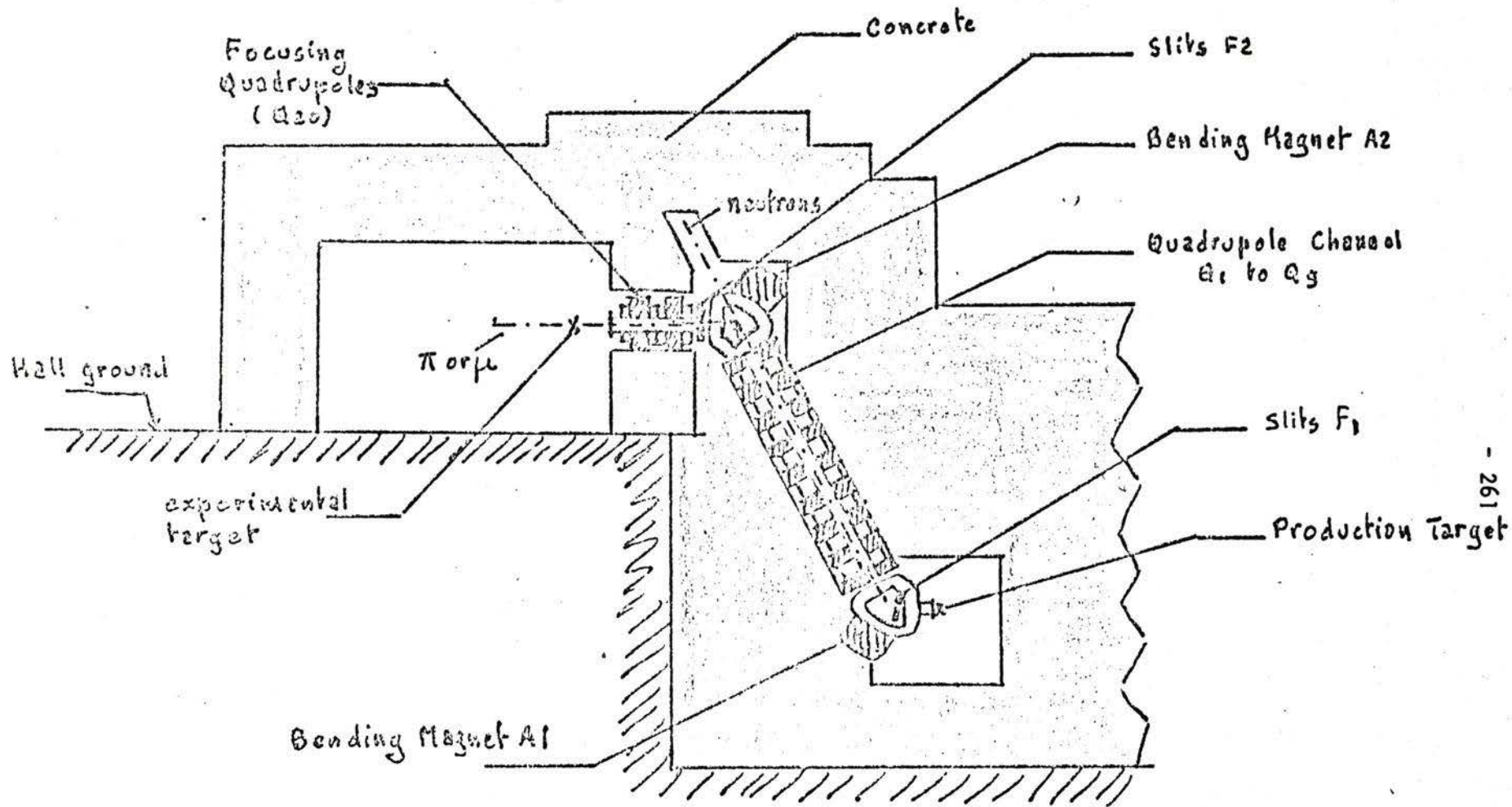


Fig. E.3 Saclay pion/muon channel. Reproduced (Duclos *et al.*, 1970).

The maximum momentum acceptance is 5.5% when the slits are fully open. Results of measurements of the π^+ yields are indicated in Fig. E.4 for several values of the channel energy and for 1 μ A 420 MeV electron beam on a 1 cm Cu target with the slit adjusted to give a $\Delta p/p_0 = 3\%$. For 75 MeV, the π^- yield was a tenth of that of the π^+ .

A preliminary measurement of the yield of 75 MeV/c muons produced by the backward in-flight decay of 150 MeV/c pions gave 2.5×10^4 per sec when extrapolated to an electron beam current of 600 μ A. However, the channel was not operating under optimal conditions for this measurement.

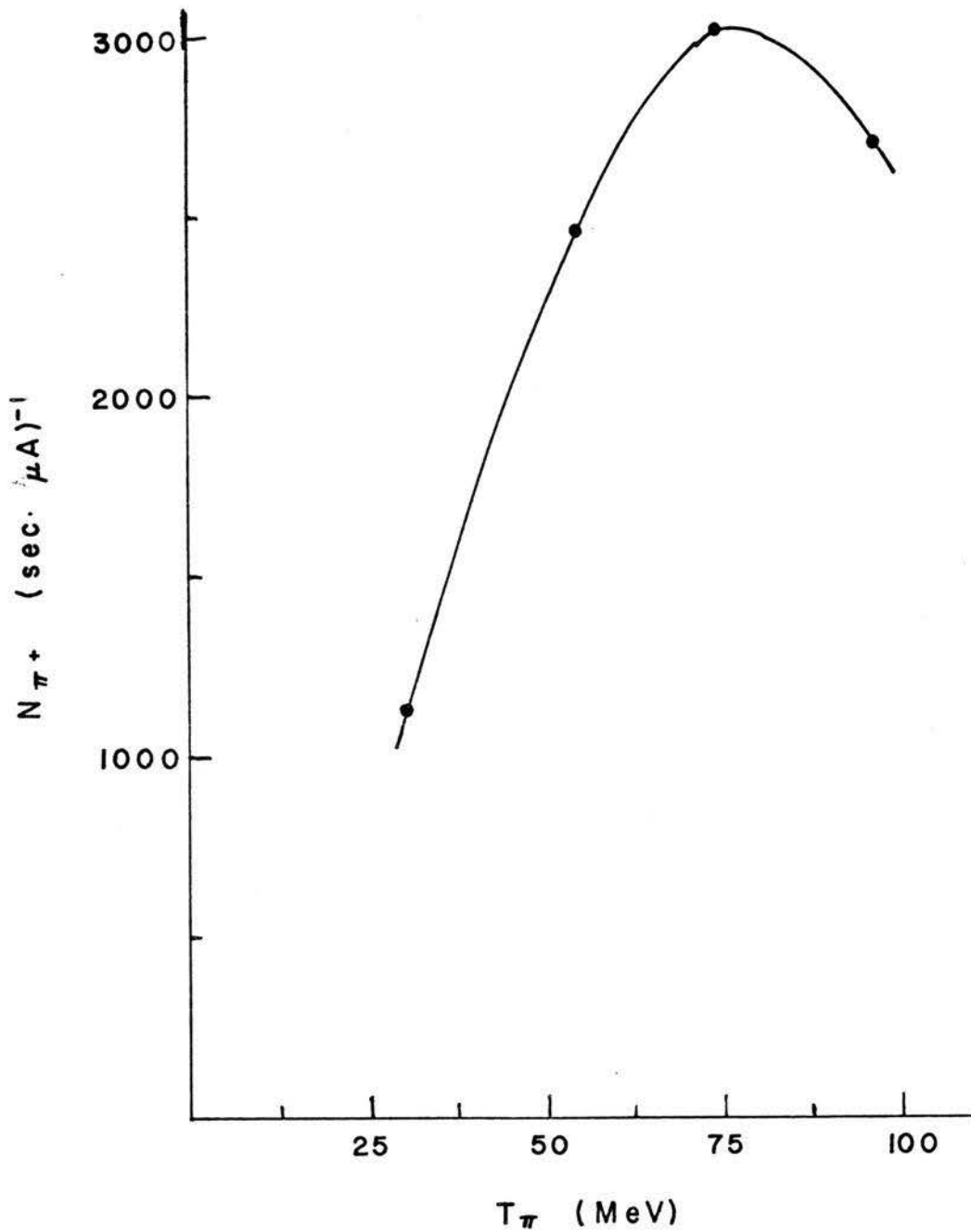


Fig. E.4 π^+ yields for a $1 \mu\text{A}$ beam of 420 MeV electrons on a 1 cm Cu target. Slits adjusted to give $\Delta p/p = 3\%$ (Duclos *et al.*, 1970).

Appendix F

ALTERNATING GRADIENT PERIODIC SYSTEMS, A MATRIX TREATMENT

The alternating gradient principle (Courant *et al.*, 1952) implies that a combination of two quadrupoles (or lenses, as they will be referred to henceforth) of opposite polarity give rise to a convergent action in both transverse planes. A periodic combination of equally spaced lenses of alternating polarity and equal strength can, therefore, be used to contain a beam of particles over a long distance. The properties of such a system may be deduced by considering the transfer matrix of one period. It is convenient to start this period in the centre of a focussing quadrupole. Thus, a complete period consists of $\frac{1}{2}F$, d , D , d , $\frac{1}{2}F$, where F and D denote focussing and defocussing lenses of equal strength and d is their separation. The transfer matrix of this period is obtained by multiplying together the matrices of the individual constituent elements. In the thin lens approximation, where the focussing action of the lens is assumed to take place at the transverse plane passing through the centre of the lens, this matrix is (Banford, 1966)

$$\begin{pmatrix} 1 - d^2 P^2/2 & d(2 + dP) \\ -dP^2(2-dP)/4 & 1 - d^2P^2/2 \end{pmatrix} \quad (F.1)$$

where P is the lens strength and is equal to $-k \sin(k\ell)$ for a focussing, and $+k \sinh(k\ell)$ for a defocussing lens. ℓ is the effective length of the lens and k is defined by

$$k^2 = G/B\rho \quad (F.2)$$

where G is the field gradient of the lens and $B\rho$ is the magnetic rigidity of the particles in the beam.

It is convenient to define

$$\eta = dP \quad (F.3)$$

and half the trace of the matrix (F.1) by

$$\cos \mu = 1 - d^2P^2/2 \equiv 1 - \eta^2/2 \quad (F.4)$$

so that the matrix for one period becomes

$$\begin{array}{cc} \cos \mu & \lambda^{-1} \sin \mu \\ -\lambda \sin \mu & \cos \mu \end{array} \quad (F.5)$$

where $\lambda = \frac{1}{2}P(2-\eta)^{\frac{1}{2}}(2+\eta)^{-\frac{1}{2}}$. Therefore, provided that μ is real, the overall action of the period is convergent. From equation (F.4), for μ to be real, η must lie between -2 and $+2$. Therefore, the condition for stability is

$$+1 > \cos \mu > -1 \quad (F.6)$$

A thick lens treatment of the system yields a similar result, assuming zero separation of lenses, with

$$\cos \mu = \cos k\ell \cosh k\ell \quad (F.7)$$

and

$$\lambda^2 = \frac{\sin k\ell \cosh k\ell - \sinh k\ell}{\sin k\ell \cosh k\ell + \sinh k\ell} \quad (F.8)$$

In this case μ is real for $k\ell < 1.87$, but higher stability bands exist (Banford, 1966), although not normally used.

Appendix G

SOME EXAMPLES OF ALTERNATING GRADIENT CHANNELS

G.1 The CERN Channel

This was the first A.G. channel constructed (Citrön *et al.*, 1963). It was designed to provide a pure muon beam at high energy. Muons with momenta up to 250 MeV/c were obtained from the backward decay of pions. Beams of lower momenta were also obtainable. The initial momentum selection is provided by the magnetic field of the synchrocyclotron. The pion decay section consists of 24 quadrupoles 8" in diameter and having 8.6" long pole pieces. The final magnetic analyzer is an alternating gradient magnet consisting of three sections making 78° total bending angle. The layout of the channel and the synchrocyclotron area are shown in Fig. G.1 reproduced from the CERN report (Citrön *et al.*, 1963). Four quadrupoles follow the bending magnet to focus the muon beam onto the target.

The channel is still in operation, providing about 5×10^4 muons per second. Pion and electron contaminations are about 3% each. Although the channel was not designed specifically for stopped muon experiments, it is being used for this purpose using a degrader in front of the target. A stopping rate of 7×10^3 muons per second was obtained in a recent experiment (Backe *et al.*, 1971). The cyclotron improvement program (Michaelis, 1970) being carried out presently is expected to increase the muon flux to about 5×10^5 muons/sec.

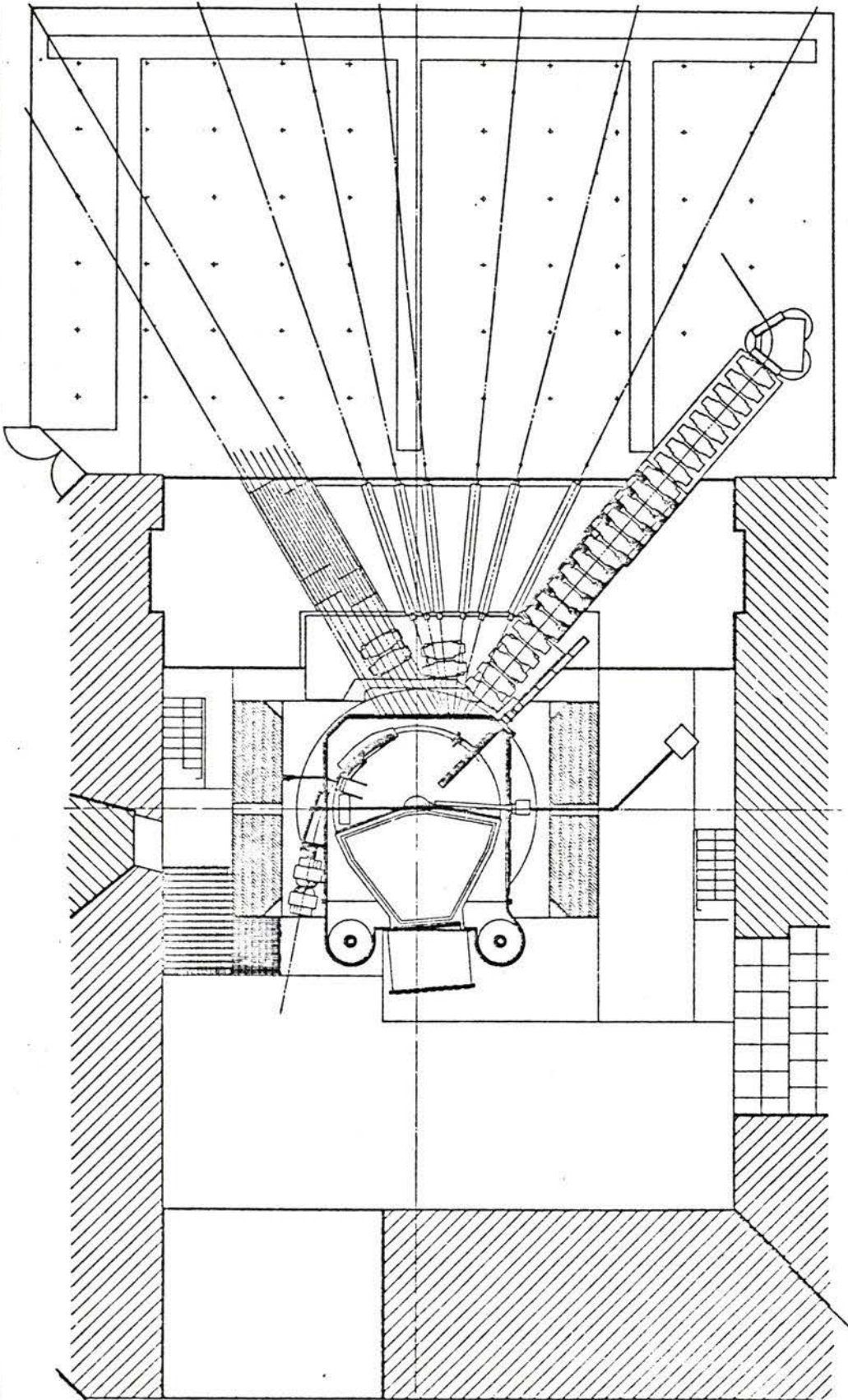


Fig. G.1 The CERN Synchro-cyclotron with the channel and the analyzing magnet.
Reproduced from CERN 63-35.

Because the cyclotron fringe fields served the function of a bend for initial momentum selection and only one bending magnet is used at the channel exit, one would expect considerable neutron contamination. This was not discussed in the report quoted above. Pion contamination, however, was measured (Citrön *et al.*, 1962) and is 1%.

G.2 The Chicago Channel

This channel (Culligan *et al.*, 1964), now dismantled, was very similar to the CERN channel in design but different in design goals. Unlike the CERN channel, it was designed specifically to provide low energy muons for stopped muon experiments. Also, a large aperture matching lens was used to match the channel to the emittance of the mesons generated internally in the cyclotron. This lens has an aperture of 15" while the aperture of each of the 28 lenses forming the channel is 8". The unique features of these quadrupoles are their simple design and low cost. The pole pieces are just over 6" long and cast rings form the cylindrical return yokes. The volume of copper was minimized to pack the lenses together with minimum drift spaces, although this resulted in higher power consumption. A bending magnet is used at the end for separating the muons from backward decay of pions with a central momentum of 155 MeV/c. The layout is shown in Fig G.2.

The average muon intensity obtained was approximately 2×10^5 muons/sec into a 5" x 5" counter placed 60 cm from the edge of the bending magnet. Electron contamination was 23% while pions formed 35% of the beam.

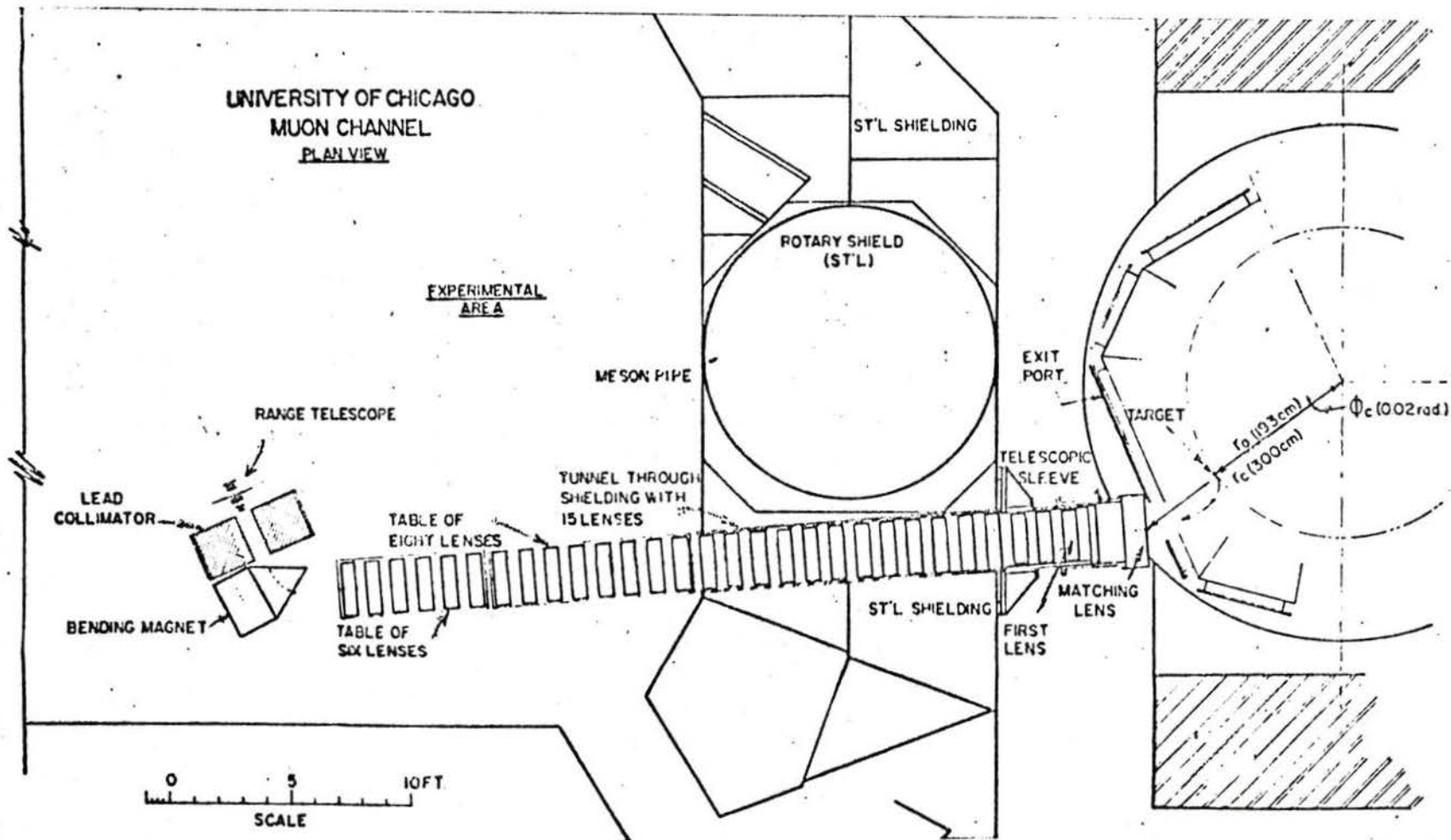


Fig. G.2 Plan view of Chicago muon channel and experimental area. Reproduced (Culligan *et al.*, 1964).

$2 \times 10^4 \mu^-$ stops per second were reported in a 10 cm diameter, 6 cm long cylinder of CH_2 placed 1 m from the magnet edge.

As in the case of the CERN channel, neutron contamination, although not reported, should be considerable because of inadequate attenuation provided by a straight channel. For a channel designed for low energy muons, the large number of quadrupoles used is perhaps excessive; a shorter channel would have given a similar performance.

G.3 The Proposed LAMPF Channel

Unlike the CERN and Chicago channels, which use the fringe field of the cyclotron for momentum selecting the internally generated pions, the LAMPF channel (Hughes *et al.*, 1970) uses a two bend system to collect the pions, generated from an external target, at an angle of 60° with respect to the primary proton beam.

The principle criteria for the proposed LAMPF channel (now under construction) are: maximum stopped muons per g/cm^2 (both polarity), variable operating momentum, muon polarization, and muon beam purity. The proposed channel, shown in Fig. G.3, is composed of three sections: a pion collection and bending section consisting of two 30° rectangular bending magnets of the C-type with quadrupole doublet in between and another doublet preceding the first magnet, a pion decay section made up of 16 quadrupoles, and an elaborate analyzing system consisting of several magnets and quadrupoles.

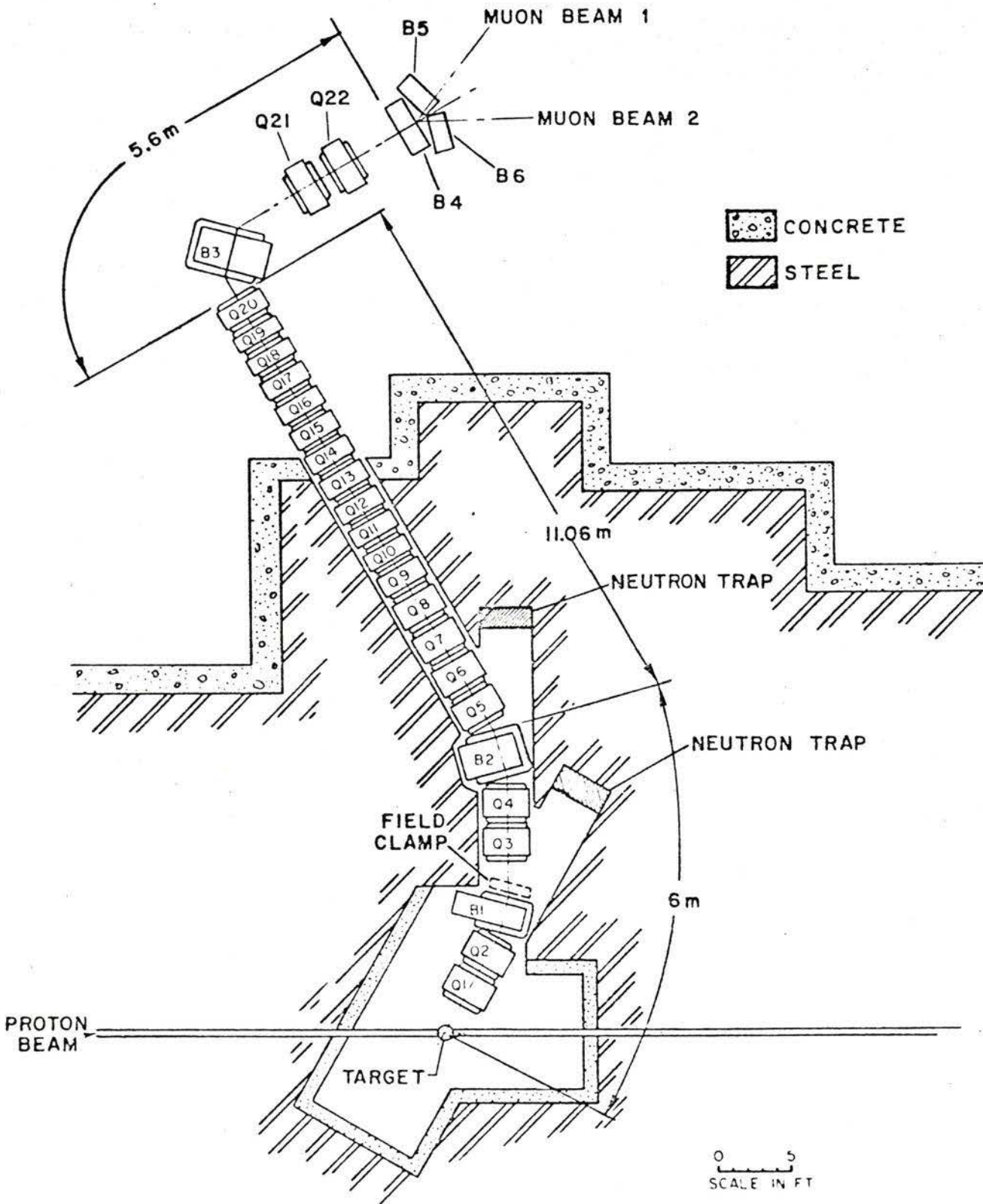


Fig. G.3 Experimental layout of the proposed muon channel. Reproduced from the LAMPF report LA-4474 (Hughes *et al.*, 1971).

The quadrupoles Q1 to Q8, Q21 and Q22 are of the wide-pole type which accepts an elliptical beam with a major axis of $2\sqrt{2}a$ where "a" is the bore radius. The first two quadrupoles, Q1 and Q2, have 14" apertures and 22" long pole pieces. The other quadrupoles have 12" apertures. The bending magnets B1, B2 and B3 have 11" gaps, and B4, B5 and B6 are 6" gap C-magnets with 3/8" septum. The splitting magnet B4 is made up of two such magnets to provide two beams simultaneously. A more sophisticated analyzing system, which uses two 45° bends instead of the single 90° bend (B3) and two extra quadrupoles between them, is proposed as an alternative design.

The expected performance of the channel was calculated for two values of the central momentum, 180 MeV/c and 90 MeV/c. The output characteristics at the end of the pion decay section (output at Q20) are summarized in Table G.1 for the two cases. Fig. G.4 shows the spectrum after Q20 for $p_0 = 180$ MeV/c, and Fig. G.5 for $p_0 = 90$ MeV/c. These results are taken from the LAMPF report (Hughes *et al.*, 1971). The figures are quoted for a 1 mA, 800 MeV proton beam striking a 3.6 cm thick Cu target. The pion production cross section for positive pions was assumed to be $41 \mu\text{b} (\text{sr} \cdot \text{MeV}/c)^{-1}$ at $p_0 = 180$ MeV/c, and $23 \mu\text{b} (\text{sr} \cdot \text{MeV}/c)$ at $p_0 = 90$ MeV/c.

The maximum yield at the end of the magnetic analyzer of positive muons from the backward decay of 180 MeV/c pions is about $2.4 \times 10^7 (\text{sec} \cdot \text{MeV}/c)^{-1}$. The forward decay muons from 90 MeV/c pions have a maximum flux of about $4.5 \times 10^7 (\text{sec} \cdot \text{MeV}/c)^{-1}$ pion-free positive muons

Table G.1

Muon Beam Characteristics

from the Pion Decay Portion of the LAMPF Channel

	<u>$p_0 = 180 \text{ MeV/c}$</u>	<u>$p_0 = 90 \text{ MeV/c}$</u>
	backward decay:	forward decay:
Maximum flux	$2.7 \times 10^7 \mu^+$ at 102 MeV/c	$1.8 \times 10^7 \mu^+$ at 117 MeV/c
(sec . MeV/c) ⁻¹	$0.7 \times 10^7 \mu^-$ at 102 MeV/c	$0.9 \times 10^7 \mu^-$ at 117 MeV/c
		backward decay:
		$0.2 \times 10^7 \mu^+$ at 50 MeV/c
		$0.1 \times 10^7 \mu^-$ at 50 MeV/c
Emittance	1 - 2	1 - 2
(cm rad)		
Polarization	$0.4 < P_\mu < 0.8$ for range between 90 and 115 MeV/c	$ P_\mu > 0.8$ for range between 115 and 125 $ P_\mu > 0.9$ for 50 MeV/c

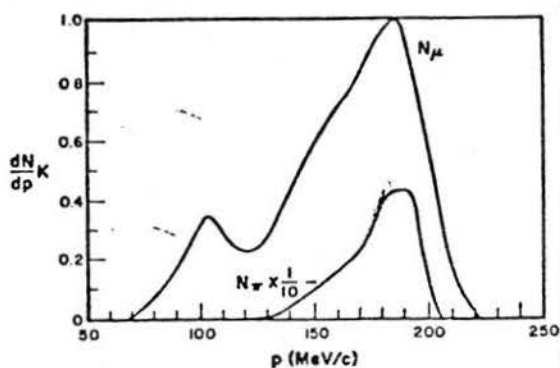


Fig. G.4 Normalized positive muon and pion spectra as a function of momentum at the output of the pion decay portion of Fig. G.3, when the pion collection and bending portion is tuned to 180 MeV/c, and the AG channel is tuned to maximize backward decay muons. The normalization constant $K = (8 \times 10^7)^{-1}(\text{sec-MeV/c})$.

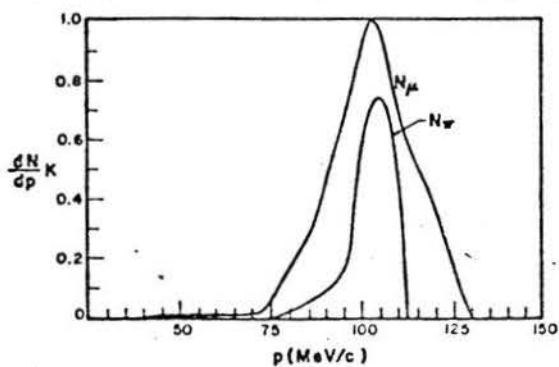


Fig. G.5 Normalized positive muon and pion spectra as a function of momentum at the output of the pion decay portion of Fig. G.3, when the pion collection and bending portion is tuned to 90 MeV/c, and the AG channel is tuned to maximize forward decay muons. The normalization constant $K = (4.1 \times 10^7)^{-1}(\text{sec-MeV/c})$.

when the more sophisticated analyzer, discussed earlier in this section, is used. The estimated fractional flux of contaminating particles are:

	from beam optics	including scattering	
π	0	0.05	
p	0	0.01	for μ^+
e	10^{-4}	$8 \times 10^{-}$	
	10^{-5}	—	for μ^+
n	10^{-6}	—	for μ^-
	10^{-6}	—	for μ^+
γ	10^{-7}	—	for μ^-

The stopping flux was calculated for specific examples of typical targets. Thus, for a $2.7 \text{ mg/cm}^2 \text{ H}_2$ gas target, $10 \text{ cm} \times 10 \text{ cm}$ in cross section, $6 \times 10^5 \mu^+/\text{sec}$ or $5 \times 10^4 \mu^-/\text{sec}$ are stopped after a carbon degrader. For a 1 g/cm^2 carbon target, $2 \text{ cm} \times 2 \text{ cm}$ in cross section, $3 \times 10^8 \mu^+/\text{sec}$ or $2.3 \times 10^7 \mu^-/\text{sec}$ are stopped after degrading the 102 MeV/c muon beam.

G.4 The Proposed Nevis Muon-Pion Channel

Unlike the Nevis pion-muon channel discussed in Section D.2, the muon-pion channel (Holland *et al.*, 1971) is intended primarily for stopped muons. Although this channel does not have a proper long A.G. pion decay section, it is discussed here since it is a conventional channel consisting of quadrupoles and bending magnets.

Fig. G.6 is a schematic layout diagram of the proposed channel. The main design criteria were: continuously variable momentum between 0 and 250 MeV/c, polarization $\sim 70\%$, low contamination and capability for capturing either forward or backward decay muons of either polarity as well as maximization of flux.

Two designs were considered. The first design is mirror-symmetric about a triplet contained between two 30° bends with a doublet before the first and after the second bend. A section containing a third bend followed by a quadrupole doublet permits momentum analysis. The second design, shown in Fig. G.6, consists of a leading doublet and two opposite vertical 35° bends which displace the pion beam downwards by 24" below proton beam level. This is followed by a five (or more) quadrupole decay section, an analyzing magnet and a quadrupole doublet.

For a $20 \mu\text{A}$, 550 MeV proton beam on a 3 cm long Be target, the fluxes at the entrance of the third bend, integrated over $p_0 \pm 10\%$, were estimated for the two designs and are reproduced (Holland *et al.*, 1971) in Table G.2. In the cases where a pion stopper is used, the pion beam is focussed, in principle, to a small spot and the estimates are the contents of the muon halo.

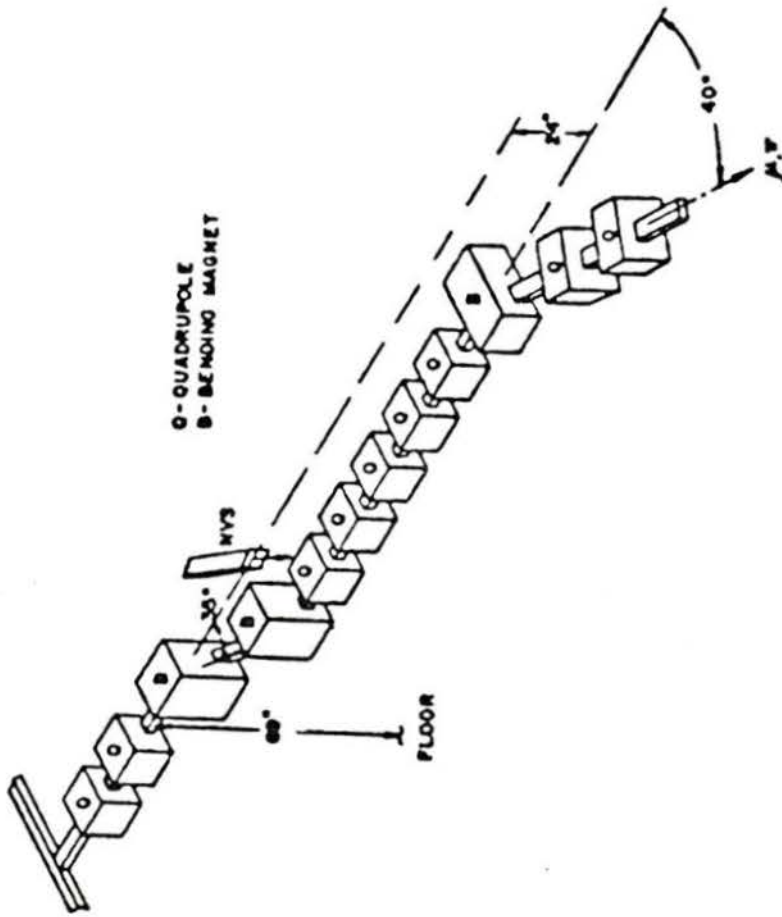


Fig. G.6 Proposed Nevis muon-pion channel. Reproduced (Holland et al, 1971).

Table G.2

Calculated Fluxes for the Nevis Muon Channel

First design

a) forward decay

1. with pion stopper	100	100	3	1	15	
2. without pion stopper	100	100	6	2	0.26	-69
b) backward decay	130	60	0.2	0.07	-	+80

Second design

forward decay

1. with pion stopper	100	110	6.6	2.2	1.2	
2. without pion stopper	100	110	14.7	4.9	0.2	-68

Appendix H

SOME EXAMPLES OF SOLENOID CHANNELS

H.1 SIN Channel

The criteria for the SIN channel are (Petitjean, 1970): maximum contamination-free stopped muons (of either polarity) per gram of stopping target material, variable energy and muon polarization of 80% or more. To achieve these aims, the proposed channel consists of three parts. An initial momentum selection system consists of a quadrupole triplet and a 45° sector bending magnet having a 4" gap followed by a doublet. The quadrupoles have 12" apertures except for the first lens which has an 8" aperture. The second part is a 50 kGauss, 10 m long, 5.5" diameter superconducting solenoid forming the pion decay section. Finally there is an analyzing section consisting of a 72° alternating gradient bending magnet with an 8" gap and a quadrupole quartet of 10" aperture. A layout diagram of the system is shown in Fig. H.1 (Petitjean, 1971) which also indicates the 0° pion extraction angle.

The most recent calculations of the expected performance of the channel, obtained from the November 1971 report (Petitjean, 1971) are summarized in Table H.1 which also includes values obtained (Petitjean and Vécsey, 1971) for an alternative design that replaces the solenoid by a conventional A.G. quadrupole channel. The figures are quoted for a $100 \mu\text{A}$, 590 MeV proton beam on a 10 cm long Be target and 0° pion extraction angle. The central momentum of the accepted pions is 200 MeV/c and muons, at a central momentum of 110 MeV/c from the backward

SIN MUON CHANNEL

STATUS NOV. 1971

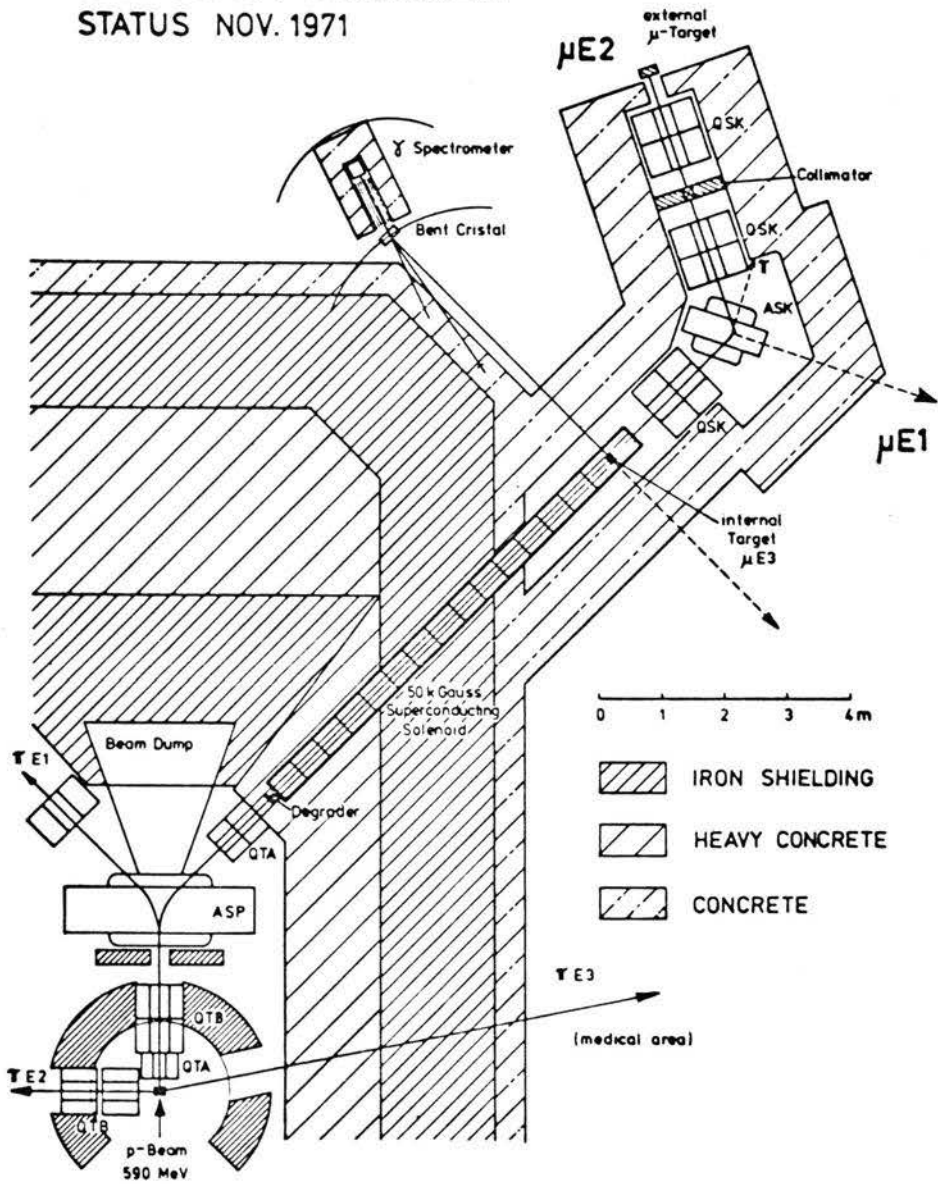


Fig. H.1 Layout of the SIN solenoid channel.

Reproduced (Petitjean, 1971).

Table H.1

Expected Performance of the SIN Channel

	<u>Solenoid</u>	<u>Quadrupole</u>
π^- production $10^9(\text{sec}\cdot\text{sr}\cdot\text{MeV}/c)^{-1}$	3.3	3.3
$\Delta\Omega_\pi$ (msr)	77	77
$\frac{\Delta p}{p}$, FWHM (%)	11	—
Total π^- flux accepted $10^9/\text{sec}$	3.8	4.6*
μ^- density in phase space $10^6(\text{MeV}/c\cdot\text{cm}^2\cdot\text{rad}^2\cdot\text{sec})^{-1}$	5.3 [†]	2.5

* This is the value before the pion injection system length was changed from 3.15 to 5.55 m.

† This value was for an 8 m solenoid with a 50 kGauss field. The backward muons had a central momentum of 115 MeV/c.

decay of the injected pions, are extracted by the analyzing section. The figures for the quadrupole channel are for a 25 lens A.G. channel having the same length as the solenoid, namely, 10 meters. The quadrupoles have 10" apertures.

A useful muon flux of $4 \times 10^6 \mu^- (\text{sec} \cdot \text{MeV}/c)^{-1}$ and an average stopping density of 2×10^5 per gram sec are expected. Fig. H.2 shows the pion and muon spectrum calculated for the solenoid and quadrupole channels at the entrance to the analyzing section. The spectra at the 70 cm² stopping target are shown in Fig. H.3 for the solenoid channel and in Fig. H.4 for the quadrupole channel. These figures are reproduced from the report (Petitjean and Vécsey, 1971) quoted above. The overall capture efficiency for the solenoid channel is 19%. This high value is partly due to the fact that the pion transverse distribution is favourable at this relatively high momentum.

A special low momentum operation mode is proposed for bent crystal spectrometer experiments. In this mode, the muon beam emittance is very large and cannot be extracted efficiently. Therefore, the stopping target has to be placed inside the solenoid. Under these circumstances, a muon stopping density of approximately ten times the values quoted above may be achieved if a wedge absorber is placed at the entrance of the solenoid so that the injection momentum can be maintained at 200 MeV/c to minimize decay in the injection section.

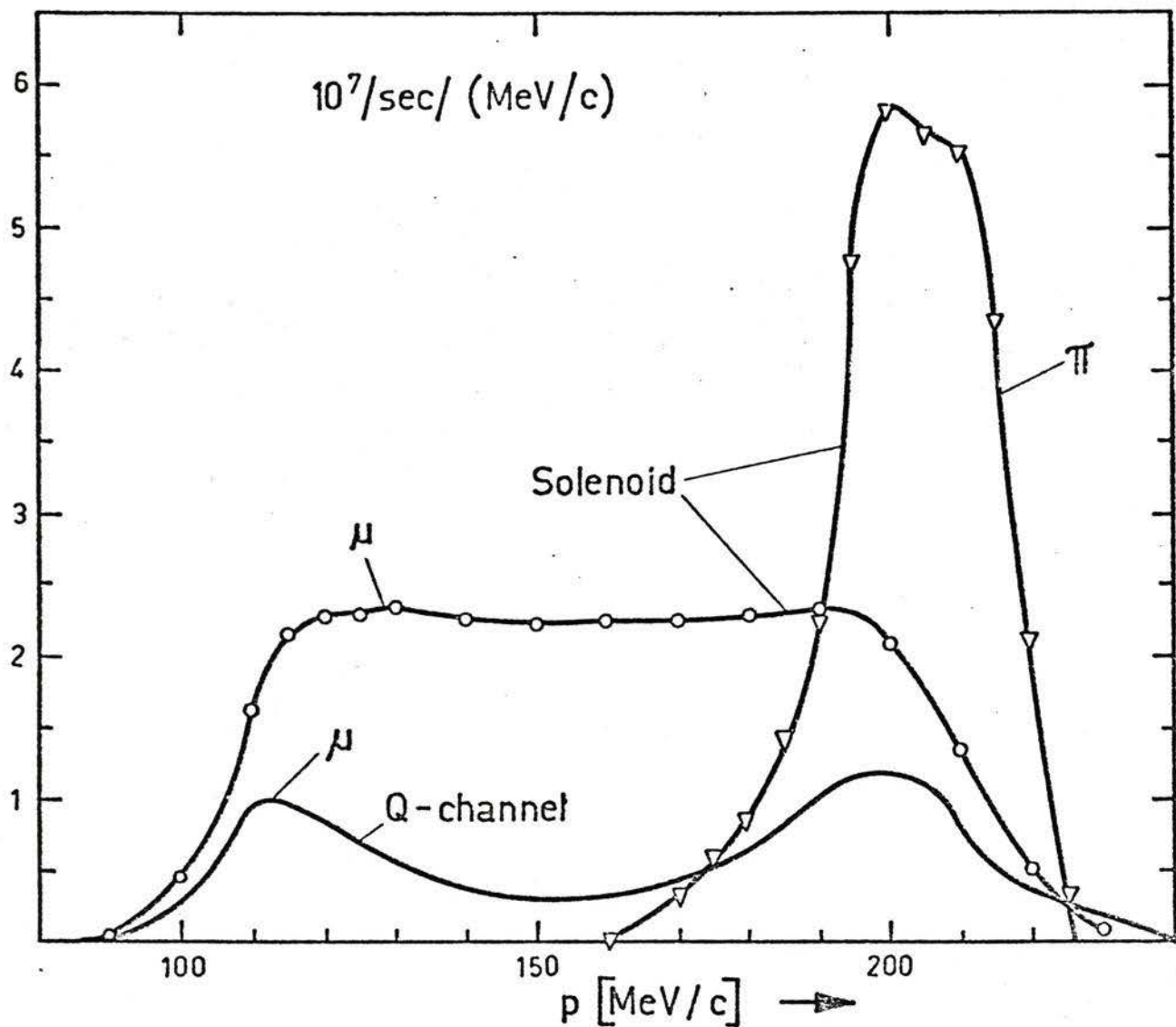


Fig. H.2 Calculated pion and muon momentum spectra at the entrance to the analyzing section. Yields quoted for a 100 μ A beam of 590 MeV protons incident on a 10 cm Be target. Reproduced (Petitjean and Vecsey, 1971).

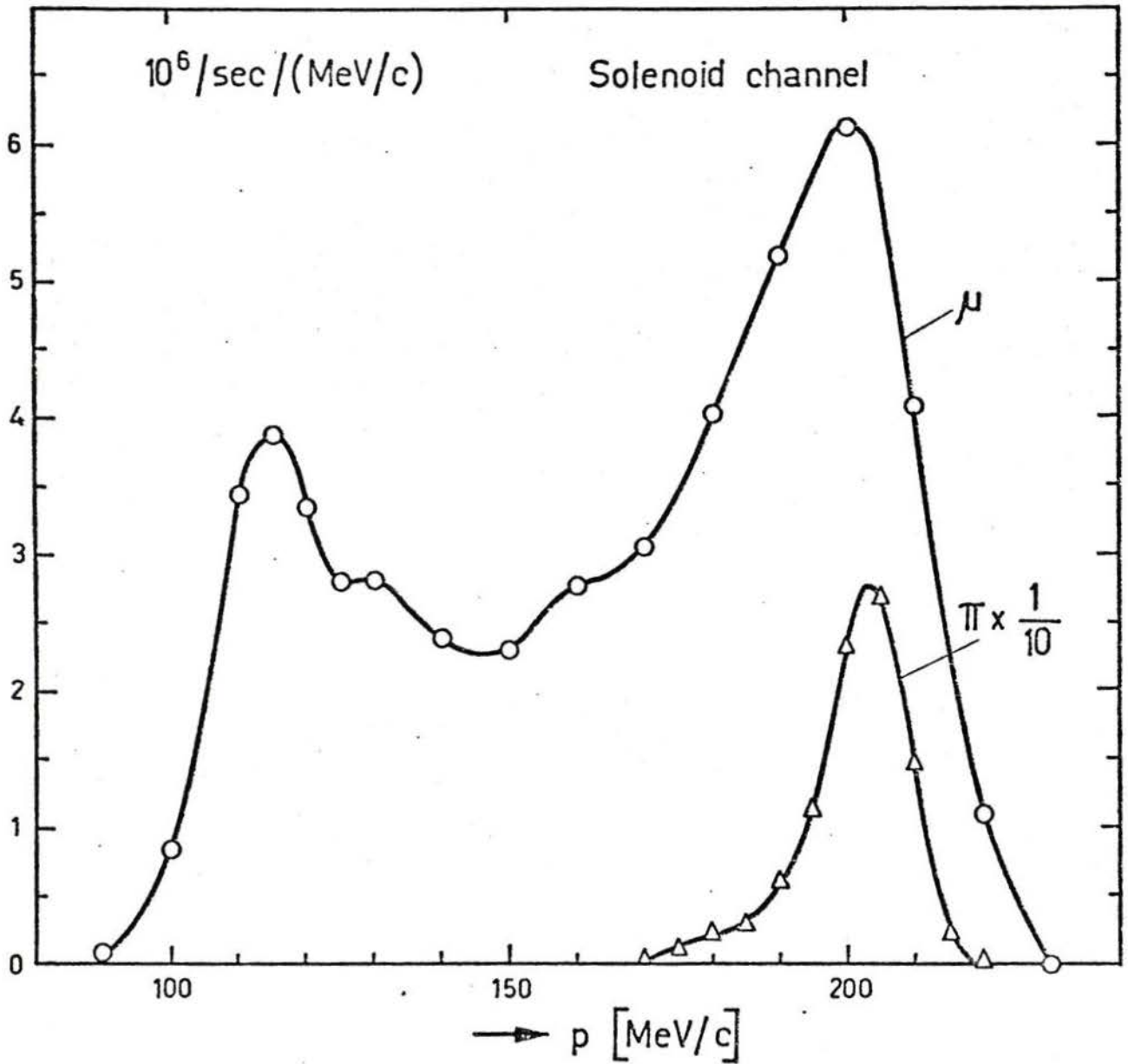


Fig. H.3 Calculated pion and muon momentum spectra at the stopping target for the beam described in Fig. H.2. Reproduced (Petitjean and Vecsey, 1971).

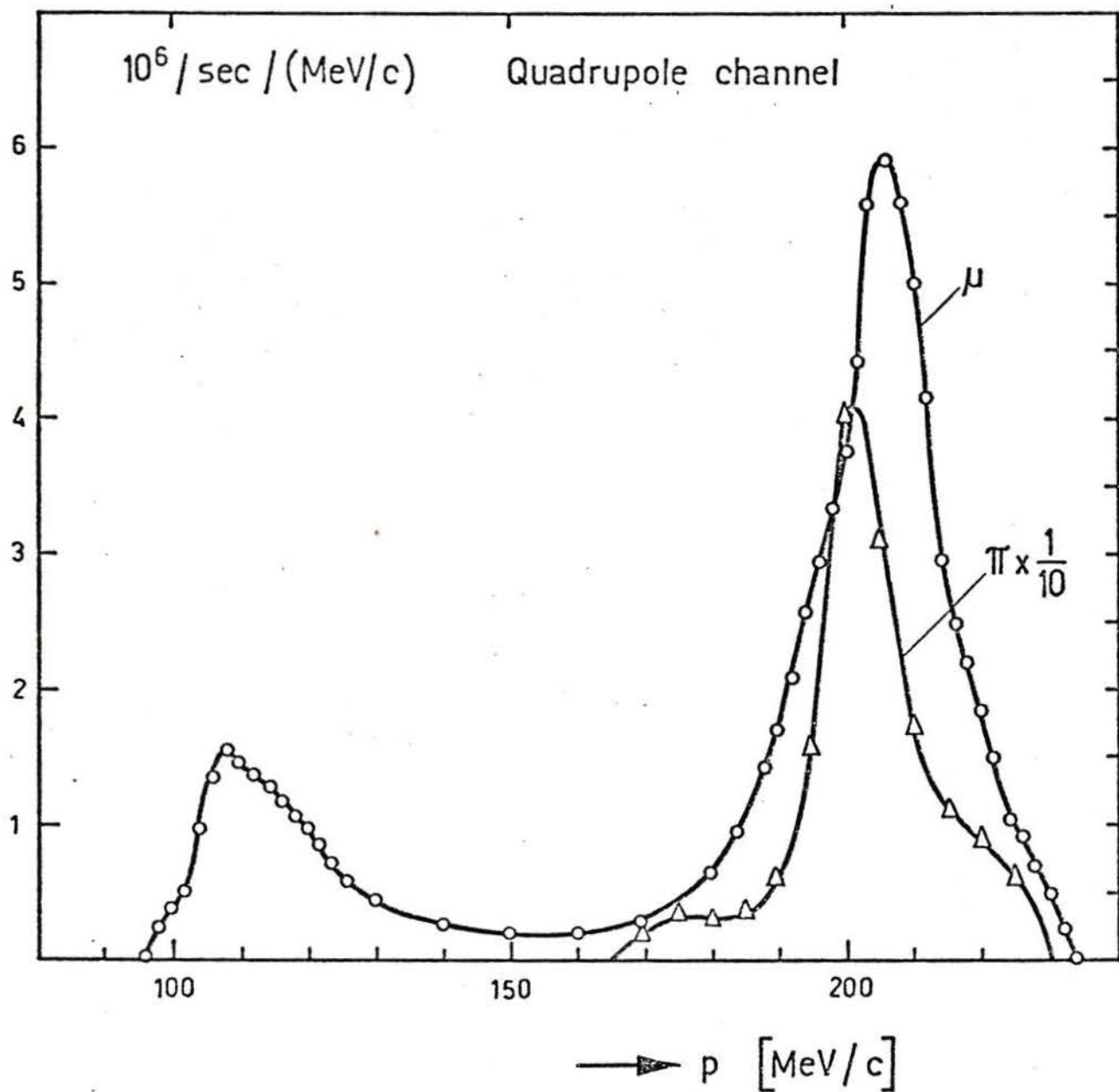


Fig. H.4 Calculated pion and muon momentum spectra at the stopping target for the beam described in Fig. H.2. Reproduced (Petitjean and Vecsey, 1971).

No estimates are made of contamination in the SIN reports. Although the initial 45° bend and the long straight section are probably sufficient to attenuate neutrons generated near the target, the background generated in the wedge absorber for the low momentum mode may be considerable.

H.2 Proposed Saclay Solenoid Channel

In the proposed channel at Saclay, the solenoid is preceded by a quadrupole doublet and one bending magnet to initially select low energy pions in the momentum range 50 to 70 MeV/c (8.5 to 16.5 MeV energy). The superconducting solenoid has an internal diameter of 8" and develops an axial field of 30 kGauss. Because of the high intensity of the low energy, photo-produced pions, the Saclay estimate for the number of stopped muons in a target of thickness 0.2 g/cm^2 and of area 300 cm^2 is $2 \times 10^7/\text{sec}$. The stopping density is about 10^8 muons per g/cm^2 per sec, or about 3.5×10^5 muons per gram per sec. These values are for the intensity at the end of the solenoid and just inside it; that is, the muon beam is not momentum analyzed. A 30% electron contamination is quoted, but these electrons have energies in the range 50 to 70 MeV, which is much higher than the muon energy.

Appendix I

AN EXAMPLE OF A COAXIAL BEAM GUIDE

A Van der Meer type beam guide (Van der Meer, 1962) has been constructed and is operational at the Carnegie Institute of Technology (Foss and Sutton, 1965). A larger guide than the existing one was planned. The proposed new guide has an inner conductor with an outside diameter of 2/3" and an outer conductor with an inside diameter of 10". The inner conductor consists of a 1/8" Cu rod with a copper spring wound around it and the assembly is placed inside the 2/3" heavy walled conductor tube. This design provides a large surface area for heat transfer to the cooling water. For a current of 12 kA in the centre conductor, the phase space acceptance is $4 \text{ rad}^2 \text{ cm}^2$. With this current, 7.5 kW of power is generated per foot of central conductor. The total length of 54 ft is made up of six sections with separate water cooling circuits. The last section is to be bent and passed through a bending magnet.

It was not possible to obtain performance data, calculated or experimental, for the channel except a figure of 11% for the muon capture efficiency.

Appendix J

AN EXAMPLE OF A MUON CLOUD CHANNEL

A muon cloud type channel was considered at LAMPF (Tanabe, 1970) as one of the alternative designs for their muon channel. A layout diagram, reproduced from Tanabe, is shown in Fig. J.1 for the suggested channel. A $10''$ aperture quadrupole doublet is followed by two parallel faced 45° magnets bending in opposite direction and finally a second doublet similar to the first one. A pion stopper and vertical asymmetric slits are placed between the two magnets.

The calculation was carried out for two cases; the initial drift length $l = 0.5$ m for the first, and 1.0 m for the second case. For each case, three values of the misalignment angle $\delta = 0^\circ, 5^\circ$ and $10''$ were considered. A production angle $\sigma = 90^\circ$ was used. As indicated in Fig. J.2, which shows the pion-to-muon ratio at the entrance of the channel, misaligning the channel alone does not eliminate the pions. Even for $\delta = 10^\circ$ the π/μ ratio is still about 4 at momenta between 60 to 80 MeV/c. For larger angles of misalignment, the loss in muon intensity increases substantially. Thus, in addition to the misalignment, a specific setup and tuning of the channel is suggested. The first half of the system is tuned to focus 75 MeV/c pions into a spatial image, with positive x-coordinate, which is blocked by one side of the asymmetric slit at the centre. However, some low energy pions are admitted because of the dispersed focus.

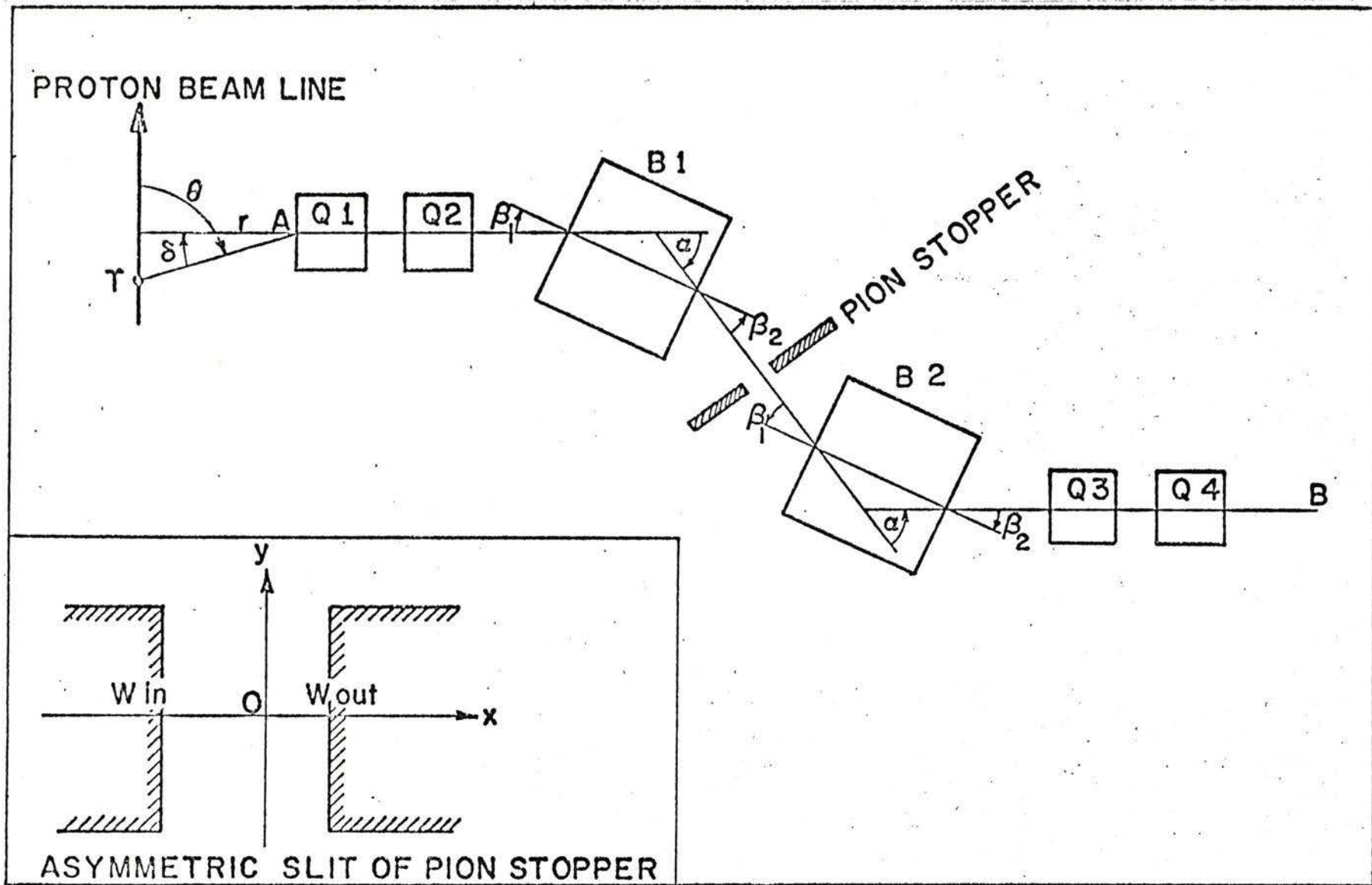


Fig. J.1 Cloud Muon Channel. Reproduced (Tanabe, 1970).

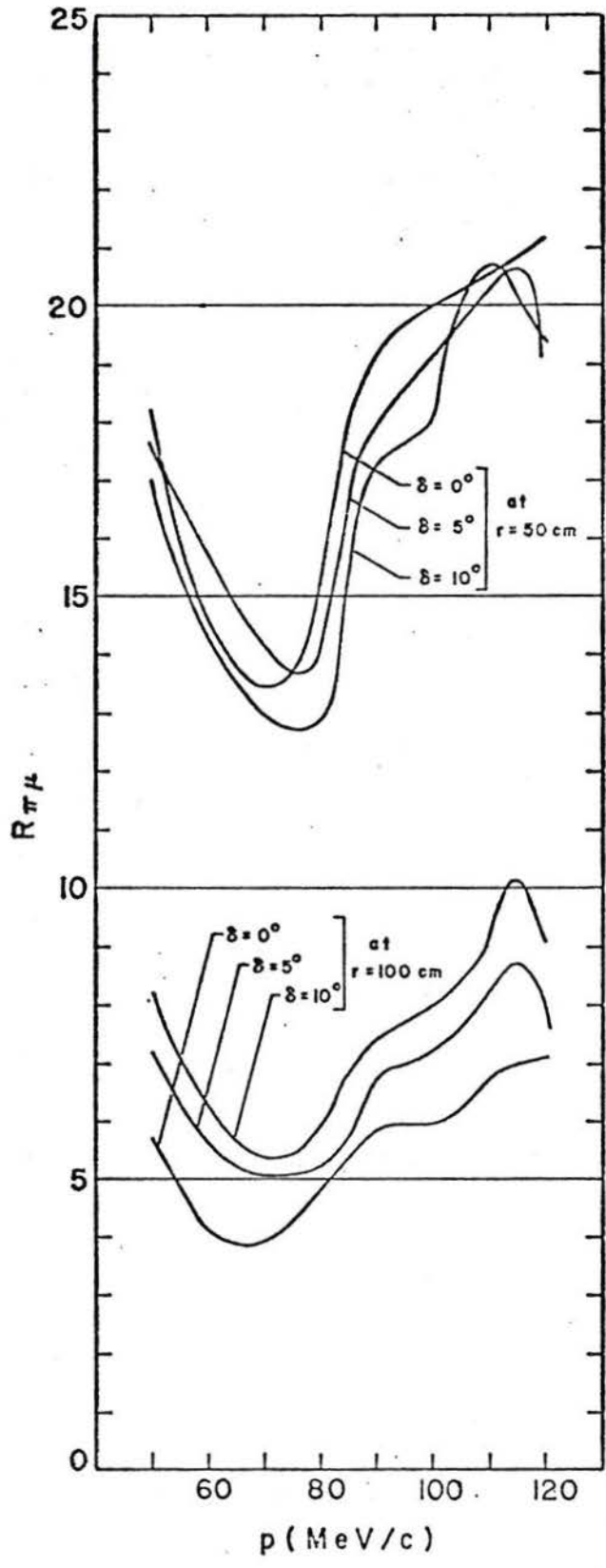


Fig. J.2 Pi-mu ratio at the channel entrance 50 and 100 cm from the pion production target (Tanabe, 1970).

To minimize the number of these pions, the second half of the channel is tuned to a central momentum of 82.5 MeV/c. A portion of the muon distribution will not be blocked by the slits because the source points are distributed between the production target and the channel entrance.

The calculated muon spectrum is shown in Fig. J.3 as a function of the muon momentum for the setup and tuning described above when the initial drift length L is 0.5 m. The integrated muon flux is $3.5 \times 10^4 \mu^-/\text{sec}$ for a $1 \mu\text{A}$, 750 MeV proton beam on a 3.4 cm Cu target. The average polarization of the muon beam is about 40%.

The flux quoted above is assumed to be free of pions. However this does not take account of the pions scattered from the walls of the second half of the channel which will also be a source of neutrons generated by pions stopped in the walls.

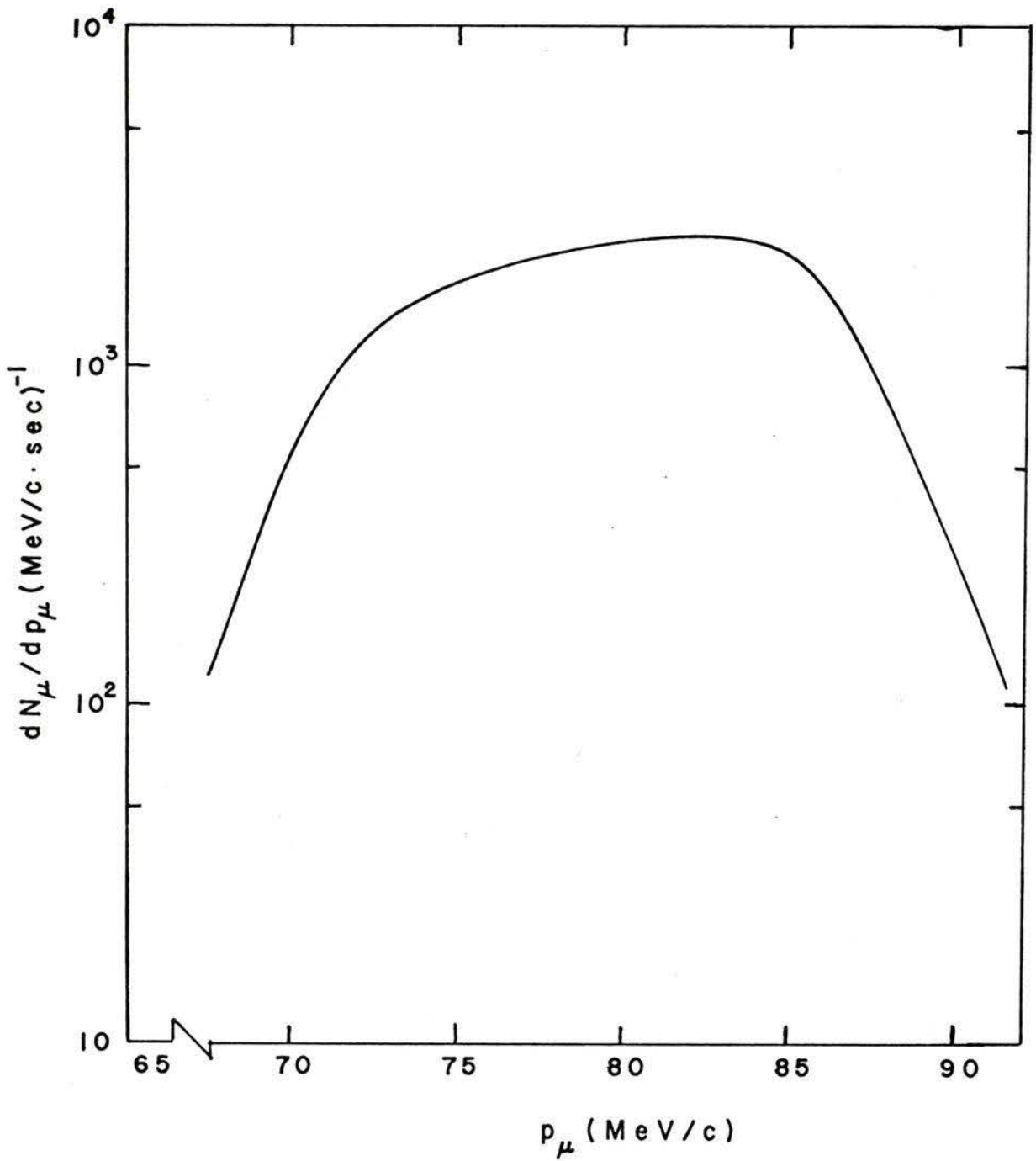


Fig. J.3 Muon Spectrum at the output of the channel shown in Fig. J.1. Yields quoted for a $1 \mu\text{A}$ beam of 750 MeV protons on a 3.6 cm Cu target (Tanabe , 1970).

Appendix K
COMPUTER PROGRAMS

K.1 TRANSPORT

This program (Brown and Howry, 1970) is a general purpose program for the design of beam transport systems in which the beam handling devices generate static magnetic fields. The program calculates first and second order matrices for the commonly used beam transport elements including sextupoles, solenoids and accelerator sections. It also has facilities for matching first order matrix elements and beam parameters, misalignment calculations and fringing field corrections to the first order optics of bending magnets. It should be pointed out that, when using the matching facility, correct solutions are obtained in some cases only if the initial guess of the values of the parameters are sufficiently close satisfying the constraints.

In TRANSPORT, the coordinates of a given particle are represented by a column vector with elements x_i , the initial coordinates are denoted by a similar vector $x_j(0)$ and the transformation by a 6×6 matrix R . Thus, the first order solution for a given system may be written as the matrix equation

$$x_i = \sum_{j=1}^6 R_{ij} x_j(0) \quad (K.1)$$

The behaviour of a beam of particles may be described by extending this matrix treatment to handle the ellipsoid representing the beam. A num-

erical notation is used for the components x_i and $x_j(0)$. Thus, the components x_i , where $i = 1, 2, 3, 4, 5, 6$ correspond to x, x', y, y', ℓ , and $\Delta p/p$ respectively as defined in Appendix B. The coordinates $x', y',$ and $\Delta p/p$ are used here instead of σ, ϕ and δ used in TRANSPORT.

The first order 6×6 matrix R appears in the TRANSPORT output in the form

$$\begin{pmatrix} R_{11} & R_{12} & 0 & 0 & 0 & R_{16} \\ R_{21} & R_{22} & 0 & 0 & 0 & R_{26} \\ 0 & 0 & R_{33} & R_{34} & 0 & 0 \\ 0 & 0 & R_{43} & R_{44} & 0 & 0 \\ R_{51} & R_{52} & 0 & 0 & 1 & R_{56} \\ 0 & 0 & 0 & 0 & 0 & 1 \end{pmatrix}$$

The zero elements in the first four columns are a direct consequence of midplane symmetry and the restriction to static magnetic fields. The zero elements in the fifth column occur because the variables $x, x', y, y',$ and $\Delta p/p$ are independent of the path length difference ℓ . The elements R_{51} and R_{52} are not normally used in beam transport design unless an isochronous system is being designed. The units for these matrix elements are as shown in the corresponding matrix below.

$$\begin{pmatrix} \text{cm/cm} & \text{cm/mr} & 0 & 0 & 0 & \text{cm/\%} \\ \text{mr/cm} & \text{mr/mr} & 0 & 0 & 0 & \text{mr/\%} \\ 0 & 0 & \text{cm/cm} & \text{cm/mr} & 0 & 0 \\ 0 & 0 & \text{mr/cm} & \text{mr/mr} & 0 & 0 \\ \text{cm/cm} & \text{cm/mr} & 0 & 0 & 1 & \text{cm/\%} \\ 0 & 0 & 0 & 0 & 0 & 1 \end{pmatrix}$$

The beam (or sigma) matrix is symmetric (Brown and Howry, 1970) and only a triangle of elements is needed. The beam matrix appears in the TRANSPORT printout, except for a column of zeros on the left which has no significance in the first order calculation, in the form

$$\begin{array}{rcccccc}
 \sqrt{\sigma(11)} & \text{cm} & & & & & \\
 \sqrt{\sigma(22)} & \text{mr} & r(21) & & & & \\
 \sqrt{\sigma(33)} & \text{cm} & r(31) & r(32) & & & \\
 \sqrt{\sigma(44)} & \text{mr} & r(41) & r(42) & r(43) & & \\
 \sqrt{\sigma(55)} & \text{cm} & r(51) & r(52) & r(53) & r(54) & \\
 \sqrt{\sigma(66)} & \text{PC} & r(61) & r(62) & r(63) & r(64) & r(65)
 \end{array}$$

The first column contains the maximum half values of the coordinates x , x' , y , y' , l , and $\Delta p/p$ in that order, with the units indicated along side each coordinate. The coefficients $r(ij)$ represent the correlation between a pair of coordinates. Thus, $r(21)$ is the correlation between x and x' and is zero at a waist in the $x - x'$ plane. The correlation $r(ij)$ measures the tilt of the ellipse and its intersection with the coordinate axes. For an upright ellipse, all these coefficients have zero values.

The second order solution is given by equation (B.14) in Appendix B. A matrix representation is given in SLAC-75 (Brown, 1967) where a 12 x 12 matrix is used. It is sufficient here, as an example, to give the expression for x in terms of the initial coordinates showing some of the important second order as well as the first order elements

obtained from the 12 x 12 matrix; thus

$$\begin{aligned}x = & R_{11} x_0 + R_{12} x_0' + R_{16} \Delta p/p + T_{111} (x_0)^2 + T_{112} x_0 x_0' \\ & + T_{116} x_0 \Delta p/p + T_{122} (x_0')^2 + T_{126} x_0' \Delta p/p + T_{166} (\Delta p/p)^2 \\ & + T_{133} (y_0)^2 + T_{134} y_0 y_0' + T_{144} (y_0')^2\end{aligned}$$

The units for the T_{ijk} elements can readily be found from the units for the coordinates. Thus, T_{126} has the units cm per mr per % and the units for T_{122} are cm per mr per mr.

For a more detailed description of TRANSPORT the report SLAC-91 (Brown and Howry, 1970) should be consulted.

K.2 TRANS

The program TRANS (Chan *et al.*, 1972) uses the first order approximation for beam optics calculation and incorporates the 6 x 6 matrix representation discussed in Section K.1. It calculates first order transfer matrices for individual elements and complete systems, ray trajectories, trajectories of individual specified rays, properties of beams which can be represented by a phase space ellipsoid, and various tolerances for beam transport elements. It has facilities for the optimization of a system to meet specified criteria.

The program uses a similar coordinate system to that used by TRANSPORT but the units employed internally are the meter and radians instead of the mm and mr used in TRANSPORT. However, the numerical values of the elements of the R-matrix (similar to the matrix discussed in Section K.1) are valid for the mm-mrad-% set of units and the cm-centiradian-% set of units. The tolerance calculations (Lobb, 1972) include tolerances on currents, rotations and displacements along the beam axis of quadrupoles and bending magnets. Also, the effects of higher harmonics are calculated for quadrupoles. For further details of these tolerance calculations, the recent paper (Lobb, 1972) should be consulted.

K.3 ACCEPTANCE

The program ACCEPTANCE (Harrison and Lobb, 1968) calculates the beam acceptance in initial phase space for a beam transport system consisting of drift lengths, quadrupoles and uniform field bending magnets. The calculation is carried out to first order assuming that the motions in the horizontal and vertical planes are independent. However, the quadrupole second order chromatic aberrations are treated directly by calculating the quadrupole strength parameters appropriate to the particle momentum.

For a given beam transport system, the program can find the limiting apertures, transform these limits back to the initial phase space at the origin of the system, and indicates which element of elements along the beam line limits the beam accepted by the system. The apertures specified for each element of the system should be rectangular, a consequence of the assumption that the horizontal and vertical motions are independent. Plots of the phase space polygons, in both the horizontal and vertical planes, are provided in the printed output.

K.4 NPFLUX

This program (Hutson, 1970) is a Monte Carlo simulation of a secondary beam, generated when a primary beam impinges on a given target, and transported through a specified beam transport system. From given primary beam dimensions and shape, and a specified target size, production angle, and momentum deviation ($\Delta p/p$), the program chooses initial position and slope coordinates randomly for a large number of particles. Using the first and second order transformation matrices provided by TRANSPORT, the program calculates the new values of the displacement coordinates x and y and compares them with the specified apertures of the various elements in the system. If the displacements are smaller than the aperture, the particle passes through to the next element; otherwise, it is considered lost and added to the beam spill at the particular point along the beam line.

At the end of the system, the density distribution of the particles, which passed through to the end, is indicated in the program output as a 2-dimensional array in the transverse plane. NPFLUX also calculates the solid angle of acceptance, for a given value of $\Delta p/p$, and provides horizontal and vertical distributions calculated from the 2-dimensional array mentioned above.

A slight modification was made to the program to obtain some of the distributions shown in Chapter 4. In the modified version, the momentum deviation $\Delta p/p$ is also generated randomly so that the program will simulate a beam of particles with a finite momentum band.

Appendix L

THE PROGRAM MBEND

A program BEND was developed at Yale (Ohnuma, 1969) to calculate pion and muon momentum spectra and the muon total flux. MBEND is a further development of this program adding the following capabilities:

- 1) tuning various parts of the channel to different momenta and calculating, in a single run, the fluxes for the total system;
- 2) from tables of the energy loss dE/dR and the range R , incorporated in the program as data, the stopping densities dN/dR for the pions and the muons are calculated providing range spectra for the particles;
- 3) calculation of the time of arrival of pions and muons at the end of the channel relative to the time of arrival of pions with momenta equal to the channel central momentum;
- 4) print out of summary tables of pion and muon fluxes as function of momentum and of range in carbon;
- 5) plots of the momentum and range spectra and of muon polarization versus momentum can be made using the separate, but complimentary, program PLOTS.

For several discrete pion momenta, the program calculates the number of decay muons and surviving pions in each element or part of an element of the system. It is assumed that the number of pions (or muons)

in a given 4-dimensional phase space is proportional to the product of areas in the $(x-x')$ and $(y-y')$ phase space. The pions and muons are assumed to be uniformly distributed within the phase space area. The two phase space areas $(x-x')$ and $(y-y')$ are assumed completely independent and are represented by convex polygons. The apertures of the various elements are represented by two parallel lines in each phase space at points along the beam line. The phase space points for decay muons are obtained from those of the parent pions by a change in the values of x' and y' by an amount proportional to the decay angle.

The pion and muon fluxes are integrated over the momentum interval used and summed to obtain the total fluxes. The average polarization of the muons is also calculated by this program.

REFERENCES

- Alexander, J.H. and Reeve, P.A. 1971. TRIUMF Internal Report VPN-71-21.
- Al-Qazzaz, N. 1969. "An Analog Computer for the Calculation of Particle Trajectories and Beam Emittance Envelopes." M.Sc. Thesis, University of Victoria, Victoria, B.C.
- Al-Qazzaz, N. and Pearce, R.M. 1971. "The TRIUMF Stopped Muon Facilities," submitted to the Colorado Muon Physics Conference Proceedings.
- Amato, J., Burman, R., Cowan, H., and Jakobson, M. 1970. LASL Internal Report MP-7-10.
- Anderson, C.D. and Neddermeyer, S.H. 1937. Phys. Rev. 51, 884.
- Auld, E. *et al.* 1971. "Proposal to Measure the Elastic Scattering of Positive Pions by Deuterons, for Pion Energies Less than 80 MeV." A proposal submitted to the Lawrence Laboratory at Berkeley.
- Backe, H. *et al.* 1971. Private communication.
- Banford, A.P. 1966. *The Transport of Charged Particle Beams.* (E. and F.N. Spon Ltd., London).
- Bethe, H.A. and Marshak, R.E. 1947. Phys. Rev. 72, 506.
- Brown, K.L. 1967. Stanford Linear Accelerator Center Report SLAC-75.
- Brown, K.L. and Howry, S.K. 1970. Stanford Linear Accelerator Center Report SLAC-91.
- Chan, C., Hunt, D. and Lobb, D.E. 1972. TRIUMF Internal Report TRI-1-72-1.
- Citrön, A. *et al.* 1962. Nucl. Instr. and Meth. 15, 121.
- Citrön, A. *et al.* 1963. CERN Report CERN-63-35.
- Cochran, D.R.F. and Jakobson, M.J. 1967. LASL Internal Report MP-6/DRFC/MJJ-1.
- Conversi, M. *et al.* 1947. Phys. Rev. 71, 209.
- Courant, E.D. *et al.* 1952. Phys. Rev. 88, 1168.
- Couteur, K.J.Le. 1967. Plasma Physics 9, 457.

- Culligan, G. *et al.* 1964. Proceedings of the Conference on High Energy Cyclotron Improvement, College of William and Mary, Williamsburg, Virginia.
- Duclos, J. *et al.* 1970. Private communication to R.M. Pearce.
- Dunaitsev, A. 1962. Zh. exp. teor. Fiz. 42, 1680.
- Dunaitsev, A. 1964. Zh. exp. teor. Fiz. 47, 84.
- Foss, M. 1968. Private communication to R.M. Pearce.
- Foss, M. and Sutlon, R. 1965. Proceedings of the International Symposium on Magnet Technology, Stanford University.
- Funston, H.D. 1971. Nucl. Instr. and Meth. 94, 443.
- Gardner, E. and Lattes, C.M.G. 1948. Science 107, 270.
- Garwin, R.L. *et al.* 1956. Phys. Rev. 105, 1415.
- Gross, E.E. 1957. UCRL-3330, unpublished Thesis.
- Harrison, R.W. and Lobb, D.E. 1968. TRIUMF Internal Report VPN-68-7.
- Hansford, R.N. 1965. Atomic Energy Research Establishment, Harwell Report R4869.
- Hirt, W. *et al.* 1969. CERN Report CERN 69-24.
- Hodges, T.A. 1970. TRIUMF Internal Report VPN-70-17.
- Holland M.M. *et al.* 1971. "Design of Secondary Beam Channels for the Nevis Synchrocyclotron Conversion Program." Unpublished memo from L.M. Lederman.
- Hughes, V.W. *et al.* 1971. LASL Internal Report LA-4474-MS.
- Hutson, R. 1970. Private communication to R.W. Harrison.
- Ignatenko, A.E. *et al.* 1958. Soviet Physics JEPT 35(8), 621.
- Jakobson, M. 1968. LASL Internal Report MP-6/MJ-1.
- Krienen, F. 1957. CERN Report CERN 57-28.
- LASL Staff. 1964. LASL Report, "A Proposal for a High Flux Meson Facility."

- Landau, L.D. and Lifshitz, E.M. 1962. *The Classical Theory of Fields*. (Pergamon Press, London; Addison-Wesley Publishing Co. Inc., U.S.A.)
- Lattes, C.M.G. *et al.* 1947. *Nature* 160, 453.
- Lee, T.D. and Yang, C.N. 1956. *Phys. Rev.*, 104, 254.
- Lillethum, E. 1962. *Phys. Rev.* 125, 665.
- Lobb, D.E. 1972a. "The Change in Beam Spot Size Due to Second-Order Effects in a First-Order Achromatic Beam Transport System." *Nucl. Instr. and Meth.* In press.
- Lobb, D.E. 1972b. "Methods for Calculating the Effects of Errors Which Increase the Beam Spot Size at the End of a Beam Transport System," submitted to *Nucl. Instr. and Meth.*
- Mann, R.A. and Rose, M.E. 1961. *Phys. Rev.*, 121, 293.
- Meshkovskii, A.G. *et al.* 1958. *Soviet Physics JETP*, 7, 987.
- Michaelis, E.G. 1970. "The CERN Synchrocyclotron Improvement Program." Presented at the SIN Sommerschule für Mittelenergiephysik, Leysin.
- Morpurgo, M. 1967. CERN Internal Report CERN-SC/4114/141.
- Nagle, D.E. *et al.* 1969. LASL pion production cross section data, private communication to L.P. Robertson.
- Ohnuma, S. 1969. Private communication.
- Ohnuma, S. 1969. TRIUMF Internal Report TRI-69-10.
- Otter, A. 1970(a). Private communication.
- Otter, A. 1970(b). Private Communication.
- Pauli, W. 1933. *Hanbuch der Physik*, Vol. 24/1. (Springer-Verlag, Berlin).
- Pearce, R.M. 1968. TRIUMF Internal Report VPN-68-4.
- Pearce, R.M. 1969. TRIUMF Internal Report VPN-69-10.
- Pearce, R.M. 1970(a). TRIUMF Internal Report VPN-70-10.
- Pearce, R.M. 1970(b). *Nucl. Instr. and Meth.*, 83, 101.

- Penner, S. 1961. Rev. Sci. Instr., 32, 150.
- Petitjean, C. 1969(a). SIN Internal Report TM-09-05.
- Petitjean, C. 1969(b). SIN Internal Report TM-09-06.
- Petitjean, C. 1969(c). SIN Internal Report TM-09-10.
- Petitjean, C. 1970(a). SIN Internal Report TM-09-12.
- Petitjean, C. 1970(b). SIN Internal Report TM-09-13.
- Petitjean, C. 1970(c). SIN Internal Report TM-09-14.
- Petitjean, C. 1971. SIN Internal Report TM-09-23.
- Petitjean, C. and Vécsey, G. 1971. "Application of a Superconducting Solenoid for the SIN Stopped μ Channel Project," submitted to the 1971 Particle Accelerator Conference, Chicago.
- Pifer, A.E. *et al.* 1971. "Copious Production of Thermal Muonium in a Vacuum," submitted to the Colorado Muon Physics Conference Proceedings.
- Reeve, P.A. 1970. Nucl. Instr. and Meth., 81, 207.
- Reeve, P.A. 1972. "Stopped π - μ Channel for Scattering Experiments." Unpublished memo to D. Measday.
- Regenstreif, E. 1964. CERN Report CERN 64-41.
- Robertson, L.P. 1971. Private communication.
- Robertson, L.P. *et al.* 1972. Private communication.
- Sakata, S. and Inoue, T. 1946. Progr. Theor, Phys., 1, 143.
- Salardi, G. *et al.* 1968. Nucl. Instr. and Meth., 59, 152.
- Steffen, K.G. 1964. *High Energy Beam Optics*. (Interscience, New York, 1965).
- Sternheimer, R.M. 1954. Rev. Sci. Instr., 25, 1070.
- Street, J.C. and Stevenson, E.C. 1937. Phys. Rev., 52, 1003.
- Tanabe, K. 1970. Yale University Report 2726-588.
- Van der Meer, S. 1962. CERN Report CERN 62-16.

Vogel, H.F. 1967. LASL Internal Report MP-4/HFV-1.

Vogt, E.W. and Burgerjon, J.J. (Editors). 1966. "TRIUMF, Proposal and Cost Estimate."

Weissenberg, A.O. 1967. *Muons*. (North-Holland Publishing Company, Amsterdam).

Yale Staff. 1964. Yale Blue Report Y-12.

Yukawa, H. 1935. Proc. Phys. Math. Soc. Japan, 17, 48.

Zel'dovich, Ya. B. 1954. Dokl. Akad. Nauk SSSR, 97, 421.

Surname: AL-QAZZAZ Given Name: NADHIM

Place of Birth: MOSUL, IRAQ Date of Birth: January 30, 1935

Educational Institutions Attended, with Dates of Entering and Leaving:

UNIVERSITY OF WALES, UCNW, BANGOR, U.K.	1955 to 1958
BATTERSEA COLLEGE OF TECHNOLOGY, LONDON, U.K.	1958 to 1959
UNIVERSITY OF WALES, UCNW, BANGOR, U.K.	1965 to 1967
UNIVERSITY OF VICTORIA, VICTORIA, B.C.	1967 to present

Degrees, Diplomas, Etc., Awarded, with Dates and Names of Institutions:

B.Sc.	1958	University of Wales, UCNW, Bangor, U.K.
B.Sc. (Honours)	1967	University of Wales, UCNW, Bangor, U.K.
M.Sc.	1970	University of Victoria, Victoria, B.C.

Honours and Awards:

University of Victoria Fellowship, 1968/69, 1969/70 and 1970/71
University of Victoria Scholarship, 1971/72

Publications:

- N. Al-Qazzaz and L.P. Robertson, An Analog Computer for Tracking Beam Envelopes, presented at the Western Regional Nuclear Conference, February, 1969.
- N. Al-Qazzaz and R.M. Pearce, The TRIUMF Stopped Muon Facilities, Colorado Muon Physics Conference Proceedings, Colorado State University, Fort Collins, Colorado.
- N. Al-Qazzaz, Q. Ingram, P.A. Reeve, and L.P. Robertson, A Pion Channel For A π, d Experiment at Berkeley, to be published.

THE UNIVERSITY OF VICTORIA LIBRARY
 MANUSCRIPT DISSERTATION (or THESIS)
 AUTHORITY TO DISTRIBUTE

AUTHOR: This dissertation may be lent or microfilm copies made available:

- (a) Without restriction [REDACTED]
- (b) With the restriction that, for a period of five years (until) the written approval of the following is required:
 - (1) The Chairman, School of Graduate Studies
 - (2) The Author
 - (3) both the Chairman, School of Graduate Studies, and the Author

BORROWERS: The borrower undertakes, by signing below, to give proper credit for any use made of the dissertation, and to obtain the consent of the author if it is proposed to make extensive quotations, or to reproduce the dissertation in whole or in part.

Signature of Borrower	Address	Date